Material Property Evolution of Underfills Encapsulants, Electronic Molding Compounds, Thermal Interface Materials and Magnetic ACAs

by

Yunli Zhang

A dissertation submitted to the Graduate Faculty of
Auburn University
in partial fulfillment of the
requirements for the Degree of
Doctor of Philosophy

Auburn, Alabama
Aug 9, 2025

Keywords: Electronic packaging, Accelerated Life Testing, High temperature aging, Material property evolution, Underfill encapsulants, Epoxy molding compound, Viscoelasticity, Flipped-chip BGA, QFN, Fatigue performance, Thermal management, Reliability assessment

Approved by

Dr. Pradeep Lall, Chair, MacFarlane Endowed Distinguished Professor of Mechanical Engineering and Director, Electronics Packaging Research Institute
Dr. Maria Auad, Charles E. Gavin III Distinguished Professor, Chemical Engineering
Dr. Daniel Harris, Associate Professor of Mechanical Engineering
Dr. Edward Davis, Associate Professor of Material Engineering
Dr. Bart Prorok, Program Chair and Professor, Material Engineering

Abstract

The evolution of material properties in electronic packaging plays a critical role in the reliability of semiconductor devices operating in harsh environments. This dissertation investigates the thermo-mechanical behaviors of underfill encapsulants, epoxy molding compounds (EMCs), thermal interface materials (TIMs), and magnetically oriented anisotropic conductive adhesives (ACAs), emphasizing their viscoelasticity, thermal stability, and interfacial integrity under high-temperature aging.

Underfill materials, critical in flip-chip technology, were characterized for their ability to mitigate coefficient of thermal expansion (CTE) mismatches between silicon dies and organic substrates. Accelerated aging tests revealed the degradation mechanisms affecting their mechanical properties and thermal reliability. DMA analyses identified changes in storage modulus, loss modulus, and glass transition temperature (Tg), demonstrating their temperature-dependent viscoelastic behavior.

For EMCs, long-term aging studies highlighted the influence of filler content and microstructure on thermal and mechanical properties. High silica filler concentrations, exceeding 80%, contributed to superior thermal stability but introduced challenges in fatigue performance. Finite element modeling elucidated stress distributions at the wire interface, correlating material aging with increased stress accumulation.

TIMs were evaluated for their efficiency in reducing thermal resistance between microelectronic components. Conventional greases and phase-change materials demonstrated limitations in high-power applications due to viscosity-induced reliability issues. Novel TIM formulations incorporating carbon-based fillers, such as carbon nanotubes and graphene, exhibited

superior thermal conductivities, though their widespread adoption remains constrained by cost considerations.

Magnetically oriented ACAs were explored for their potential in flexible and stretchable electronics. By aligning conductive particles under a magnetic field, these materials achieved directional conductivity and robust mechanical performance. Experimental and finite element studies demonstrated enhanced interconnect reliability under mechanical and thermal cycling.

This work provides valuable insights into material design and selection strategies for electronic packaging, addressing challenges posed by elevated temperatures and mechanical stresses. The findings contribute to the advancement of packaging technologies, enabling reliable performance in applications ranging from consumer electronics to automotive and aerospace systems.

Acknowledgments

First and foremost, I would like to express my deepest gratitude to my advisor, Dr. Pradeep Lall, for providing me with the invaluable opportunity to pursue my Ph.D. under his mentorship. His unwavering guidance, patience, and intellectual rigor have been instrumental in shaping not only my research but also my academic and professional growth. Dr. Lall has given me the incredible opportunity to participate in multiple cutting-edge research projects, including four Semiconductor Research Corporation (SRC) projects, the NextFlex project, and several collaborations with industry-leading companies. These experiences have been invaluable in deepening my technical expertise and broadening my understanding of real-world engineering challenges.

Beyond research, Dr. Lall has actively encouraged me to engage with the broader academic community, providing me with numerous opportunities to attend SRC's Annual Review, Techcon, ITHERM, InterPACK, and ECTC conferences. Through these experiences, I was able to present my work, exchange ideas with leading experts, and gain insights into the latest advancements in the field. His persistent encouragement to publish my research and participate in technical conferences has helped me develop both my scholarly contributions and professional confidence. His dedication to mentorship, openness to new ideas, and commitment to pushing boundaries in research have been truly transformative. I am immensely grateful for his unwavering support, trust in my abilities, and the countless hours he has invested in guiding me through this journey. I would also like to extend my sincere appreciation to my doctoral committee members: Dr. Maria Auad from Chemical Engineering, Dr. Daniel Harris from Mechanical Engineering, and Dr. Edward Davis from Materials Engineering. Dr. Auad's course was my gateway into the world of polymers science, providing me with a strong foundation in polymer science and engineering that became

essential for my research. Her guidance deepened my understanding of polymer behavior and applications. Both Dr. Davis and Dr. Auad provided tremendous support in the experimental aspects of my research, allowing me to perform extensive material characterization experiments, which significantly contributed to my work. Their expertise and willingness to offer hands-on guidance in the lab played a crucial role in refining my research methodologies. I am also incredibly grateful to Dr. Harris, whose support enabled me to continue my exploration of thermal science, a field closely aligned with my master's research. His encouragement and insights reinforced my passion for this subject and provided me with opportunities to build upon my prior knowledge in meaningful ways. I feel privileged to have learned from such distinguished scholars, whose mentorship has been instrumental in my academic journey.

I am profoundly grateful to the Auburn Electronics Packaging Research Institute (AUEPRI) and all its sponsors for their financial support, which made my research possible. Their commitment to advancing research and innovation has played a crucial role in my academic progress.

A heartfelt thank you goes to my father, Zhang Lan, and my mother, Yu Weifen, whose unconditional love, sacrifices, and unwavering belief in me have been the foundation of my perseverance. Their encouragement, care, and unshakeable faith in my abilities gave me the courage to pursue my dreams far from home. The journey of studying abroad has been filled with challenges but knowing that I have their unconditional support and warmth, even from thousands of miles away, has been my greatest source of strength. They have always placed my education and aspirations above everything else, making countless sacrifices to ensure that I have the opportunities they never had. Words cannot express the depth of my gratitude for their constant

love and the values they instilled in me—resilience, integrity, and the pursuit of excellence. This achievement is as much theirs as it is mine.

I would also like to extend my appreciation to the technical and administrative staff at Auburn University, including Mr. Jason Smith, Ms. Elizabeth Campbell, and Mr. Josh Pearson, for their invaluable assistance with laboratory equipment, logistics, and administrative matters. Their support has made my research experience significantly smoother. A special note of thanks to Dr. Jeff Suhling, whose expertise and guidance have strongly influenced my research direction and my Ph.D. journey.

A significant part of my Ph.D. journey has been shaped by the collaborative and stimulating research environment fostered by my lab mates and colleagues. I am incredibly grateful to Haotian Wu, Jin Wu, Jun Chen, Xin Wei, Jinesh Narangaparambil, Nakul Kothari, Tony Thomas, Hyesoo Jang, Madhu Kasturi, Aathi Raja Ram Pandurangan, Ved Soni, Vishal Mehta, Mrinmoy Saha, Sungmo Jung, Padmanava Chowdhury, Fatahi Musa, Md Golam Sarwar, Shriram Kulkarni, Daniel Karakitie, and Aditya Harsha. Their camaraderie, support, and willingness to exchange ideas have made this journey not just intellectually rewarding but also deeply enjoyable. The moments of collaboration, brainstorming, and even lighthearted discussions have enriched my experience beyond measure. Thank you for standing by me through both the highs and lows, celebrating successes and overcoming setbacks together.

Finally, I would like to dedicate this dissertation to all of you—my advisor, committee members, mentors, family, friends, colleagues, and everyone who has played a part in my journey. Your encouragement, guidance, and belief in me have made this endeavor possible and meaningful. This milestone is a reflection of all the support, kindness, and inspiration I have received along the way.

Table of Contents

List of Tables

List of Figures

List of Abbreviations

AEC	Automotive Electronic Council
BGA	Ball Grid Array
EMC	Epoxy Mold Compound
FCBGA	Flip Chip Ball Grid Array Packages
FEA	Finite Element Analysis
JEDEC	Joint Electron Device Engineering Council
TIM	Thermal Interface Material
UF	Underfill
MACA	Magnetically-oriented Anisotropic Conductive Adhesive
DIC	Digital Image Correlation
PCB	Printed Circuit Board
CTE	Coefficient of Thermal Expansion
PBGA	Plastic Ball Grid Array Packages

Chapter 1 General Introduction

1.1Review on electronic packaging

1.1.1What is semiconductor microelectronic packaging

Semiconductor microelectronic packaging, established during the Moore's Law era of the 1960s, is traditionally defined as the process of interconnecting, protecting, powering, and cooling devices. However, the role of packaging has evolved significantly with advancements in device integration technologies and changes in end-product systems, such as smartphones.

Today, the ultimate goal of packaging is to create a complete heterogeneous system, where all components are seamlessly interconnected. Thus, a more comprehensive definition of packaging is the process of interconnecting, powering, cooling, and protecting all system components that collectively form the entire system. Electronic packaging serves four major functions in the performance of electronic systems, which include:

1. Interconnect: Interconnection of electrical signals at several levels of packaging.
2. Protect: Mechanical and environmental protection of the components, circuits, and devices.
3. Power: Distribution of power to electronic circuits and devices.
4. Cool: Dissipation of the heat generated by these devices.

These four functions are the basic drivers advancing the state of the art in packaging technology.

1.1.2Devices and Moore’s law

The history of electronic packaging dates back to 1884 with the founding of the American Institute of Electrical Engineers (AIEE). Early advancements in electronics were largely driven by

innovations in radio and wireless systems. In 1895, Guglielmo Marconi conducted the first successful radio transmission, and by 1925, the first demonstration of television had been achieved. World War II further accelerated progress in electronics, culminating in the invention of radar systems in 1940.

A pivotal moment in electronic development occurred in 1947 with the invention of the bipolar transistor by John Bardeen, Walter H. Brattain, and William B. Shockley at Bell Laboratories. This breakthrough paved the way for the development of the first integrated circuit (IC), invented by Texas Instruments in 1958, and the subsequent commercialization of digital ICs by Fairchild Semiconductor.

The establishment of the Institute of Electrical and Electronics Engineers (IEEE) in 1963, following the merger of the AIEE and the Institute of Radio Engineers (IRE), created a professional platform that facilitated further advancements in electronic packaging. Key milestones during this period include the development of semiconductor RAM, dynamic memory cells, and microprocessors. These innovations have consistently increased in performance and decreased in size, aligning with Moore's Law.

As IC chips have become more compact and complex, ensuring their reliability has emerged as a critical challenge. This dissertation addresses these challenges by presenting a novel technique for measuring and predicting the reliability of electronic components.

At the end of 2016, with a world population at 7.4 billion, there were 8 billion connected devices globally.[1] In the following decades, the Internet of Things (IoT), a subset of cyber-physical systems or CPS, would connect more things around the world exponentially. With increasing processing power, reducing costs and sizes of microchips, microchips are well

recognized for the advancement of electronics technology that drive the IoT with phenomenal growth and have transformed almost every facet of daily life.

"Half a century ago, a young engineer named Gordon E. Moore took a look at his fledgling industry and predicted big things to come in the decade ahead. In a four-page article in the trade magazine *Electronics*, he foresaw a future with home computers, mobile phones, and automatic control systems for cars. All these wonders, he wrote, would be driven by a steady doubling, year after year, in the number of circuit components that could be economically packed on an integrated chip,"[2] written by Dr. Chris Mack in IEEE's *The Multiple Lives of Moore's Law*.

Dr. Gordon Moore, a visionary engineer and innovator who cofounded Intel Corporation with Robert Noyce on July 18, 1968, forecasted a bright future of electronics that integrated electronic circuits would become less costly and more powerful over time. On April 19, 1965, 3 years before he cofounded Intel, he predicted the number of transistors on a silicon chip would double every 12 months. Moore's law is updated in 1975 that the number of transistors on a chip would double every 18 to 24 months.

In an interview with IEEE, Moore stated, "I used to give talks about how other industries might have progressed. You know, had the auto industry made progress at the same rate [as silicon microelectronics], you would have gotten a million miles per gallon of fuel, and cars that could go several hundred thousand miles an hour." Intel® 4004 processor, the first general-purpose programmable processor, was built in 1971 and contained 2300 transistors. Fast forward to 2015, the 5th Generation Intel® Core™ Processor is a 14-nanometer (nm) technology with 1.3 billion transistors inside. Comparing to the 4004 processor in 10,000 nm, Intel's 14-nm chips can deliver 3500 times the performance at 90,000 times the efficiency, and at 1/60,000th the cost.[3]

"No exponential ever goes on forever without some kind of disaster happening at the end. Sure it has a limit," Gordon Moore said. "Materials are made of atoms, and we're not too far from where that starts to bite us."[4] Miniaturization may be slowing down. But, through invention and innovation, there are derivative technologies such as micro-electric-mechanical systems (MEMS), flexible and printed electronics, light emitting diodes (LED), photovoltaic solar, silicon photonics, etc., bringing benefits that improve our living standards and sustainability. Those technologies play vital roles in the age of Internet of Things. Moore's law will proliferate and continue on for many years to come.

1.2Reliability of Electronic Packaging

1.2.1Flip Chip Technology

Flip chip technology was invented by IBM in 1960's. This technology, also known as "C4" (Controlled Collapse Chip Connection), is a method for interconnecting dies, such as semiconductor electronic devices, to external circuitry using solder bumps. Initially, it utilized a ceramic substrate with thin-film interconnection conductors deposited onto it. However, due to cost concerns—ceramic substrates costing approximately $100 compared to less than $1 for printed circuit boards—the ceramic substrate was later replaced by printed circuit boards made of thermoset polymer. However, it also increased the CTE mismatch, which is one of the major concerns for reliability issues.

Most people think IBM was the company that pioneered flip chip. It could certainly be that GE were the first to put it in a paper in 1963[21], but it was IBM who actually used it for commercial products in the 1960s. "The process was originally introduced commercially by IBM in the 1960s for individual transistors and diodes packaged for use in their mainframe systems."[3] IBM was also the only company to use it for about 25 years until others also tried.

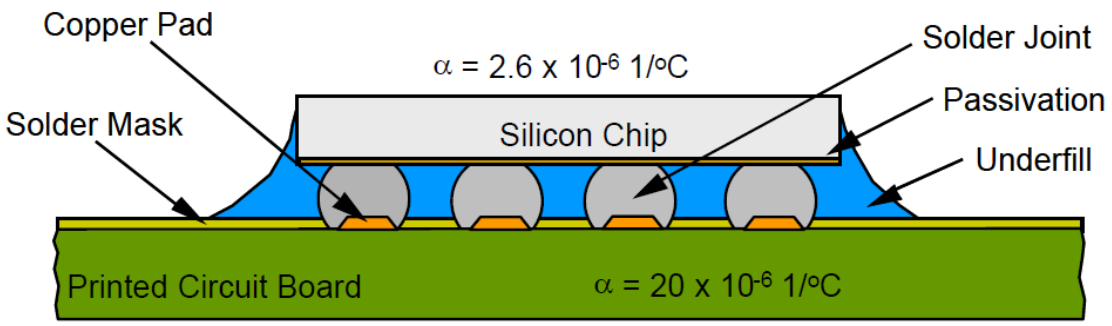

Figure 1-1 Cross-Sectional Schematic of Flip Chip BGA

The cross-sectional schematic of the flip chip is shown in [reference figure or section]. The table provides the material properties of the constituents commonly used in flip chip packages. For ceramic substrates, the CTE is approximately 6 ppm/°C, whereas for glass PCBs, the CTE ranges from 15 to 20 ppm/°C. This significant CTE mismatch greatly increases the risk of structural failure during thermal cycling. Such failures occur due to the stress induced by the large coefficient of thermal expansion (CTE) mismatch.

Table 1-1 CTE of Flip Chip BGA

Material	CTE (10-6 1/°C)
Silicon	2.3
Ceramic Substrate	6
FR4/Glass PCB	15-20
Underfill	25-30
63/37 Solder	21
Copper	17

Underfill is required by most flip chips to avoid rapid solder joint fatigue failures. Since its first use by IBM in the 1970s, underfill systems have been widely adopted by industry following the movement from ceramic substrates to organic substrates, which are the ultimate goal for flip chip technology [4]. Flip chips with organic substrates are often referred to as second generation flip chip technology.

Underfill materials are glass filler filled epoxy. The percentage of filler content is usually around 60% - 70%. However, the CTE of epoxy alone is high The CTE of the cured epoxy resin under glass transition temperature is typically in the range of 55–80 ppm/°C[5] and the elastic modulus is lower than 1 GPa. Thus, glass fillers are filled to decrease the CTE and increase the elastic modulus.

1.2.2 **Reliability Issues in Flip Chip**

The typical failure issues in flip chip include:

- Solder joint fatigue
- Underfill Delamination
- Die Cracking
- Die Cratering
- Underfill Cracks
- Board Cracks

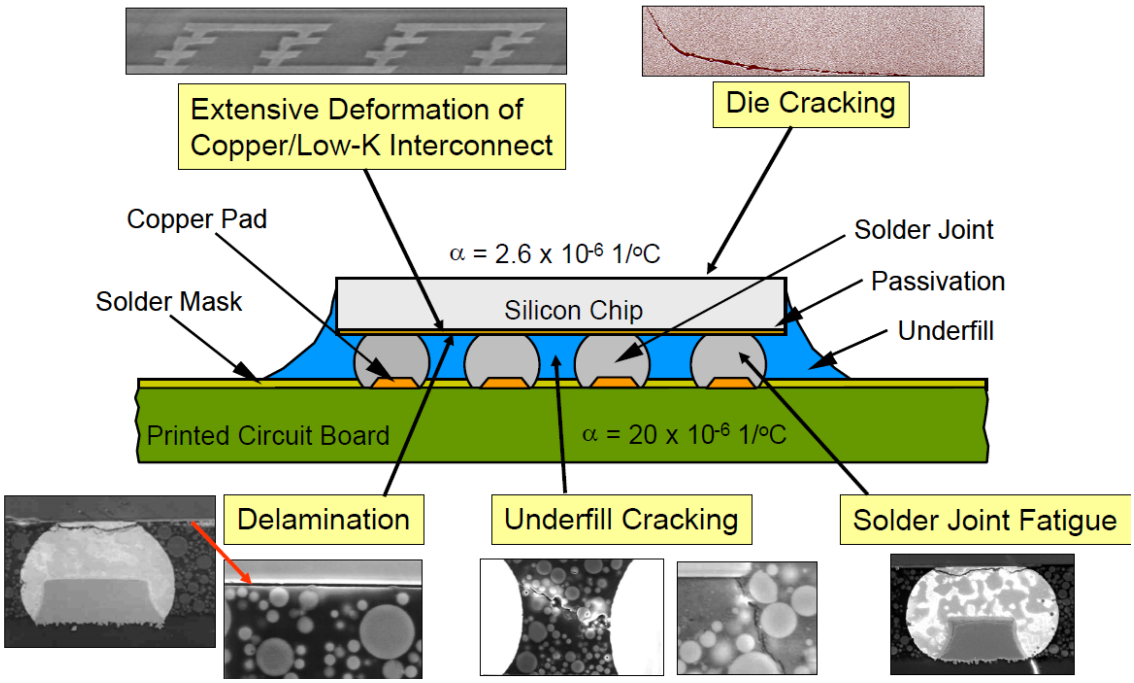

Figure 1-2 Flip Chip Mechanical and Reliability Concerns

The figure highlights several typical failure modes in flip chip, including deformation of copper/low-k interconnects, die cracking, delamination, underfill cracking, and solder joint fatigue. The copper/low-k interconnect structure inside the silicon chip is prone to significant deformation under thermal or mechanical stress, as shown in the top-left image. On the top-right, die cracking is depicted, often resulting from thermal expansion mismatches, high mechanical loads, or defects introduced during fabrication.

At the interface of the packaging structure, delamination can occur, particularly between the underfill material and the silicon die or solder mask. Specifically, the delamination between the underfill and the silicon chip occurs at the passivation layer of the chip. This observation indicates that the fracture is cohesive in nature, meaning the failure occurs within the material (e.g., the passivation layer) rather than at the interface between two different materials. Such cohesive fractures are often a result of material weakness, high stresses, or environmental degradation within the passivation layer, which compromises its structural integrity under thermal or

mechanical loading. Cracking of the underfill material, which often arises due to thermal cycling or mechanical fatigue, can significantly impact the overall reliability of the package. Furthermore, solder joint fatigue, illustrated at the bottom-right, involves the propagation of cracks at the top of solder joints caused by repetitive thermal cycles or mechanical stresses.

It also highlights the mismatch in the coefficients of thermal expansion (CTE) between different materials, such as the silicon chip with a CTE of 2.6×10^{-6}/°C and the printed circuit board (PCB) with a much higher CTE of 20×10^{-6}/°C. This thermal expansion mismatch is a primary driver of many failure mechanisms.

An analytical estimate of the solder joint shear strain (γ) can be found by using the distance to neutral point approximation (DNP):

$$\Delta\gamma = \frac{(\alpha_{pcb} - \alpha_{sc})\Delta T}{h}\,[D.N.P] \qquad \textbf{Equation 1-1}$$

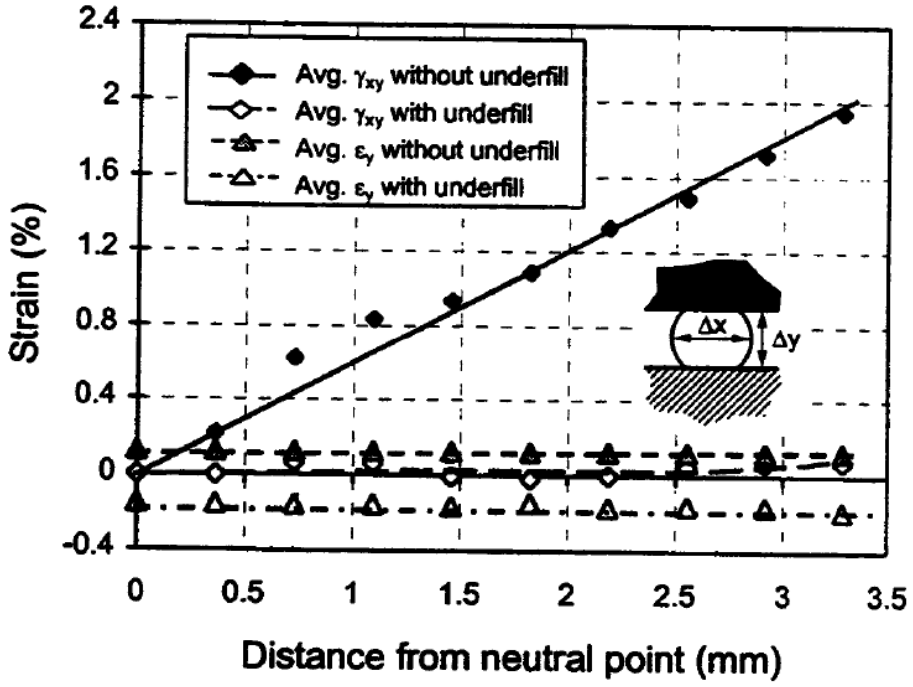

Figure 1-3 Flip Chip - Strain Data

The strain data of flip chip is shown in Figure 1-3 : . It shows the strain without underfill could be accurately predicted by DNP relation. For Flip Chip on laminate packaging, the trends can be predicted accurately when no underfill is used. However, the trend is predicted incorrectly when underfill is applied. Despite this, underfill is essential to achieve the necessary reliability for the package under thermal and mechanical stress. As a result, the standard DNP (Distance from Neutral Point) formula is not suitable for Flip Chip configurations with underfill. Instead, Finite Element Analysis (FEA) based predictions are required to obtain accurate results and ensure reliability.

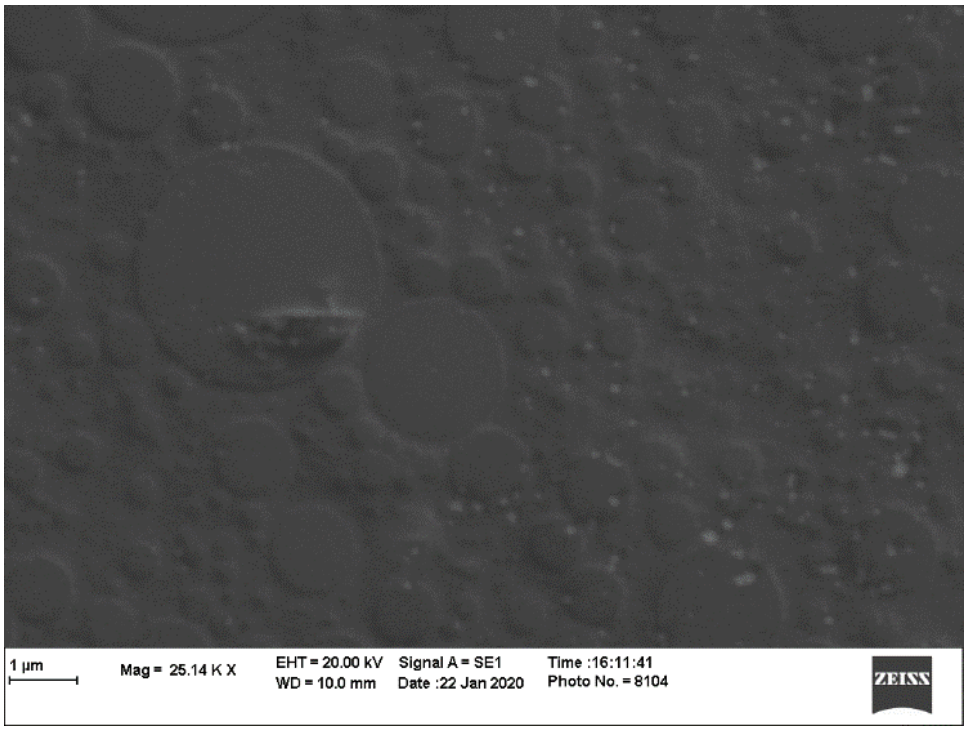

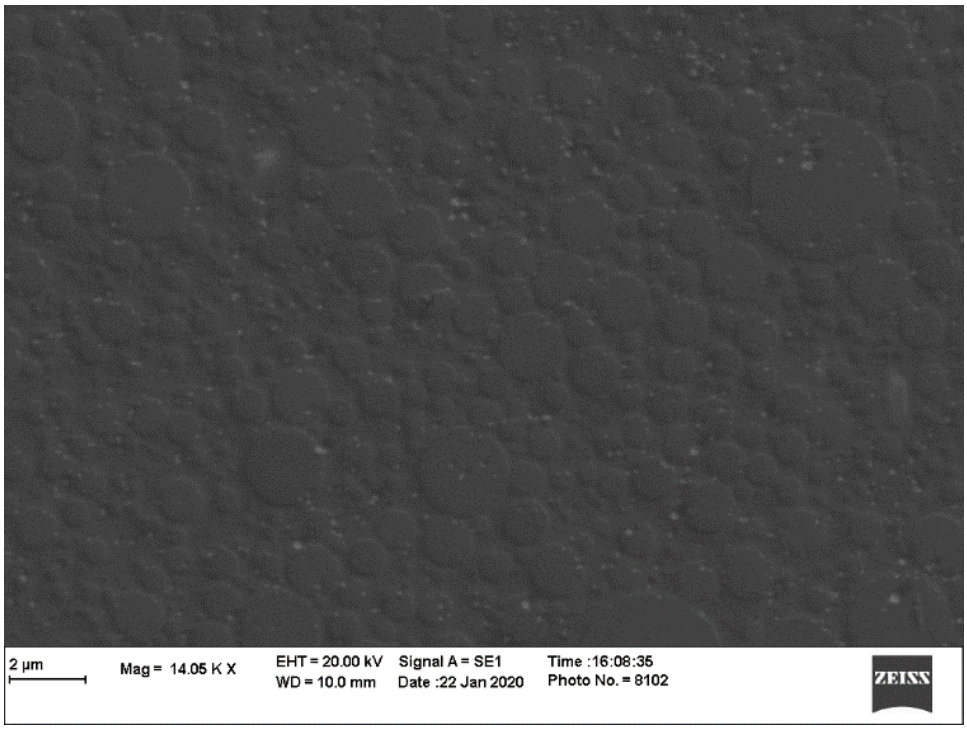

Figure 1-4 SEM image for UF Encapsulants

1.2.3 Flip Chip Mechanical and Reliability Concerns in Harsh Environments

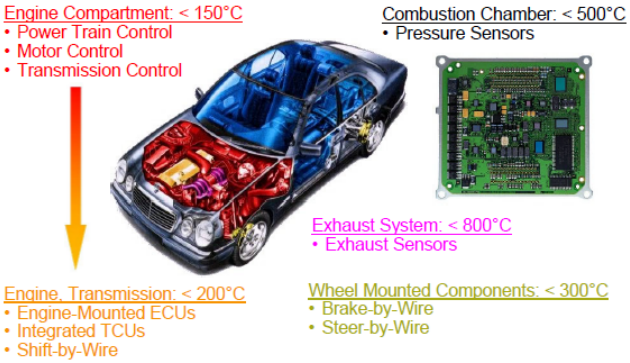

Consumer	0 to 100 °C
Military/NASA	-55 to 125 °C
Well Logging (Oil and Gas)	75 to 225 °C
Geothermal Walls	200 to 350 °C
Gas Turbine Engines	-55 to 1200 °C
Space (Surface of Mars)	-120 to 20 °C
Space (Jupiter Multi-Probes)	-180 to 380 °C
Automotive and Other Ground Vehicles	-40 to 125 °C
Automotive (Passenger Compartment)	-40 to 85 °C
Automotive (Underhood Remote)	-40 to 105 °C
Automotive (Underhood)	-40 to 125 °C
Automotive (On-Engine)	-40 to 150 °C
Automotive (On-Transmission)	-40 to 175 °C
Automotive (Wheel Based)	-40 to 250 °C
Automotive (Exhaust)	-40 to 800 °C

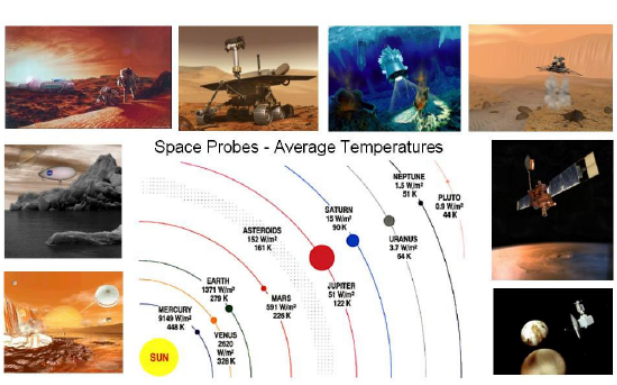

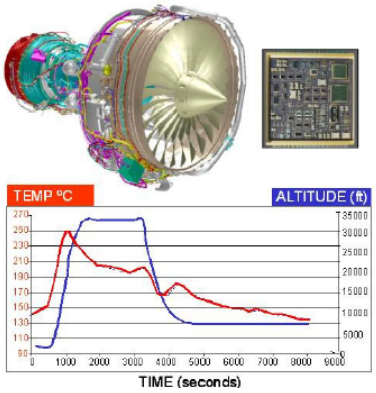

Figure 1-5 Harsh Environments for Automotive andAerospace

Temperature ranges and requirements for various industries, including automotive, aerospace, and space exploration, are shown in Figure 1-5. In the automotive sector, different components operate under specific temperature limits: the engine compartment works below 150°C and houses systems such as powertrain control, motor control, and transmission control. Engine transmission systems, which include engine-mounted ECUs, integrated TCUs, and shift-by-wire systems, operate below 200°C. The exhaust system can reach up to 800°C, while wheel-mounted components like brake-by-wire and steer-by-wire systems function under 300°C.

It also shows the temperature ranges for various applications. Consumer electronics operate between 0 to 100°C, from the freezing point of water to boiling water, while military and NASA systems withstand -55 to 125°C, which is called harsh environment. Extreme conditions are seen in geothermal walls (200 to 350°C) and gas turbine engines (-55 to 1200°C). Space applications, such as Mars surface exploration, operate within -120 to 20°C, and Jupiter multi-probes endure temperatures from -180 to 380°C. Automotive systems have varied temperature ranges: passenger compartments (-40 to 85°C), underhood components (-40 to 125°C), on-engine components (-40 to 150°C), wheel-based components (-40 to 250°C), and exhaust systems (-40 to 800°C).

It also highlights aerospace and space exploration applications. Pictures of space probes and rovers demonstrate the harsh environments these systems endure, with a chart showing average planetary temperatures, from Mercury's 340 K to Pluto's 44 K. A detailed depiction of a gas turbine engine emphasizes the high-temperature demands in aerospace. Lastly, a graph presents the relationship between temperature and altitude, showcasing how aerospace systems are designed to operate in extreme atmospheric conditions.

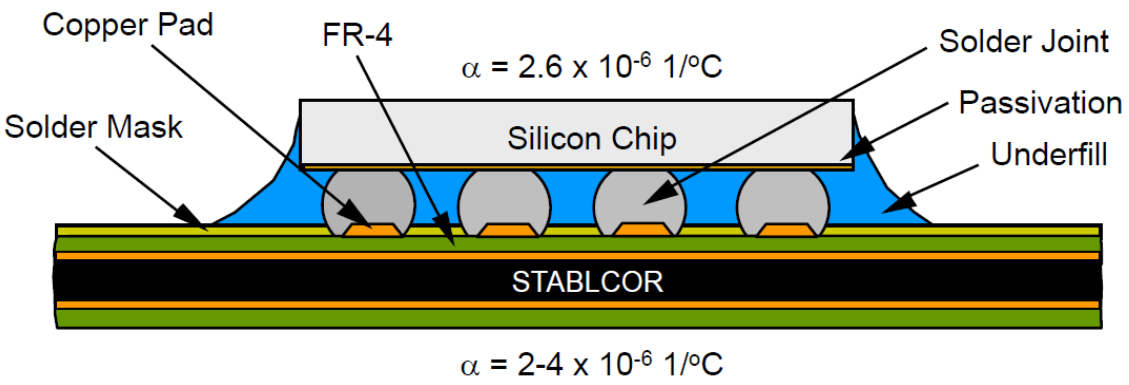

Figure 1-6 Flip Chip on Laminate

The purpose of Underfill is to decrease the CTE mismatch between silicon chip and printed circuit board. In addition to the use of underfill encapsulants, further improvements in the reliability of flip chip on laminate assemblies can be obtained by reducing the CTE of the substrate material. An example for obtaining laminated substrates with extremely low thermal expansion coefficients (similar to silicon) has been established in the 2000s, using the trade name STABLCOR [6]. In the developed approach, hybrid laminates are formed that include a combination of standard glass fiber reinforced resin layers with carbon fiber reinforced resin layers. The carbon fiber based central core (STABLCOR) features both high stiffness and high thermal conductivity, as well as near zero thermal expansion coefficient. The outer top and bottom regions are typical glass fiber reinforced FR-4 lay-ups, which can contain multiple layers with patterned copper traces. Because of the extremely low expansion coefficient of the carbon fiber core and the bonded nature of the laminate, the surface CTE of the hybrid laminate PCB stack-up is typically in the range of 2.0-4.0 ppm/°C over the temperature range of -55 to 150 °C, which is much lower than the typical 13.0-20.0 ppm/°C seen with standard FR-4 based laminates. In addition, the high stiffness of the carbon fiber-based core can help reduce PCB warpage issues, as well as vastly improve the net heat conduction characteristics of the PCB substrate.

Using Low CTE Hybrid Composite Laminate Technology, experimental thermal shock reliability tests have been conducted across a temperature range of –55°C to 150°C using 5 x 5 mm Daisy Chain Flip Chip Test Dies (PB8). These tests demonstrated an over 8x improvement in thermal cycling solder joint reliability with the STABLCOR substrate compared to conventional FR-406 and NELCO substrates. Notably, significant reliability was achieved with the new substrate material even without the use of underfill.

CTE measurements on the low-expansion laminates were performed using strain gauges, showing that the outer layer PCB expansion coefficient ranged from 1.5 to 4.1 x 10^{-6}/°C over the temperature range of –55°C to +150°C. These values closely match the CTE of silicon across the entire temperature range, supporting the observed improvements in reliability when utilizing low thermal expansion core assemblies.

1.3 Introduction to thermal management

1.3.1 What is thermal management

Thermal management of electronics involves maintaining operating temperatures below a certain temperature during usage of the electronic products. The need for thermal management is driven by two important factors: electrical performance and reliability. In modules with silicon chips, to achieve the specified performance, reliable operation of chips requires maintaining their continuous operation temperatures below about 85°C. Packaging to achieve these performance and reliability goals relies on a combination of thermal materials, interfaces, and geometries, as well as interconnections between chips and package substrates with desired electrical, thermal, and mechanical properties.

This section focuses on heat removal from silicon ICs by thermal technologies. The goal of thermal management is to maintain the silicon IC junction temperature (T_j) at or below an

acceptable value to ensure device performance and reliability, typically about 85°. A common nomenclature in use is to separate out thermal solutions into (a) package thermal solutions, that is, thermal management features included as part of the packaging process; and (b) system thermal solutions, that is, system-level cooling solutions potentially used to cool more than one package. Thermal management can be effectively explained using the example of high-power devices. An example of thermal architectures used for cooling a high-power device is shown in figure. In the example, it is reasonable to assume that the bulk of the heat from the die is transferred in the direction illustrated. There are two significant focus areas that drive thermal management challenges:

1. Driven by transistor scaling, the overall local power densities (aka: hot spots) increase generation over generation.

2. With the demand for heterogeneous integration on package, different (stacked and unstacked) dice have different die heights/warpage profiles, different surface finish on the inactive side of the die, leading to a wide range of thermal hot spot locations within the silicon. This poses a significant challenge to optimizing package thermals.

Thermal resistance models are typically used in analyzing and optimizing the thermal performance of a package and system thermal configuration. Advances in package thermal resistance are traditionally measured in terms of an area of normalized resistance, R_{jc}, defined as:

$$R_{\mathrm{jc}} = \frac{\left(T_{\mathrm{jmax}} - T_{case}\right)}{P} \times A_{die} \qquad \text{Equation 1-2}$$

Where P is the power dissipated uniformly on the die, $T_{j\mathrm{max}}$ is the maximum die temperature; and T_{case} is a typical point on the heat spreader or the heatsink.

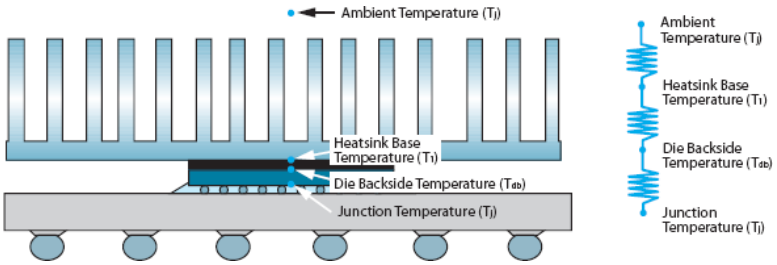

Figure 1-7 Resistance network in bare die architecture

1.3.2Thermal interface material

Thermal interface materials are materials with higher thermal conductivity than air, used to fill the interface between mating surfaces to decrease contact resistance. They are used as the interfaces between mating interfaces, such as those between the chip and lid (as seen in Figure 1-7), or between the lid and the heat sink, in order to decrease contact resistance. *Contact resistance* is thermal resistance that occurs between two adjacent solid bodies as a result of surface imperfections and non-uniformities. Although the chip or lid surfaces appear smooth, a microscopic examination of the surfaces shows characteristic roughness profiles, as illustrated in Figure **1-8**, for a lid surface. The roughness is about 0.5–1.25 microns for the copper lids used in high-end server packages and two orders of magnitude lower at about 25–30 nm for silicon chips. If no TIM is present between the chip and the lid, air would fill the microscopic peaks and valleys. With air's thermal conductivity of 0.027 W/m · K, the thermal resistance across the air gap is very large.

A typical TIM assembly architecture is shown in Figure 1-8, illustrating two different interface materials for effective heat dissipation from active chip to the heat sink. A thin layer of thermal interface materials (TIMs), e.g., TIM1 between the chip and the heat spreader, and TIM2 between the heat spreader and the heat sink, is introduced to create strong adhesion between the surfaces. The surface asperities greatly limit the contact between solid surfaces (e.g., die–heat

spreader and heat spreader–heat sink), undermining the thermal conduction. TIMs fill the gap between the asperities to reduce the contact thermal resistance.

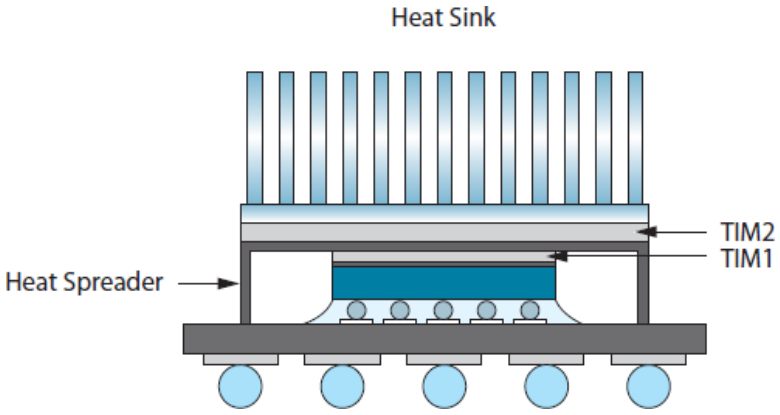

Figure 1-8 Schematic illustration of TIM architecture: (a) TIM1 between the chip and the heat spreader, and (b) TIM2 between the heat spreader and the heat sink.

1.4Fundamentals of polymer materials

1.4.1What is polymer and why

Polymer science was born in the great industrial laboratories of the world of the need to make and understand new kinds of plastics, rubber, adhesives, fibers, and coatings. Only much later did polymer science come to academic life. Perhaps because of its origins, polymer science tends to be more interdisciplinary than most sciences, combining chemistry, chemical engineering, materials, and other fields as well.

Chemically, polymers are long-chain molecules of very high molecular weight, often measured in the hundreds of thousands, where the “poly” means many and “mer” means repeating units. For this reason, the term “macromolecules” is frequently used when referring to polymeric materials. The trade literature sometimes refers to polymers as resins, an old term that goes back before the chemical structure of the long chains was understood.

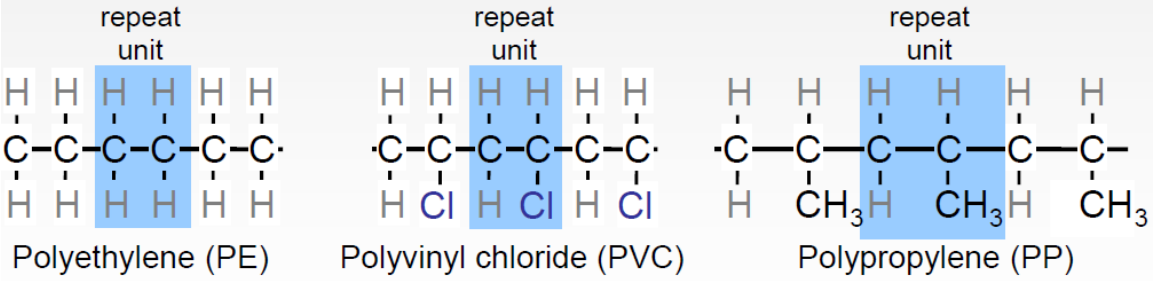

Figure 1-9 Typical polymers

The first polymers used were natural products, especially cotton, starch, proteins, and wool. Beginning early in the twentieth century, synthetic polymers were made. The first polymers of importance, Bakelite and nylon, showed the tremendous possibilities of the new materials. However, the scientists of that day realized that they did not understand many of the relationships between the chemical structures and the physical properties that resulted. The research that ensued forms the basis for physical polymer science.

1.4.2Thermoplastic vs thermoset

Those polymers that can be heat softened in order to process into a desired form is called a Thermoplastic. Waste Thermoplastics can be recovered and re fabricated by application of heat and pressure (example: polystyrene, polyolefins (polyethylene, polypropylene), etc. Thermosets are polymers whose individual chains have been chemically linked by covalent bonds during polymerization or by subsequent chemical or thermal treatment during fabrication. These crosslinked networks resist heat softening, creep and solvent attack, but cannot be thermally processed. Such properties make thermosets suitable materials for composites, coatings and adhesive applications. (examples: epoxy, phenol, unsaturated polyesters)

1.4.3Mechanical Properties

Crystallization is an example of a first-order transition, in this case liquid to solid. Most small molecules crystallize, an example being water to ice. Thus this transition is very familiar. A less classical transition is the glass–rubber transition in polymers. At the glass transition temperature, Tg, the amorphous portions of a polymer soften. The most familiar example is ordinary window glass, which softens and flows at elevated temperatures. Yet glass is not crystalline, but rather it is an amorphous solid. It should be pointed out that many polymers are totally amorphous. Carried out under ideal conditions, the glass transition is a type of second-order transition. The basis for the glass transition is the onset of coordinated molecular motion is the polymer chain. At low temperatures, only vibrational motions are possible, and the polymer is hard and glassy (Figure 1-10, region 1) (7). In the glass transition region, region 2, the polymer softens, the modulus drops three orders of magnitude, and the material becomes rubbery. Regions 3, 4, and 5 are called the rubbery plateau, the rubbery flow, and the viscous flow regions, respectively.

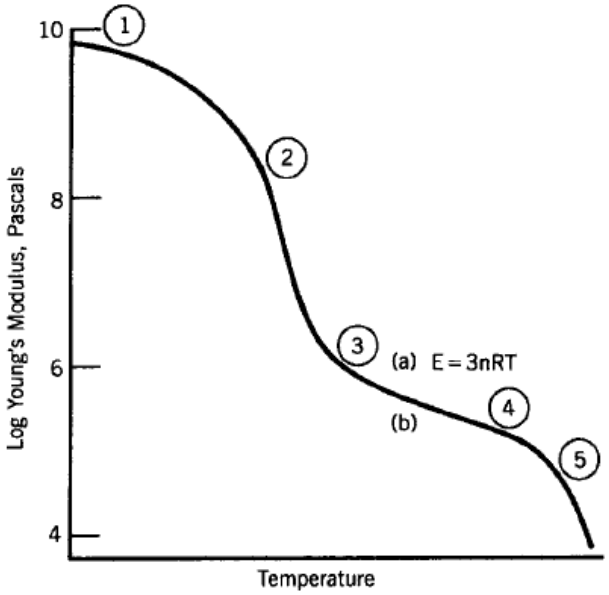

Figure 1-10 Idealized modulus–temperature behavior of an amorphous polymer. Young's modulus, stress/strain, is a measure of stiffness.

Depending on the region of viscoelastic behavior, the mechanical properties of polymers differ greatly. Model stress–strain behavior is illustrated in Figure 1-10 for regions 1, 2, and 3. Glassy polymers are stiff and often brittle, breaking after only a few percent extension. Polymers in the glass transition region are more extensible, sometimes exhibiting a yield point (the hump in the tough plastic stress–strain curve). If the polymer is above its brittle–ductile transition, rubber-toughened, or semicrystalline with its amorphous portions above Tg, tough plastic behavior will also be observed. Polymers in the rubbery plateau region are highly elastic, often stretching to 500% or more. Regions 4 and 5 flow to increasing extents under stress. Cross-linked amorphous polymers above their glass transition temperature behave rubbery. Examples are rubber bands and automotive tire rubber. In general, Young's modulus of elastomers in the rubbery-plateau region is higher than the corresponding linear polymers, and is governed by the relation $E = 3nRT$, in Figure 1-10 (line not shown); the linear polymer behavior is illustrated by the line (b). Here, n represents the number of chain segments bound at both ends in a network, per unit volume. The quantities R and T are the gas constant and the absolute temperature, respectively. Polymers may also be partly crystalline. The remaining portion of the polymer, the amorphous material, may be above or below its glass transition temperature, creating four subclasses of materials. While polyethylene and natural rubber need no further introduction, common names for processed cellulose are rayon and cellophane. Cotton is nearly pure cellulose, and wood pulp for paper is 80 to 90% cellulose. A well-known trade name for poly (methyl methacrylate) is Plexiglas®. The modulus–temperature behavior of polymers in either the rubbery-plateau region or in the semicrystalline region are illustrated further. Actually, there are two regions of modulus for semicrystalline polymers. If the amorphous portion is above Tg, then the modulus is generally

between rubbery and glassy. If the amorphous portion is glassy, then the polymer will actually be a bit stiffer than expected for a 100% glassy polymer.

1.4.4Viscoelasticity and Rheology

The state of the solid depends not only on the forces actually impressed on it but on all the strains to which it has been subjected during its previous existences.

--James C. Maxwell (1866)

During the latter half of the nineteenth century, scientists began to note that a number of materials showed time dependence in their elastic response (silk, gum rubber, etc). After the elastic period they continued deforming ("creep'). Today we call this time dependent response VISCOLEASTICITY, where "VISCO" means time dependent. It is typical of all polymeric materials. Polymers may exhibit mechanical behavior characteristic of either solid or a viscous liquid. If we stretch a crystalline solid (pure elastic), the energy is stored in the chemical bonds. If we apply a shear stress to a viscous fluid, the energy is dissipated in the flow. The actual response depends upon temperature, in relation to the Tg of the polymer and to the time scale of the deformation. Viscoelastic behavior may be characterized by a variety of techniques that record the time dependent response of a polymeric solid, melt, or solution to a periodic perturbation such as the application of a sinusoidal strain or an electrical voltage.

1.4.5**Time -Temperature Superposition**

It is important to know how a material behave (creep or stress relaxation) at a fixed temperature, but over along time period (months, years…). Long time behavior can be evaluated by measuring stress relaxation or creep data over a short period of time but at several different temperatures. Information from each of these different curves may be combined to yield a mater curve at a single temperature by horizontally shifting each curve along the log time scale. This

technique is called time temperature superposition. The importance of these ideas becomes clear when one considers that data can be obtained conveniently over only a narrow time scale, say, from 1 to 10^5 s. The time-temperature superposition principle allows an estimation of the relaxation modulus and other properties over many decades of time. The shift factor a T is defined as the ratio of the real time to reach a particular value of the modulus at some temperature to the reference scale time coordinate, t_r corresponding to the same value of modulus in the master curve at the reference temperature T_r.

Figure 1-12 illustrates the time-temperature superposition principle using polyisobutylene data. The reference temperature of the master curve is 25°C (298K). The reference temperature is the temperature to which all the data are converted by shifting the curves to overlap the original 25°C curve. Other equivalent curves can be made at other temperatures. The shift factor shown in the inset corresponds to the WLF shift factor. Thus, the quantitative shift of the data in the range Tg to Tg × 50°C is governed by the WLF equation, and this equation can be used both to check the data and to estimate the shift where data are missing.

$$a_T = \frac{t}{t_r} \qquad 1\text{-}3$$

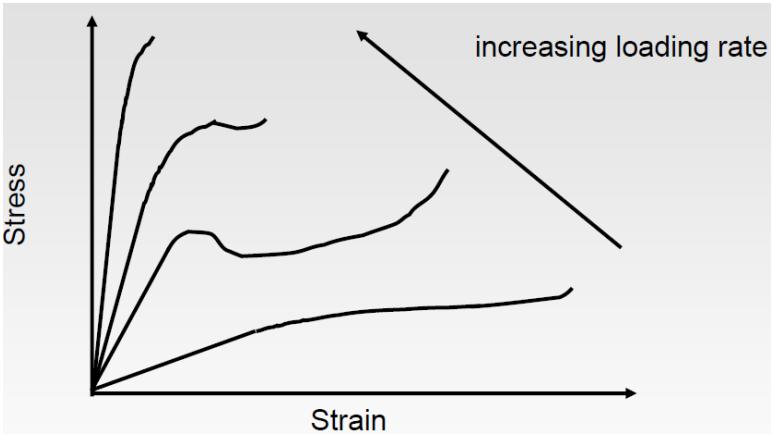

Figure 1-11 Stress vs. Strain experiment: is the deformation rate important?

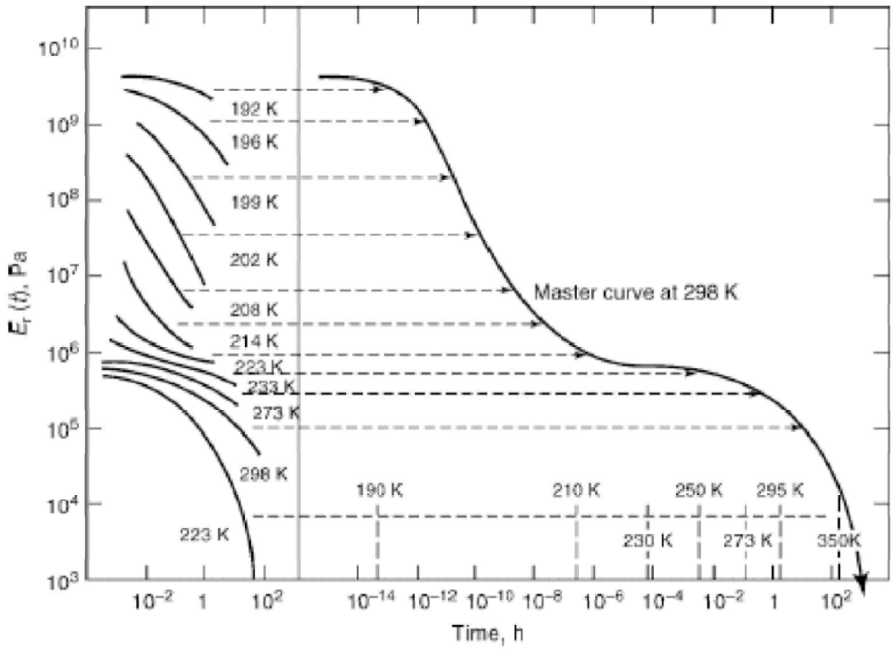

Figure 1-12 The making of a master curve, illustrated with polyisobutylene data. The classical Tg at 10s of this polymer is -70°C (source: Sperling L H. Introduction to physical polymer science[M]. John Wiley & Sons, 2005.)

1.5Research Motivation

When a product performs the functions for which it is designed, the product is said to be reliable. When it does not, it is said to be unreliable. In particular, thermo-mechanical reliability is defined as the probability of the survival of a functional component or product for an expected period of time, when subjected to periodic changes in environment stress or an overstress event that is thermal or mechanical in nature. A few examples include thermal loading, power dissipation, and mechanical shock, such as drop, bending, and vibration. The purchaser of an automobile expects the automobile to start and run when the ignition is turned on. If it does, it is said to be reliable. Also, when maintained properly, the purchaser expects the automobile to function reliably for many years and over 100,000 kilometers of driving. That is considered "long-term" reliability. Similarly, a personal computer is designed to last between five and seven years; an automotive

controller is designed to last between 10 and 15 years; and a defense electronic component is designed to last for over 30 years. Clearly, it is not economically viable to test these devices for reliability for several years before shipping to the customer. To ensure that the electronic packaging will be reliable over an extended period of time, two approaches need to be followed: 1) design the packaging up-front for reliability, and 2) conduct an accelerated test on packages for reliability after the package is designed, fabricated, and assembled. In the first approach, one could predetermine various potential failure mechanisms that could result in product failure. Knowing these fundamental mechanisms, one could create designs and select materials and processes that would minimize or eliminate the chances for failure. Such an up-front design, even before the system is physically built and tested, is called "design for reliability" and is the subject of this chapter.

In the second approach, the system is subjected to accelerated test conditions such as thermal cycling, temperature and humidity cycling, and power cycling after a package is built and assembled. The tests are conducted for short periods of time by applying extreme temperatures, humidity, voltage, and pressure to accelerate the failure processes. This is called testing for reliability, or reliability testing.

Traditional industrial practice involves testing for reliability after the IC and the packages are fabricated and assembled. If problems are found in reliability testing, the IC and the packages are redesigned, refabricated, reassembled, and retested. Such a rebuild and retest process is expensive and time-consuming. Therefore, the design for reliability aims to understand and fix the reliability problems up-front in the design process, even before the IC and the packaged ICs are fabricated.

1.5.1 Temperature effect of electronic packaging failure

Recent advancements in semiconductor device power density, coupled with the emergence of supercomputers, quantum computing, and high-power electronic systems, have increasingly required electronic components to perform reliably in extreme environments. Among these challenges, temperature remains the most critical factor contributing to electronic equipment failures.

The automotive underhood environment exemplifies such demanding conditions, far exceeding those encountered in conventional office settings. These environments require components to sustain higher operating temperatures, endure wider temperature fluctuations, and maintain reliability over extended lifespans. For example, in 2023, the Automotive Electronics Council (AEC) introduced a classification system for automotive electronics, dividing components into four grades (Grade-0 through Grade-3) based on their thermal endurance [22].

Grade-0 components are subject to the most rigorous requirements, capable of withstanding temperature ranges from -40°C to 150°C over 1,000 thermal cycles. Additionally, they must endure prolonged high-temperature exposure, such as 175°C for 1,000 hours or 150°C for 2,000 hours. Grade-1 components, by comparison, are rated for 150°C for 1,000 hours (42 days) or 175°C for 500 hours (21 days). Grades 2 and 3 are designed for less extreme conditions, typically 125°C for 1,000 hours or 150°C for 500 hours. Furthermore, ceramic-packaged components can tolerate up to 250°C for 10 hours or 200°C for 72 hours.

Historically, components used in automotive, and power electronic systems were designed to operate within a temperature range of 55–85°C for lifespans of approximately 3–5 years—far below the stringent requirements set for Grade-0 components in 2014. To meet these heightened

demands, modern packaging materials are engineered with a focus on achieving significantly improved reliability.

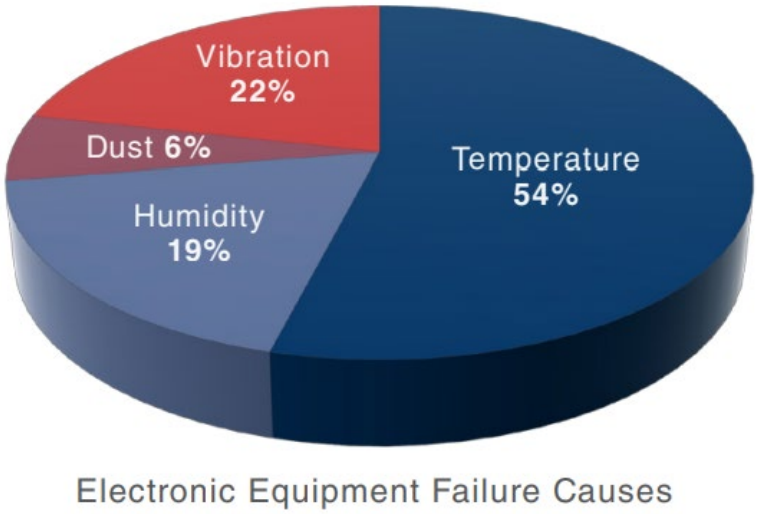

Figure 1-13 Electronic Equipment Failure Causes (Source: Electronic Equipment Failures: Cause, Effect and Resolution)

Chapter 2 Literature Review

2.1Aging effect (high temperature storage) of Epoxy Molding Compounds

Electronic encapsulation materials are quite important in an electronic package for protecting the integrated circuits (ICs) and other electronic components from external forces, such as heat, moisture, pressure and chemical corrosion. Compared with other conventional encapsulation materials such as metals and ceramics, polymer materials have the advantage of low cost and eligibility for mass production.[7] With the development of polymer technology, the reliability of polymer encapsulation materials is no longer a major concern. Materials such as epoxy[2][3],silicone,[4][5]polyimide[6][7]and polysulfide[8][9]have been applied as encapsulants for electronic devices.

Epoxy-based molding compounds (EMC) are commonly used for housing the semiconductor chip and other internal circuitry of electronic packages, in order to provide resistance against mechanical shock, chemical loads, heat, and moisture [16]EMC is a com- posite material consisting of epoxy resin as the matrix, silica as the filler material, hardeners, and other additives [17]A typical EMC contains very high content of silica filler (up to 90%), which helps in attaining desired thermomechanical properties [18]. Figure **2-1** shows a scanning electron microscopy (SEM) image of an EMC specimen, in which the high filler content can be clearly observed. This high filler content offers low shrinkage, and superior chemical and moisture resistance[19]. Fig. 2 shows a schematic diagram of a typical electronic package used for an automotive application. Among all of its components, the one most exposed to the atmosphere is EMC. Therefore, its degradation over time is one of the most relevant aging mechanisms, which could affect the reliability of electronic packages. Aging can be defined as the long-term, irreversible changes that occur in a material due to its exposure to ambient conditions. The changes can be in the structure, composition, and morphology of the material.

Underfill is required by most flip chips to avoid rapid solder joint fatigue failures. Since its first use by IBM in the 1970s, underfill systems have been widely adopted by industry following the movement from ceramic substrates to organic substrates, which are the ultimate goal for flip chip technology[20]. Flip chips with organic substrates are often referred to as second generation flip chip technology. Underfill encapsulants are either thermosetting or thermoplastic polymers, both of which are widely used in industry. Figure 1.4 shows the volume distribution for use of thermoplastic polymers in the United States in 2001, and the electronic packaging market was the largest [21]

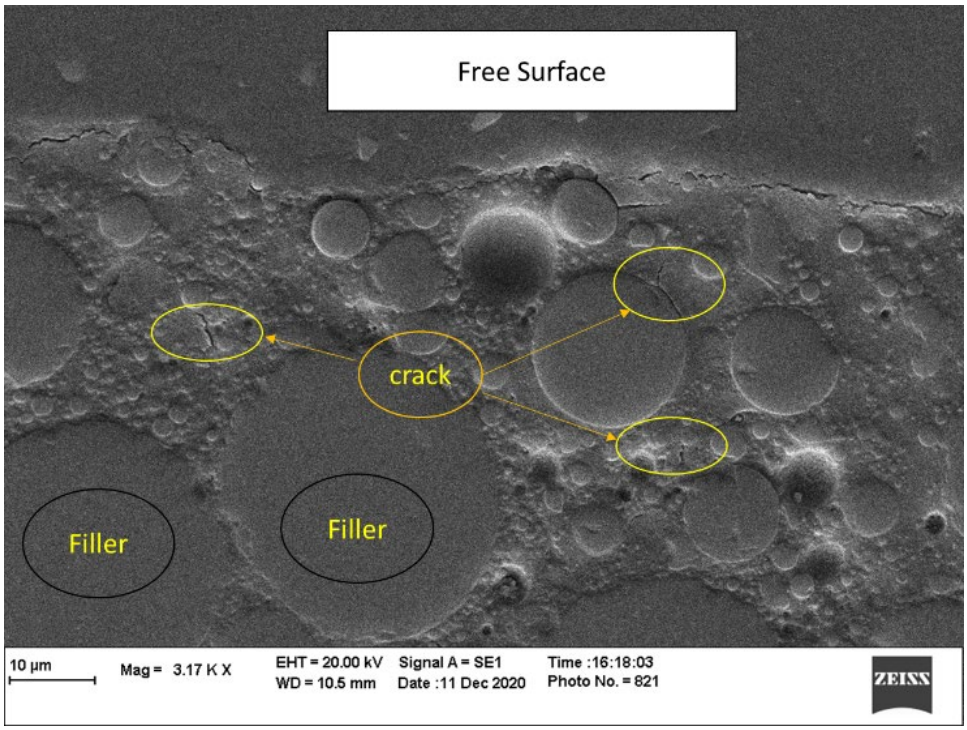

Figure 2-1 Scanning electron microscopy (SEM) image of a typical EMC after 150C 400 days exposure

To solve the CTE mismatch problem, an underfill material is used to fill the gap between the integrated circuit die and the substrate in a flip chip package to improve the solder joint fatigue life [22], [23]. Underfill not only connects the chip and the substrate but also provides an additional thermal path from the chip to the substrate. The introduction of underfill gives the solder interconnections more mechanical robustness, and a significant increase in solder fatigue resistance results [24]. Moreover, underfill promotes evenly distributed and reduced solder joint strains during temperature changes, thus improving solder joint fatigue life, often by factor of 10 or more [24]. The underfill encapsulant also protects the chip from moisture, radiation, and other hostile operating environments such as mechanical shock and vibration.

The mechanical properties of underfill materials have a great influence on the reliability of flip chip packages. For example, Figure 1.5 illustrates finite element prediction of the solder joint

strains in a flip chip assembly subjected to a temperature change from -40 to 125 °C. The strain levels are much smaller when using an underfill with low CTE and high elastic modulus.

2.2Aging Effect of Underfill Encapsulant

Over four decades ago, flip-chip technology was introduced as a means of interconnecting CPU chips in high-performance computers[21]. Today, flip-chip interconnect technology is widely employed, thanks to the advancement of packaging architectures such as flip-chip ball-grid arrays. To enhance the reliability of flip-chip solder joints, underfills are extensively utilized. The primary issue addressed by underfill materials is the discrepancy in coefficient of thermal expansion (CTE), which leads to thermal fatigue and plastic deformation in the solder balls. By mitigating the CTE mismatch between the chip and the substrate during power cycling or ambient thermal cycling, underfill materials help alleviate these concerns.

In general, the CTE of silicon at room temperature is approximately 2.5 x 10^{-6} K^{-1}, while an organic substrate typically exhibits a CTE of 10-20 x 10^{-6} K^{-1} in the plane and over 20 x 10^{-6} K^{-1} out of the plane. As automotive technology has advanced, incorporating features like collision avoidance, pedestrian detection, driver alertness monitoring, lane departure warning, guidance, and navigation, electronic systems are now required to withstand harsh conditions within the automotive underhood environment for extended durations. The Automotive Electronics Council (AEC) classifies automotive electronics into four grades: Grade-0, Grade-1, Grade-2, and Grade-3 [22]. Grade-0 components are expected to operate in temperatures ranging from -40℃ to 150℃, while Grade-1 components are designed to withstand sustained temperatures up to 175℃ for over 1000 hours. The automotive underhood environment poses greater challenges than conventional office settings, demanding higher sustained temperatures, wider temperature extremes, and longer lifespans.

Numerous researchers have explored the behavior of epoxy molding compounds (EMCs) in harsh environments. Recent publications have focused on both numerical and experimental investigations into the performance of electronic packaging materials in such challenging conditions. However, there has been relatively less emphasis on studying the behavior of underfill encapsulants when exposed to sustained high temperatures for extended periods. Epoxy, as a crosslinked thermoset polymer, is designed to operate in a glassy state. The properties of thermoset materials are closely tied to the density of the cross-linking network, which controls the mobility of polymer chains. Higher mobility leads to lower modulus but increased elongation percentage. Conversely, a rigid structure exhibits higher stiffness but greater brittleness, highlighting the inherent conflict between stiffness and brittleness [19], [25], [26], [27], [28]

Typically, polymers can be divided into five distinct regions: the glassy region, glass transition region, rubbery region, viscous transition region, and viscous flow region. The material properties within these regions are influenced by microstructural factors such as crystallinity, the degree of cross-linking, and entanglement. In the case of thermoset polymers, which possess a rigid network structure unable to flow, only three regions are present: the glassy state, the glass transition region, and the rubbery region.

In the glassy state, the modulus is initially high and experiences a slight decrease with increasing aging time. Within the glass transition region, the modulus undergoes a significant drop over a range of temperatures. Finally, in the rubbery region, the modulus shows a slight increase as the temperature rises.

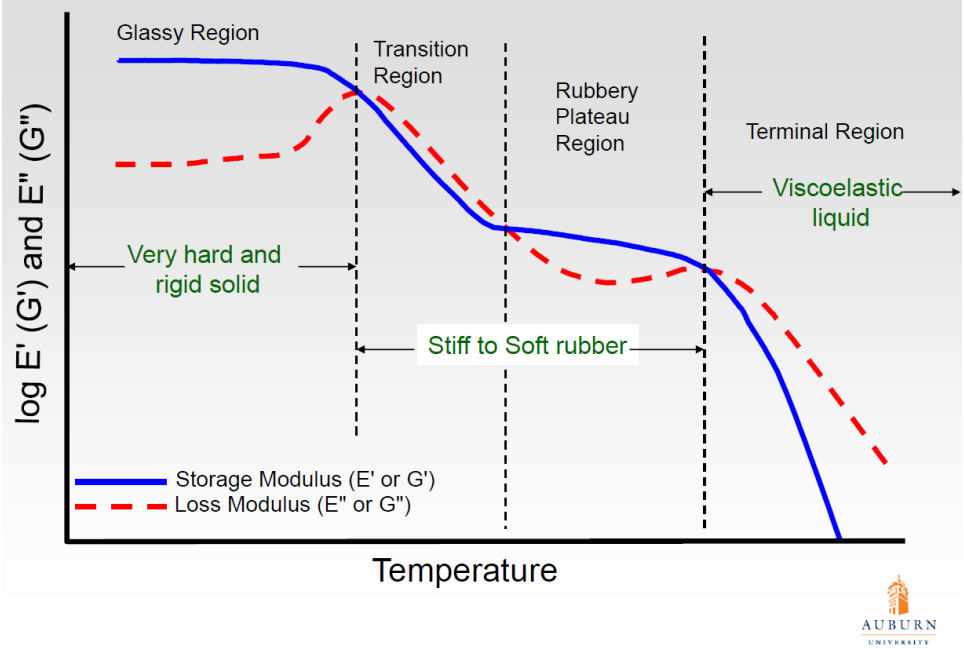

Figure 2-2 Dynamic Temperature Ramp: Material Response

Underfills in some ways are similar to epoxy molding compounds incorporating filler particles in an epoxy matrix. Material systems intended for operation in automotive temperature extremes require high thermal-mechanical stability, high modulus, high impact resistance, and low creep. In addition, the underfill material requires high interfacial fracture toughness at the chip-UF and substrate-UF interface under thermal cycling. Underfill fillers are used to enhance the material properties and strength. In general, the modulus of UFs drops by a factor of 5x to 10x at temperatures higher than the glass transition temperature. Filler materials used in underfills have a higher modulus and a lower coefficient of thermal expansion than epoxy matrix. In comparison with epoxy molding compounds, UF materials generally have a lower filler content and filler size. The filler content for EMC is about 86-percent, while it is 65-percent for UFs. Filler size is more than 50μm for EMC, while it could be only 1~2μm for UFs[29].

UFs have been shown to be viscoelastic materials. It is a material with property between pure elastic and viscous fluid. Perfect-elastic material stores all energy and dissipates nothing, i.e.,

it recovers the deformation completely once the load is removed without a permanent set. A pure viscous fluid dissipates everything and stores no energy. Phase angle between stress and strain is 90 degrees. For viscoelastic material, the phase angle is between 0 to 90 degrees. A popular way to characterize viscoelastic material properties of glass and rubbery state is using the dynamic mechanical analyzer (DMA). Since there is no melting point for thermoset, we conducted dynamic loading test to investigate viscoelastic properties as the function of aging. Storage modulus, loss modulus and Tan δ are measured. Tan δ represents the phase angle between stress and strain. The max of tan δ is used to characterize the glass transition temperature[30], [31], [32], [33].

2.3Thermo-mechanical reliability analysis of packaging system

As discussed above, the silicon die in flip chip technology is connected to the substrate by small solder joints. Eutectic or near eutectic tin/lead (Sn-Pb) solder has been widely used in the electronics industry due to its outstanding solderability and reliability. Due to harmful effects on the environmental and health concerns, recent legislation has been enacted to require the removal of lead from electronics. Several new lead free solders have been developed as alternatives to Sn-Pb solder, such as Sn-Ag-Cu (SAC) alloys [34]. Flip chip solder joints melt completely during the reflow process, but the surface tension in the molten solder supports the chip so that the extent of the joint collapse is controlled by the wettable area of the pads. A solder joint based flip chip interconnection is also referred to as a controlled collapse chip connection (C4). Solder bumps in flip chip assemblies serve as the structural links, electrical connections, and heat dissipation paths between the chip and the substrate. Thus, failure of any of the solder joints will typically result in failure of the entire product.

Among the failure modes present in flip chip assemblies, the major concern is typically the thermal-mechanical fatigue life of the solder joints. Table 1.1 shows the material properties of the

constituents generally used in flip chip packages. During thermal cycling, large shear strains are developed in the solder joints due to the large coefficient of thermal expansion (CTE) mismatch between the silicon die and the substrate, as illustrated in Figure 1.3. Consequently, fatigue cracks often initiate at the edges of the joints and then propagate through the interior, resulting in bump failure. The likelihood of solder bump thermal fatigue failure is related to the chosen solder material, substrate and chip metallization, and the development of intermetallic compounds [35].

2.3.1 The DNP relation

An analytical estimate of the solder joint shear strain (γ) can be found by using the distance to neutral point approximation (DNP):

$$\Delta\gamma = \frac{(\alpha_{pcb} - \alpha_{sc})\Delta T}{h}\,[D.N.P] \qquad 2\text{-}1$$

where α_{pcb} and α_{sc} are the coefficients of thermal expansion of the PCB and silicon chip, respectively, h is the height of the solder ball joints, ΔT is the temperature change, and D.N.P is the distance to the neutral point. The solder joint fatigue life can be estimated by applying failure criteria such as the Coffin-Manson Equation. For example, for SnPb eutectic solder joints the expression is:

$$N_f = 1.29\,(\Delta\gamma)^{-1.96} \qquad 2\text{-}2$$

where N_f is the estimated number of thermal cycles at which the solder joint will fail and $\Delta\gamma$ is the shear strain change during one cycle. From these equations, it can be clearly seen that the solder joint fatigue life can be increased by using a smaller die, increasing the height of the solder ball joints, reducing the temperature change, and minimizing the CTE mismatch between the die and the substrate.

For most flip chip configurations of interest, the thermal fatigue life is unacceptable and early joint failure occurs. Thus, it is necessary to add an underfill encapsulant between the chip

and substrate to assist the solder joints in maintaining the mechanical integrity of the assembly. For Flip Chip on laminate packaging, the trends can be predicted accurately when no underfill is used. However, the trend is predicted incorrectly when underfill is applied. Despite this, underfill is essential to achieve the necessary reliability for the package under thermal and mechanical stress. As a result, the standard DNP (Distance from Neutral Point) formula is not suitable for Flip Chip configurations with underfill.

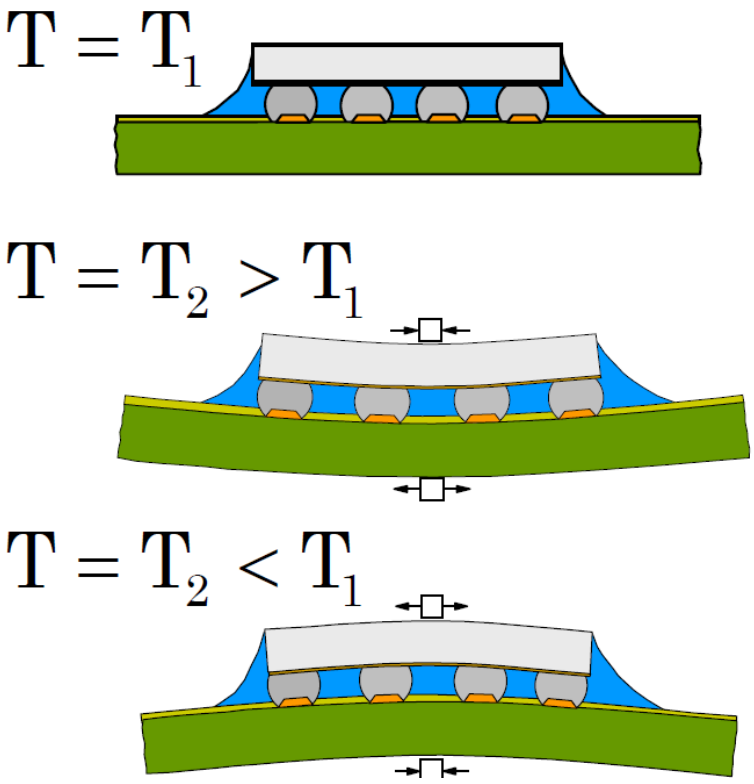

Figure 2-3 Solder Joint Fatigue During Thermal Cycling

2.4*Electronic Packaging Interface and Interface Testing*

In the field of electronic packaging, an interface is a common boundary between different materials or layers. The performance and reliability of electronic packages depend on good interfaces. Typical examples of interfaces are the semiconductor chip/underfill interface, the substrate/underfill interface, the EMC/substrate interface, and the potting/PCB interface.

Interfacial reliability is the ability of an interface to preserve its structural and functional integrity under different operating conditions. Proper handling of such interfaces would ensure good electrical connectivity, along with mechanical stability and heat dissipation. Interfaces play a significant role in ensuring the lifetime or performance of electronic devices because failure points arise there, which may lead to a malfunction of the whole device. Various types of test structure methodologies for characterizations in IC package materials are discussed in [36]. Interfacial failures in electronic packages and the need to understand interfacial strength and evolution have been discussed in detail in [37], [38], [39], [40]

Figure 2 shows the schematic of a typical FCBGA electronic package, highlighting some of the critical interfaces. Interfacial reliability pertains to the integrity and durability of these interfaces under various operational and environmental conditions, such as thermal mismatch, temperature cycling, moisture ingress, mechanical stress, and electrical load, which can degrade interfaces. Interfacial delamination has been one of the major failure modes observed in electronics packaging, and other failure modes include cracking, void formation, and corrosion. Delamination is the separation of layers at the interface due to weak adhesion or high stress.

Besides proper temperature control, curing times, and cleanliness during manufacturing, defects could be avoided, and the interface reliability can be improved. Severe thermal mismatch, mechanical stresses, moisture ingress, chemical incompatibility, and manufacturing defects are some of the severe impacts on reliability at these interfaces. Material selection, surface treatments, encapsulation, conformal coating, design optimization, thermal management, and strict process control are techniques to achieve improved interfacial reliability. In addition, addressing such factors and using such methodologies can substantially improve the overall reliability and

longevity of electronic devices, thus enabling robust performance in various operational environments.

Material selection with matched CTE and high adhesive strength reduces the probability of interface failure from thermal or mechanical stresses. New material development related to advanced interfacial reliability, like low-stress epoxies, nano-fillers, and compliant interlayers, seems very promising. Pretreatment of the surface with plasma cleaning, roughening, or application of adhesion promoters may further improve bond strength and stability. The interfaces can be environmentally protected through encapsulants like epoxy resins, silicones, or polyimides. Conformal coatings can prevent moisture ingress and chemical exposure. Proper heat sinks, vias, and conductive adhesives could avoid thermal stresses and enhance the interfacial stability.

Microelectronic packages consist of multiple bimaterial interfaces that have a significant impact on both device design and reliability. The failure of these interfaces is influenced by both shear and tensile loads, commonly known as "mode-mixity." Although the failure of these bimaterial interfaces has been extensively studied, their performance under fatigue conditions, specifically in relation to mode-mixity, remains inadequately explored. Understanding interfacial delamination is crucial for studying and supporting the design and manufacturing of microelectronic packages. Bimaterial interfaces are commonly found in modern microelectronics and have garnered significant attention. Previous research has primarily focused on studying the behavior of these interfaces under monotonic loading, where failure occurs gradually [41], [42], [43], [44], [45], [46]. Additionally, their reliability has been investigated when exposed to extreme environments, such as high temperatures and humidity [47]The failure observed under monotonic loads provides insights into potential issues arising during the fabrication process due to thermal stresses. However, the real-world reliability of microelectronic devices is also influenced by the

fatigue failure of these interfaces, which occurs under cyclic loading conditions. Fatigue analysis remains a critical area of research and continues to receive significant attention regarding bimaterial interfaces [25], [48], [49], [50], [51], [52], [53], [54], [55]

Understanding interface mechanics involves knowledge of stresses, deformations, and failure mechanisms at interfaces. The interfaces can be subjected to stresses and strains due to thermal expansion, mechanical loading, and environmental causes. These stresses, if exceeding the material properties, will cause deformation and eventually failure. Interfacial delamination at component and board level is dealt with by various methods and approaches in [56], [57], [58], [59]. In this regard, it is very valuable and essential to study the crack initiation and propagation at interfaces for understanding and predicting interfacial failure. Crack tip stress intensities, namely, K_I and K_{II}, and the energy release rate (ζ_{SS}), are some of the important parameters to be determined in such interfaces to arrive at strength. Interfaces are dynamic in nature; hence, their properties may change with time owing to thermal cycling, mechanical loading, and environmental exposure. When one intends to predict and avoid interfacial failures, understanding the change in such properties is of critical importance. Long exposure to high temperature sets off changes in material properties such as embrittlement, oxidation, and diffusion of atoms across the interface which weakens the bond. Moisture ingress through interfaces causes swelling, hydrolysis of bonds, and corrosion that degrades the interfacial properties. damage due to repeated mechanical loading leads to crack initiation and crack growth at the interface.

2.5 *Thermal Interface Material*

Thermal management is critical in electronics cooling as power densities continue to increase, projected to exceed 100 W/cm² (1 W/mm²) [60], [61], [62]. This increase, driven by device miniaturization and growing performance demands, has intensified thermal challenges.

Recognizing the need to address these challenges, the International Electronics Manufacturing Initiative (iNEMI) identified thermal management as a research priority in 2013 [63]. A central focus of thermal management is reducing thermal resistance between the microprocessor chip and the heat sink, achieved through the use of thermal interface materials (TIMs), which effectively transfer heat from the silicon die to the heat sink to ensure reliable device operation.

In low-power applications (less than 30 W, such as laptops), the silicon die is directly connected to the heat sink using a TIM. For medium- to high-power applications (greater than 30 W, such as desktops and servers), the die is connected to the heat sink via an integrated heat spreader (IHS). This configuration requires two TIM layers: TIM1 between the die and the IHS, and TIM2 between the IHS and the heat sink [64], [65], [66].

An ideal TIM should exhibit high thermal conductivity, low thermal resistance at thin bond line thickness (BLT), conformability under low to moderate pressure, excellent wetting properties, ease of application, and cost-effectiveness, while also being environmentally friendly and safe [62], [67], [68]. TIM performance depends on factors such as surface roughness, flatness (waviness), and contact pressure[67], [69].Additionally, application-specific challenges, including non-uniform heat flux, pressure distribution, and die warpage, can significantly impact efficiency [65], [66]. TIMs must also exhibit high tensile strength and tear resistance to prevent degradation during operation, where semiconductor packages are subjected to sustained mechanical stress. Fillers are commonly added to TIMs to enhance thermal conductivity, balancing performance, cost, and reliability. Polymers are typically used as the matrix material due to their excellent insulation properties, low processing costs, and superior mechanical characteristics [70]. However, the intrinsic thermal conductivity of polymers is very low (less than 0.5 W/mK), which falls short of meeting the high thermal conductivity requirements for TIMs. To address this, inorganic fillers

with high thermal conductivity are widely incorporated into polymer matrices to improve performance.

Traditional TIMs include greases, phase-change materials (PCM), gels, and pads, which typically consist of polymer matrices loaded with conductive particles (metal or ceramic) to enhance thermal conductivity [64], [65], [66], [67], [68], [69], [71]. Greases are the most widely used TIMs, with thermal resistance ranging from 0.1 to 1 $cm^2°C/W$ [65], [71], [72]. For example, polyethylene glycol (PEG)-based thermal pastes mixed with boron nitride (BN) have demonstrated thermal resistance as low as 0.05 $cm^2°C/W$[73]. However, greases have significant drawbacks, including high viscosity, which makes them difficult to apply and remove, and reliability issues such as pump-out, phase separation, and dry-out, limiting their long-term effectiveness [65], [67], [69], [71].

Polymer-based TIMs include thermal greases, phase-change materials, gels, and adhesives [65], [67], [74], [75], [76], [77], [78]. These materials are effective at filling microscopic voids and grooves on mating surfaces. For thicker bond lines, their thermal performance is primarily influenced by bulk thermal conductivity rather than contact resistance [65]. However, when thin bond lines are used, their thermal performance may be dominated by interfacial resistance. Additionally, polymer-based TIMs exhibit poor thermal stability at elevated temperatures, as the glass transition temperatures of most polymer matrices are generally below 150°C, regardless of their thickness.

Solders provide even lower thermal resistance, reaching values as low as 0.05 $cm^2°C/W$ [71], [73]. However, practical challenges, such as limited reworkability, high-temperature processing, thermal stress, and void formation, restrict their broader use [65], [69], [71]. In recent years, carbon-based materials such as carbon nanotubes (CNTs) and graphene have gained

attention as potential TIM solutions. CNTs, whether used directly or as fillers in composite TIMs, exhibit exceptional thermal conductivity (6600 W/m°C for single-walled CNTs and 3000 W/m°C for multi-walled CNTs) [60], [61], [79], [80]. Thermal resistance values for CNT-based TIMs range from 0.01 to 0.19 cm^2°C/W, as summarized by Cola [61]. Similarly, graphene exhibits outstanding thermal properties [81], [82]. However, the high cost of carbon-based TIMs, particularly CNTs, remains a significant barrier to widespread adoption[82].

Over the past decades, electronic devices, especially advanced processor chips, have faced increasing power densities, leading to more complex thermal challenges. Effective thermal management is now indispensable for ensuring reliable operation and optimal performance. Conductive heat transfer is commonly employed to distribute heat across larger surface areas, often with the aid of a heat sink. TIMs play a critical role in reducing contact resistance and enhancing heat transfer efficiency by filling air gaps between surfaces and ensuring secure attachment of components.

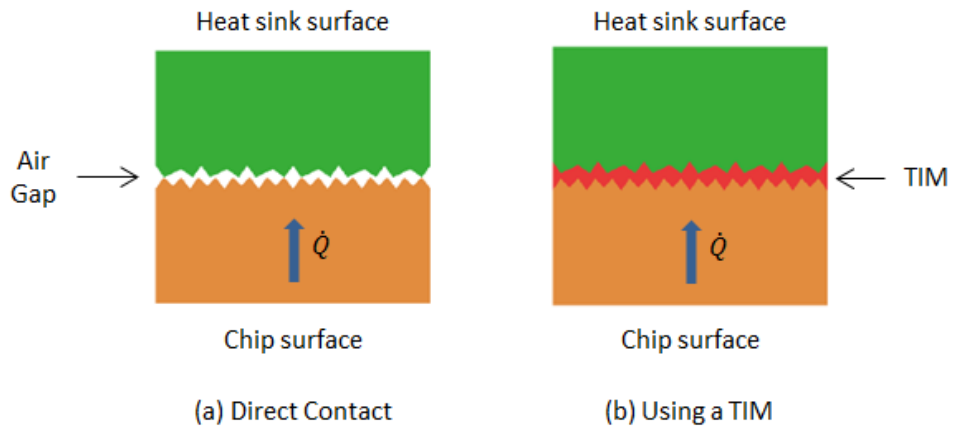

Figure 2-4 Thermal interface materials (TIMs) arthesed to fill the asperities between the mating surfaces in a semiconductor package

The thermal resistance R across a TIM layer was used in this paper to describe the thermal performance and can be expressed by the sum of the thermal contact resistances $R_{contact\_bottom}$ and $R_{contact\_top}$ at each interface and the bulk resistance of the TIM

$$R_{total} = \frac{BLT}{kTIM} + R_{contact\_bottom} + R_{contact\_top} \quad \text{Equation 2-3}$$

where BLT is the bondline thickness and kTIM is the bulk thermal conductivity of the TIM layer. Many techniques exist to measure the thermal conductivity of TIMs, and the appropriateness of a method can depend on the type of TIM being studied. The laser flash method and the modified hot-wire method are relatively fast transient methods that can be used to measure various TIM types, such as greases and adhesives. Steady-state techniques, such as the guarded heat flow method and the guarded comparative longitudinal heat flow method, are commonly used by TIM vendors. However, the validity of the standards associated with these measurement methods, namely, ASTM D5470 [83]and ASTM E1530 [84], has been questioned since reproducibility of vendor data is often difficult of achieve and the test conditions, such as the contact pressures and sample thicknesses, often do not correspond to typical in use conditions [85]. Deficiencies in the ASTM standards have prompted many researchers to offer modifications or develop new test methods [86], [87], [88].

2.6*Magnetically-Oriented ACA for Flexible and Stretchable Electronics*

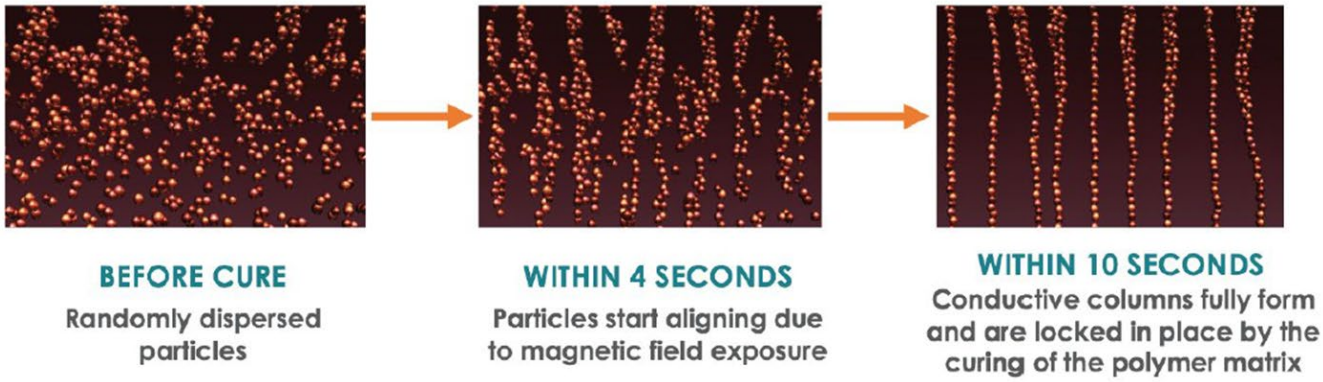

Figure 2-5Curing Process of Magnetic ACA: How does it work

Parameter	Magnetic-ACA	No-Lead Solder	ACF
Curing Temperature (°C)	70-200 or UV	250 - 340	130 - 150
Feature Size (microns)	<100	<50	>150
Z-Axis Connection Resistance (mOhms)	7 - 20	<7	20 - 1000
X-Y Insulation Resistance (0hms)	$>10^{11}$	$<10^{10}$	$>10^{10}$
Thermal Conductivity (W/m-k)	3.5 - 7.3	60 - 100	0.5 - 5

Figure 2-6 ZTACH ACE: Properties

The primary cause of fatigue failure in electronic devices is the significant thermal variation experienced by electronic packages, particularly during the operation of high-power-density devices or under harsh environmental conditions. Flexible Hybrid Electronics (FHE), extensively used in the automotive industry, are often subjected to prolonged exposure to elevated temperatures, which can adversely impact their reliability [89]. Extended operation in high ambient temperatures poses challenges to the mechanical reliability of both bulk materials and interfaces [25].

Future advancements in electronics rely on the development of customizable devices and systems that enable quick, cost-effective manufacturing and integration on diverse multifunctional substrates, potentially in conformable forms. This study explores the application of magnetically

aligned Anisotropic Conductive Epoxy (ACA) as a fundamental component in the production of flexible and stretchable electronics. The methodology employs a rapid and reconfigurable Surface Mount Technology (SMT) production technique, facilitating accelerated development and manufacturing processes for Flexible Hybrid Electronics (FHE) across various functions and applications.

Magnetically Aligned ACA (MACA): An Overview

Magnetically aligned ACA (MACA) is an advanced composite material comprising metal microparticles and epoxy resins, designed to provide superior electrical, structural, and reliability properties. Electrical conductivity is achieved by aligning columns of conductive particles in the z-direction under a magnetic field during reflow. MACA's low-temperature curing process, which incorporates micron-sized ferromagnetic particles, supports the creation of high-density interconnects while preserving the conformal and flexible nature of the substrate.

Interconnection Techniques in Flexible Hybrid Electronics

Traditional interconnection methods for flexible hybrid electronics include low-temperature solder, ultra-low-temperature solder, electrically conductive adhesives (ECAs), and anisotropic conductive adhesives (ACAs). Unlike isotropic ECAs, which enable conductivity in all directions, magnetic ACA ensures conductivity exclusively in the z-direction. This z-axis connectivity minimizes the risk of unintended in-plane interconnections and supports the precise application of materials at finer pitches.

Anisotropic Conductive Adhesives (ACAs): Performance and Applications

Conductive adhesives containing silver particles are often used as alternatives to solder for bonding electronic components. These adhesives exhibit isotropic conductivity due to suspended

silver particles and require multiple patterning steps—such as pneumatic dispensing, screen printing, and stenciling—for application in high-density circuitry.

In contrast, ACAs are employed in applications demanding low-loss vertical interconnects [90], [91]. ACAs have been utilized across industries, including flat-panel display manufacturing and the attachment of bare chips to flexible and rigid substrates [92], [93], [94]. ACAs are especially effective for interconnects shorter than 120 μm, making them a cost-efficient solution for high-density circuitry [95].

ACAs are available in two main forms: anisotropic conductive films (ACFs) and anisotropic conductive adhesives (ACAs). These materials use randomly dispersed conductive particles to achieve unidirectional conductivity under applied pressure and heat. The deformation of the particles during this process forms reliable electrical connections. Over the last decade, ACAs have demonstrated excellent performance as cost-effective solutions, further developed for low-cost mass production [96], [97], [98].

Research and Challenges in ACAs

Extensive research has been conducted to understand the electrical and mechanical performance of ACAs:

- [90]demonstrated an ACA design that ensures stable, low-resistance electrical connections by trapping conductive particles between pads and solidifying the adhesive to lock in residual stresses.
- [99]analyzed the conduction mechanism of trapped conductive particles, examining DC current paths through solder bumps, individual particles, and pads. The study also modeled the resistance dependence on the deformation of Ni/Au particles.

- [100] reviewed prior studies to provide insights into the basic conductive properties of ACAs.
- [101] developed an analytical model based on Holm's theory and Hertz's elastic theory, describing interconnection resistance in terms of sample geometry, particle size, and applied pressure.
- [93] examined two ACA particle systems—rigid and deformable—and their performance under different conditions.
- [102] proposed a conduction model to calculate particle resistance as a function of deformation degree.

Despite these advancements, several challenges remain in ACA development [93]:

- **High-frequency behavior** and its coupling effects with semiconductor devices, including cross-talk between particles above 20 GHz.
- **Current-carrying capacity** at high frequencies and after exposure to environmental stress tests.
- **Substrate planarity**, which impacts ACA joint reliability.
- Development of **lifetime prediction models** for ACA joints

Chapter 3 Experimental Methodology and Material Preparation

3.1Stress and strain analysis

Underfill samples were prepared using an assembled mold, which is shown in Figure 3-1. This sample preparation technique has been well developed and described in previous work. There are three different layers on this figure. The bottom layer is a steel plate. The top layer is a steel plate with a couple of slots. Both top and bottom layers are coated with Teflon in order to prevent

the underfill samples stick to the steel. The middle layer is two Teflon shims. The three layers would assemble and clip with four clippers at the corner. After that, the middle layer would create a gap between the top and bottom layer. There would be space under the cross bars of top layers, which would define the thickness of the specimens. The shim is 0.5mm in this study. The size of steel plate should not be too big, otherwise there would be deflection on the plate after isothermal aging at high temperature.

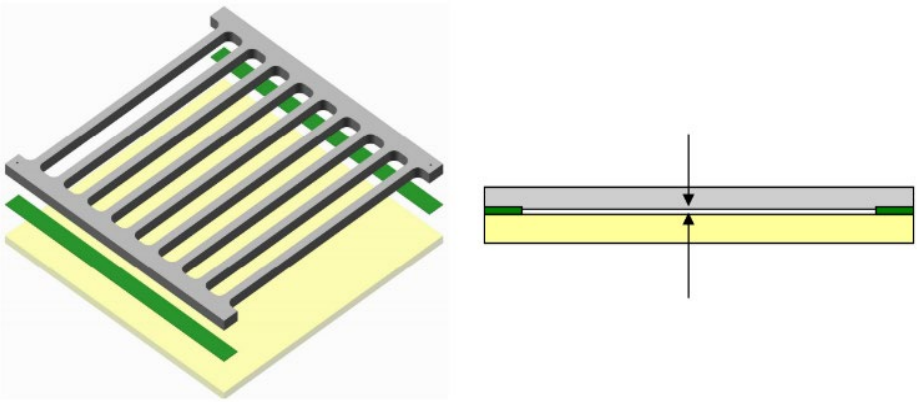

Figure 3-1 Mold Assembly

Before the test, mold is cleaned by acetone. The mold would be assembled and placed on hot plate at 150℃ to remove the moisture. Underfill is sensitive to moisture, which would be absorbed into underfill and affect the mechanical properties. Four underfill samples are restored in the negative 40℃ environments. Once a syringe of underfill is taken out, it could not be returned to the freezer, otherwise this procedure would weaken the underfill material. Take one syringe of underfill out from the freezer for about one hour in room temperature until it is fully melted into liquid. Set the temperature of hot plate above 100℃. The higher the temperature, the lower viscosity of underfill so it would be easier for sample preparation. However, the material would start curing if the temperature is too high. The recommended temperature of hot plate would be around 110℃ to 120℃. Dispense the underfill near the one side of cross bar of the mold. The

underfill would flow into the gap of the top and bottom layers of the mold since the capillary flow effect. Put the mold into oven setting at curing temperature. The curing conditions of the 4 kinds of underfills are listed in Table 1.

Table 3-1Cured Conditions

	UF1	UF2	UF3	UF4
Curing Temperature	150℃	165℃	165℃	150℃
Curing Time	2 hours	2 hours	2 hours	2 hours
Viscosity@25℃ (Pa·s)	47	60.8	16.5	52.8

After the curing procedure, the uniaxial tensile tests sample would appearance is shown in Figure 3-2 and Figure 3-3. The typical dimensions of samples are shown in Table 3-2.

In the method described above, it is easier to cure the specimen with the certain uniform thickness. Since the underfill would not stick to the Teflon coated plate, the specimen would be easier to remove from the mold without the aid of any chemical released agent. The ratio of length and width is more than 20 so it would be applicable to run the tensile test.

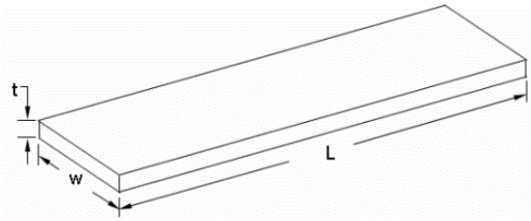

Figure 3-2 Specimen Profile

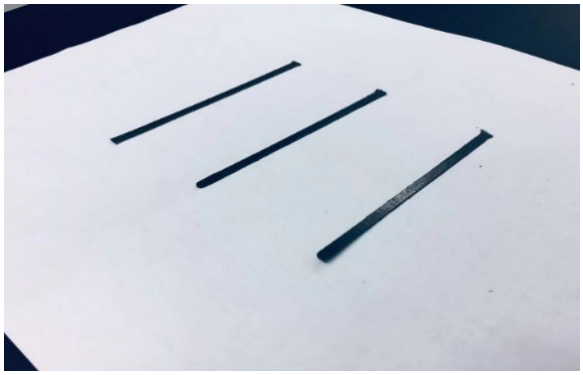

Figure 3-3 Specimen for Monotonic Tensile Test

Table 3-2: Typical Dimensions of Specimen

Dimension	
Length(mm)	60
Width(mm)	3
Thickness(mm)	0.6

The Instron 3367 mechanical test system is utilized to run the tensile test. This series testing system is shown in Figure 3-4. The computer-controlled actuators provide a uniaxial displacement. It is a displacement driven test system. The samples are fixed by torque wrench at top and bottom sides to make sure it is fixed in a proper way.

Figure 3-4 Instron 3360 Series Test System

During the uniaxial tensile test, the force and displacement would be measured. The stress and strain would be calculated by the relationship of applied uniaxial tensile force and displacement.

$$\sigma=F/A \qquad \epsilon=\Delta L/L=\delta/L \qquad \textbf{3-1}$$

Where the σ is uniaxial stress. F is the uniaxial applied force. A is the cross-section of underfill samples. Є is uniaxial strain. L is specimen gage length, which is 60mm in this study. δ is displacement. Since the underfill material properties are time dependent, the strain rate should be controlled. For this test, the displacement is 0.6mm/min. As the result, the strain rate is 0.000167 mm/s. Test temperature is 20℃.

In this study, the test matrix is shown on Table 3-3. At least three samples would be tested under each test condition. The typical tensile stress-strain curve for UF1 pristine material properties are shown in Figure 3-5.

Table 3-3 Uniaxial Test Matrix for 4 Underfills

AGING DAYS	AGING TEMPERATURE	
	100℃	150℃
0	√	
30	√	√
60	√	√
90	√	√
120	√	√
120	√	√
240	√	√
360	√	√

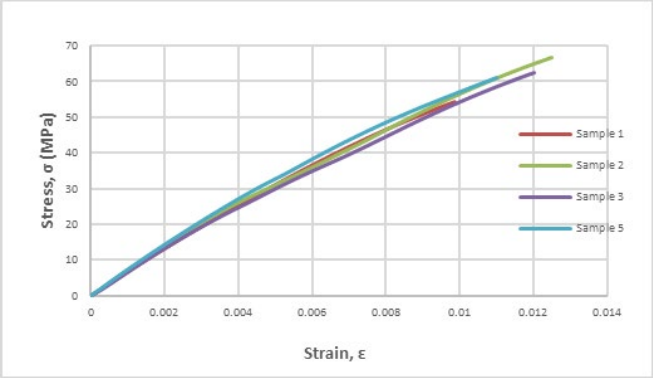

Figure 3-5 UF1 Pristine Stress-Strain Curve and Property

3.2 Mechanical Property characterization by nanoindentation test

The mechanical properties of the UF were evaluated at room temperature using a Hysitron TI 950 TriboIndenter, as illustrated in Figure 3-6. This equipment includes a stage that maintains ambient conditions, making it suitable for nanoindentation tests. Uniformly spaced indentations were created across the solder joints, and for each indentation, the relationship between the applied load and the indentation depth was recorded.

Indents were made utilizing a Berkovich tip at a constant loading rate of 3 mN/sec until the load reached 30 mN. To address any potential issues of creep, which could affect the accuracy of the measurements, this maximum load was deliberately held constant for a period of 30 seconds. The same rate of 3 mN/sec was employed for the unloading sequence. The Oliver and Pharr [103], [104]technique was applied to extract the material properties, ensuring reliability by averaging the results of at least 10 indentations.

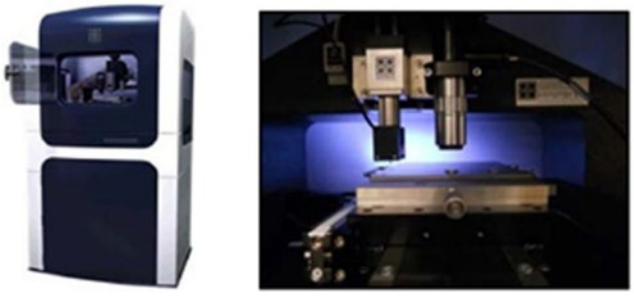

Figure 3-6 Hysitron Nanoindentation System

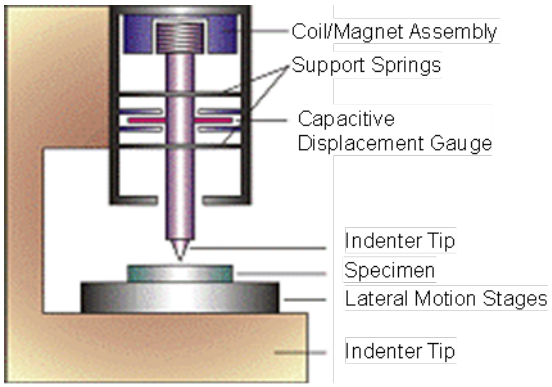

Figure 3-7 Schematic of nanoindenter system

Prior to conducting tests on the solder samples, calibration of the indenter axis was performed. This included calibrating measurements of hardness and elastic modulus using standard fused silica and quartz samples to ensure the precision of the test outcomes. Additionally, each test incorporated a measurement and correction for thermal drift to offset any temperature variation effects, maintaining a drift rate below 0.05 nm/sec.

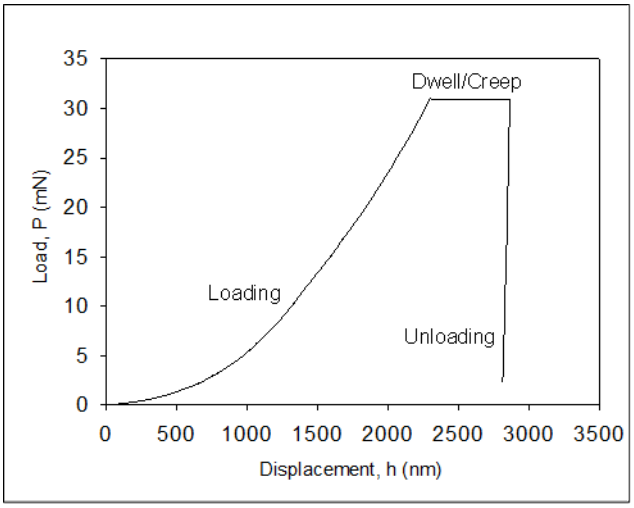

Figure 3-8 Load vs. Displacement profile

Elastic modulus and hardness measurements for all samples were obtained using a nanoindentation technique. This approach involved recording the load versus displacement data during the nanoindentation process. The load displacement curve is shown Figure 3-7. The slope of the unloading curve at its peak load, noted as S (where S is the change in load per unit displacement,

dP/dh), is known as the unloading stiffness. The Oliver and Pharr method [103], [105] is used to determine the elastic modulus (E) and hardness (H) at the point of maximum indentation. This calculation requires the stiffness S, the peak load ($P_{\max}$), the peak displacement ($h_{\max}$), the material's Poisson's ratio (ν), and the indenter tip's geometric and material constants.

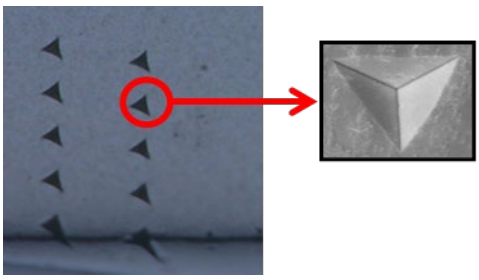

Figure 3-9 Mark of nanoindentation

Hardness (H), also referred to as Meyer hardness, is calculated by dividing the maximum load ($P_{\max}$) by the indentation's projected contact area (A) at the maximum load point. Hardness signifies the material's resistance to plastic deformation.

Here, $h_{\max}$ signifies the maximum indentation depth ascertained from the load-displacement graph (P vs. h), and h_s denotes the surface displacement at the edge of the indenter's contact area. Furthermore, the constant ε, which is approximately 0.75, is a geometric constant associated with the Berkovich indenter tip. Integrating these variables allows for the correlation of hardness (H) and the projected contact area (A) with the empirical data, maximum load (P_{max}), maximum displacement (h_{max}), and unloading stiffness (S), obtained from the nanoindentation experiment. From the calculated hardness value, it is possible to determine the material's yield stress, based on the assumption that the contact area remains constant during the retraction phase of the indenter.

The unloading stiffness (S) from the recorded nanoindentation curve is given by

$$S = \frac{dP}{dh} = \frac{2\beta\sqrt{A}}{\sqrt{\pi}} E_r$$

is a geometrical factor for the chosen indenter tip and E_r is the reduced modulus. The reduced elastic modulus, E_r can be calculated by

$$E_r = f(S) = \frac{\sqrt{\pi}}{2\sqrt{A}} S$$

3.3Characterization of Linear Viscoelastic Behavior

As the underfill materials are viewed as viscoelastic material, the mechanical properties are time-temperature-dependent. Viscoelasticity is a mechanical behavior including both elasticity and viscous effect. One way to characterize viscoelastic properties is dynamic mechanical analysis (DMA), where dynamic response of material is measured at oscillation frequency of interest over a wide range of temperatures. Compared to the traditional mechanical test method, DMA could offer the complex modulus in specific frequency domain. The complex modulus in the frequency domain can be transformed to relaxation modulus in the time domain by using an appropriate relationship. After the transformation, data of frequency scan over two decades could be used to predict the material behavior over ten decades, covering the most mechanical behavior of interest. In this paper, 2 different kinds of Underfill have been cured and aged under two temperatures: 100℃ and 150℃. Since the glass transition temperature (Tg) of these underfills from the data sheets are around 115℃ to 120℃ by dynamic mechanical analysis (DMA) under 3 points bending mold, these aging tests are conducted under the temperature below and above the Tg.

Figure 3-10 PerkinElmer DMA 8000

In this study, a novel method has been developed to prepare test specimen for DMA testing (Figure 3-6). The properties of underfill materials such as storage modulus, loss modulus, and tan δ were investigated using DMA (Dynamic Mechanical Analyzer). Tg (glass transition temperature) significantly affects the mechanical properties. Glass transition temperature represents the level of cross-linking of polymer. High glass transition temperature represents high cross-linking density.

PerkinElmer DMA 8000 is utilized to run the DMA test. Dynamic temperature ramp test is conducted in 3 points bending (dual cantilever beam) mode with the frequency of 1 Hz. This mode would produce most reliable and repeatable result (Figure 3-7). The DMA test is running from room temperature to 280°C, since the reflow process would be about 260°C, which is the highest temperature for Underfill material. The testing temperature increase by rate of 3°C/min. Strain is 0.05. The storage modulus, loss modulus, and tanδ are determined by the instrument software. The T_g of the samples can be determined as the peak of the loss modulus curve, peak of the tanδ curve, and onset slop of the storage modulus curve at the transition phase.

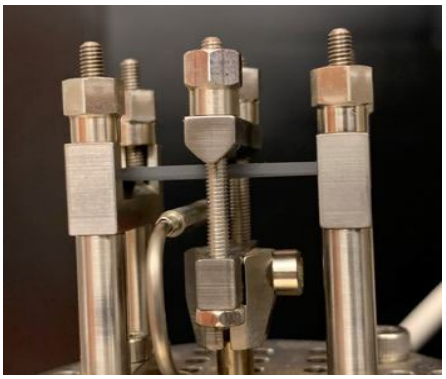

Figure 3-11 Three Points Bending Setup with Specimen

In this study, the TA RSA3 dynamic mechanical analyzer system is employed to perform the Dynamic Mechanical Analyzer (DMA) test. The test is conducted using the three-point bending mode (as shown in Figure. 3-8), with a gage length of 10mm. The temperature ramp ranges from 25℃ to 280℃, considering that the reflow process typically reaches temperatures around 260℃, which is the highest temperature encountered during the packaging stage. To control the temperature, a temperature oven is utilized, and the temperature is increased at a rate of 5℃/min. A strain of 0.1 is applied during the test. It is important to use a relatively low strain since the stiffness of the polymer decreases significantly above the glass transition temperature. Higher strains could potentially lead to sample breakage during the temperature ramp test.

The instrument software is used to collect data on the storage modulus, loss modulus, and tan δ as functions of frequency. The glass transition temperature (Tg) of the samples can be determined through various methods, such as identifying the peak of the loss modulus curve, peak of the tan δ curve, or slope of the storage modulus curve during the transition phase.

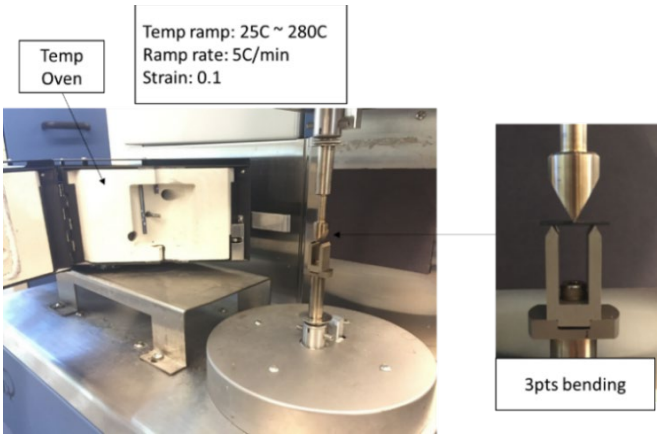

Figure. 3-12 DMA Test System

In the dynamic loading test, the sinusoidal stress can be represented by the following equation:

$$\sigma = \sigma_0 sin\omega t \qquad (3\text{-}2)$$

Where t is time and ω is angular frequency of stress vector. For the viscoelastic material, the strain would lag behind due to the viscous effect. As the result, the corresponding strain is:

$$\boldsymbol{\varepsilon = \varepsilon_0 sin\ (\omega t - \delta)} \qquad (3\text{-}3)$$

Where δ is phase lag. For stress leading the strain, we can write:

$$\varepsilon = \varepsilon_0 sin\omega t \qquad (3\text{-}4)$$

$$\sigma = \sigma_0 \sin(\omega t + \delta) \qquad (3\text{-}5)$$

The stress could be rewritten as:

$$\sigma = \sigma_0 \sin\omega t\, cos\delta + \sigma_0 sin\delta\, cos\omega t \qquad (3\text{-}6)$$

Based on the analysis above, two dynamic moduli could be proposed in the equation(3-7)(3-8):

$$E_1 = \frac{\sigma_0 \cos\delta}{\varepsilon_0} \qquad (3\text{-}7)$$

$$E_2 = \frac{\sigma_0 \sin\delta}{\varepsilon_0} \tag{3-8}$$

E_1 and E_2 could be calculated by the amplitude of stress and strain, and the phase lag δ. The complex modulus would be written as the equation(3-9):

$$E^* = \frac{\sigma}{\varepsilon} = \sqrt{{E_1}^2 + {E_2}^2} = E_1 + i\,E_2 \tag{3-9}$$

E_1 is storage modulus and $E_2$is loss modulus. The storage modulus represents the elastic energy in stored and loss modulus represent the energy or viscous loss. The loss tangent:

$$\tan\delta = \frac{E_1}{E_2} \tag{3-10}$$

3.4Measurement of Coefficient of Thermal Expansion

Coefficients of thermal expansion (CTE) could be applied to characterize the material expansion under different temperature environments. EMC has relatively low CTE due to the high-density filler content. There are two CTEs of polymer, One in glassy state and the other in rubbery state. CTE in rubbery state is much larger than CTE in glassy state. Thus, CTE is usually used to characterize the glass transition temperature.

In this study, we develop a novel approach to characterize CTE by dynamic loading test framework. Traditionally, CTE is measured by static fixture. Thus, TMA and DMA tests have to rely on different instruments. DMA normally works by applying the oscillating force to the material as shown in Figure 3-9. The resultant displacement of sample is measured. When determining expansion, the oscillating force function is turned off. The displacement of the sample is measured as it expands as the function of temperature. By plotting the displacement as the function of temperature, the expansion of thermal coefficient could be calculated.

However, Since DMA instruments are used to apply dynamic loading test, fixture expansion under temperature ramp could not be ignored. In order to conduct CTE measurement, we have to do calibration and compensation. We prepared an Al sample with similar size to our EMCs. Once a sample is placed in tension mode, the displacement gives an indication of how the geometry of the sample will change over the given temperature range. CTE of Al sample is known. A calibration of the instrument with a known Al could be done before the experiment, in order to compensate for the expansion of the driveshaft and clamps.

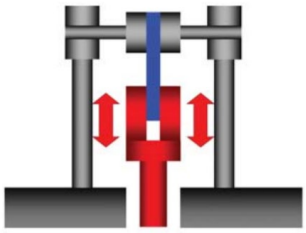

Figure 3-13 CTE Measurement

3.5Fracture and fatigue analysis

3.5.1Introduction to fatigue performance analysis

S-N Curve

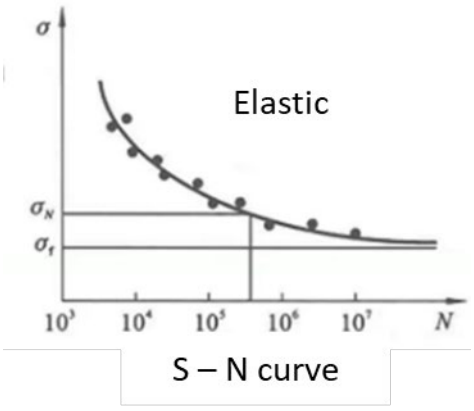

Figure 3-14 S-N Curve for Elastic Fatigue

The figure focuses on the S-N curve, which represents the relationship between stress and the number of cycles to failure. The upper plot shows the curve in a log-log scale, indicating that higher stress amplitudes result in a shorter fatigue life. The lower plot illustrates a cyclic stress history, highlighting key parameters such as:

- Stress Range ($\Delta\sigma$): The difference between the maximum and minimum stress in a cycle

$$\Delta\sigma = \sigma max - \sigma min \quad (3\text{-}11)$$

- Stress Amplitude (σa): Half of the stress range

$$\sigma a = 1/2\Delta\sigma \quad (3\text{-}12)$$

- Mean Stress (σm): The average of the maximum and minimum stresses.

$$\sigma m = 1/2\ (\sigma max + \sigma min) \quad (3\text{-}13)$$

- Stress Ratio (R): The ratio of minimum to maximum stress

$$R = \sigma min\ /\ \sigma max \quad (3\text{-}14)$$

Strain-Life Curve

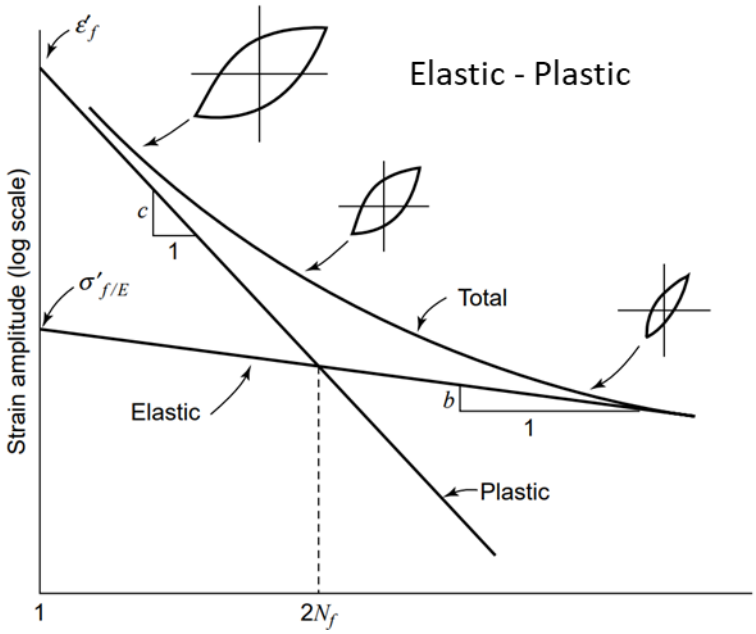

Figure 3-15 Superposition of plastic and elastic strain life curves to produce the total strain life fatigue relation for 18% Ni maraging steel. (Source: Deformation and Fracture Mechanics of Engineering Materials 6th edition. p.540)

Figure 3-11 focuses on the strain-life curve, plotting strain amplitude (ε_a) against the number of reversals to failure (2N) in a log-log scale. Strain amplitude is composed of two parts:

1. Elastic Strain (ε_{ea}): Governed by the material's elastic properties.
2. Plastic Strain (ε_{pa}): Dominated by plastic deformation.

The strain amplitude is expressed as:

$$\varepsilon_a = \frac{\varepsilon_{ea}}{\varepsilon_{pa}} = \frac{\sigma_f^{'}}{E}(2N)^b + \varepsilon_f^{'}(2N)^c \quad (3\text{-}15)$$

- $\frac{\sigma_f'}{E}(2N)^b$: Elastic strain amplitude.

- $\varepsilon_f^{'}(2N)^c$: Plastic strain amplitude.

- $\sigma_f^{'}$, $\varepsilon_f^{'}$: Fatigue strength and ductility coefficients, respectively.

- b, c: Material-specific fatigue exponents.

This plot demonstrates the transition from elastic-dominated behavior at high cycle counts to plastic-dominated behavior at low cycle counts.

Basquin's Equation

For materials in the elastic regime, the stress-life relationship is described by Basquin's equation:

$$\lg\sigma = a + b\lg N \tag{3-16}$$

where σ is the stress amplitude, N is the number of cycles to failure, and a and b are material-specific constants derived from experiments.

Hypothesis

The fatigue performance of epoxy molding compounds (EMCs) can be characterized using the S-N curve and Basquin's equation.

3.5.2Fatigue Failure

The Figure 3-12 shows the construction of the Instron 5948 micromechanical tester. The machine has a ball screw-driven rail table that is equipped with a servo motor. This allows for a high axial displacement resolution of 20nm. The testing system is made up of the Instron 5948 Micro-mechanical testing system, designed for high accuracy and comes with a specially designed fixture. The uniaxial tensile fixture is used to clamp the EMC specimen vertically, while the actuator of the Instron Micro Tester, assembled with an upper fixture, monitors the accuracy of the vertical displacement at a nanometer level. The 2kN load cell is assembled with the bottom fixture and fixed on the base to record any change of forces. The specimen is placed precisely between the two fixtures, and the load cell connected to the bottom fixture can detect the load

applied to the specimen. The system can simultaneously monitor force and displacement, with the top fixture mounted with an actuator that creates an axial movement. The displacement rate selected for this study was 0.1mm/s. Maximal displacement or load per cycle can be programmed in the system in order to investigate the customized sample in both the stress-controlled test and strain-controlled test. The deformation of the stainless-steel beam in the fatigue test is less than 1μm, which is neglectable.

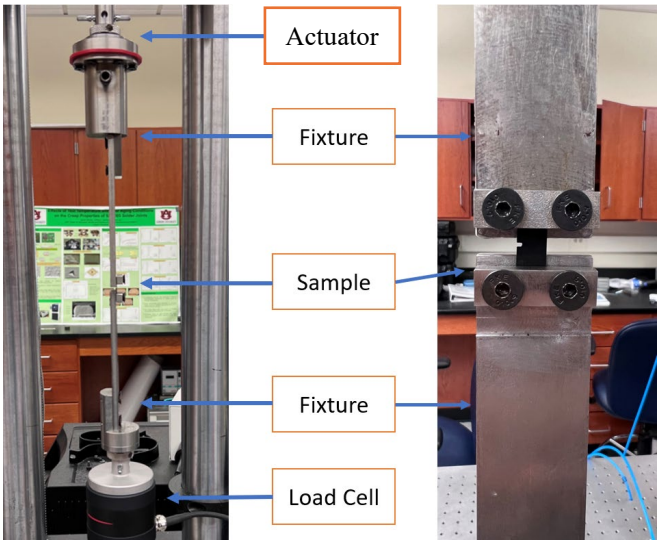

Figure 3-16 Micromechanical tester Instron 5948 and fixtures schematic

Stress Intensity Factor Calculation

EMC is a brittle material with a small percentage of elongation. With the high percentage content of silica fillers, their mechanical properties are close to glass. It is hard to generate cracks naturally by cyclic loading tests. Pre-notch is introduced to accelerate crack generation. The stress intensity factor of material with a notch is computed.

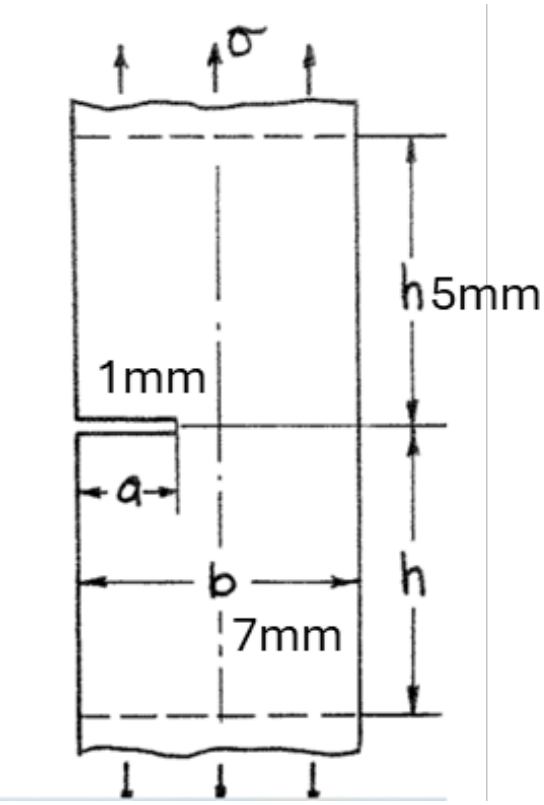

Figure 3-17 Single Edge Notch Test Specimen

Stress intensity factor is of single edge notch test specimen (Figure 3-13) is in the form:

$$K_I = \sigma\sqrt{\pi a}F(\frac{a}{b}) \tag{3-17}$$

Where K_I is stress intensity factor. a is the length of notch. b is the width of specimen. σ is uniaxial tensile stress applied to the specimen. In our test, b is 7mm, h is 5mm. Numerical values of F(a/b) could be computed by (3-18):

$$F\left(\frac{a}{b}\right) = 1.122 - 0.231\left(\frac{a}{b}\right) + 10.550\left(\frac{a}{b}\right)^2 - 21.71\left(\frac{a}{b}\right)^3 + 30.382\left(\frac{a}{b}\right)^4 \tag{3-18}$$

Standard definitions about key load or stress variables are shown in Figure 3-14 Nomenclature to describe test parameters involved in fatigue test.

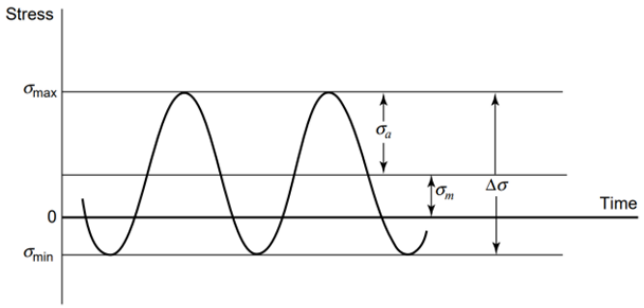

Figure 3-18 Nomenclature to describe test parameters involved in fatigue test

ΔK is stress intensity factor range. σ_m is average stress.

$$\Delta K = \frac{1}{2}(K_{max} - K_{min}) \quad \textbf{(3-19)}$$

$$\sigma_m = \frac{1}{2}(\sigma_{max} + \sigma_{min}) \quad (3\text{-}20)$$

For elastic material, stress- life relationship can be described by the Basquin equation.

$$log(\sigma) = a + b.log(N) \quad (3\text{-}21)$$

where σ is stress amplitude, N is number of life cycles. a and b are material properties that are determined by experimental data.

3.5.3Selection of Interface Specimen Geometry

Geometry of a test specimen in the determination of interfacial properties is very influential on the results obtained. Proper design of the specimen is vital for correct and repeatable testing. This section discusses the importance of geometry for an interfacial specimen, how this geometry affects test results, and several things that should be considered when designing an optimal specimen. Geometry determines how stresses are distributed at the interface and influences the failure location and mode. The specimen geometry can affect the sensitivity of the test to interfacial properties. A discussion has been made on the effects of specimen geometry and notch geometry on interfacial modes of fracture in electronics packages and composite laminates. In order to compare results from other similar results reliably, consistent specimen geometry is necessary. The design parameters are the location of the interface, dimensions of the specimen, material

thickness, pre-crack, and notch dimensions. Loading rates can influence the observed failure mechanisms.

One of the most utilized techniques for determining fracture toughness in a bi-material interface is the four-point bending of centrally notched specimens. Such a configuration allows controlled crack initiation and propagation within the interface, providing valuable insight into material resistance to fracture. These parameters of fracture toughness quantify the interfacial resistance to crack propagation. For bi-material interfaces, the fracture mode is typically mixed mode with both opening (Mode I) and shear (Mode II) components. The stress intensity factor (K) characterizes the near-tip stress field due to applied load, specimen geometry, and crack length. Under four-point bending, the specimen is supported at two points and loaded at two intermediate points. Under such a loading configuration, a pure bending moment creates a tensile stress field on the bottom surface of the specimen. If a central notch exists, a crack starts at the notch tip and grows along the interface by the action of the bending stress. Accurate fracture toughness determination requires precision within the central notched specimen dimensions in terms of width, thickness, notch length, and radius. Figure 3-15 provide a representation of CNF specimens.

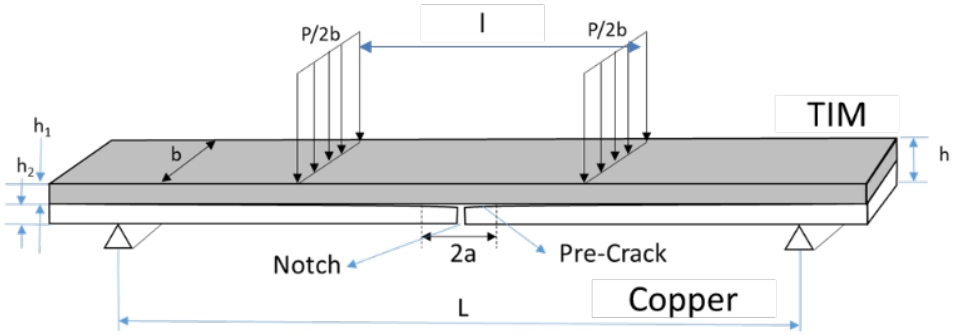

Figure 3-19 Interfacial Fatigue Calculation

3.5.4 Fracture Toughness Calculations

In this study, the strength of the bond between potting material and a printed circuit board (PCB) has been measured by determining the peak critical load required to initiate a crack at the interface. To calculate the stress intensity factor of the interface, the peak critical loads have been recorded for each testing condition. The interfacial fracture toughness of structural materials has also been studied, and expressions for determining it have been developed by Charalambides. The current study has a crack geometry similar to Charalambides' previous work, so the same expressions have been applied here. The strain energy release rate exhibits steady-state characteristics. It has been determined by computing the difference between the strain energy of a cracked beam and an uncracked beam, as outlined by Charalambides in their works from 1989 and 1990.

Previous research has examined similar studies on specimens made of two different materials [35]. The strain energy release rate demonstrates consistent behavior over time. In earlier investigations, scientists have explored equations to determine the fracture toughness at the interface of bi-material specimens, specifically focusing on structural materials. In this current study, the fracture toughness expressions developed previously for bi-material specimens have been adopted, as the crack geometry resembles that of the four-point flexure test analyzed by Charalambides. The steady-state value is obtained by calculating the disparity in strain energy between the beam with a crack and the beam without a crack.

$$\zeta_{ss} = \frac{M^2(1-\nu_2^2)}{2E_2}\left(\frac{1}{I_2} - \frac{\lambda}{I_c}\right) \tag{3-22}$$

Where $\lambda = E_2(1-\nu_1^2)/E_1(1-\nu_2^2)$, ν is Poisson ratio and E is Young's modulus of the materials. In this study, material 1 is TIM and Material 2 is bare copper.

$$M = Pl / 2b \tag{3-23}$$

$$I_2 = h_2^3 / 12 \tag{3-24}$$

$$I_c = \frac{h_1^3}{12} + \frac{\lambda h_2^3}{12} + \frac{\lambda h_1 h_2 (h_1 + h_2)^2}{4(h_1 + \lambda h_2)} \tag{3-25}$$

$$\zeta = \frac{E_2 \zeta_{ss} h^3 b^2}{P^2 l^2 (1 - \nu_2^2)} \tag{3-26}$$

M is moment. I is moment of inertia per unit width. P is the applied load; b is the width of sample. L is the gage length. $h_1$is thickness of TIM, and h_2 is the thickness of bare copper.

The bi-material constant, ε for plane strain, is defined as following:

$$\varepsilon = \frac{1}{2\pi} \ln \left(\frac{\frac{3 - 4\nu_1}{G_1} + \frac{1}{G_2}}{\frac{3 - 4\nu_2}{G_2} + \frac{1}{G_1}} \right) \tag{3-27}$$

The modulus of the K, related to the plane strain energy release rate, is defined as follows:

$$|K| = \sqrt{\frac{4 \cosh^2(\pi\varepsilon)\zeta}{\frac{1 - \nu_1}{G_1} + \frac{1 - \nu_2}{G_2}}} \tag{3-28}$$

A simplifying assumption has been made to allow the relative displacements of the two surfaces of the crack $\left[8(\Delta u_x)\right] = \Delta u_y$ in the equation based on experimental measurements:

$$\Delta u_x + i \Delta u_y = e^{j\phi} \sqrt{(\Delta u_x)^2 + (\Delta u_y)^2} \tag{3-29}$$

This allows $\phi = \pi / 8$. The phase angle is computed as follows:

$$\psi = \omega + \beta \tag{3-30}$$

Where $\omega = \tan^{-1}(2\varepsilon)$

$$\beta = \phi - \varepsilon(\ln r) = (\frac{\pi}{8}) - \varepsilon(\ln r) \tag{3-31}$$

The stress intensity factor values for mode 1 and 2 are determined as follows. The real part is mode 1. The imaginary part is mode 2.

$$\begin{aligned} Re(K) &= |K| cos(\omega + \beta) \\ Im(K) &= |K| sin(\omega + \beta) \end{aligned} \tag{3-32}$$

3.5.5 **Paris Power Law**

The Paris power law was developed by Paris and Erdogan as a fundamental model describing the sub-critical crack growth under cyclic loading. According to this law, the crack growth rate, da/dN, depends upon the stress intensity factor range, ΔK, a parameter involving the cyclic applied stress at the crack tip. In mathematical terms, the above relationship takes the form of the so-called Paris equation.

Paris power law is used to characterize cyclic fatigue behavior. Experimental study was conducted to examine the correlation between the rate of fatigue crack growth (da/dN) and the range of stress intensity factor (ΔK). The results of this study can be presented on a logarithmic-logarithmic graph (Figure 3-16). Typically, such a graph exhibits three distinct regions.

At the lower end of the graph, there exists a threshold region characterized by ΔK values below which cracks do not propagate. This threshold value, known as ΔK_{th}, is influenced by both the mean stress level and environmental conditions.

At the upper end of the graph, the rate of fatigue crack propagation may increase if the upper limit of the applied stress intensity factor range approaches the material's fracture toughness. This indicates a critical point where crack growth becomes more rapid.

Between these two regions, the graph generally displays a linear relationship on logarithmic scales. It is a stable region. In this study, we only focus on the steady linear region 2. The form follows the Paris power law:

$$\frac{da}{dN} = C(\Delta K)^n \tag{3-33}$$

- da/dN = crack growth rate per cycle
- C = material constant (intercept)
- n = slope, indicating material sensitivity to cyclic loading
- ΔK = Kmax − Kmin = stress intensity factor range during loading.

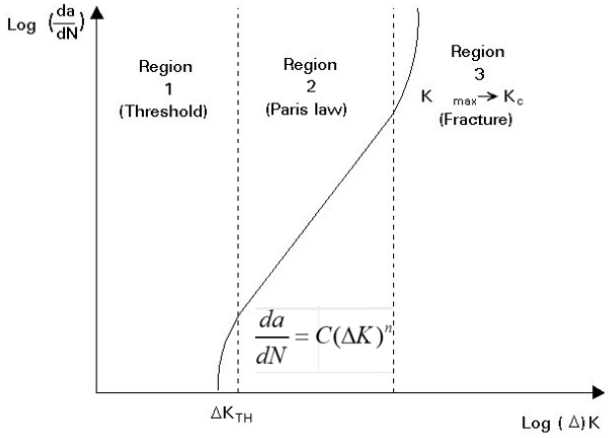

Figure 3-20 Typical fracture mechanics fatigue crack growth

3.6*Thermal analysis methods: conduction*

Thermal analysis of electronic systems involves predicting the junction temperatures of the integrated circuits used in both analog and digital circuits. It also involves predicting the temperature of other circuit components like resistors, capacitors and transformers. The analysis is extremely important as the system reliability and system availability are strongly dependent on component temperatures and relatively small temperature changes can have a marked effect on both component and system reliability.

3.6.1Steady state heat transfer by conduction

Conduction is the transfer of heat from a higher to a lower temperature by random molecular interactions. It is the primary mode of heat transfer near the chip level. 1D steady-state conduction with no internal heat generation is governed by a simplified version of Fourier's Law, as shown in

$$T_h = T_c + \frac{qL}{kA} \tag{3-34}$$

where q is the heat transfer rate or power in Watts (W), k is the thermal conductivity of the medium (W/m · K), T_h and T_c are hot and cold temperatures (K), A is the area normal to the direction of heat flow (m^2), and L is the distance of heat transfer (m). $q'' = q/A$ is referred to as the heat flux or power density (W/m^2).

3.6.2 Contact resistance

Materials and Sample Preparation

One PFAS and two Non-PFAS TIMs are prepared for interfacial thermal resistance study. The dimension of sample is showing in Table 1. The mold for sample preparation is showing in Figure 1. The material information is listed in the Table 3-5.

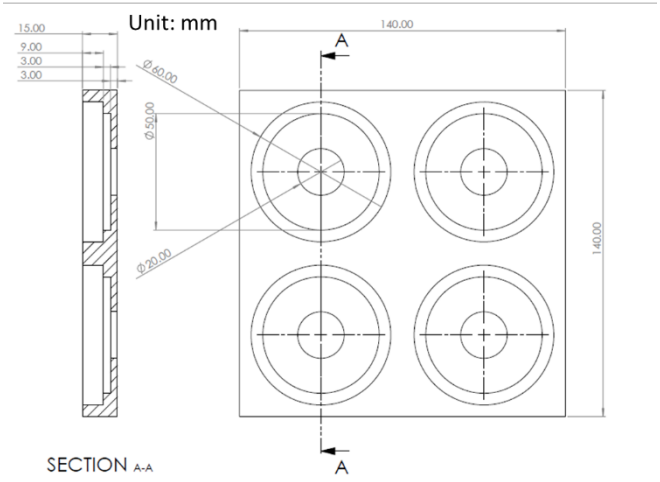

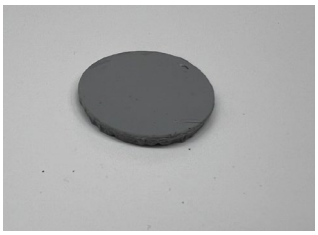

Figure 3-21 Mold Design and Sample Preparation

Table 3-4 Dimension of the samples

Thickness(inch)	0.11
Diameter(mm)	30

Table 3-5 Material Properties for TIMs

Material System	Viscosity	Thermal Conductivity (W/m-K)	Cure Profile
NP_TIM1	130000	5.2	125°C/ 30 mins +150°C/ 60 mins.
NP_TIM2	78000	3.5	125°C/ 30 mins +150°C/ 60 mins
P_TIM 3	66000	1.92	150°C/ 30 mins

Experimental Method

The evolution of thermal interfacial properties under high temperature and humidity exposure is characterized. Test matrix is showing as Table 3-6 . JESD22-A101 specifies that samples should survive 85°C/85%RH conditions for over 1000 hours. In our investigation, samples were exposed to 85°C/85%RH for over 1000 hours to evaluate their reliability performance.

Table 3-6 Test Matrix

Aging Hours	85C85%RH

0	done
200	done
400	done
600	done
800	done
1000	done

(a) Tester system

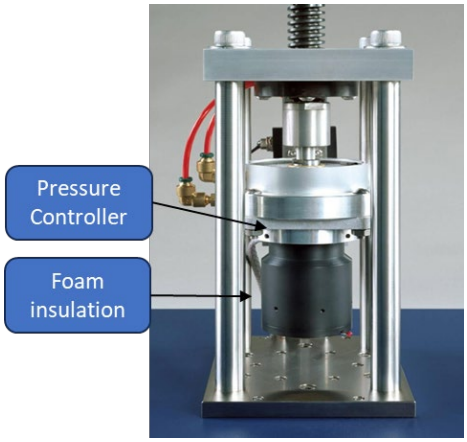

(b) Testing setup

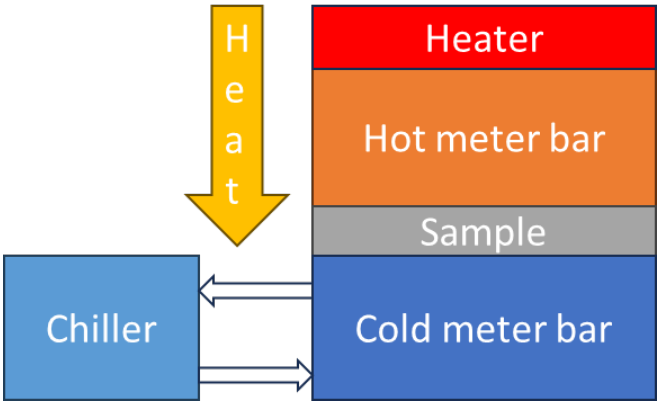

(c) Schematics of the testing methodology

Figure 3-22 TIM Tester 1400

The C-Therm Trident Thermal Conductivity Analyzer is a versatile instrument for measuring the thermal conductivity of solids, powders, and liquids, utilizing two methods: the Modified Transient Plane Source (MTPS) and Flex Transient Plane Source (TPS). The MTPS method, a variation of the transient plane source technique, employs a one-sided interfacial sensor integrated with controller electronics and computer software. The sensor features a central spiral heater surrounded by a guard ring to approximate one-dimensional heat flow into the test material. During testing, the voltage drop across the spiral heater is monitored before and during transient heating, and this data is used to determine the material's thermal effusivity and calculate its thermal conductivity based on the slope of the voltage readings. This method enables precise and reliable characterization of thermal properties, making the analyzer valuable for material research and quality assurance.

Figure 3-23 Modified Transient Plane Source Method Test System

The tester is commercially available through Analysis Tech. The detailed specifications of the apparatus used can be found in Ref. [41]. In this setup (Figure **3-18**), heat flows through the upper meter bar and the lower meter bar, which is cooling with a chiller. This tester uses a linear variable differential transformer sensor to measure the in situ thickness of the TIM joint. An applied pressure can be controlled from 50 to 2600 kPa using several different pressure kits. For the testing of TIMs, a pressure sensor in the range of 50–650 kPa was used which was accurate to

±20 kPa. The electronic thickness measurement accuracy is ±25 μm. The test surfaces of this testing device are a highly smooth, nickel polished finish with a flatness within 7–8 μm. The meter bars are thermally insulated to minimize the heat loss to the surroundings. In this research, thermal impedance across the TIM depends on the temperature drop (ΔT) from top and bottom (T_h and T_c), heat flux (Q_{ave}) through the TIM, thermal conductivity of the disk material (k), and the thickness of the TIM sample (L). The thermal impedance of the TIMs (RA) reported hereafter was obtained after adding the conduction resistances of the disk material and contact resistances as presented in Eqn. (1).

$$RA = R \times A = \frac{T_h - T_c}{Q_{ave}} \times A = (2R_{cont} + \frac{L}{k}) \times A \tag{3-35}$$

3.6.3Modified plane source methods

Materials and Sample Preparation

Non-PFAS underfill and non-PFAS TIM are prepared for thermal conductivity study. The information of non-PFAS UF is showing in Table 3-7. The curing condition is 150C/10mins. The glass transition temperature is 160C by TMA method. The coefficient of thermal expansion is 26ppm/C below Tg and 103ppm/C above Tg. The storage modulus is 6GPa. The mold for sample preparation is showing in Figure 3-20.

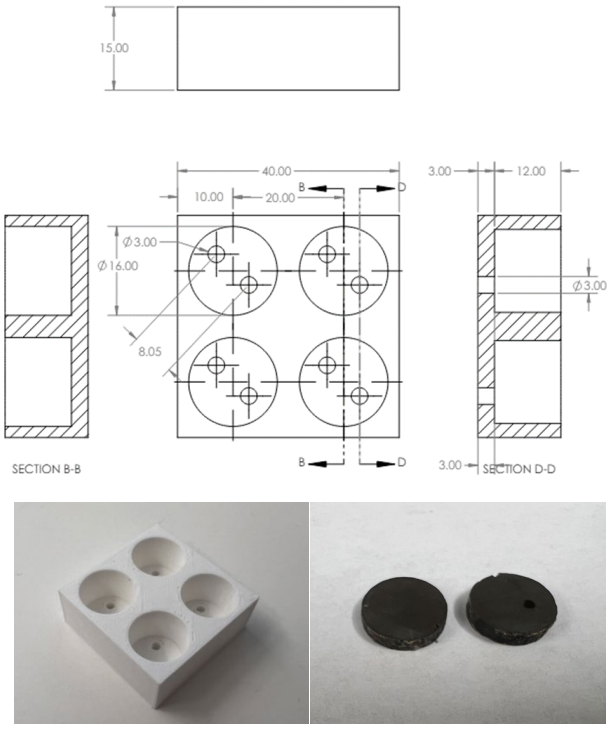

Figure 3-24 Mold Design and Sample Preparation

Table 3-7 Material Properties for UFs

Non-PFAS UF1	
Property	Value
Base Resin	Epoxy Amine
Stroage Modulus	6GPa
Worklife	48 hours at 23C
Curing Condition	150C/10mins
Tg (by TMA)	160C
Coefficient of Thermal Expansion (CTE)	26×10^{-6}(<Tg) 103×10^{-6}(>Tg)
Non-PFAS UF2	
Property	Value
Base Resin	Epoxy Amine
Stroage Modulus	6GPa
Worklife	5 days at 25C
Curing Condition	150C/10mins

Tg (by TMA)	125C
Coefficient of Thermal Expansion (CTE)	35 $\times 10^{-6}$(<Tg) 131 $\times 10^{-6}$(>Tg)

Table 3-8 Material Properties for TIMs

Material System	Viscosity	Thermal Conductivity (W/m-K)	Cure Profile
NP_TIM1	130000	5.2	125°C/ 30 mins +150°C/ 60 mins.
NP_TIM2	78000	3.5	125°C/ 30 mins +150°C/ 60 mins
P_TIM 3	66000	1.92	150°C/ 30 mins

Test Method

The evolution of thermal conductivity under high temperature and humidity exposure is characterized. Test matrix is showing as Table 3-9. According to JESD22-A113, samples are exposed to both 60C60%RH and 85C85%RH for 168 hours duration. JESD22-A101 specifies that samples should survive 85°C/85%RH conditions for over 1000 hours. In our investigation, samples were exposed to 85°C/85%RH for over 2000 hours to evaluate their reliability performance.

Table 3-9 Test Matrix

Aging Hours	60C60%RH	85C85%RH
0	done	done
24	done	done
48	done	done
72	done	done

96	done	done
120	done	done
144	done	done
168	done	done

Aging Hours	85C85%RH
500	done
600	done
700	done
800	done
900	done
1000	done
1100	done
1200	done
1300	done
1400	done
1500	done
1600	done
1700	done
1800	done
1900	done
2000	done
2200	done

Figure 3-25 C-Therm Trident Thermal Conductivity Analyzer

The C-THERM Trident Thermal Conductivity Analyzer is applied to thermal conductivity testing. It can do thermal conductivity measurement of solid, powder and liquid samples. There are two test methods: The modified Transient Plane Source Method (MTPS) and Flex Transient Plane Source (TPS). The MTPS method is based on a transient plane source method. The MTPS method comprises of following elements (a) a one-sided interfacial sensor, controller electronics, and computer software (b) a central heater and sensor element inside the sensor in the shape of a spiral surrounded by a guard ring which generates heat in addition to the spiral heater. The arrangement approximates one-dimensional heat flow from the sensor into the material under test in contact with the sensor. The voltage drop on the spiral heater is measured before and during the transient. The voltage data is then translated into the effusivity value of the tested material. The conductivity is calculated from the slope of the voltage data.

Effusivity is defined as the square root of the product of thermal conductivity k, density ρ and specific heat capacity C_p, and has the units of $\frac{W\sqrt{s}}{m^2K}$. The TCi system used for the material characterization in this paper measures effusivity directly and determines conductivity from this

measurement. The heat equation in one dimension with a constant supply of heat per time per volume, G', is given below:

$$\rho C_p \frac{\partial T}{\partial t} = \lambda \frac{\partial^2 T}{\partial x^2} + G' \tag{3-36}$$

Where λ is the thermal conductivity, T is the temperature, t is time, x is the dimension measured along the speciment thickness with x=0 located at the sensor-specimen interface, G is the power flux supplied to the sensor (W/m^2). For one-dimensional heat flow and no thermal contact resistance at the interface between the sensor and sample under test, the temperature change on the sensor surface (x=0) is given by:

$$\Delta T(x = 0, t) = \frac{1.1284 G\sqrt{t}}{e_1 + e_2} \tag{3-37}$$

Where ΔT = change in sensor surface temperature (ºC), G = power flux supplied to sensor (W/m^2), t = time measured from start of process (sec), e_1 = equivalent effusivity of sensor ($\frac{W\sqrt{s}}{m^2 K}$), e_2 = effusivity of measured material ($\frac{W\sqrt{s}}{m^2 K}$). The voltage change of the sensor is represented by:

$$\Delta V(t) = \frac{1.1284.\, I.\, A.\, G\sqrt{t}}{e_1 + e_2} \tag{3-38}$$

Where I is the sensor current, and A is the specimen cross-sectional area. The voltage output of the sensor is measured. The effusivity value of the tested material is computed from the voltage data. Then, the conductivity of the specimen is calculated from the slope of the voltage data. The sensor applies a constant current heat source to the sample. The sample is heated at approximately 1-3°C during the testing. The sample absorbs some of the heat depending on its thermal conductivity, and the rest causes a temperature rise at the sensor interface. The rate of the increase in temperature at the sensor surface is inversely proportional to the ability of the sample to transfer heat. Thermal conductivity and effusivity are measured.

The C-Therm Trident Thermal Conductivity Analyzer Flex configuration employs the Transient Plane Source (TPS) technique in characterizing the thermal conductivity, thermal diffusivity and specific heat capacity of materials, conforming to ISO Standard 22007-2. The TPS method employs a double-sided sensor to simultaneously determine thermal conductivity, thermal diffusivity and specific heat capacity of materials from a single measurement. It employs a double-sided sensor, and the user iteratively develops the timing and power parameters. Intended for rough and heterogeneous materials not well-suited to a single-sided test method, this configuration allows researchers the maximum versatility in test parameters and experimental design. The measurement includes 4 steps:

1. Power is applied to the sensor's spiral heating element, providing a small amount of heat. This results in a rise in temperature at the interface between the sensor and the sample, which induces a voltage change across the sensor element.

2. The results from the initial scouting run are used to estimate test time, power level, and ideal sensor size. The experiment is run with the new parameters. This may need to be repeated until the correct parameters are identified. Guidance is provided in ISO 22007-2.

3. The test result is a plot of temperature vs time.

4. The results are analyzed with an iterative solving procedure to generate thermal property data such as thermal diffusivity and thermal conductivity.

This method requires two identical samples. The diameter of the samples should be 2.5X sensor diameter (e.g. 6 mm sensor requires sample diameter of 15 mm). Thickness should be at minimum the same diameter as the sensor (e.g. 6 mm sensor requires 6 mm thick samples (Figure 3-22).

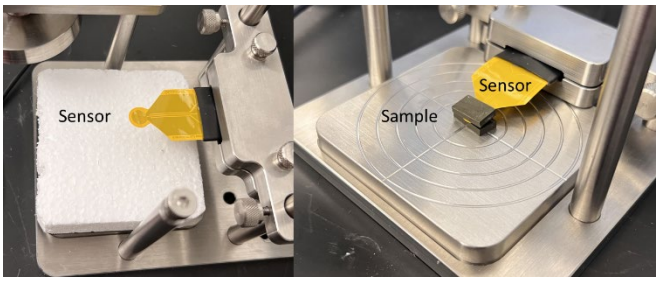

Figure 3-26 Flex TPS Sensor and Sample Placement

Chapter 4 Material property evolution of Underfill Encapsulant (UF)

4.1*Thermogravimetric Analysis*

Thermogravimetric analyzer (Q500 TGA, TA Instruments) was used to analyze the thermal degradation properties of cured samples under dry air environment. The testing temperature is from room temperature to 800℃.

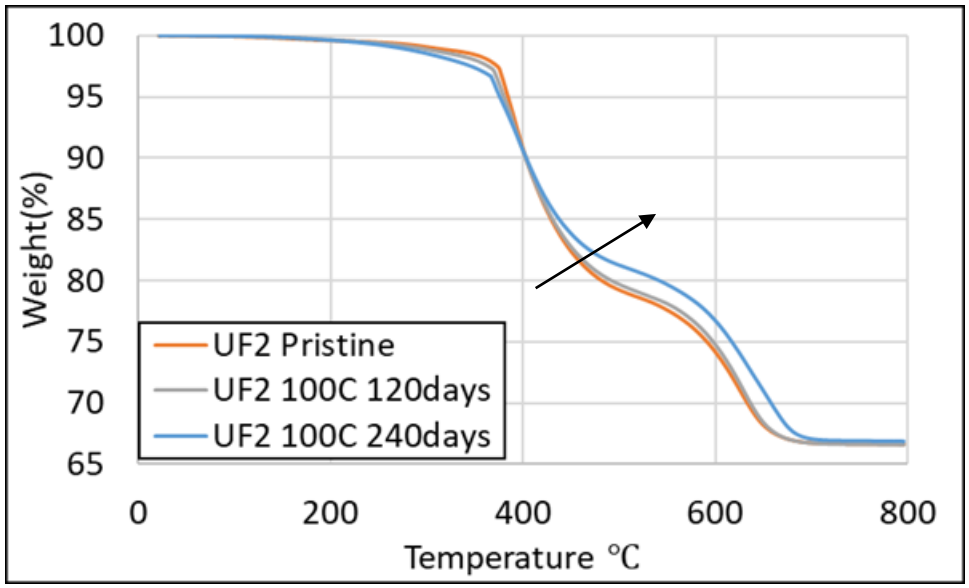

Fig. 4-1: Weight loss of UF2 under 100℃

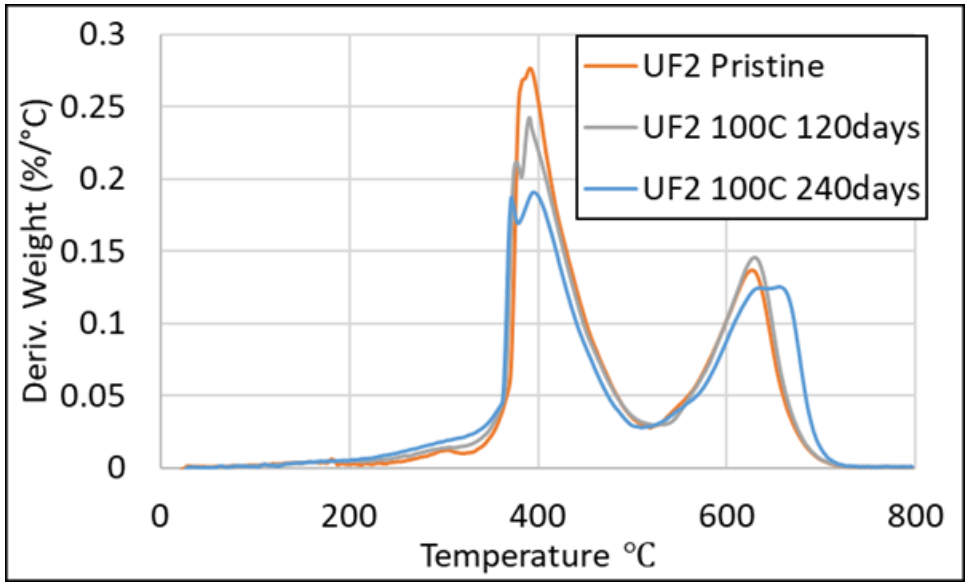

Fig. 4-2: Weight Derivative of UF2 under 100℃

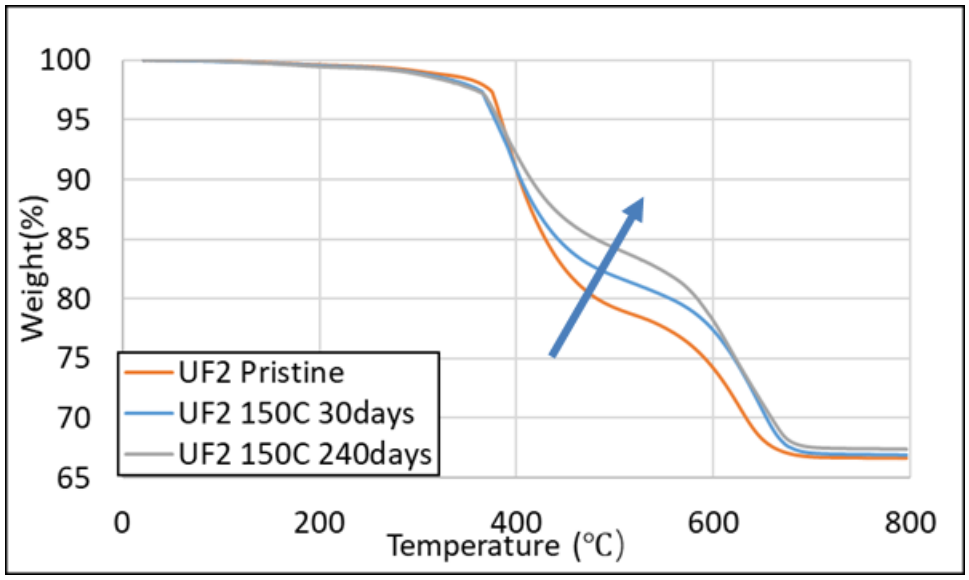

Fig. 4-3: Weight Loss of UF2 under 150°C

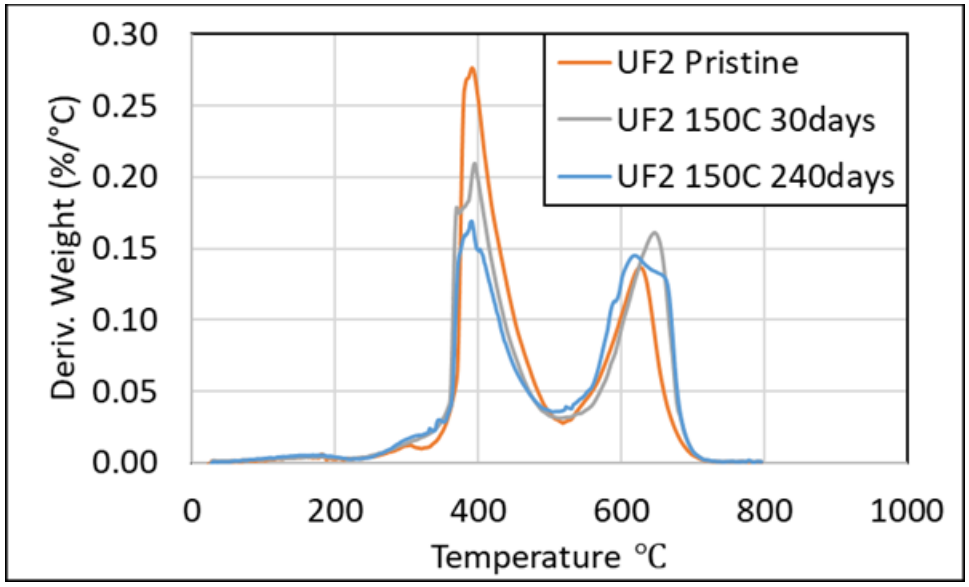

Fig. 4-4: Weight Derivative of UF2 under 150°C

Fig. 4-1 to Fig. 4-6 depict the weight loss and derivative weight measurements. The epoxy matrix undergoes two-stage decomposition in the temperature range of approximately 380°C to 680°C. The weight loss plots reveal that UF2 has a filler content of 66%, while UF3 has a filler content of 60%. After long-term aging at high temperatures, particularly in the range of 450°C to 650°C, the material becomes more resistant to decomposition. This can be attributed to an increase

in cross-linking density. As the aging temperature rises, the material becomes stiffer, resulting in a higher decomposition temperature.

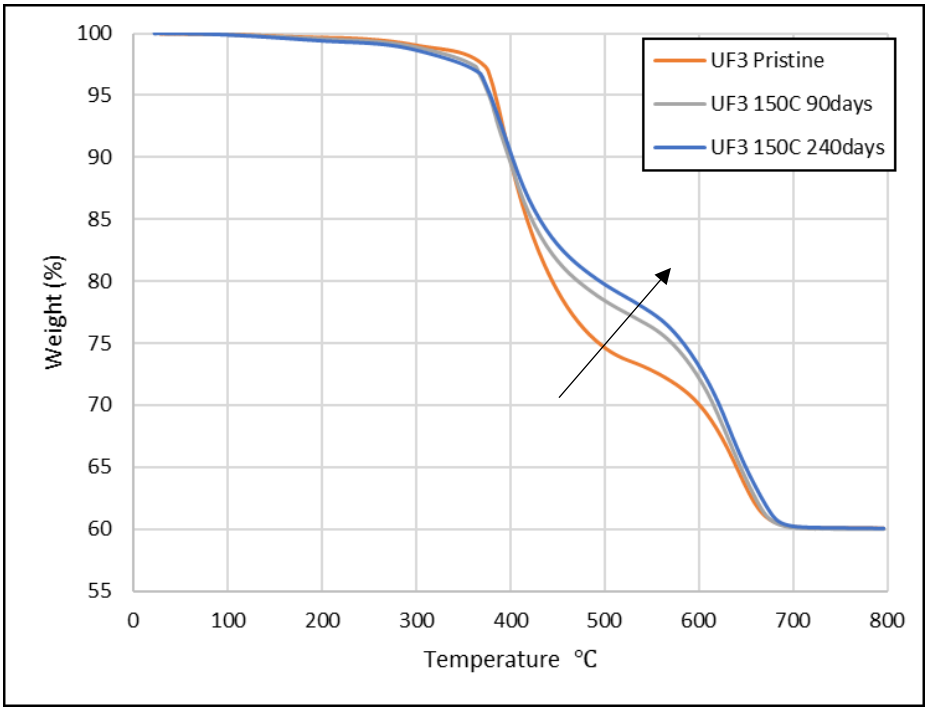

Fig. 4-5: Weight Loss of UF3 under 150℃

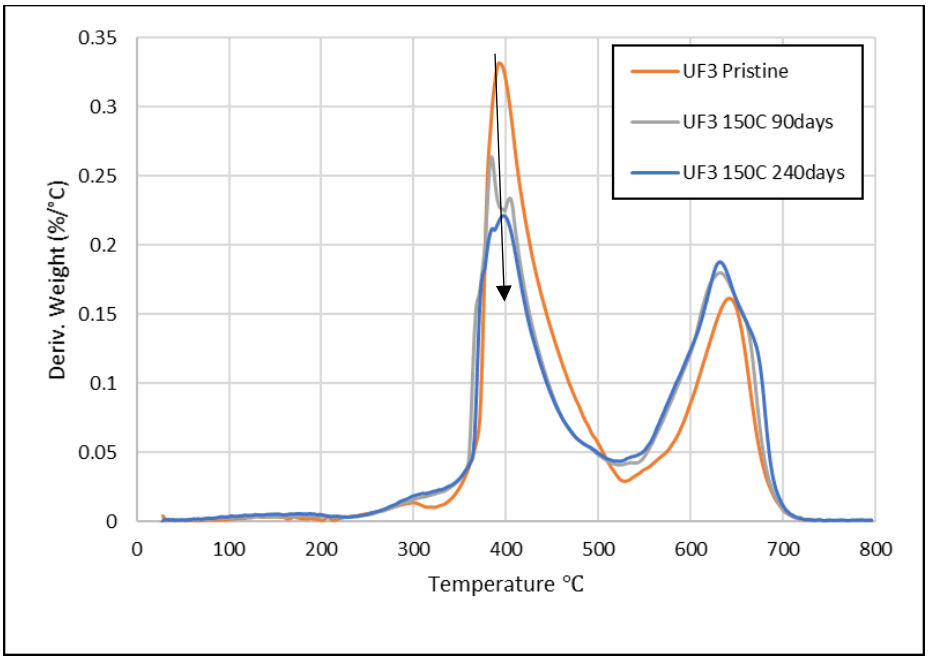

Fig. 4-6: Weight Derivative of UF3 under 150°C

The derivative weight plots demonstrate the rate of weight change over time. Two peaks are observed in the derivative weight curves. The first peak occurs at around 400°C, while the second peak is located at approximately 630°C. Aging significantly influences the first peak. With increased aging time and temperature, the maximum of the first peak decreases. On the other hand, the second peak at 630°C remains relatively stable and does not undergo significant changes after aging.

4.2Differential scanning calorimetry (DSC)

Differential scanning calorimetry (DSC) is applied to four types of Underfill materials. A heat-cool-heat procedure is followed. The uncured sample is heated up from 40°C to 260°C, then cooled down to 40°C and heated up to 260°C again. The results are shown in **Figure 4-7**. The curing energy for UF1 is 76.71J/g. The glass transition temperature is 116.08°C. The peak of curing occurs at 196.04°C. The curing energy for UF2 is 76J/g. The glass transition temperature is 95.4°C. The peak of curing occurs at 188.83°C. Glass transition temperature of UF3 is 85.74°C. The peak

of curing occurs at 192.9℃. The curing energy is 79.46J/g. Glass transition temperature for UF4 is 120.06℃. The peak of curing occurs at 198.02℃. the curing energy is 70.83J/g. Table 4-1 shows the glass transition temperature measured DSC. Glass transition temperature for UF1 and UF4 are similar, around 115℃. The glass transition temperature of UF2 and UF3 are much lower. Glass transition temperature for UF2 is 93℃. The glass transition temperature for UF3 is 85℃.

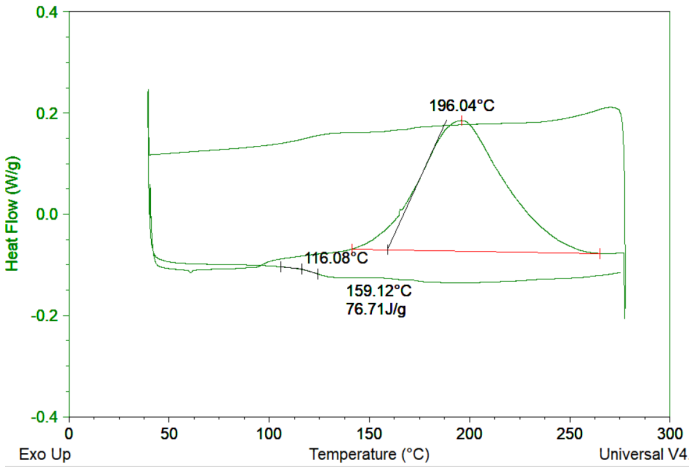

a) UF1 curing profile

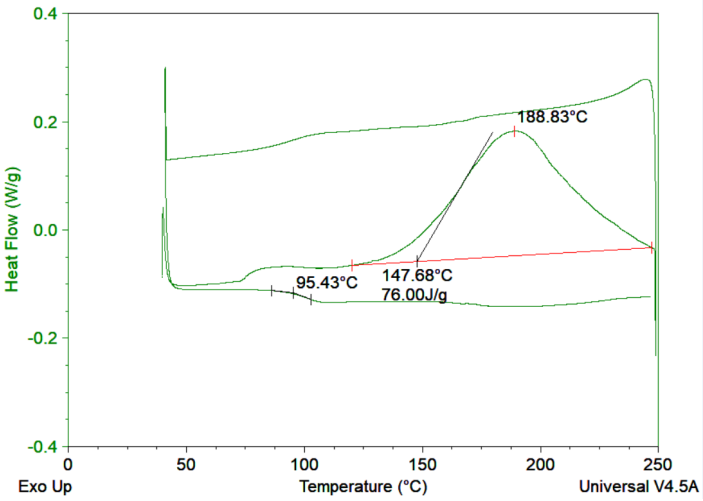

b) UF2 curing profile

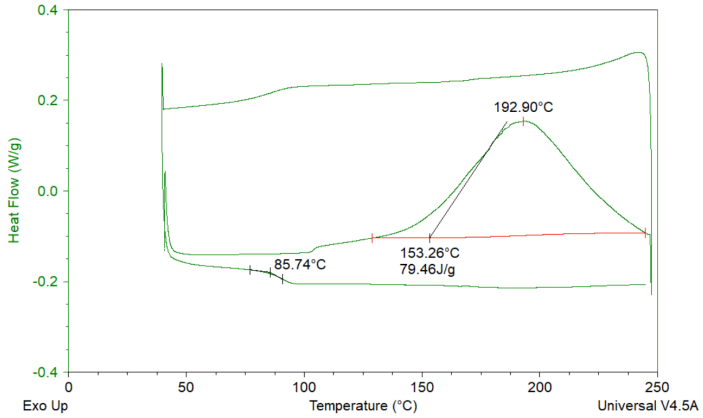

c) UF3 curing profile

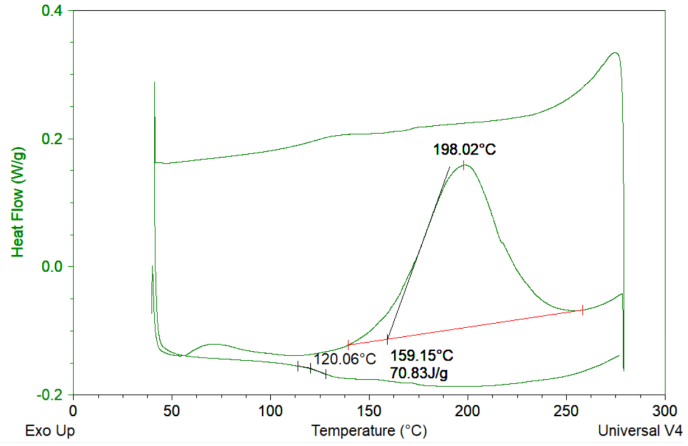

d) UF4 curing profile

Figure 4-7 DSC Result of uncured materials

Table 4-1 Glass Transition Temperature of UFs by DSC

	UF1	UF2	UF3	UF4
Tg	116.08℃	95.4℃	85.74℃	120.06℃

The DSC tests are also conducted to the aged specimen, to study the curing behavior as the function of aging time and aging temperature. Figure 4-9 shows the result of UF3. The sample right after curing shows the glass transition temperature about 98℃. It is also showing perfectly curing without residual cure. After 120 days, the glass transition temperature shift to about 115℃ for 100℃ curing and about 123℃ for 150℃ curing. For 100℃ curing condition, it also shows a

small bump, indicating post cure, occurs about 100℃. There is a small evaporation occurs at about 110℃. For 150℃ aging condition, the post cure also occurs, but we do not observe any evaporation behavior. For 240 days aging, at 100℃ temperature, the glass transition temperature shift to 124℃. We also observe the small post cure and evaporation. At 150℃, there is no evaporation observed. The glass transition temperature divide into two domains. We could observe two glass transition separately. One is about 125℃, the other is about176℃.

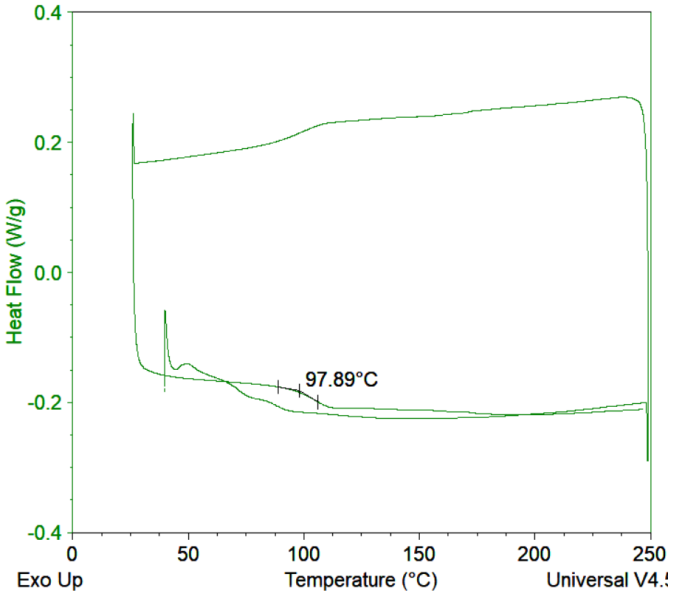

a) UF3 pristine condition

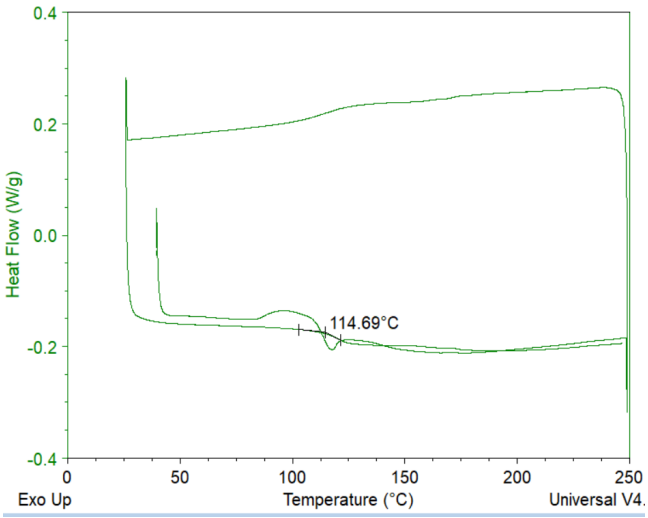

b) UF3 100°C 120 days

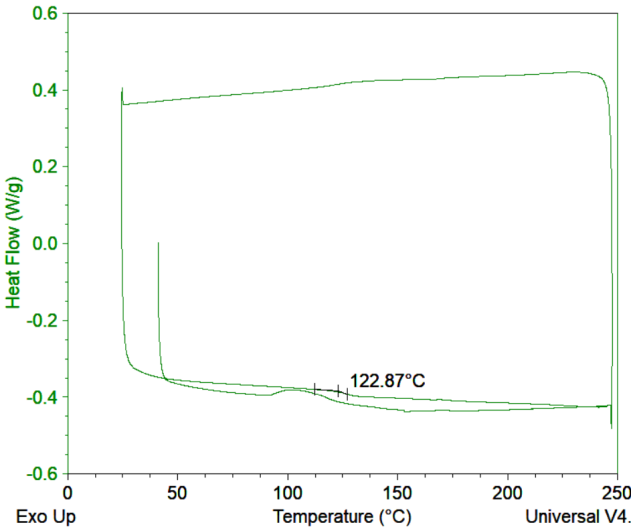

c) UF3 150°C 120 days

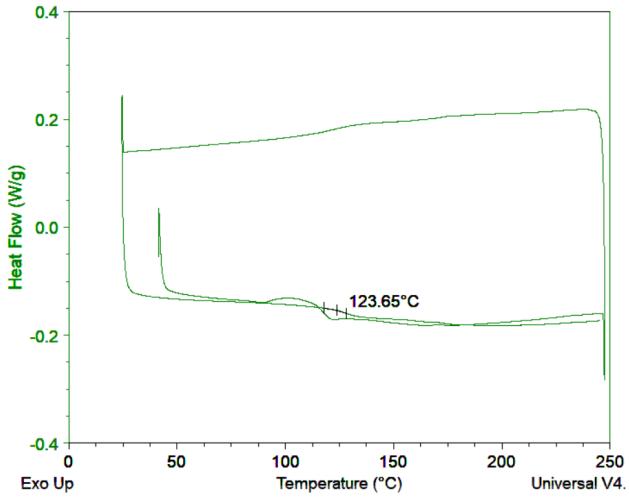

d) UF3 100°C 240 days

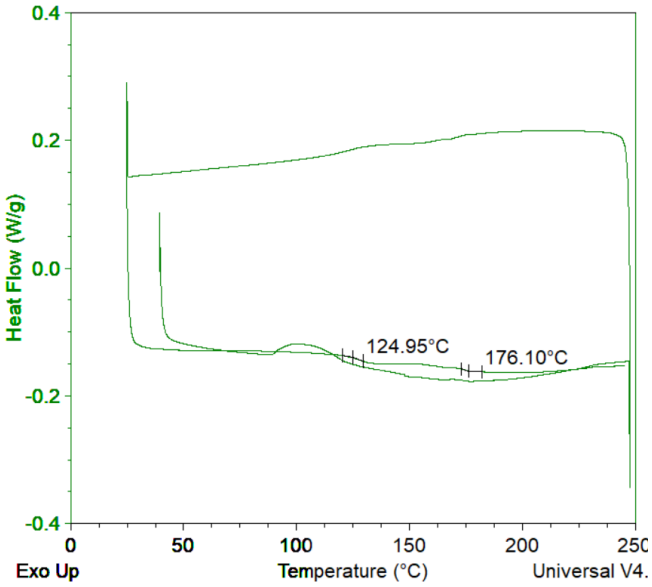

e) UF3 150°C 240 days

Figure 4-8 Curing behavior for UF3 as the function of aging time and temperatures

4.3Monotonic Tension Test

The evolution of elastic modulus under high temperature aging is unclear for Underfill encapsulants. [106] reports that the modulus increases as the aging time increases, indicating the increased brittleness due to higher cross-linking density. Conversely, [107] reports the modulus creases as the aging time increases, which could be attributed to the material degradation. In this study, the elastic modulus evolution as the function of long term aging is reported in Figure 4-7 - Figure 4-14. Samples are tested from pristine, 30 days, 60 days, 90 days, 120 days, 240 days and 360 days under 100C and 150C environment. 5 duplicate specimens are tested under each test condition. The results indicate that the elastic modulus remains stable or increases under 100°C aging. However, for 150°C exposure, the modulus begins to decrease with prolonged aging.

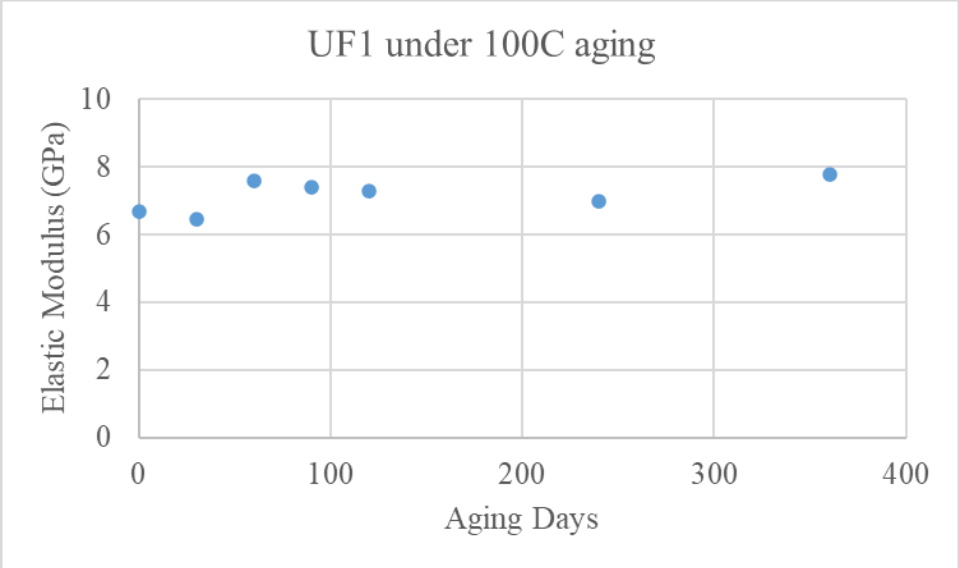

Figure 4-9 Elastic Modulus of UF1 under 100C aging condition

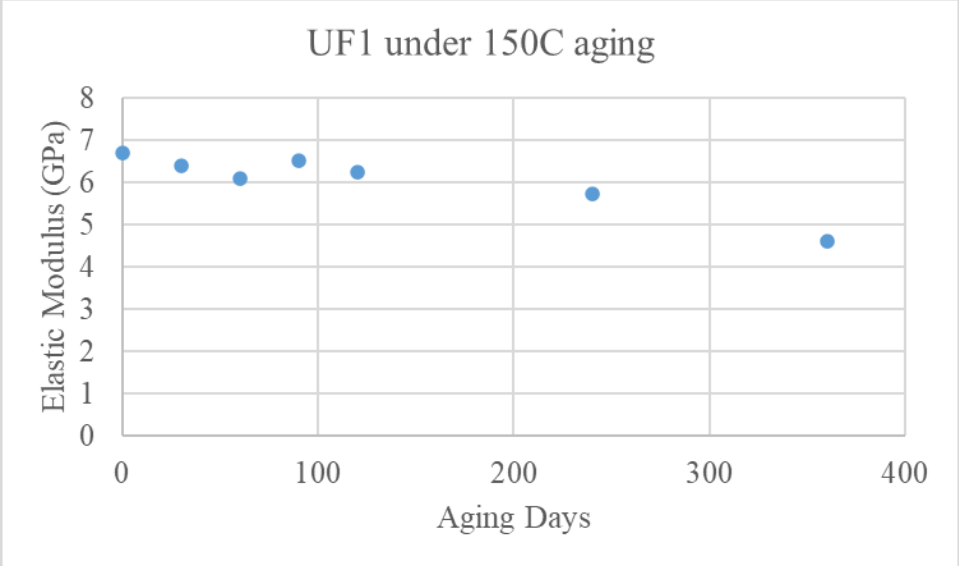

Figure 4-10 Elastic Modulus of UF1 under 150C aging condition

For UF1, under the 100°C aging condition, the elastic modulus increases from 6.7 GPa to 7.79 GPa over 360 days. In contrast, under the 150°C aging condition, the modulus decreases from

6.7 GPa to 6.24 GPa within the first 120 days and further declines from 6.24 GPa to 4.63 GPa between 120 and 360 days.

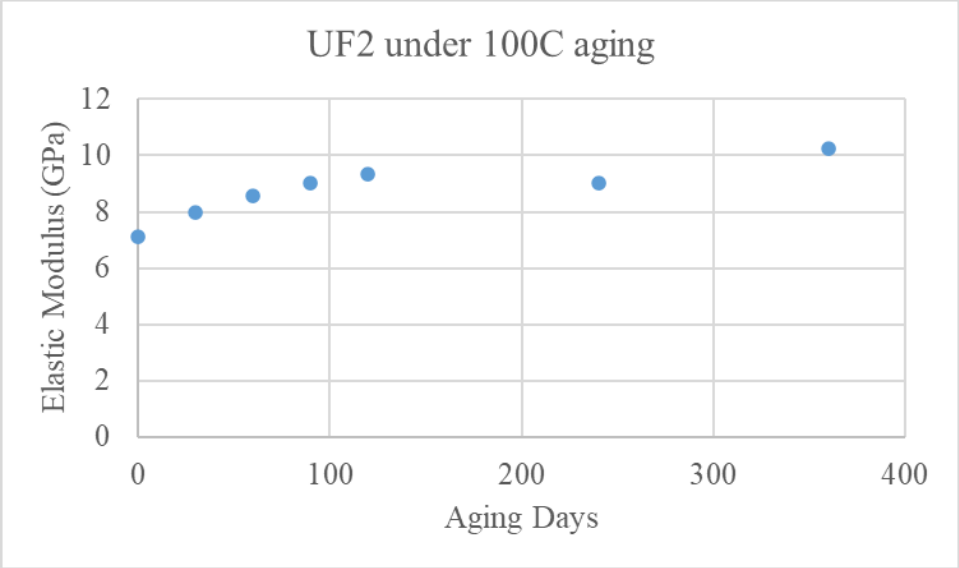

Figure 4-11 Elastic Modulus of UF2 under 100C aging condition

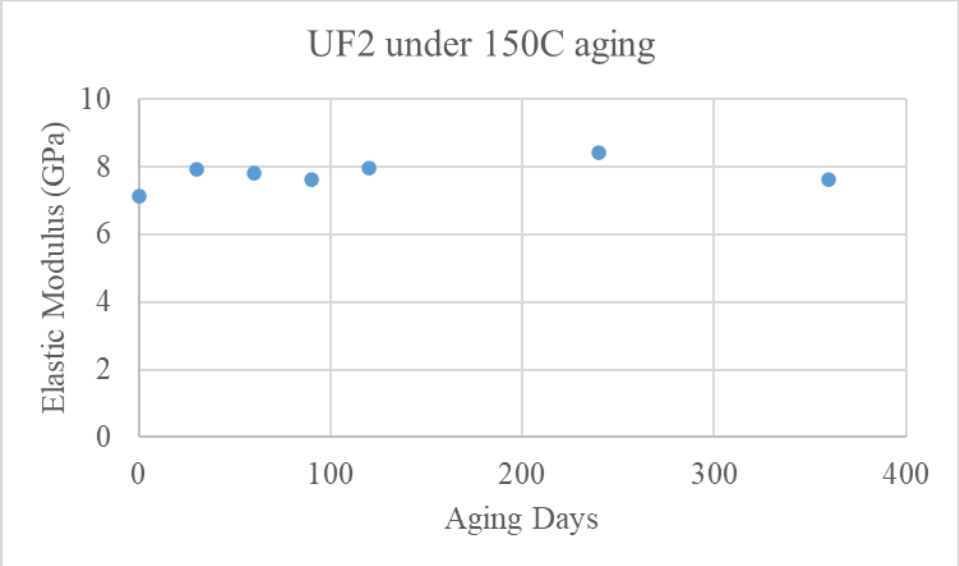

Figure 4-12 Elastic Modulus of UF2 under 150C aging condition

For UF2, under the 100°C aging condition, the elastic modulus increases significantly from 7.13 GPa to 10.24 GPa over 360 days. In contrast, under the 150°C aging condition, the modulus

initially decreases from 7.13 GPa to 7.96 GPa within the first 120 days and then remains relatively stable, declining slightly from 7.96 GPa to 7.63 GPa between 120 and 360 days

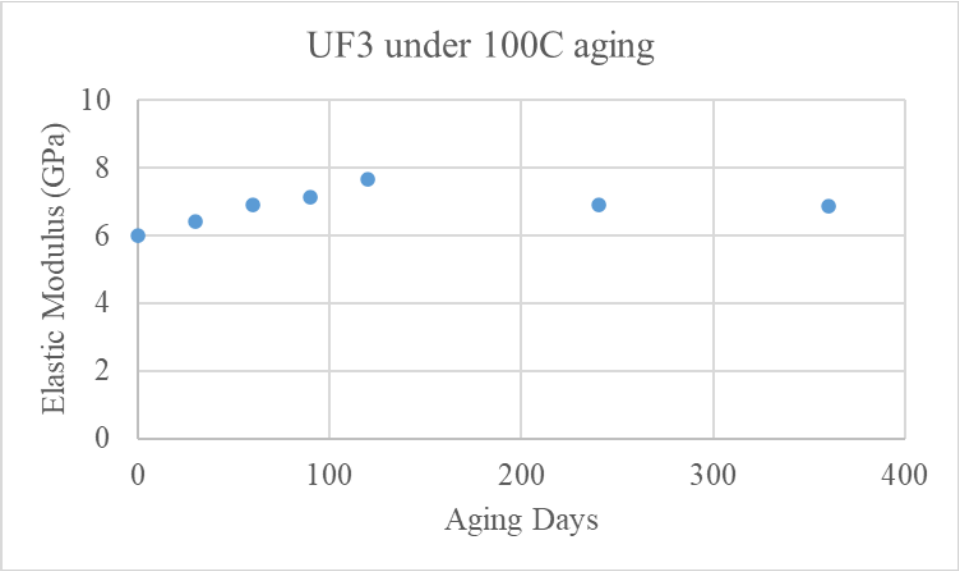

Figure 4-13 Elastic Modulus of UF3 under 100C aging condition

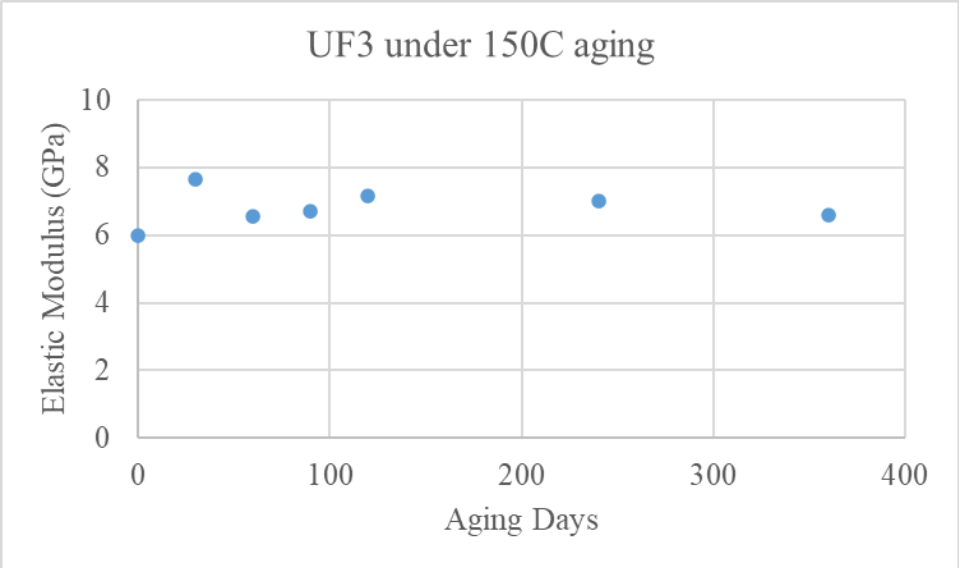

Figure 4-14 Elastic Modulus of UF3 under 150C aging condition

For UF3, under the 100°C aging condition, the elastic modulus increases from 6 GPa to 6.9 GPa over 360 days. Under the 150°C aging condition, the modulus initially increases from 6

GPa to 7.17 GPa within the first 120 days but then stabilizes, with a slight decrease from 7.17 GPa to 6.6 GPa between 120 and 360 days.

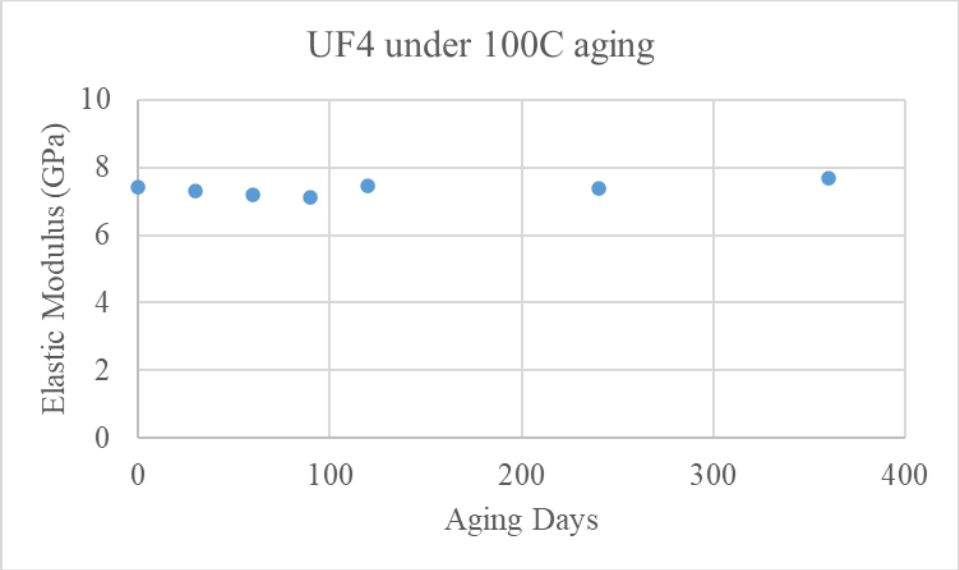

Figure 4-15 Elastic Modulus of UF4 under 100C aging condition

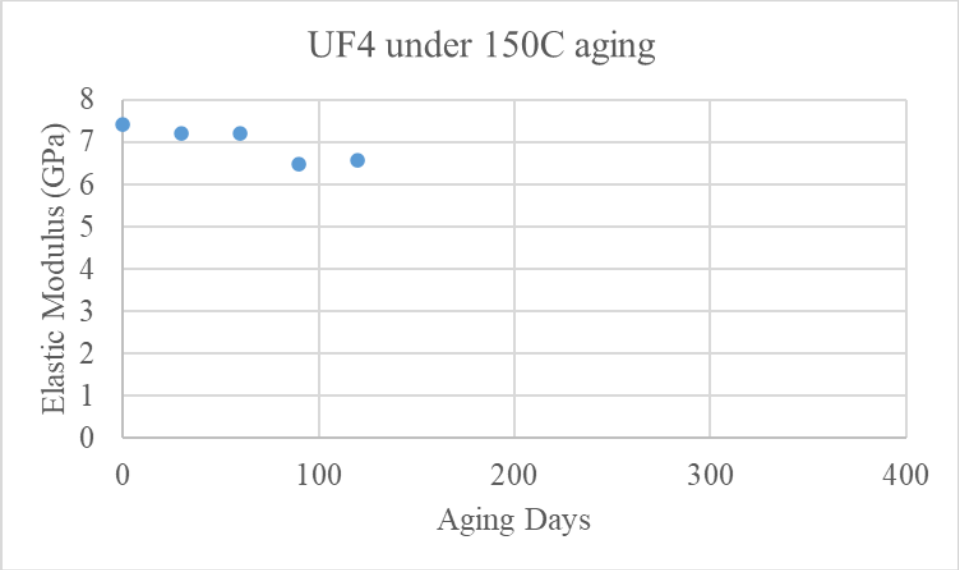

Figure 4-16 Elastic Modulus of UF4 under 150C aging condition

For UF4, under the 100°C aging condition, the elastic modulus increases slightly from 7.41 GPa to 7.7 GPa over 360 days. In contrast, under the 150°C aging condition, the modulus decreases from 7.41 GPa to 6.58 GPa within the first 120 days, followed by failure.

Uniaxial tensile tests are carried out on four underfills (UFs) in order to examine the evolution of percentage elongation and ultimate tensile strength (UTS) with respect to aging time, as shown in Fig. 4-7 to Fig. 4-14. The degradation process can be divided into two distinct stages, and the slopes of the curves (referred to as K1 and K2) are plotted to analyze the trends.

In general, both UTS and percentage elongation initially increase from the pristine state to a peak point, referred to as the inflation point. However, beyond the inflation point, both UTS and percentage elongation start to decrease when subjected to a 100°C environment. For the 100°C aging condition, K1 is positive while K2 is negative. On the other hand, when subjected to 150°C aging, the material experiences significant degradation (over 80%) during the first step (K1) and then remains relatively stable. As a result, the value of K1 for the 150°C aging condition is much lower compared to K2. This discrepancy suggests the presence of two distinct degradation mechanisms for the 100°C and 150°C aging conditions.

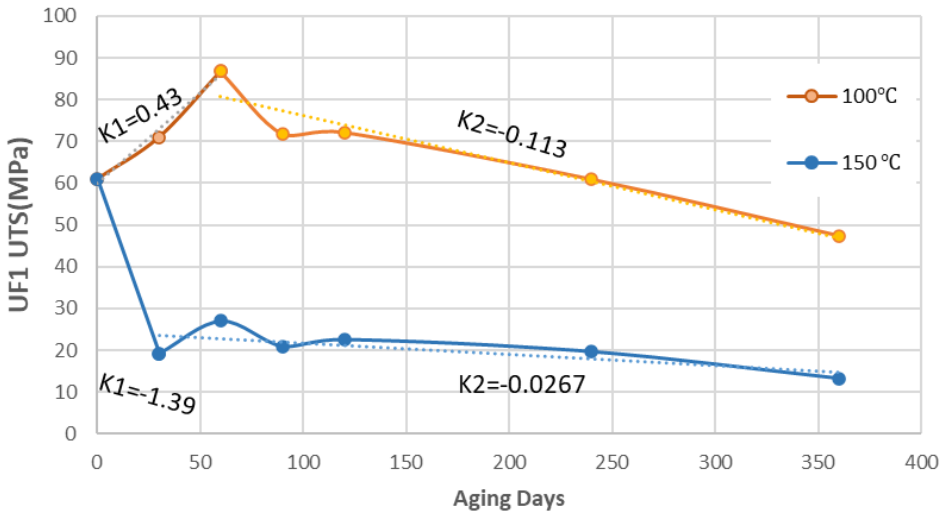

Fig. 4-17 UF1 UTS

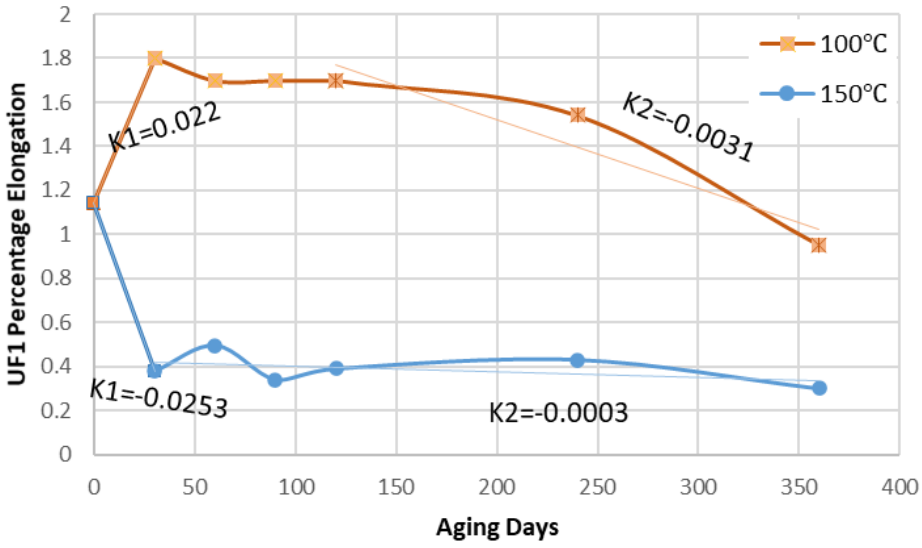

Fig. 4-18 UF1 Percentage Elongation

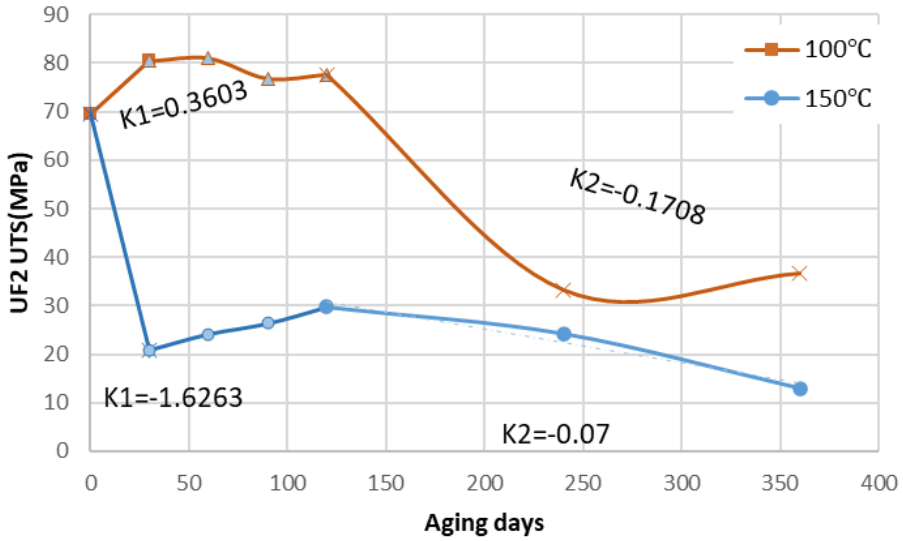

Fig. 4-19 UF2 UTS

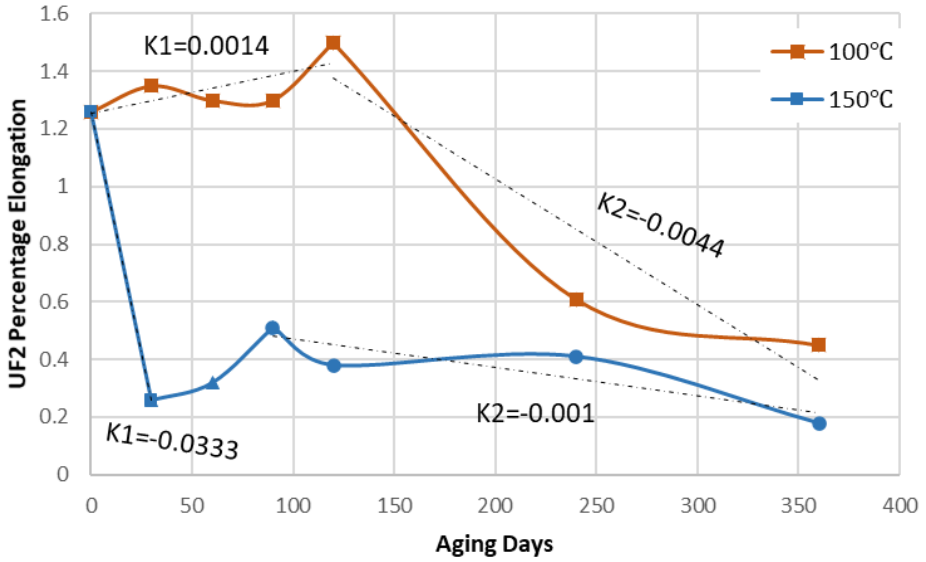

Fig. 4-20 UF2 Percentage Elongation

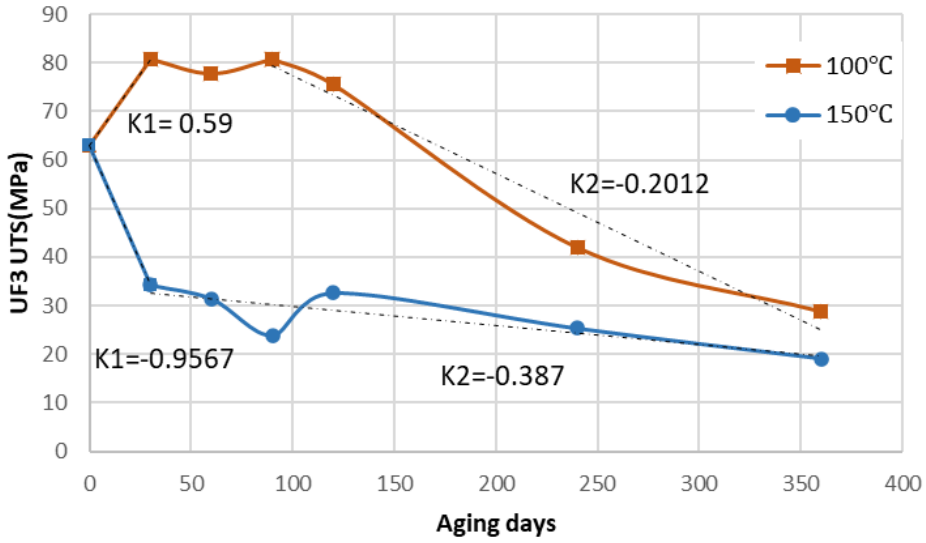

Fig. 4-21 UF3 UTS

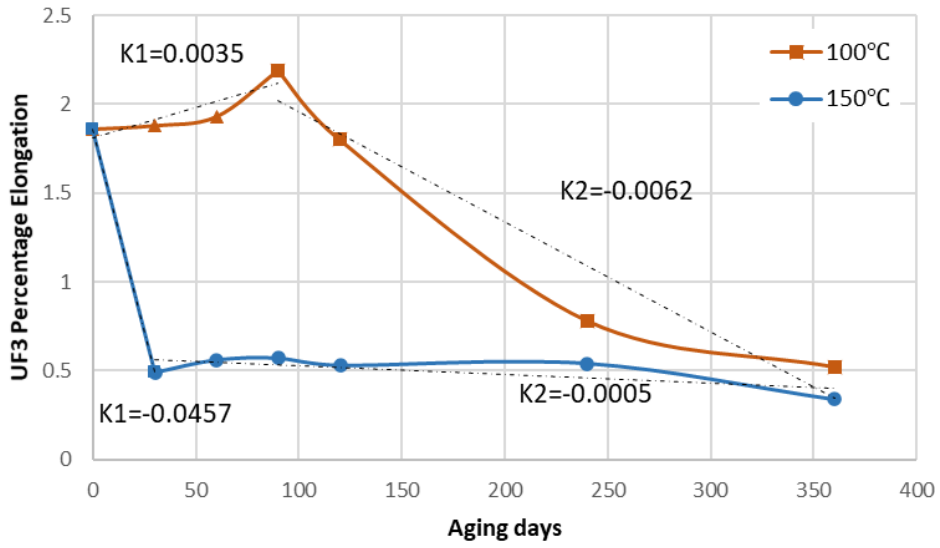

Fig. 4-22 UF3 Percentage Elongation

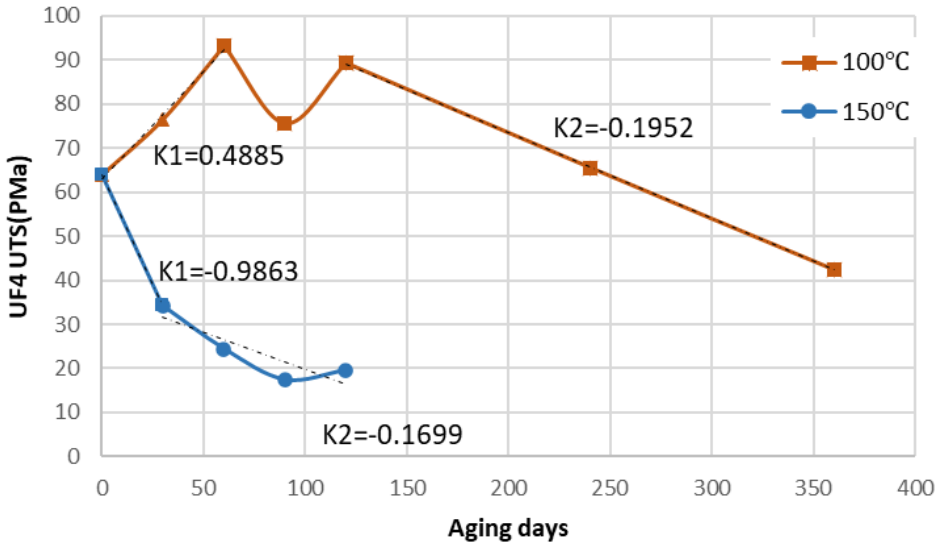

Fig. 4-23 UF4 UTS

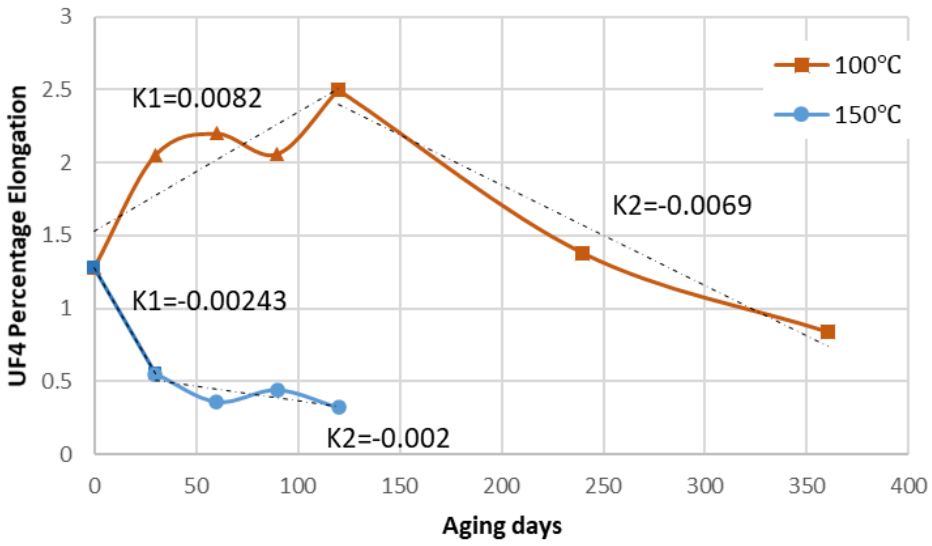

Fig. 4-24 UF4 Percentage Elongation

In a 100°C environment, the ultimate tensile strength (UTS) and percentage elongation of four different UF samples increase by approximately 15% from their pristine state to the inflection point. However, degradation begins after reaching the inflection point. When exposed to a 150°C environment, both UTS and percentage elongation experience a significant decrease of around 80% within 30 days compared to their pristine state. This suggests that the primary mechanical degradation occurs during the initial 30-day period of aging at 150°C.

Specifically, UF2 and UF3 share the same epoxy resin matrix but differ in filler content. UF2 has a filler content of 66%, while UF3 has a filler content of 60%. When subjected to a 100°C environment, UF2 demonstrates a 14% increase in UTS from its pristine state over 120 days, but starts to degrade after 120 days. On the other hand, UF3 exhibits an inflection point at 90 days. Percentage elongation begins to decrease after 120 days for UF2 and 90 days for UF3. These findings suggest that a higher filler content can result in a longer inflection point during aging at 100°C. The maximum UTS achieved for both UF2 and UF3 under 100°C conditions is approximately 80MPa. However, the percentage elongation of UF3 is significantly higher than that

of UF2 for both 100°C and 150°C aging conditions. This difference in percentage elongation can be attributed to the higher level of filler content in UF2.

Furthermore, raising the aging temperature significantly increases the degree of cross-linking and leads to the formation of immiscible polymers in the boundary region. This creates a conflict between stiffness and brittleness. The increased cross-linking reduces the mobility of polymer chains, resulting in a rigid polymer structure that enhances material stiffness but decreases fracture toughness.

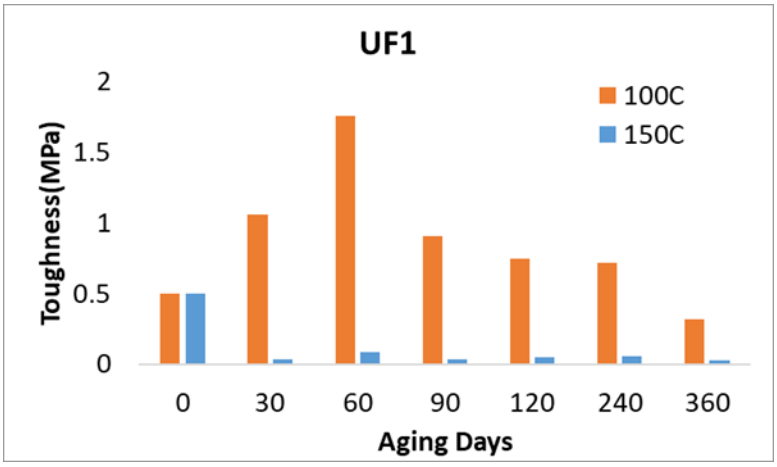

Figure 4-25 UF1 Toughness

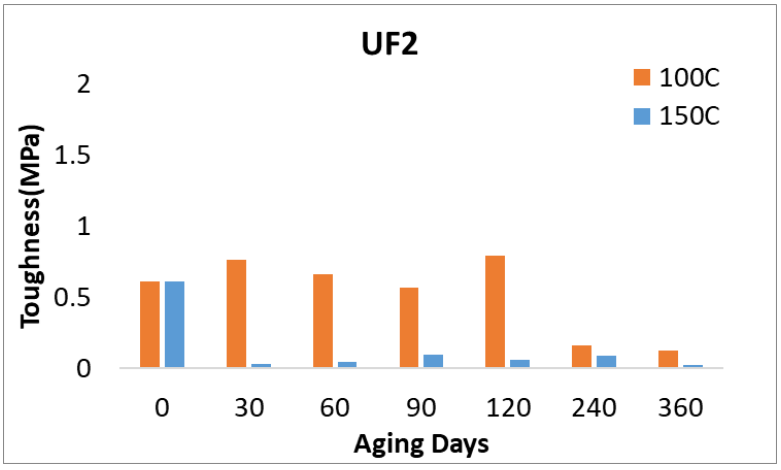

Figure 4-26 UF2 Toughness

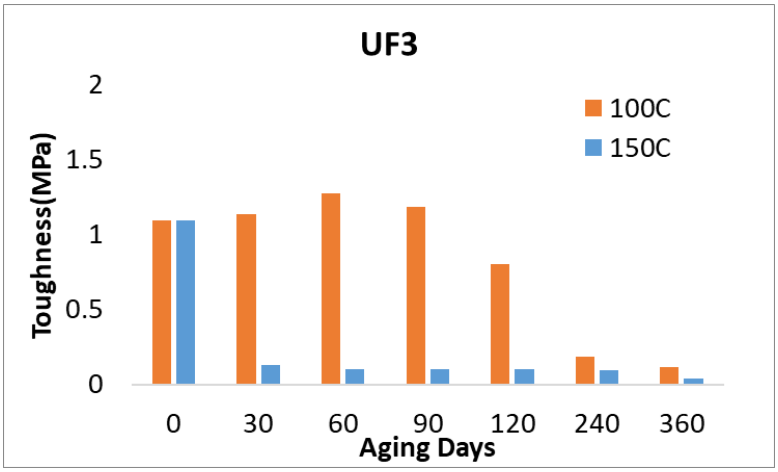

Figure 4-27 UF3 Toughness

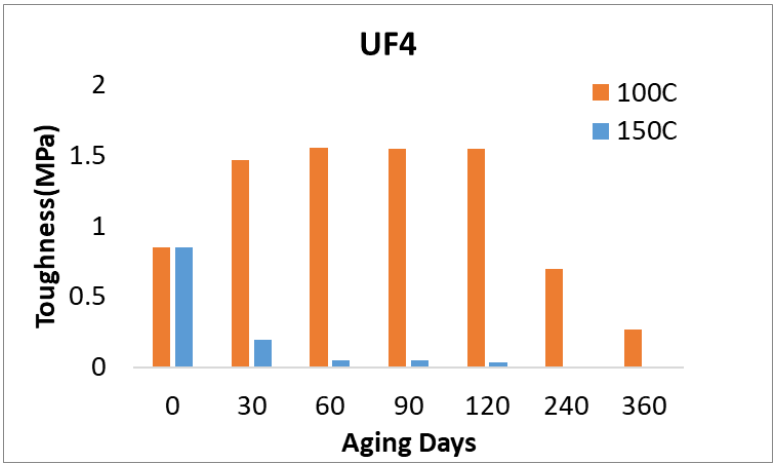

Figure 4-28 UF4 Toughness

Fig. 4-7-Fig. 4-14 illustrate the evolution of ultimate tensile strength (UTS) and percentage elongation as a function of aging time. Material degradation can be divided into two distinct steps, characterized by the linear regression slopes K1 and K2. The summarized toughness of 4 UFs are listed below:

	UF1 100C	UF1 150C	UF2 100C	UF2 150C	UF3 100C	UF3 150C	UF4 100C	UF4 150C
Toughness(MPa)	5.998998	0.78804	3.680972	0.944006	5.802117	1.672149	7.915234	1.171466

For aging at 100°C, both UTS and percentage elongation initially strengthen during the first step and then degrade during the second step. The slope (K1) during the first step is positive, indicating an increase in strength, while the slope (K2) during the second step is negative, indicating degradation.

In contrast, when subjected to 150°C aging, all four UF samples experience significant degradation during the first step and degrade at a slower rate during the second step. The slope (K1) during the first step is negative, showing a decrease in mechanical properties, while the slope (K2) is close to zero compared to slope (K1). This suggests that the material degrades rapidly initially and then exhibits a slower degradation rate.

The inflection time represents the transition point of material degradation. In the case of UTS at 100°C, the inflection time ranges from 30 days for UF2 to 90 days for UF3, indicating that UF3 degrades later compared to the other samples. At 150°C, the inflection time is 30 days for all four UF samples.

Regarding percentage elongation, at 100°C, the inflection time is 120 days for UF1, UF2, and UF4, but 90 days for UF3. At 150°C, the inflection time is 30 days for all four UF samples. It is evident that the inflection time decreases significantly with increasing aging temperature.

The toughness, as depicted in Figure 4-15-Figure 4-18, exhibits a similar trend to percentage elongation and UTS. At 100°C, the material initially strengthens during the first step and then experiences significant degradation after 120 days. The inflection time ranges from 60 to 120 days. At 150°C, the material undergoes significant degradation from the pristine state to 30 days, indicating a pronounced degradation at the beginning of the aging test. The inflection time is 30 days, highlighting the earlier onset of material degradation with increased aging time. The slope (K2) is relatively small in all cases, indicating slower degradation after the inflection time.

It is noteworthy that all materials become embrittled under 150°C environments, indicating the significant impact of aging temperature on material degradation. At 100°C, below the glass transition temperature, the underfills initially tend to strengthen and then remain stable from 30 to 120 days. However, most underfills exhibit significant degradation after 120 days. Based on the test results, UF1, UF2, and UF3 are predicted to be more reliable than UF4 for sustained high-temperature environments.

4.4*Microstructure Evolution*

The examination of microstructure provides valuable insights into the mechanical properties and thermal stability of materials. In the case of UF2 uniaxial tensile samples, a polarized optical microscope was used to analyze the cross-section area (refer to Fig. **4-19**). The micrographs revealed the presence of boundary layers under both 100°C and 150°C aging conditions.

The boundary layers indicate a higher level of cross-linkage, which has higher modulus but lower fracture toughness. As a thermoset polymer, high cross-linking level cause stiff-brittle conflict. Lower cross-linkage leads to lower modulus but increased strength. On the other hand, a rigid structure exhibits higher stiffness but greater brittleness, highlighting the inherent conflict between stiffness and brittleness.

When aged at 100°C, it was observed that the thickness of the boundary layer increased as the aging time progressed. This indicates that the boundary layer develops and grows over time during the aging process at 100°C.

In contrast, when exposed to a temperature of 150°C, the formation of the boundary layer occurred within a relatively short period of time and remained relatively stable afterward. This

suggests that the generation of the boundary layer happens rapidly during the early stages of aging at 150°C, and its thickness does not undergo significant changes thereafter.

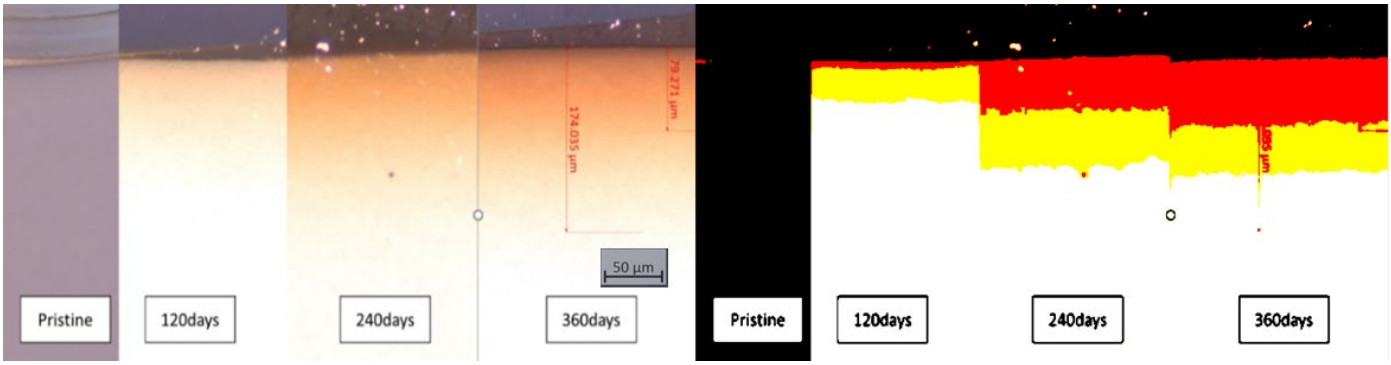

UF2 at 100°C aging condition

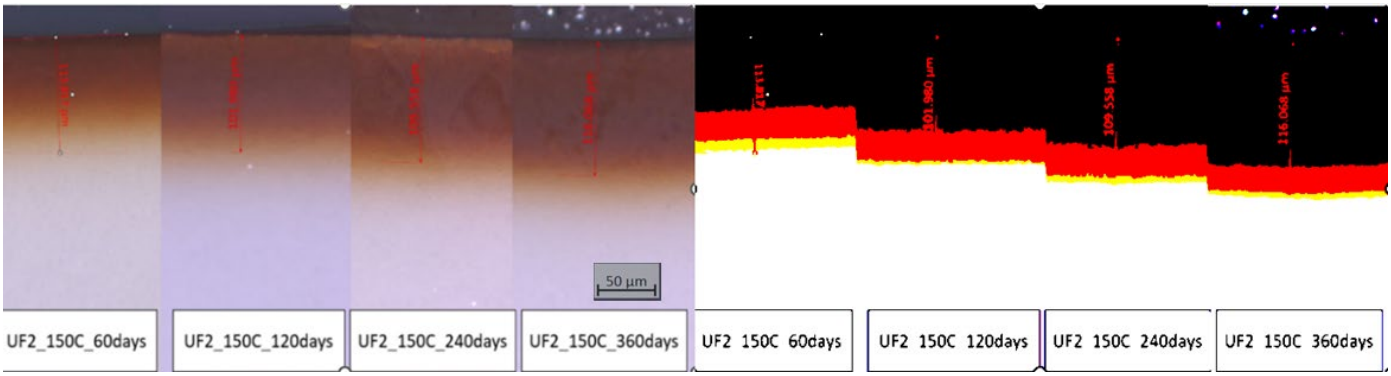

UF2 at 150°C aging condition

Fig. 4-29 Boundary Region for UF2 under Optical Microscope

The extensive cracking in the boundary layer of the underfill material results in its brittleness compared to the pristine state. Consequently, the dark and thick boundary layer is expected to exhibit low percentage elongation and ultimate tensile strength (UTS) when subjected to 150°C conditions. Microcracks are observed in UF4 at 150°C (refer to Fig. 4-20), originating from the boundary region. This provides evidence for the lower fracture toughness of the boundary materials. The cracks propagate from the boundary towards the middle area. Initially, the cracks appear straight (at 90 days), allowing for the collection of UTS and percentage elongation data. UF4 ultimately fails after 120 days, indicating that failure does not occur immediately upon crack

generation. Subsequently, the cracks become curved and bifurcated (at 240 days and 360 days), making it impossible to collect UTS and percentage elongation data. All observed cracks originate from the boundary region, and no cracks are observed in the middle area.

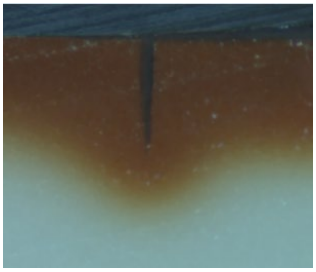

90 days

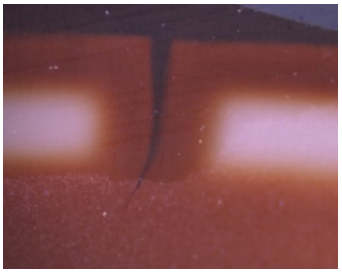

240 days

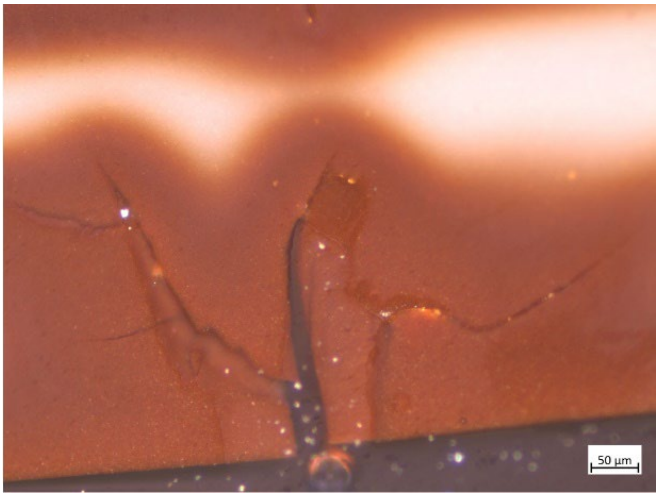

360 days

Figure. 4-30 UF4 150℃ 90days, 240days &360days

The measurement of UF2-4 oxidation layer thickness was conducted. To determine the thickness, a binary image was created through thresholding, and the results were visualized in Figure 4-21-Figure 4-23. In the plot, the blue dots represent the thickness for samples subjected to 150°C aging, while the orange dots represent the thickness for samples exposed to a 100°C environment.

Observing the plot, it can be observed that the oxidation layer exhibits slow growth initially during the 100°C aging process. However, for samples exposed to 150°C, the oxidation layer experiences significant growth right from the beginning. This stark contrast suggests that the degradation primarily occurs in the early stages for the 150°C environment.

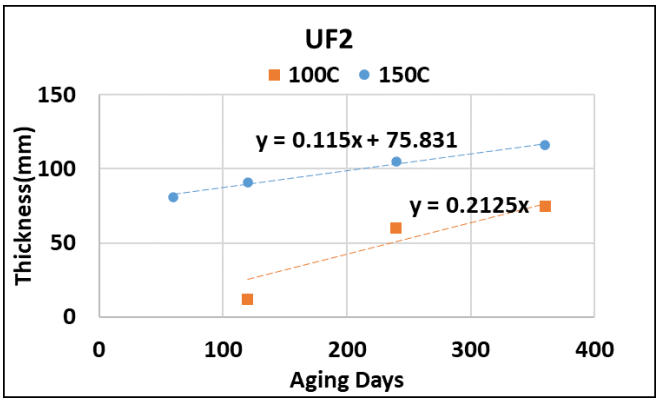

Figure 4-31 Oxidation thickness for UF2

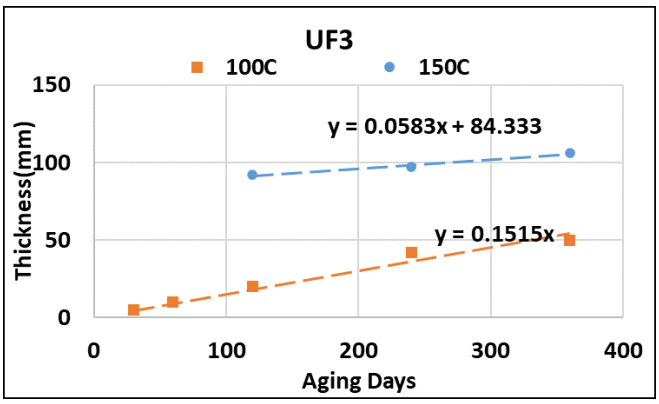

Figure 4-32 Oxidation thickness for UF3

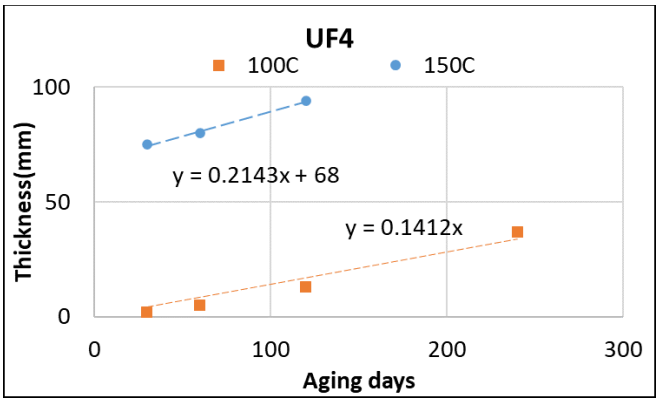

Figure 4-33 Oxidation thickness for UF4

4.5 *Nanoindentation Test*

Nanoindentation tests are conducted on the cross-sectional area of UF3 samples to investigate the effect of the oxidation layer on mechanical properties. Indentations were placed from the edge toward the center of the UF3 cross-section, with a spacing of 20 μm between each indent Figure 4-34.

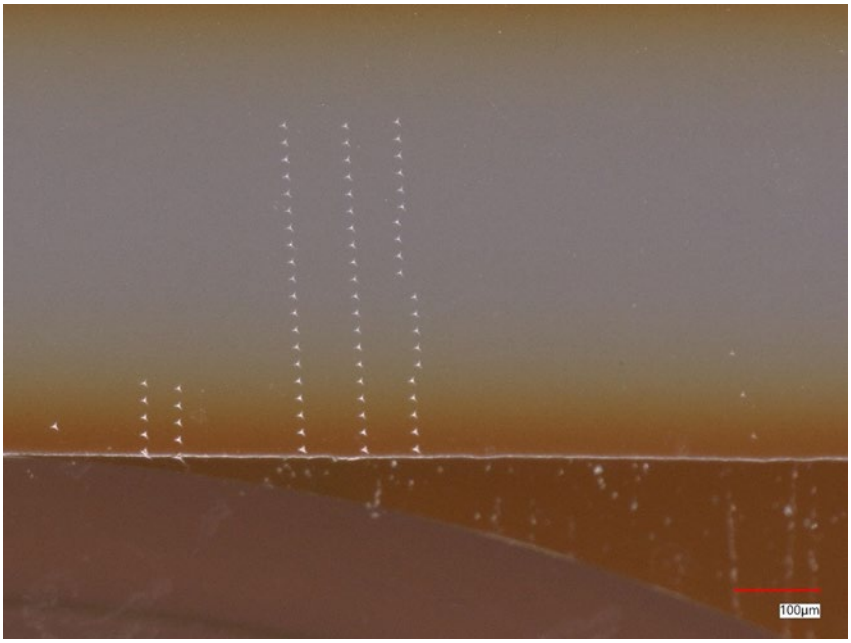

Figure 4-34 Nanoindentation for UF3 100C 360days

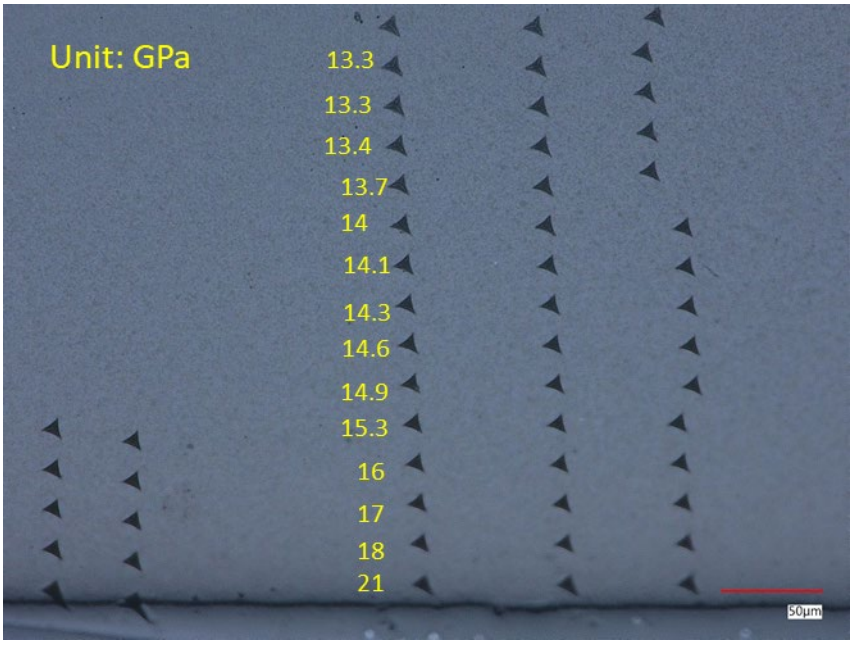

Figure 4-35 The average elastic modulus from edge to the center of UF3 100C 360days

Nanoindentation tests were performed from the center to the boundary of UF3 samples aged for 360 days at 100 °C, along with the corresponding elastic modulus distribution (Figure 4-35). The results show that the average elastic modulus increases by 56% from the center to the edge. The average modulus at each position was calculated as the mean of three measurements taken at the same distance from center to edge.

Nanoindentation tests were performed from the center to the boundary of UF3 samples aged for 360 days at 150 °C, with a 20 μm spacing between each indent (Figure 4-36), starting from the center and progressing toward the boundary.

The results show that the average elastic modulus in the boundary layer—approximately the first 100 μm from the edge (first four indents)—remains relatively consistent (from 21GPa to 18GPa). Beyond this region, a modulus gradient is observed, with the values gradually decreasing until they reach a level comparable to that of the 100 °C-aged sample. This suggests that aging at higher temperatures increases the thickness of the oxidized boundary layer.

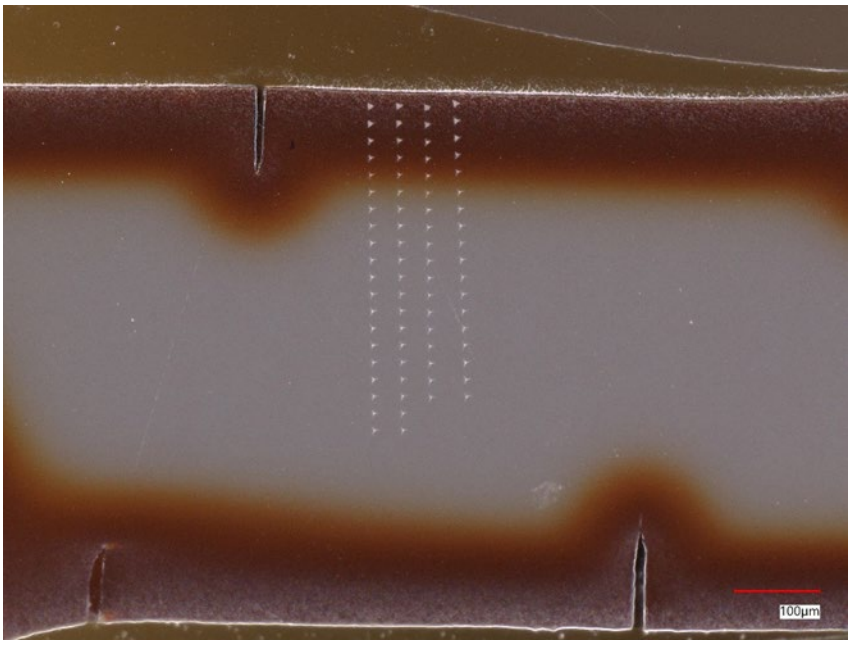

Figure 4-36 Nanoindentation for UF3 150C 360days

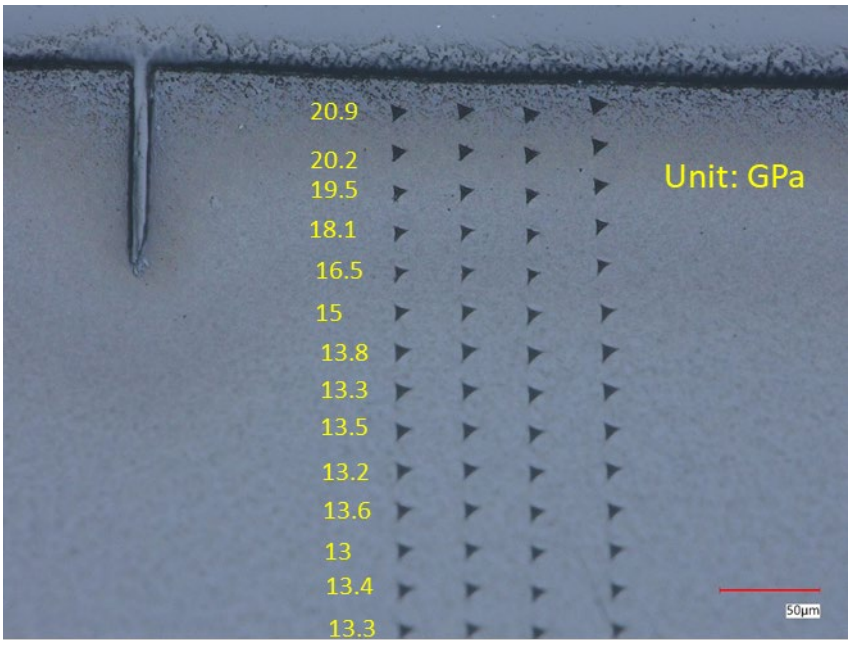

Figure 4-37 The average elastic modulus from edge to the center of UF3 100C 360days

Interestingly, the modulus at the very edge (in contact with air) and the modulus at the center (far from the oxidation front) are nearly identical. This implies that the oxidation boundary, rather than uniform degradation, is the primary indicator of aging effects on mechanical properties.

The average modulus at each position was calculated as the mean of three measurements taken at the same distance from the center.

Th elastic modulus distribution from the edge to the center are compared in Figure 4-39. At distances close to the edge (0–100 μm), both temperature conditions show relatively high elastic modulus values (around 20–22 GPa). As distance increases, the modulus drops sharply up to about 100 μm. Beyond approximately 150–200 μm, the elastic modulus values for both temperatures stabilize and plateau around 13–14 GPa. The 150°C condition consistently shows higher modulus values than the 100°C condition near the edge.

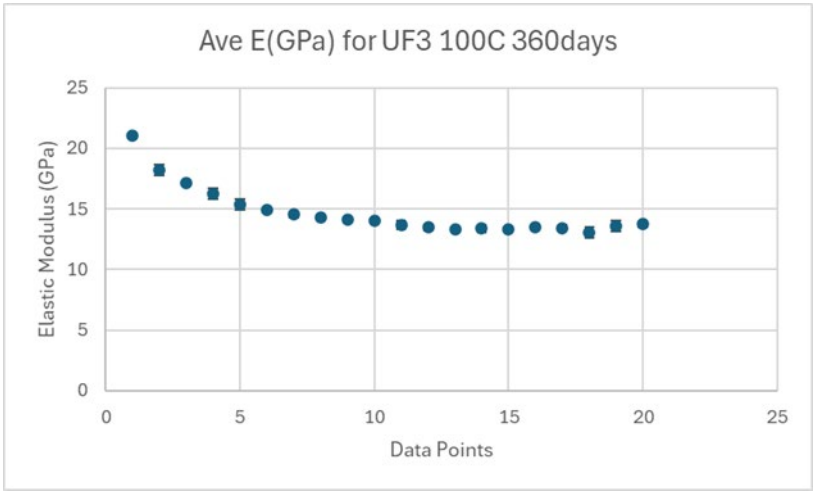

Figure 4-38 Average modulus for UF3 100C 360days

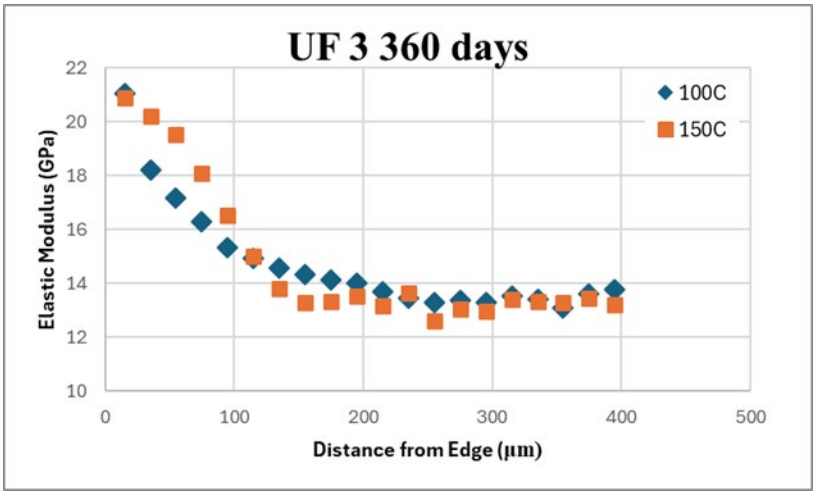

Figure 4-39 Elastic modulus distribution as the function from the edge

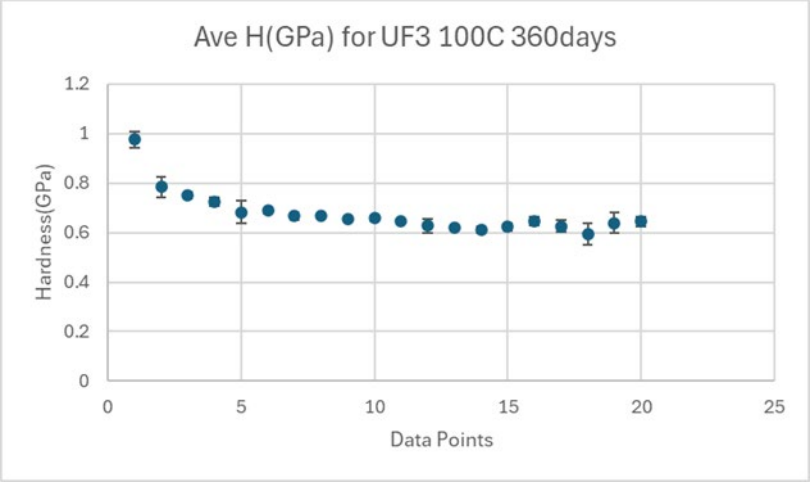

Figure 4-40 Average Hardness for UF3 100C 360days

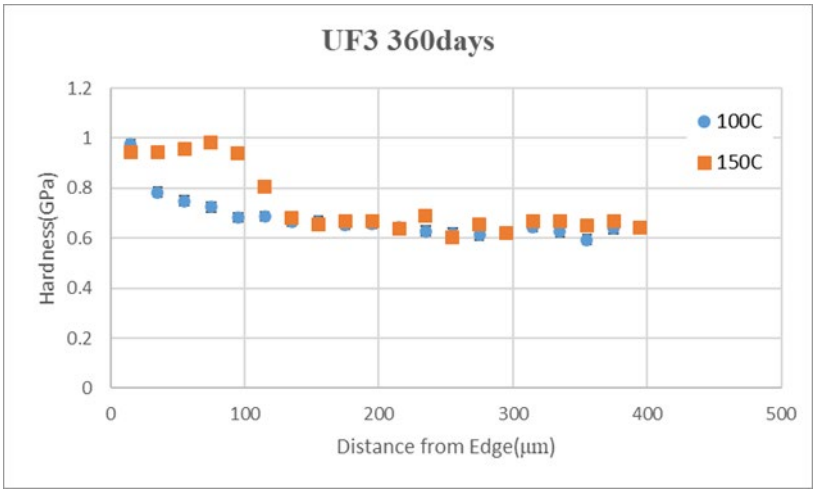

Figure 4-41 Hardness distribution as the function from the edge

The average hardness at each position was calculated as the mean of three measurements taken at the same distance from the center (Figure 4-40). It shows the very consistent values with small variance, indicating that the material property is only affected by the distance from the edge.

Initial Region (0–100 μm):

- 150°C samples show higher hardness (~1.0 GPa) than 100°C samples (~0.7 GPa).
- Hardness decreases for 100C aging but keep consistency for 150C aging, which could be explained by the boundary effect.

Beyond 100 μm:

- Hardness values stabilize for both temperatures, maintaining a nearly constant value around 0.6–0.65 GPa.

The higher hardness near the edge suggests possible thermal or oxidative effects at the surface due to prolonged aging. The 150°C condition causes more pronounced surface hardening, but this effect diminishes with depth. At deeper regions (beyond 200 μm), the material appears to be less affected by thermal aging, as indicated by the plateaued hardness values.

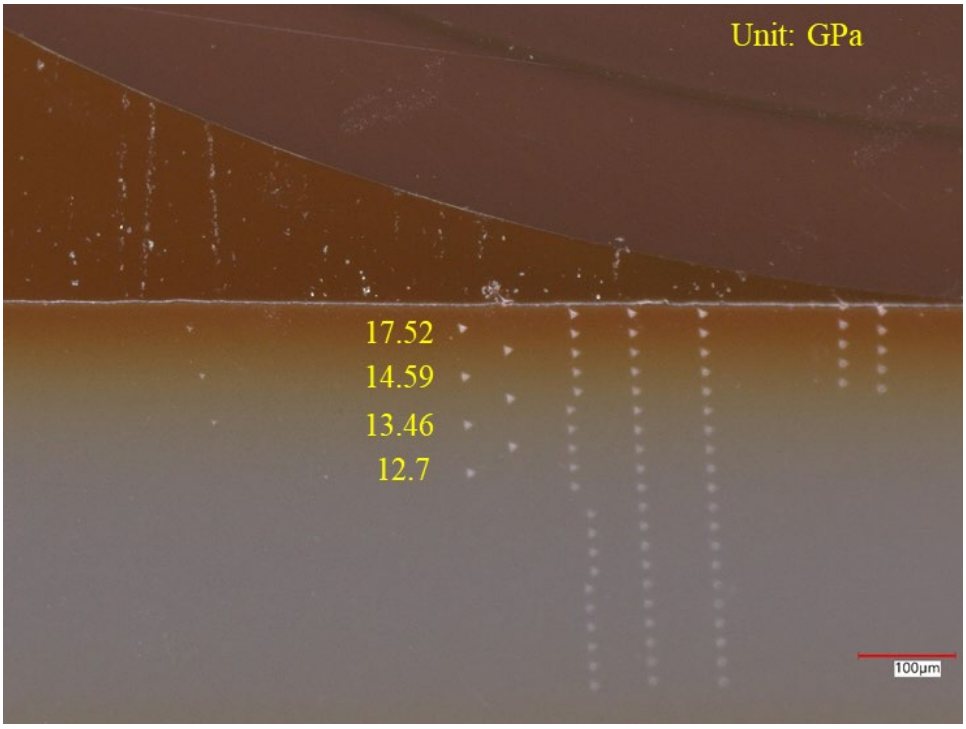

Figure 4-42 The elastic modulus for UF3 100C 360days with a 50μm spacing between indents

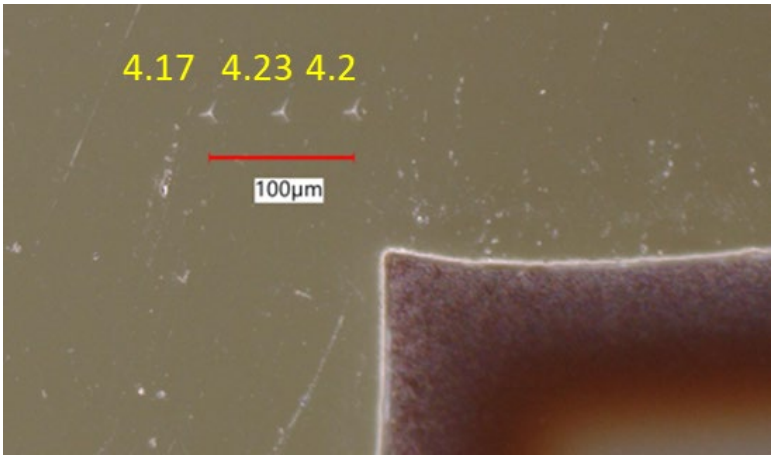

Figure 4-43 The elastic modulus for surrounding epoxy with a 50μm spacing between indents

Table 4-2 Mean and Standard deviation of modulus

Mean Reduced Modulus (GPa)	Std. Dev. of Reduced Modulus (GPa)
4.202	0.031

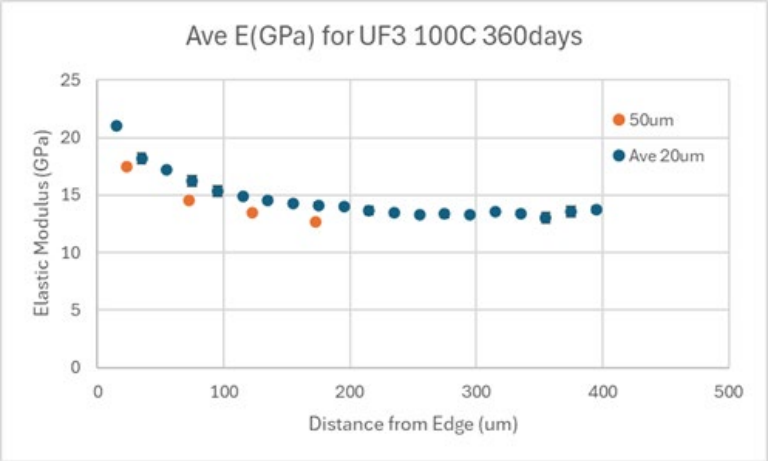

Figure 4-44 Elastic modulus for spacing 50μm and 20μm indents

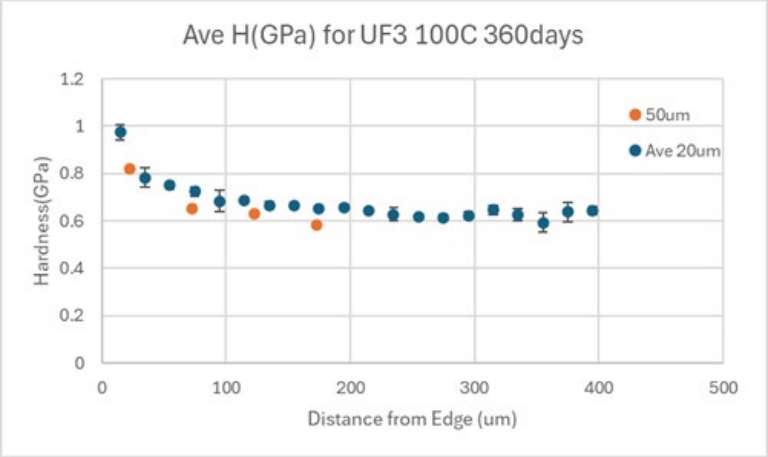

Figure 4-45 Hardness for spacing 50μm and 20μm indents

The neighboring effect is also discussed. The modulus of surrounding epoxy is measured. It is much smaller than the modulus of UF. It is only about 4.2GPa with a variance of 0.031(Table 4-2). The modulus and hardness for both 50μm and 20μm spacing are compared in Figure 4-44 and Figure 4-45 data point at 50 μm below—it shows less than 5% lower compared to the data at 20 μm distance, with the same decreasing trend.

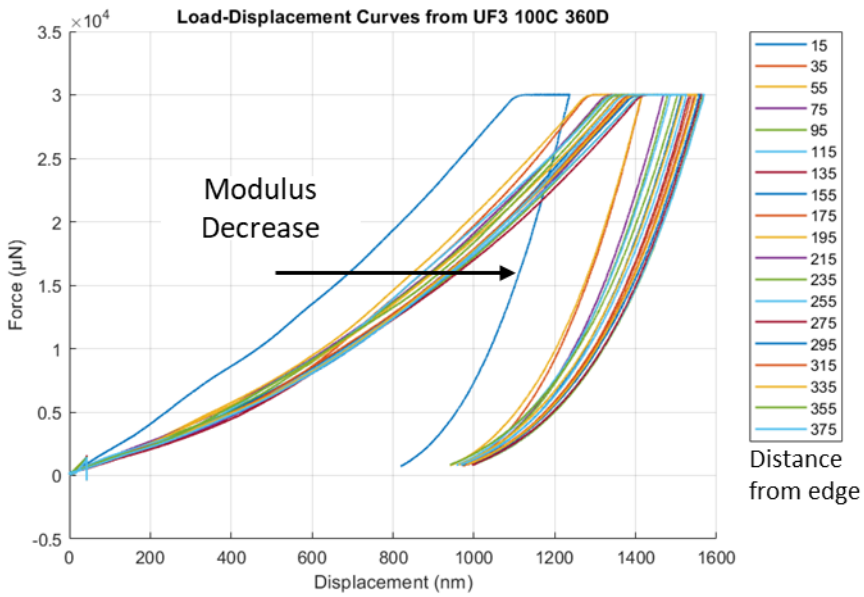

Figure 4-46 Load-displacement Curves from UF3 100C 360 days

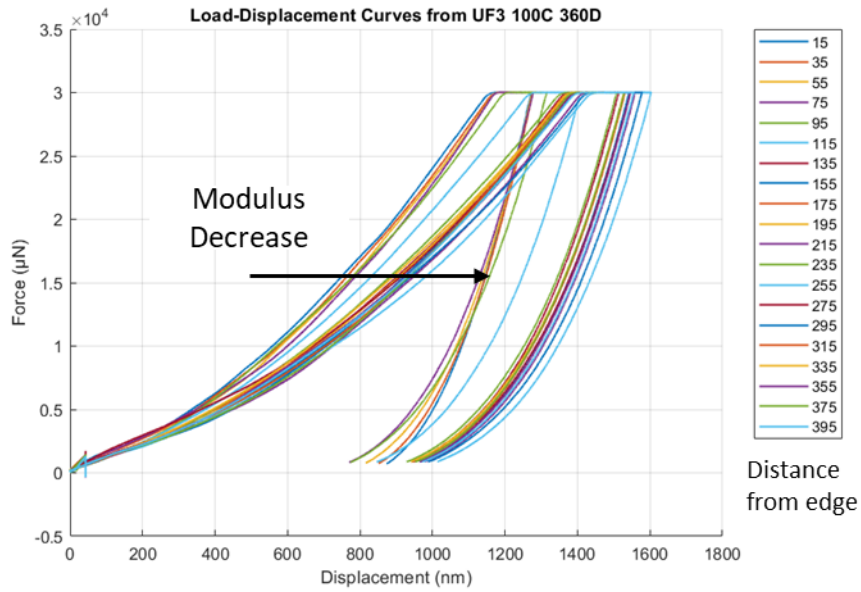

Figure 4-47 Load-displacement Curves from UF3 100C 360 days

It was observed that the maximum displacement during nanoindentation gradually increases from the boundary to the center for both 100 °C and 150 °C aging conditions. The rightward shift of the load–displacement curves indicates a softening of the material toward the center. Additionally, a decrease in the unloading slope is evident in both cases, further suggesting a reduction in mechanical properties from boundary to center. These findings highlight the

cumulative effects of thermal aging on the material's structural integrity. This degradation is quantitatively reflected in the reduced unloading stiffness and increased indentation depth, as revealed by the nanoindentation results.

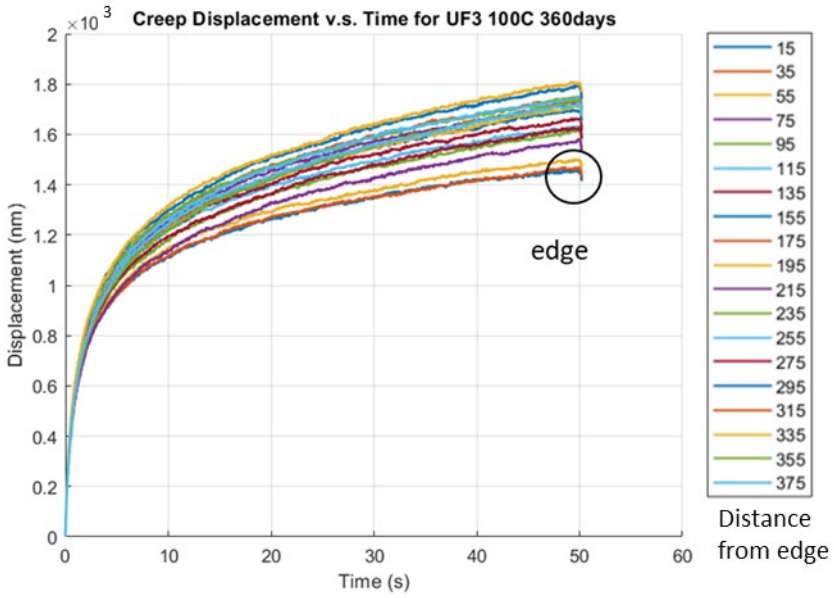

Figure 4-48 Creeping displacement v.s. Time for UF3 100C 360days

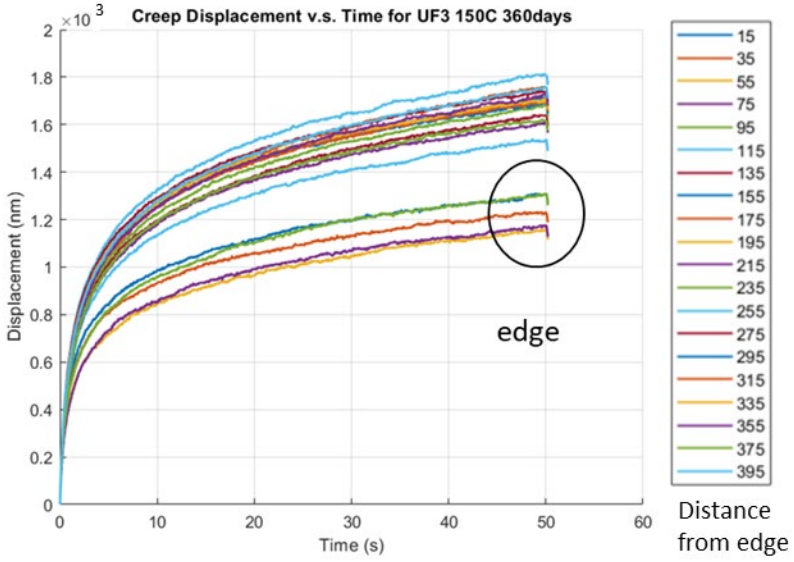

Figure 4-49 Creeping displacement v.s. Time for UF3 150C 360days

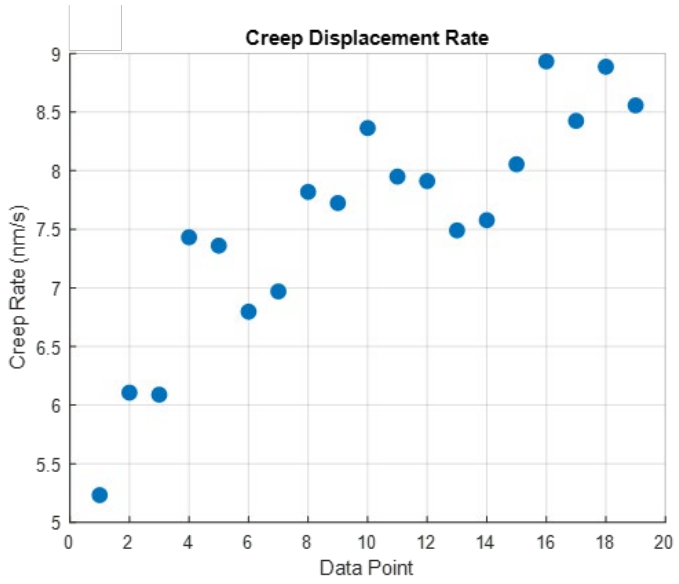

Figure 4-50 Creep Displacement rate for UF3 100C 360days

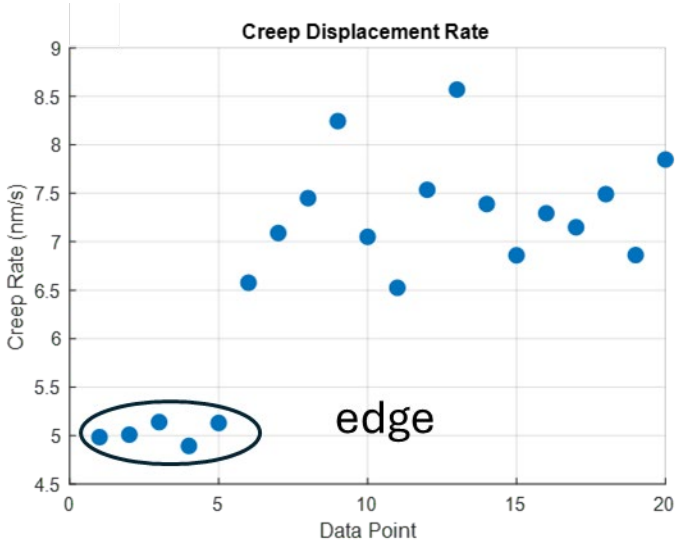

Figure 4-51 Creep Displacement rate for UF3 100C 360days

Creep performance was evaluated from the load-hold (stable) region as shown in Figure 4-48 and Figure 4-49. The results indicate that the boundary layer effect also has a significant impact on creep behavior. It is observed that the maximum displacement gradually increases from boundary to the center for both 100C and 150C aging conditions. The creep rate is the slope of the

secondary creep. Notably, for the 150 °C aging condition, the difference in creep rate between the boundary and the center is particularly pronounced.

4.6*Viscoelastic Property Evolution by Dynamic Mechanical Analyzer*

Glass transition temperature, often called Tg, is the temperature when considering polymers for a particular end-use. [15-16] The physical properties would be dramatically different above and below glass transition temperature. However, the glass transition temperature is not a certain temperature. It would be in a range of temperature depending on the test method. The TMA, DSC and different modes of DMA often offer different Tg. In this study, 2 different kinds of underfills are studied under two aging temperatures. The test matrix is shown in the Table 4-2.

Table 4-3 Test Matrix for Underfills

AGING DAYS	AGING TEMPERATURE	
	100℃	150℃
0	√	
30	√	√
60	√	√
90	√	√
120	√	√
240	√	√
360	√	√

The typical DMA test results for UF 1 pristine material properties are shown in the Figure 4-35 .

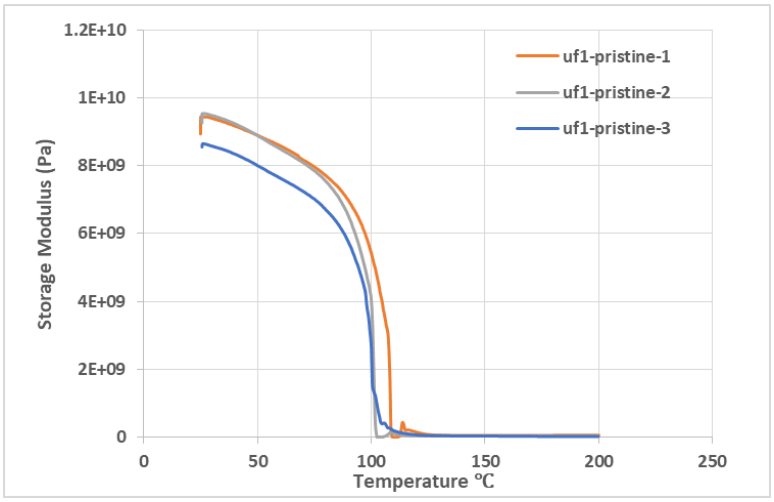

a) UF1 Storage Modulus

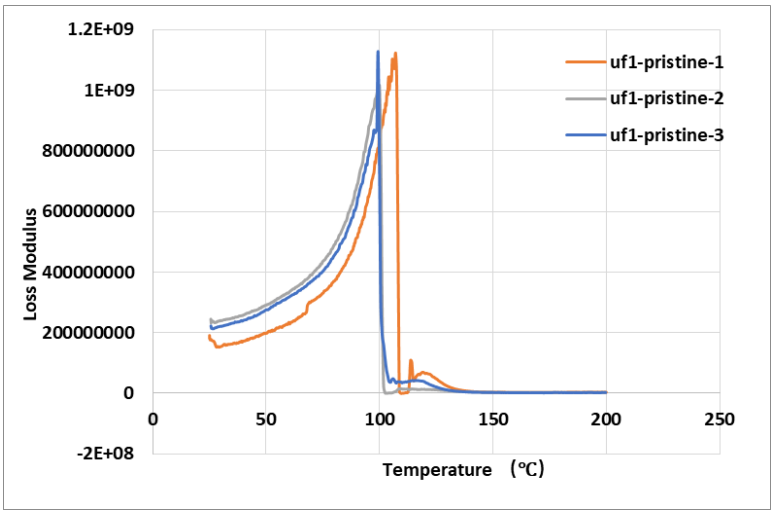

b) UF1 Loss Modulus

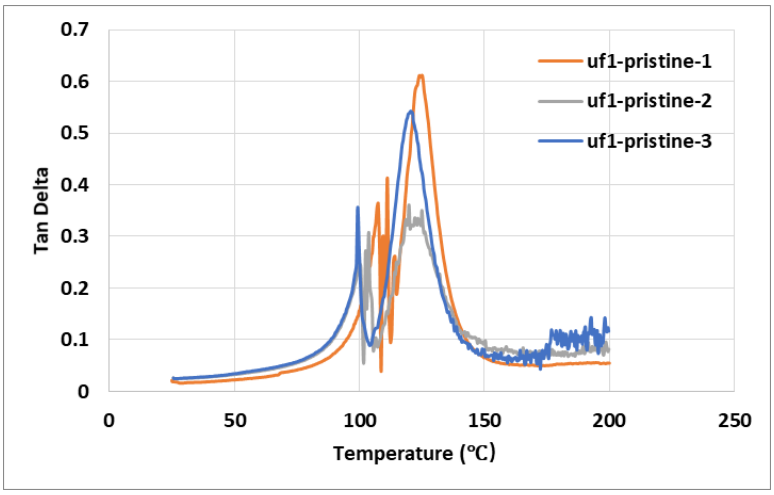

c) Tan Delta

Figure 4-52 UF1 Pristine DMA Results

The average values of curves in Figure 10 have been calculated to get the Glass transition temperature from storage modulus, loss modulus and tan delta.

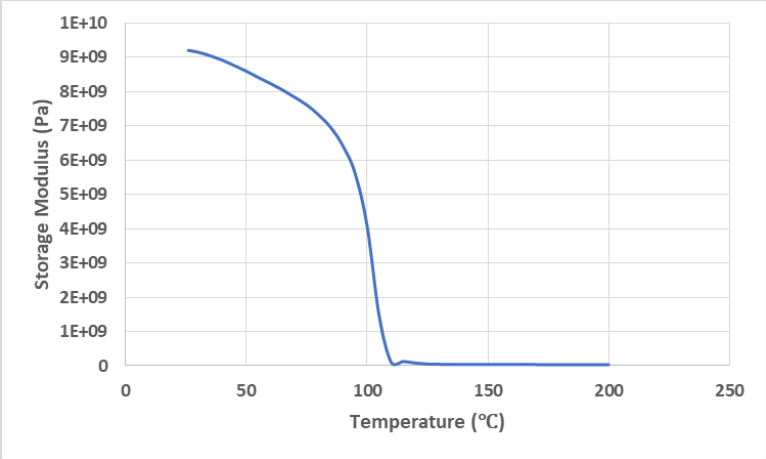

a) UF1 Storage Modulus

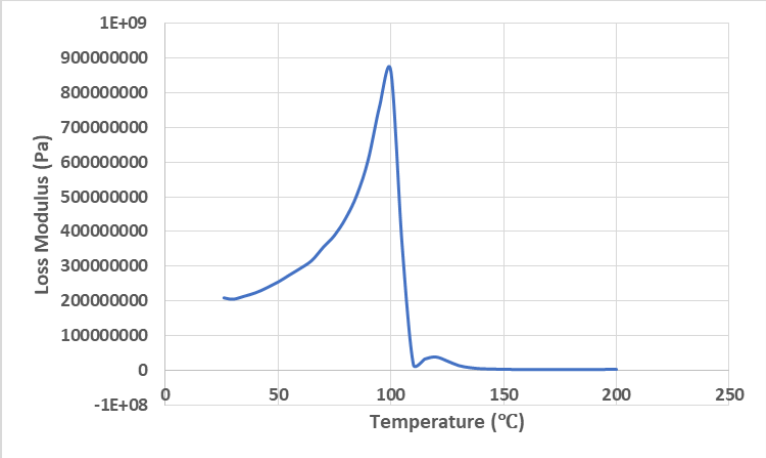

b) UF1 Loss Modulus

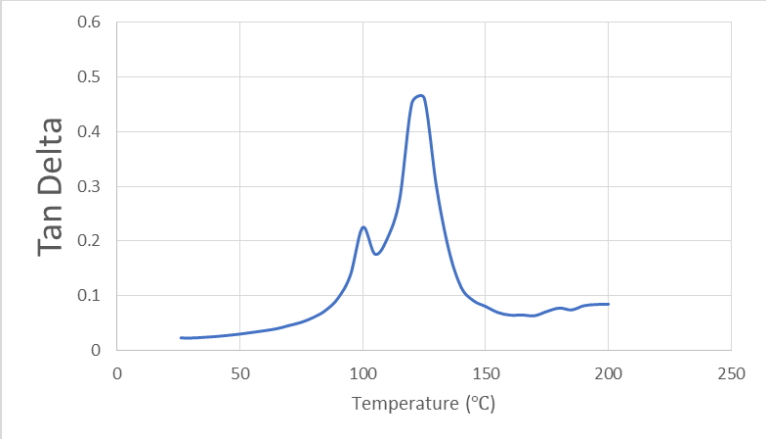

c) Tan Delta

Figure 4-53 UF1 Pristine DMA Results Average Value

Table 4-4 Glass Transition Temperature of Pristine UF 1

	Tg(°C)
Storage Modulus	94
Loss Modulus	100
Tan Delta	121

The glass transition temperatures are shown in **Error! Reference source not found.** & 7. The glass transition temperatures would be different depending on different calculation methods. Following the same procedures, the DMA results of UF1 and UF2 are shown in the **Error! Reference source not found.** and **Error! Reference source not found.**.

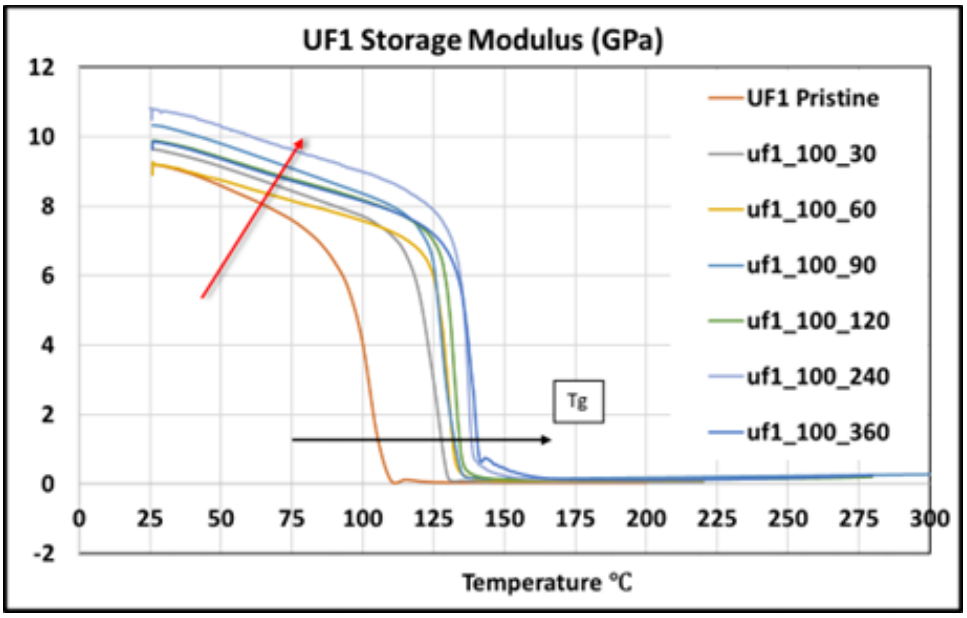

a) UF1 100 ℃ aging

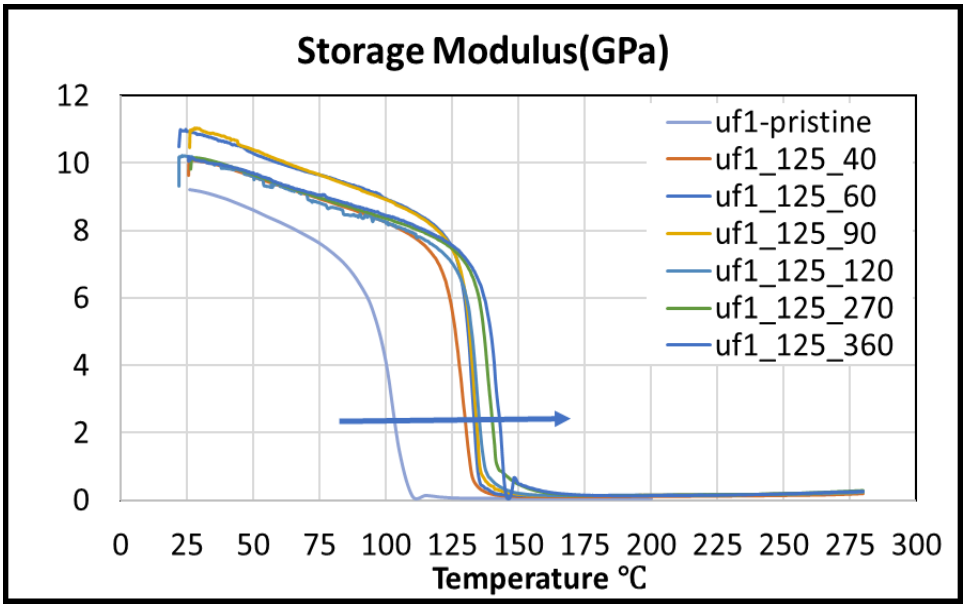

b) UF1 125℃ aging

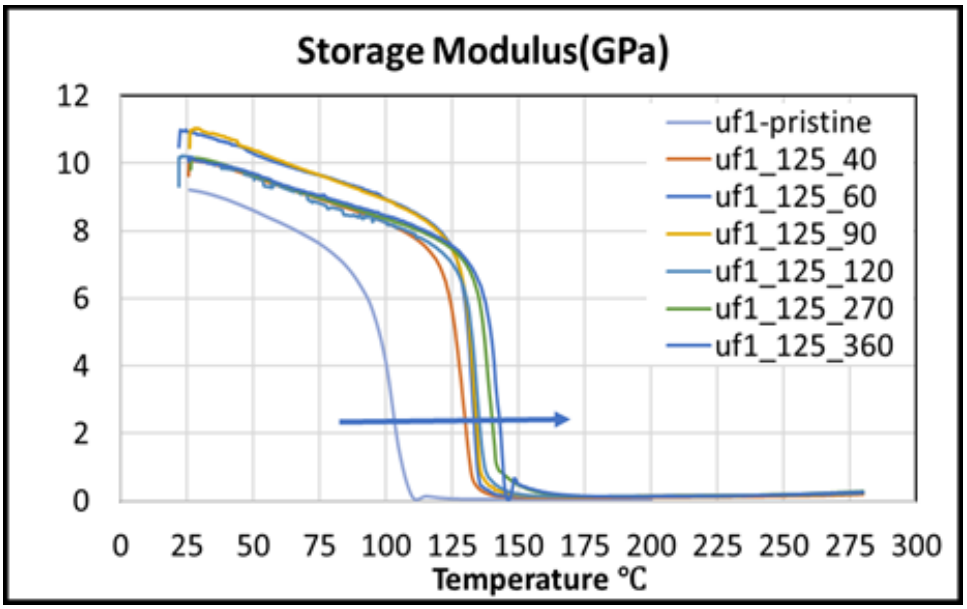

c) UF1 150 ℃ aging

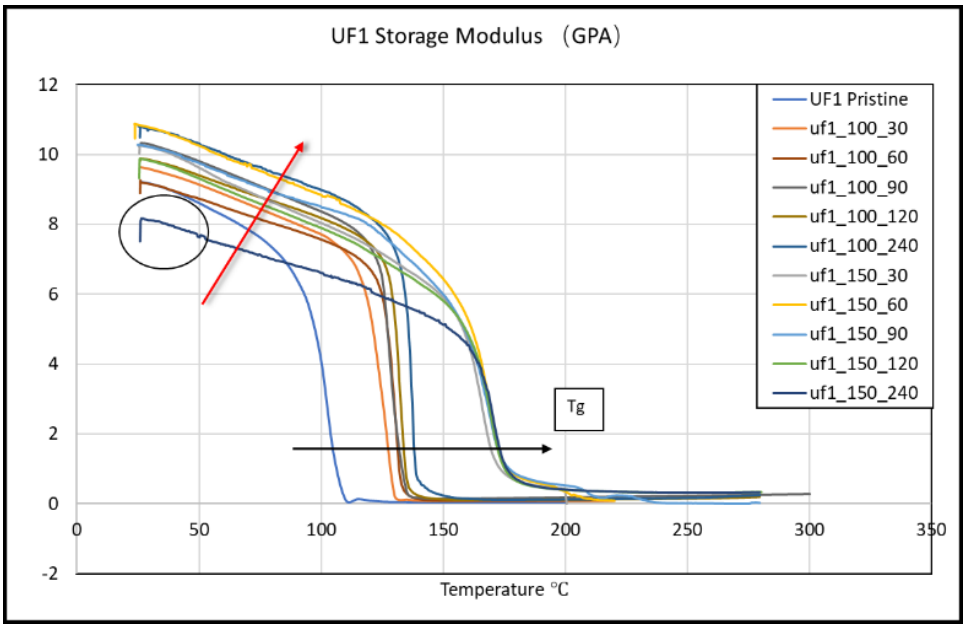

d) UF1 under different conditions

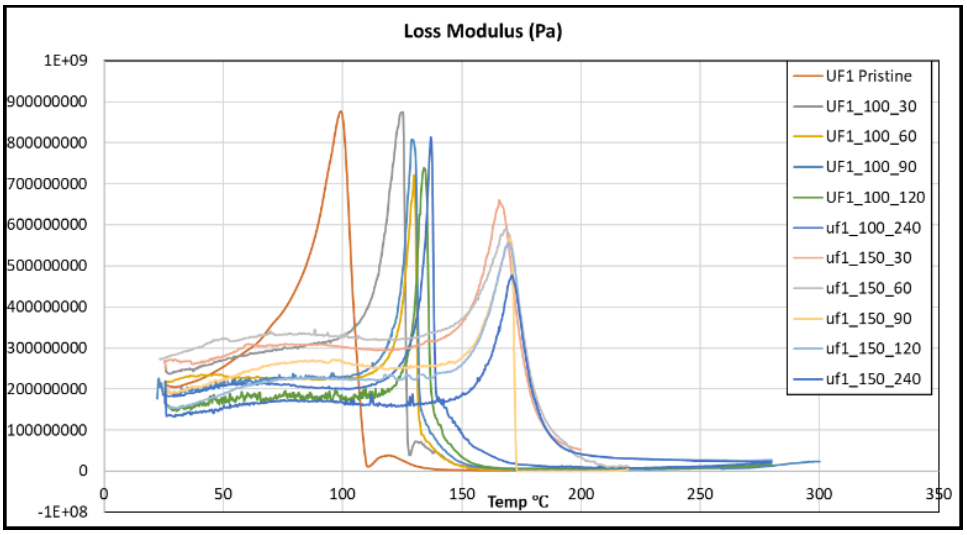

e) UF1 Loss Modulus under Different Aging Condition

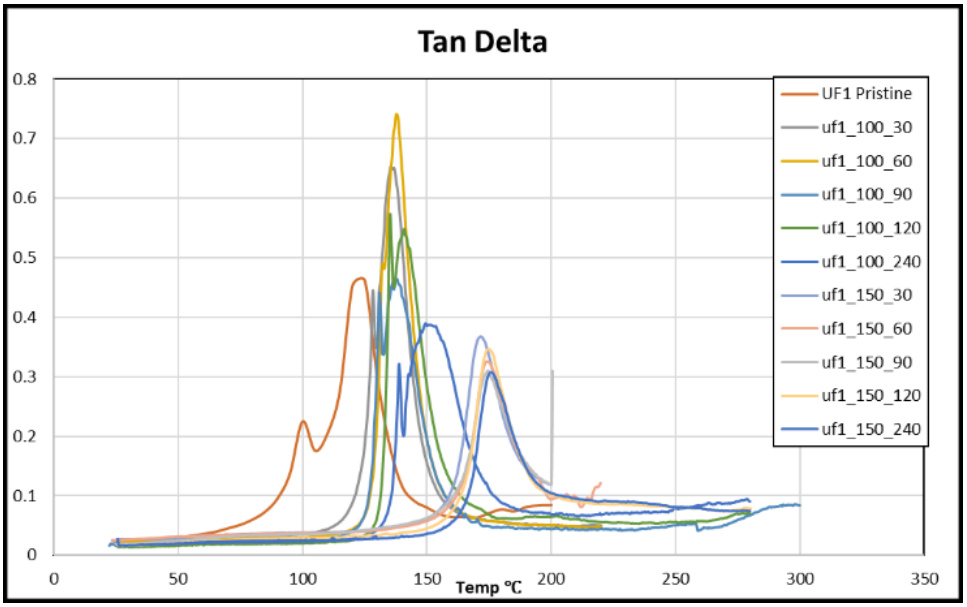

f) UF1 Tan δ under Different Aging Conditions

Figure 4-54 Comparison of UF1 DMA Results under Different Aging Conditions

The storage modulus increases as the aging time increases. The glass transition temperature continuously increases under 100℃ as the aging time increases. The glass transition temperature does not increase significantly under 150℃. As the aging time and aging temperature increases, the storage modulus curves are flatter, which indicate the increase of cross linkage level.

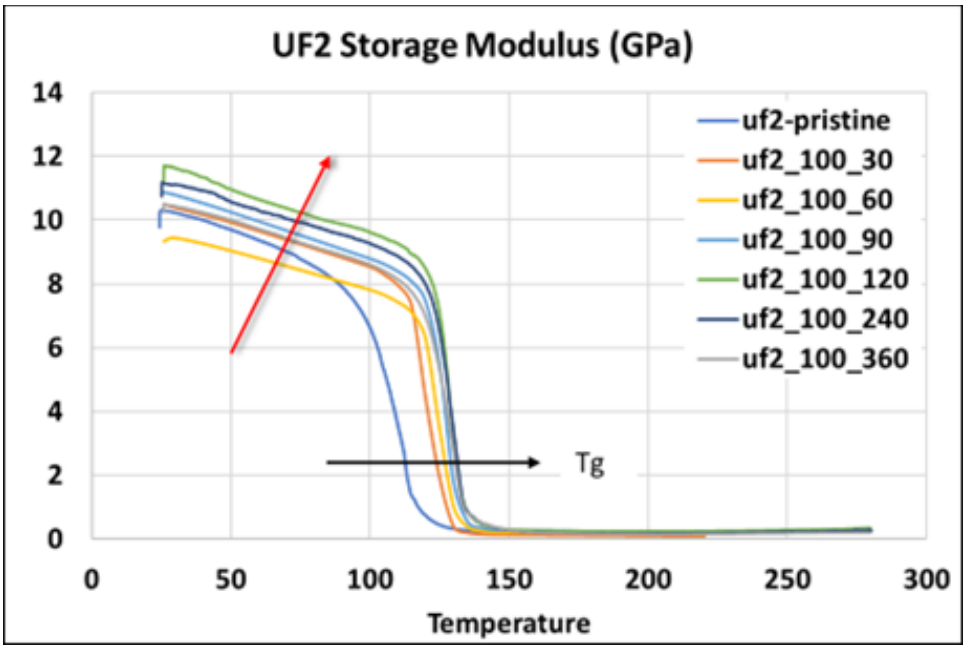

a) UF2 100 ℃ aging

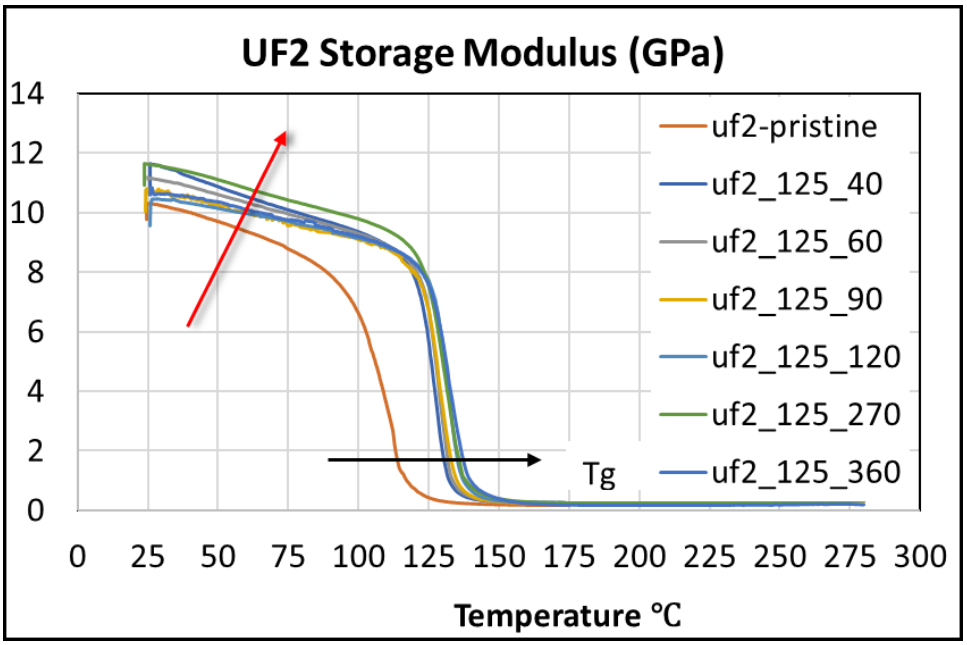

b) UF2 125℃ aging

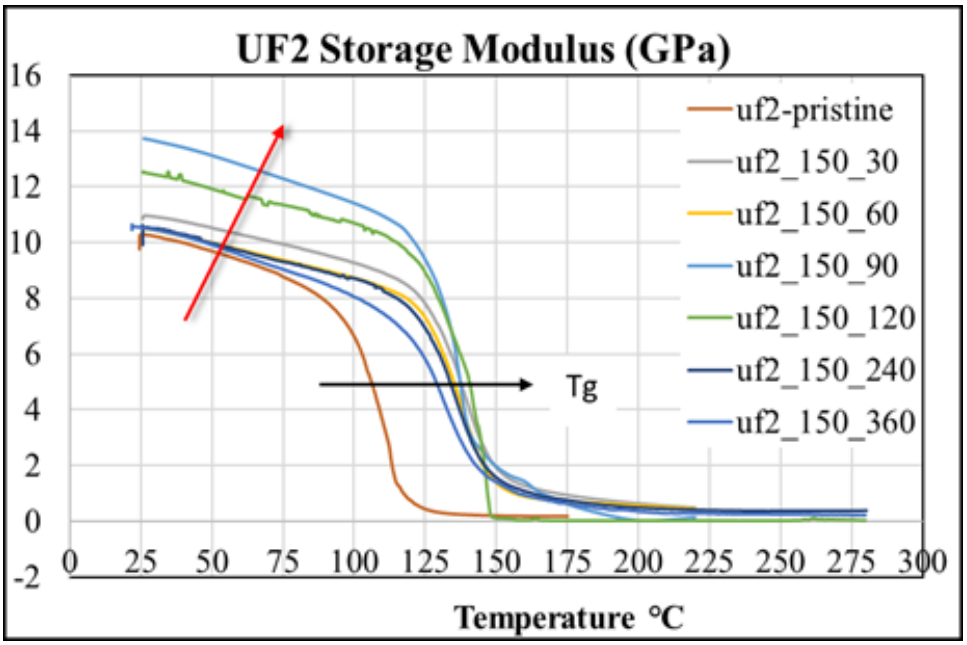

c) UF2 150 ℃ aging

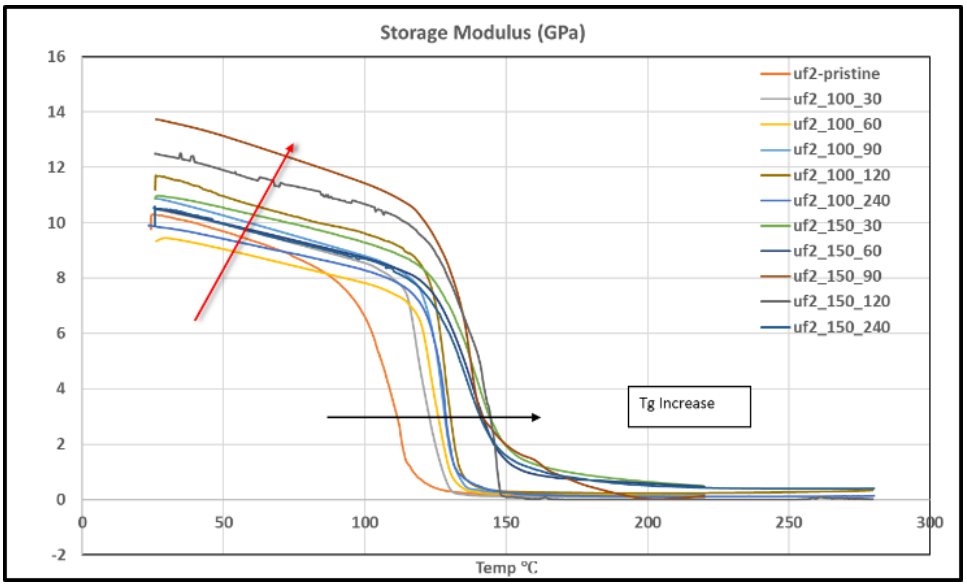

d) UF2 under Different Conditions

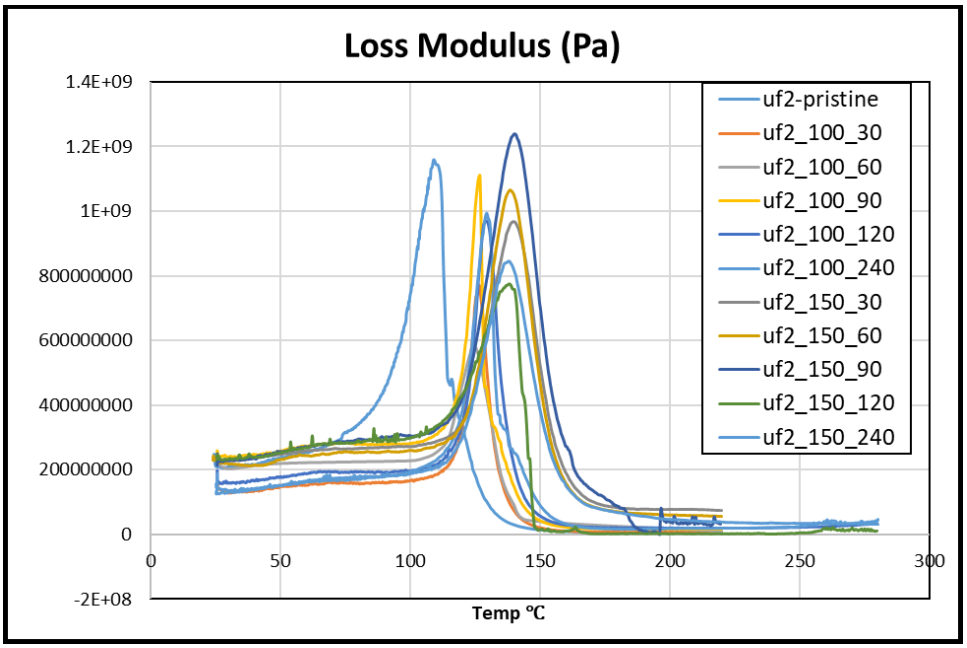

（d）UF2 Loss Modulus under Different Aging Condition

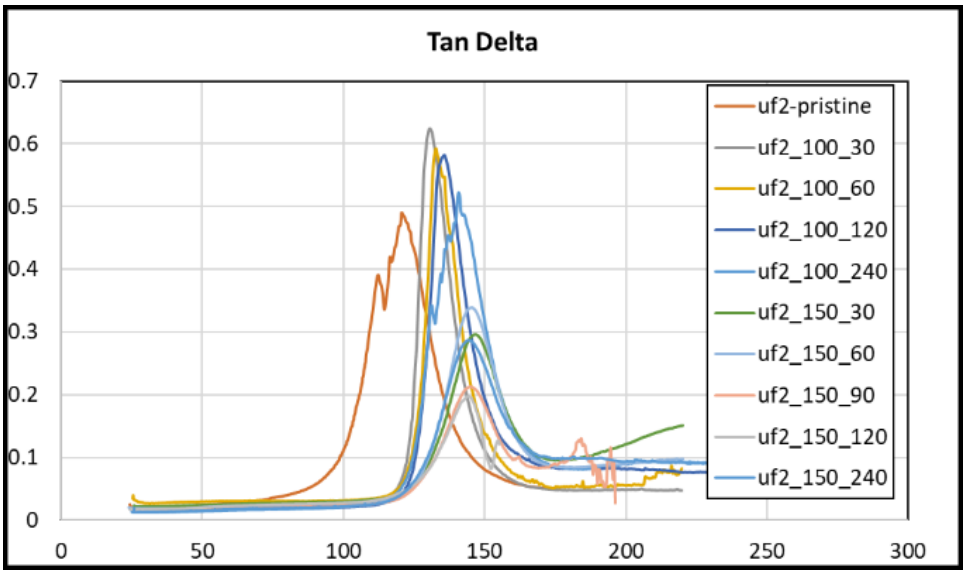

(e) UF2 Tan δ under Different Aging Conditions

Figure 4-55 Comparison of UF1 DMA Results under Different Aging Conditions

Error! Reference source not found. lists the UF 1 under different aging conditions. The sample name uf1_100_30 means UF1 in 100 ℃ for 30 days. The sample name uf2_150_60 means UF2 in 150 ℃ for 60 days. From **Error! Reference source not found.** (a) and (b), it shows that

the storage modulus increases as the aging time increase. For 100 ℃ aging, the storage modulus keeps increasing to 240 days. For 150 ℃, the storage modulus increases to 60 days and then decrease to 240 days. At 240 days, the storage modulus is lower than the pristine value. From the figure 10(c), it shows that the glass transition region continuously increases at 100℃ as the aging time increases. However, for 150℃ aging, the Tg reach the highest point as the aging started. (d) shows the loss modulus changing as the function of time and aging temperature. The peak of loss modulus represents the glass transition temperature. As the aging temperature increases, the peak of loss modulus decreases. (e) shows the tanδ of UF1. The peak of tanδ represents the glass transition temperature. The height of tanδ indicates the polymer structure. For 100℃ aging, the glass transition temperature continuously increases. The peak of tanδ increases from pristine to 60 days and then decreases. For 150 ℃ aging, the glass transition temperature does not increase a lot. The peak of tanδ decreases as the aging time increase. UF 2 shows the similar trend as UF1 in **Error! Reference source not found.**. At 100℃ aging, the storage modulus is higher than the pristine condition. The glass transition region continuously right-shift as well. (b) shows that the storage modulus is higher than pristine condition at 150℃ aging. The storage modulus increases from pristine to 90 days and then decreases to 240 days. (c) shows that the glass transition region continuously right-shift as the aging temperature increases. The storage modulus increases as the aging temperature increases. The peak of storage modulus occurs at 150℃ 90 days aging. (d) shows the loss modulus change as the function of aging time. The peak of the loss modulus indicates the glass transition temperature. (e) shows the tanδ changing as the function of aging time and temperature. At 100℃, the height of tanδ increases from pristine to 30 days and then decrease from 30 days to 240 days, but still higher than pristine condition. At 150℃, the height of tanδ is lower than pristine condition, showing the decreasing trend.

The other significant observation is the increase of cross-linkage level. We could identify the cross-linkage by the shape of storage modulus. The lower level of cross linkage, the steeper storage modulus change in glass transition region. The higher level of cross linkage, the flatter storage modulus change in temperature ramp test.

Table 4-5 Glass Transition Temperature of UF 1

	Tan Delta	Loss Modulus	Storage Modulus
uf1	121	100	94
uf1_100_30	134	124	119
uf1_100_60	137	130	125.5
uf1_100_90	137.5	130	126
uf1_100_120	141	132	126
uf1_100_240	149	137	134
uf1_150_30	172	166	155
uf1_150_60	174	166	162
uf1_150_90	175	166	157
uf1_150_120	175	169	157
uf1_150_240	176	171	163

Table 4-6 Glass Transition Temperature of UF 2

	Tan Delta	Loss Modulus	Storage Modulus
uf2	121	109	101
uf2_100_30	133	121	119

uf2_100_60	134.3	126	121
uf2_100_90	135	127	123
uf2_100_120	137	125	123
uf2_100_240	141	129	123
uf2_150_30	146	140	127
uf2_150_60	146	139	127
uf2_150_90	145	138	127
uf2_150_120	143	139	127
uf2_150_240	144	138	123

For UF1, the Tg based on Tanδ increases from 121℃ to 134℃ under 100℃ aging for 30 days. When the aging days of 100℃ increases from 30 to 240 days, the Tg increases from 134℃ to 149℃. As the UF1 samples under 150℃, the Tg increases from 121℃ to 172℃ for 30 days aging, and then it increases from 172℃ to 176℃ when the aging days increases from 30 days to 240 days. Basing on the Tg from Tanδ, it increases from 121℃ to 133℃ when the UF2 samples are under 100℃ aging for 30 days. It increases from 133℃ to 141℃ when the samples are under 100℃ from 30days to 240 days. When the UF2 samples are under 150℃ aging, the Tg increases from 121℃ to 146℃ for 30days aging. The Tg even slightly decreases from 146℃ to 144℃ as the aging days are from 30 to 240 days.

As the result, we find that under 100℃ aging, UF1 and UF2 show the similar behavior of Tg, which increases from 121℃ to 134℃. After that, the Tg still keep increasing when the aging days are from 30 to 240 days. The higher the glass transition temperature indicates the higher cross-linking level. However, under 150℃ aging, the Tg of UF1 increases significantly from 121℃ to 172℃, when the Tg of UF2 increases from 121℃ to 146℃. After that, the Tg of UF1

still increases from 172℃ to 175℃ when the Tg of UF2 decreases slightly from 146℃ to 143℃. Figure 13 shows the glass transition temperature from tanδ evolves under different aging conditions.

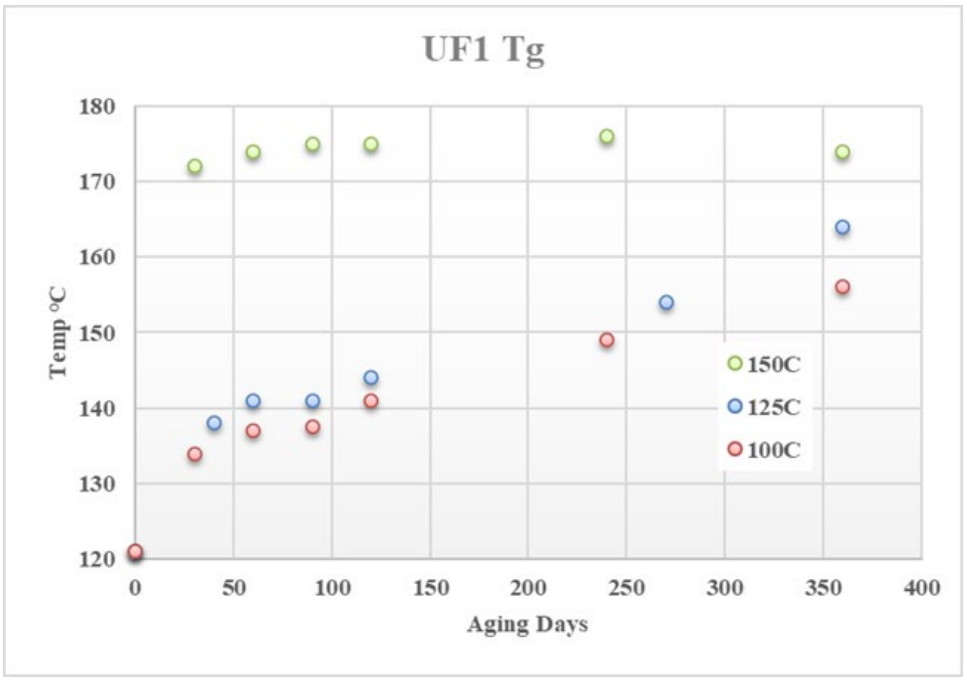

a) Tg for UF1

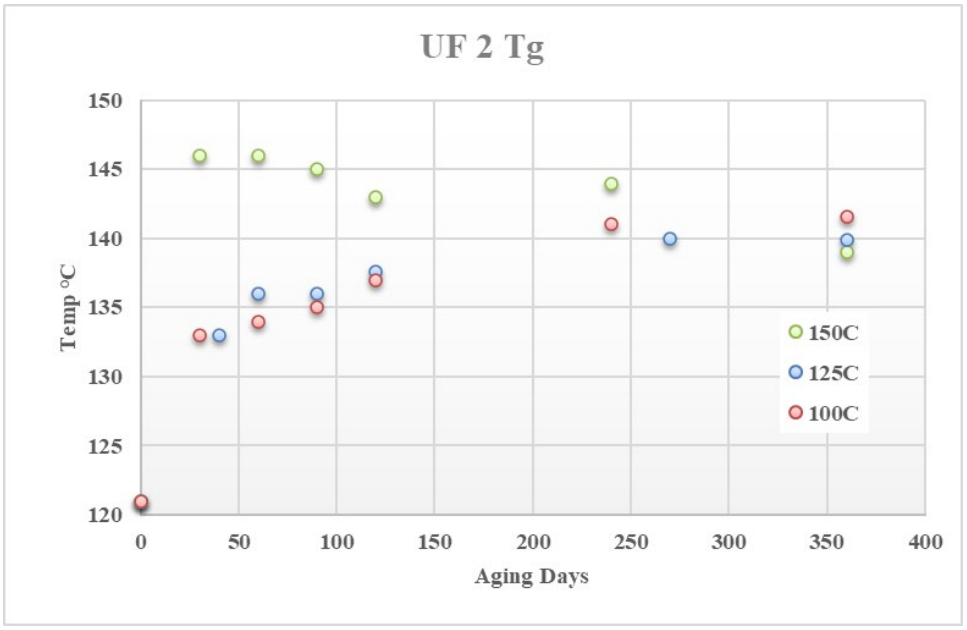

b) Tg for UF2

Figure 4-56 Tg for UF1 and UF2 under 100℃ and 150℃ aging from pristine to 240 days.

4.7*Normalized Prony Series Generation*

Frequency sweep test is conducted to UF1&2. Study of the linear viscoelastic behavior of UF is achieved by performing TTS (time- temperature superposition) to generate the master curves. Time-temperature superposition is based on TRS assumption, assuming that master curve could be formed by single shift factor. Data collected at various temperatures are horizontally shifted with respect to time until the curves merge into one smooth function. The shift factor ($\boldsymbol{a_T}$) is fitted by WLF (William-Landel-Ferry) equations. Master curve in frequency domain could be represented by Prony constants in frequency form. Master curve in time domain has been reconstructed by shifting the individual isotherm curves. Shift factor could be fitted by Williams-Landel-Ferry (WLF) Equation:

$$\log(a_T) = -\frac{C_1(T - T_r)}{C_2 + (T - T_r)} \qquad (4\text{-}1)$$

Where log (a_T) is the decadic logarithm of the WLF shift factor, T is test temperature, T_r is a reference temperature chosen to construct the master curve. C_1 and C_2 are empirical constants. Master curves of UF1 at 100°C over 360 days are shown in Fig. 4-29. We observe that storage modulus at high frequency is similar. However, in low and median frequency area, storage modulus increases as aging time increases, indicating loss of viscosity and increase the stiffness in aging process.

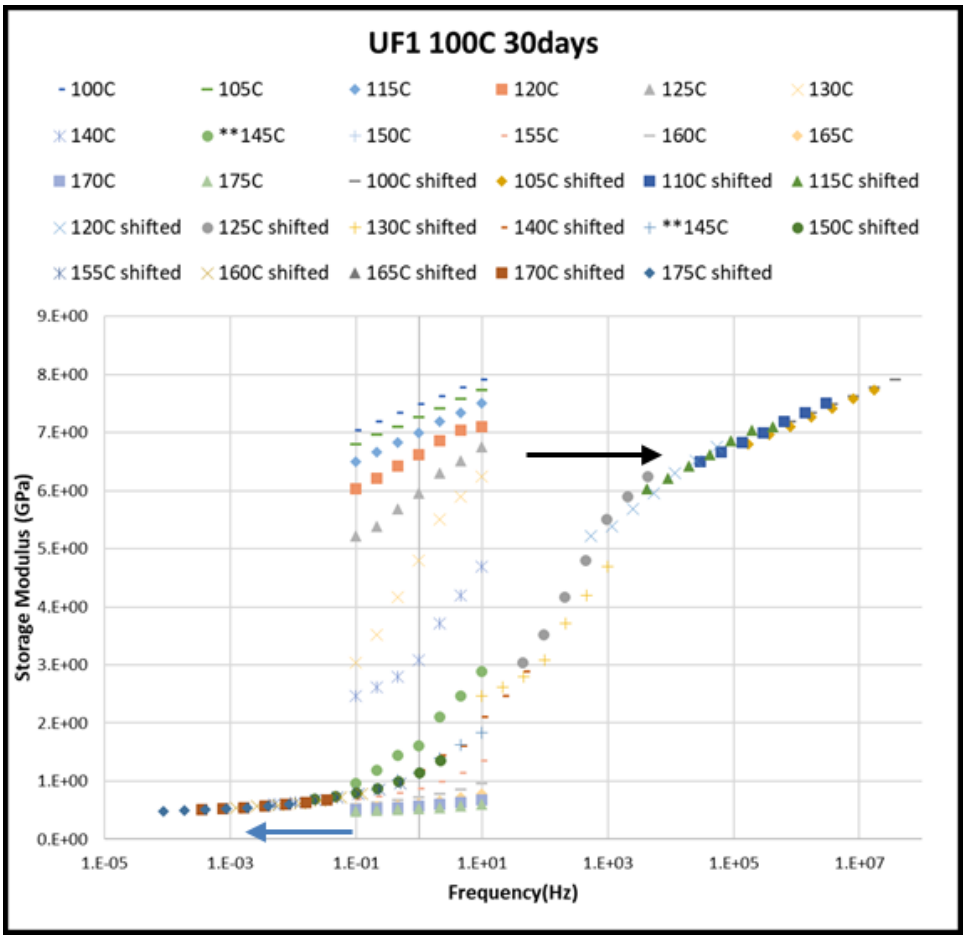

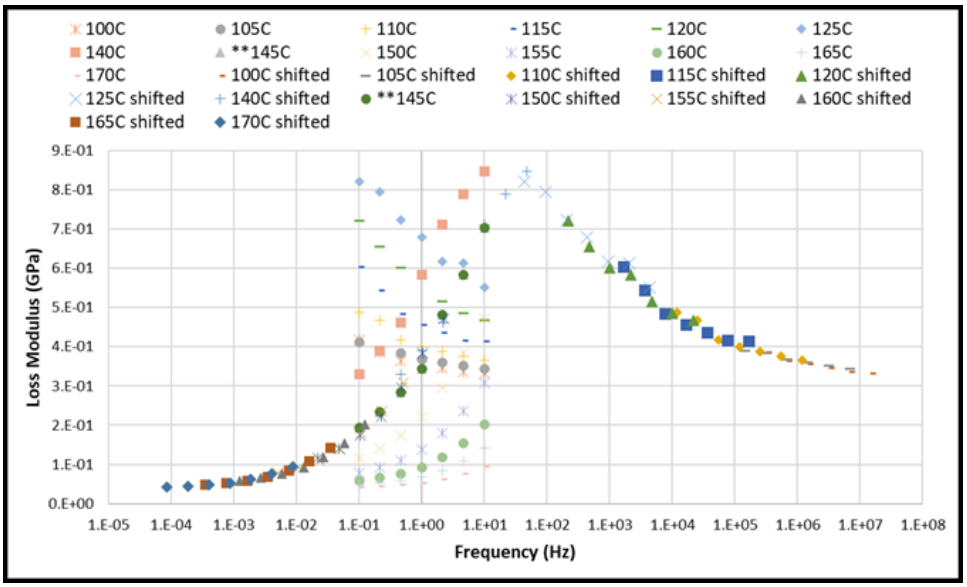

Figure 4-57 Master Curves Construction for UF

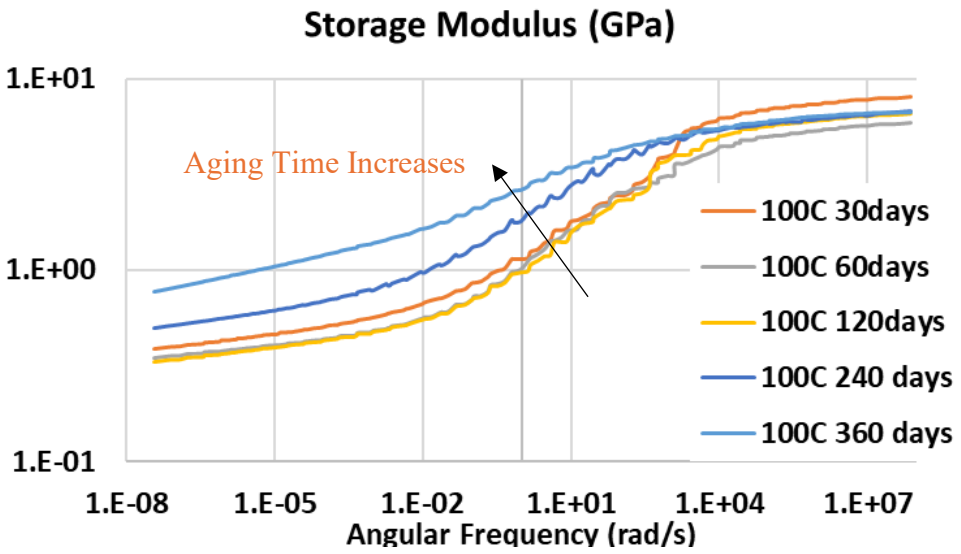

Fig. 4-58 Master Curves of UF1 at 100℃ aging over 360 days

- Freq sweep tests are conducted
- Master curves are constructed using TTS
- C1 = -2; C2 = -21.66

To fit the relaxation modulus data with the Prony series equation, the residual between the series prediction and the experimentally measured value is computed.

$$E = E_{\infty} + \sum_{i=1}^{n} E_i \exp\left(-\frac{t}{\tau_i}\right) \qquad (4\text{-}2)$$

The relaxation modulus is used to find the bulk (K) and shear (G) modulus using following equations:

$$K = \frac{E}{3(1-2\nu)} \qquad (4\text{-}3)$$

$$G = \frac{E}{2(1+\nu)} \qquad (4\text{-}4)$$

Similarly, the Prony series equation for bulk and shear modulus is given by:

$$K = K_{\infty} + \sum_{i=1}^{n} K_i \exp\left(-\frac{t}{\tau_i}\right) \quad (4\text{-}5)$$

$$G = G_{\infty} + \sum_{i=1}^{n} G_i \exp\left(-\frac{t}{\tau_i}\right) \quad (4\text{-}6)$$

Table 4-7. Prony pairs for UF1 aged at 100°C for 0, 30-days

UF1-Pristine				UF1-100°C-30d			
Bulk Modulus		Shear Modulus		Bulk Modulus		Shear Modulus	
K_∞	1.70E-01	G_∞	1.70E-01	K_∞	1.28E-08	G_∞	1.28E-08
K_1	2.83E-01	G_1	3.00E-01	K_1	1.42E-01	G_1	2.70E-01
τ_1	4.20E-02	τ_1	1.28E-03	τ_1	3.03E-01	τ_1	1.50E-03
K_2	3.00E-01	G_2	2.83E-01	K_2	2.70E-01	G_2	1.42E-01
τ_2	1.28E-03	τ_2	4.20E-02	τ_2	1.49E-03	τ_2	3.03E-01
K_3	7.02E-02	G_3	7.02E-02	K_3	2.18E-01	G_3	2.18E-01
τ_3	2.06E+01	τ_3	2.06E+01	τ_3	2.40E-02	τ_3	2.41E-02
K_4	1.77E-01	G_4	1.77E-01	K_4	3.35E-02	G_4	2.55E-01
τ_4	9.37E-01	τ_4	9.37E-01	τ_4	9.83E+04	τ_4	6.26E-05
				K_5	8.17E-02	G_5	8.16E-02
				τ_5	3.40E+00	τ_5	3.40E+00
				K_6	2.55E-01	G_6	3.35E-02
				τ_6	6.25E-05	T_6	9.85E+04

Table 4-8. Prony pairs for UF1 @100°C for 60 and 120-days

UF1-100°C-60d				UF1-100°C-120d			
Bulk Modulus		Shear Modulus		Bulk Modulus		Shear Modulus	
K_∞	1.80E-03	G_∞	5.00E-06	K_∞	9.19E-02	G_∞	9.19E-02
K_1	3.73E-01	G_1	3.07E-01	K_1	1.95E-01	G_1	2.58E-01
τ_1	1.29E-04	τ_1	7.23E-03	τ_1	5.43E-02	τ_1	5.38E-03
K_2	3.13E-01	G_2	1.80E-01	K_2	2.54E-01	G_2	1.34E-01
τ_2	5.43E-03	τ_2	1.79E-01	τ_2	3.13E-04	τ_2	5.04E-01
K_3	1.90E-01	G_3	7.39E-02	K_3	1.34E-01	G_3	6.73E-02
τ_3	1.41E-01	τ_3	3.36E+00	τ_3	5.04E-01	τ_3	4.70E+00
K_4	8.15E-02	G_4	4.08E-02	K_4	2.58E-01	G_4	2.54E-01
τ_4	2.70E+00	τ_4	1.24E+04	τ_4	5.38E-03	τ_4	3.13E-04
K_5	4.09E-02	G_5	3.99E-01	K_5	6.73E-02	G_5	1.95E-01
τ_5	9.02E+03	τ_5	1.65E-04	τ_5	4.70E+00	τ_5	5.43E-02

Table 4-9. Prony pairs for UF1 @150°C for 30 and 60-days

UF1-150°C-30d				UF1-150°C-60d			
Bulk Modulus		Shear Modulus		Bulk Modulus		Shear Modulus	
K_∞	1.36E-01	G_∞	1.36E-01	K_∞	9.60E-02	G_∞	9.34E-02
K_1	8.24E-02	G_1	2.27E-02	K_1	1.39E-01	G_1	2.14E-01
τ_1	1.13E+01	τ_1	1.83E+03	τ_1	6.89E-06	τ_1	6.68E-03

K_2	1.33E-01	G_2	1.82E-01	K_2	1.23E-01	G_2	1.84E-01
τ_2	3.25E-05	τ_2	7.88E-01	τ_2	1.73E+00	τ_2	2.38E-04
K_3	1.82E-01	G_3	8.24E-02	K_3	1.88E-01	G_3	1.89E-01
τ_3	7.88E-01	τ_3	1.13E+01	τ_3	4.04E-04	τ_3	1.21E-01
K_4	2.05E-01	G_4	1.33E-01	K_4	1.85E-01	G_4	1.33E-01
τ_4	2.98E-03	τ_4	3.25E-05	τ_4	1.42E-01	τ_4	3.30E-06
K_5	2.27E-02	G_5	2.05E-01	K_5	2.10E-01	G_5	6.09E-02
T_5	1.83E+03	τ_5	2.98E-03	T_5	9.06E-03	τ_5	1.81E+01
K_6	2.39E-01	G_6	2.39E-01	K_6	6.02E-02	G_6	1.26E-01
τ_6	5.66E-02	T_6	5.66E-02	τ_6	1.84E+01	T_6	1.59E+00

Table 4-10. Prony pairs for UF1 @150°C, 120 days and UF2 0-days

UF1-150°C-120d				UF2-Pristine			
Bulk Modulus		Shear Modulus		Bulk Modulus		Shear Modulus	
K_∞	1.88E-01	G_∞	1.88E-01	K_∞	1.67E-01	G_∞	1.67E-01
K_1	9.76E-02	G_1	2.72E-01	K_1	9.20E-02	G_1	6.26E-02
τ_1	2.22E-01	τ_1	2.95E-03	τ_1	6.77E+01	τ_1	1.67E+04
K_2	4.42E-01	G_2	4.42E-01	K_2	1.98E-01	G_2	8.93E-02
τ_2	5.99E-05	τ_2	5.99E-05	τ_2	5.85E-02	τ_2	7.31E+01
K_3	2.72E-01	G_3	9.76E-02	K_3	1.80E-01	G_3	1.10E-01
τ_3	2.95E-03	τ_3	2.22E-01	τ_3	7.31E+00	τ_3	2.15E-03

	K_4	2.25E-01	G_4	1.80E-01
	τ_4	7.22E-01	τ_4	7.64E+00
	K_5	2.70E-02	G_5	2.27E-01
	τ_5	4.39E+03	τ_5	7.29E-01
	K_6	1.11E-01	G_6	2.00E-01
	τ_6	2.44E-03	T_6	5.65E-02

Table 4-Table 7 lists the Prony series pairs for UF1. The effect of aging on the viscoelastic behavior of the underfills was assessed using the procedure outlined in Equations (1)-(6). The prony-pairs have been computed for all the aging conditions for duration up to 60-days. Table 4 lists the Prony series pairs for aged UF1, UF2 underfills.

4.8*Summary and Conclusions*

This chapter presents a comprehensive investigation into the thermal stability, mechanical properties, and viscoelastic behavior of underfill encapsulants as a function of aging time and temperature. The study aims to establish the relationships between material properties, processing conditions, and overall performance by examining various underfill encapsulants that have been subjected to elevated temperatures for up to one year. Uniaxial tensile testing is utilized to collect data and analyze the material's aging behavior.

The research findings highlight the contrasting aging behaviors observed above and below the glass transition temperature. The materials exhibit increased stiffness due to a higher level of cross-linking after aging. This enhanced cross-linking density contributes to the material's improved resistance to decomposition in high-temperature environments, as indicated by thermal gravimetric analysis (TGA) results.

To understand the degradation mechanisms under long-term high-temperature aging, the study investigates the evolution of ultimate tensile strength and percentage elongation. The higher cross-linking density leads to increased brittleness, resulting in reduced ultimate tensile strength and percentage elongation, as observed in the tension test results.

The curves depicting the evolution of material properties generally exhibit an inflection point, with different slopes before and after this point. Prolonged exposure to high-temperature conditions is found to induce the formation of cracks in the oxidative boundary layer of the bulk underfill material.

By examining these aspects, the research sheds light on the effects of aging time and temperature on underfill encapsulants, providing valuable insights into their long-term performance and degradation mechanisms.

Chapter 5 Material Property evolution of Epoxy Molding Compound (EMC)

5.1 *Thermogravimetric Analysis*

Thermogravimetric Analysis is to characterize the thermal stability of EMCs.

Figure 5-1 illustrates the contrasting thermal stability behaviors of materials under different aging conditions within the temperature range of 350℃ to 650℃. In the case of pristine material, a significant weight reduction occurs around 400℃. However, for EMC1 samples aged for 240 days, a slight weight decrease is observed around 400℃, followed by a linear decline in weight between 420℃ and 600℃, with a substantial drop occurring after 600℃. The change of derivative weight plot exhibits a peak for the aged samples, suggesting that the material becomes more resistant to decomposition after aging.

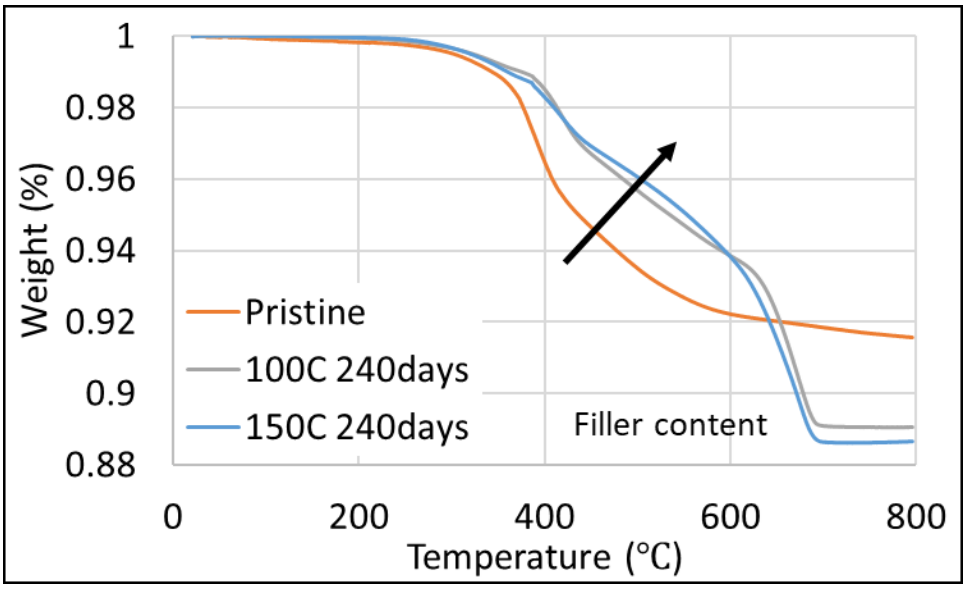

(a) Weight Loss as Function of Temperature

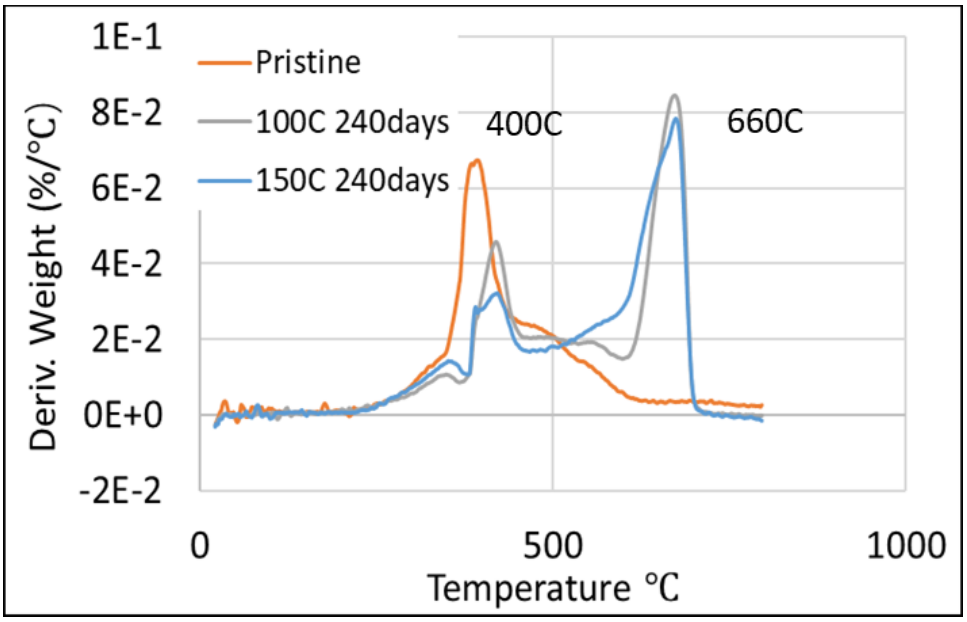

(b) Derivative Weight Loss as Function of Temperature

Figure 5-1 TGA results for EMC-1

Furthermore, when comparing the decomposition characteristics of the material at 150℃ (blue line) and 100℃ (grey line), it is evident that the material at 150℃ exhibits slightly greater resistance to decomposition than at 100℃ between the temperature range of 400℃ and 600℃. This indicates that the material strengthens after aging, potentially due to a higher level of cross-links and the formation of an oxidative layer.

Additionally, the analysis reveals that the filler percentage in EMC-1 is approximately 92%. However, the filler content decreases after aging, which can be attributed to the loss of fillers during prolonged exposure to high temperatures. This decrease in filler content is particularly pronounced due to the initially high filler content in the pristine material.

Overall, the TGA results provide valuable insights into the thermal stability and compositional changes occurring in the material, indicating an increased resistance to decomposition after aging, potentially attributed to cross-linking and the generation of an oxidative layer.

5.2 *Viscoelastic Property Evolution by Dynamic Mechanical Analyzer*

Dynamic mechanical analysis (DMA) is a technique used to characterize the glass transition temperature and the evolution of modulus over time. DMA test results typically include storage modulus, loss modulus, and tan delta. The storage modulus represents the material's elastic behavior, while the loss modulus characterizes the viscous dissipation of the material.

In the case of pristine EMC, the storage modulus at room temperature is approximately 25 GPa. It reaches around 900 MPa immediately after the glass transition region, which is higher than the storage modulus of most epoxy resins. The difference in storage modulus before and after the glass transition temperature is smaller compared to most epoxy resins. This higher modulus after the glass transition region can be attributed to the effect of filler content.

The glass transition temperature can increase with both aging time and temperature due to the increase in cross-links. For pristine EMC1, the glass transition temperature is 118℃, while for pristine EMC2, it is 157℃.

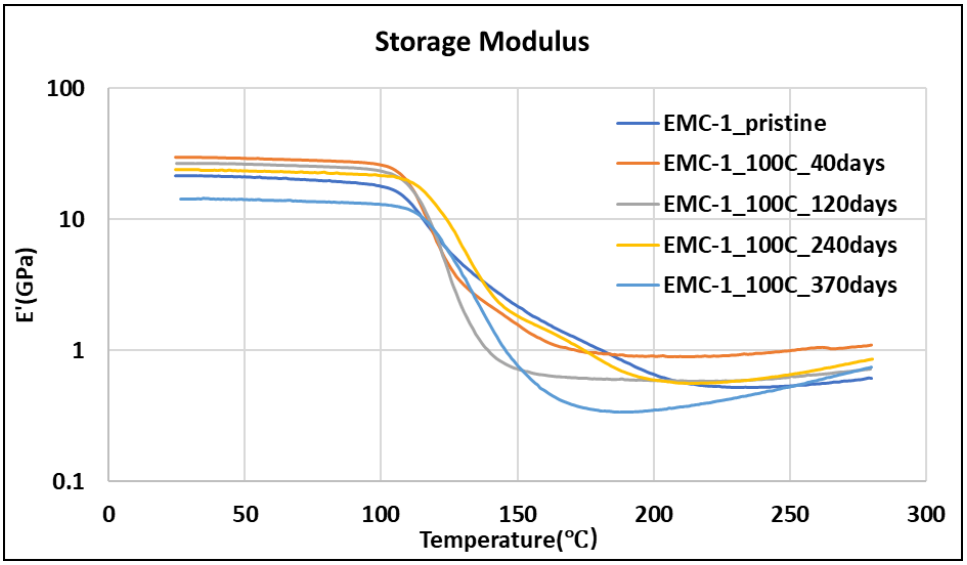

(a) EMC1 expose to 100℃

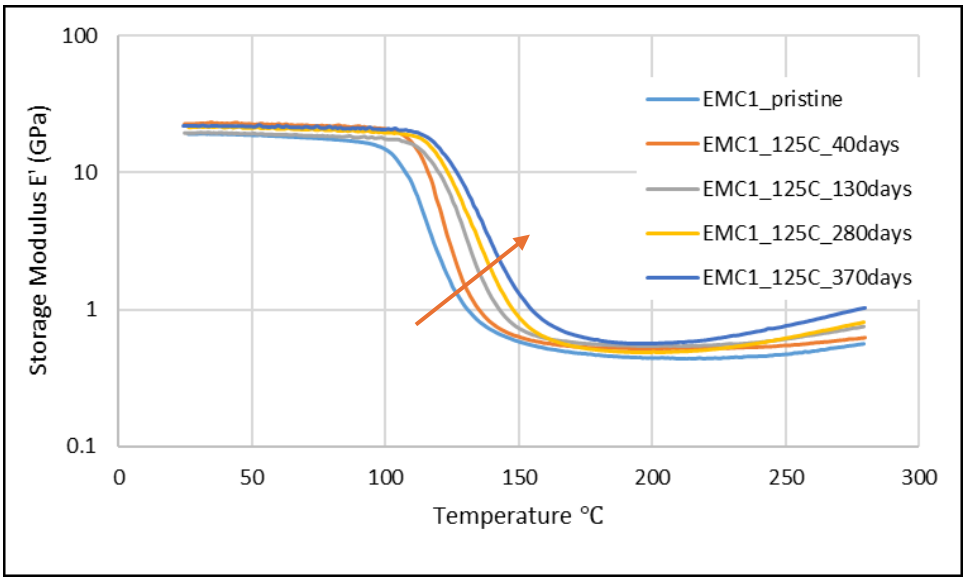

(b) EMC1 expose to 125°C

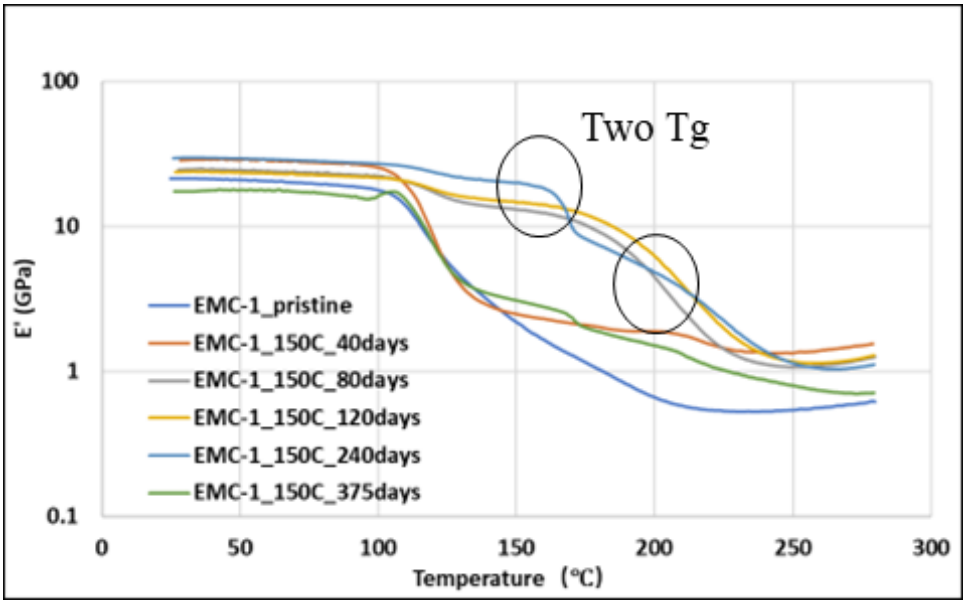

(c) EMC1 expose to 150°C

Figure 5-2 Storage Modulus of EMC1 under different aging temperatures

The aging behaviors exhibit notable differences depending on whether the aging temperature is higher or lower than the glass transition temperature. This suggests distinct degradation mechanisms for temperatures above and below the glass transition region. The storage

modulus, as observed during temperature ramp tests, displays significant variations after exposure to different sustained high-temperature environments (as depicted in Figure 5-2).

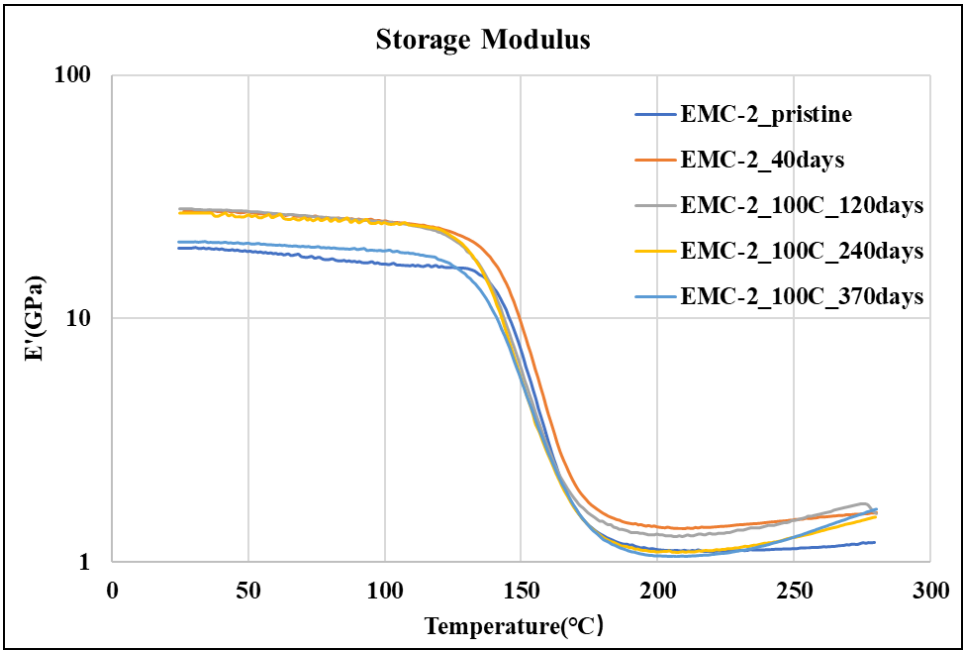

a) EMC2 expose to 100℃

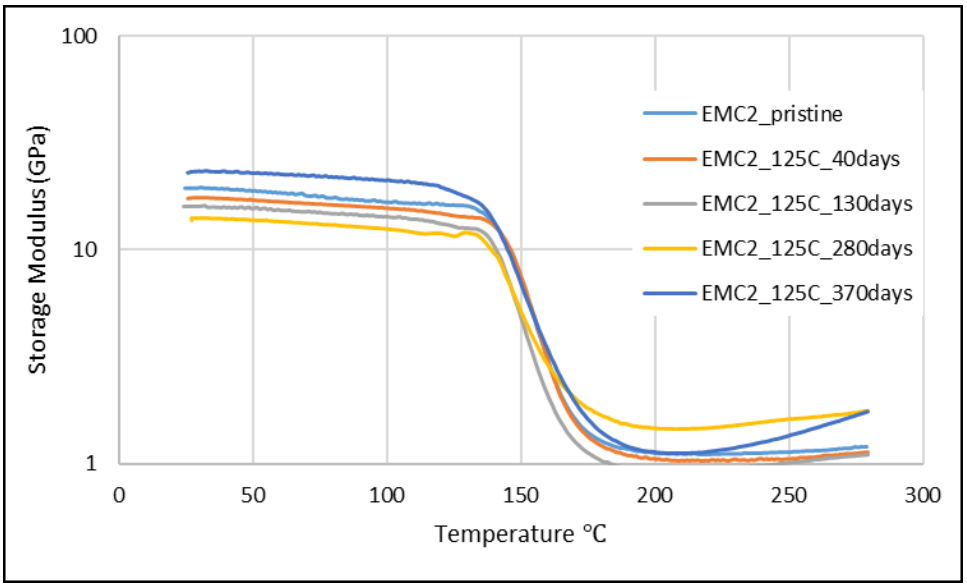

b) EMC2 expose to 125℃

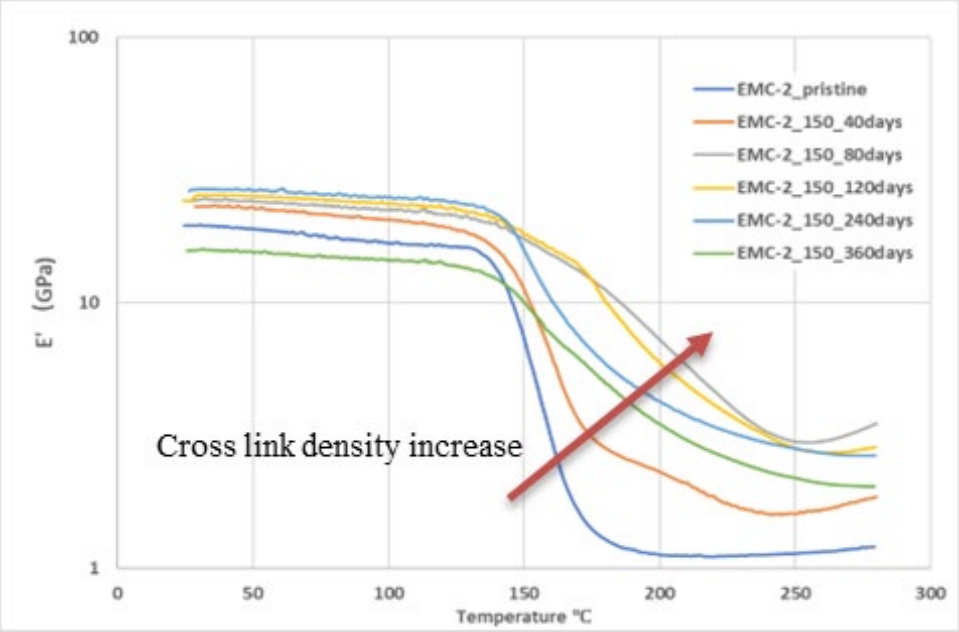

c) EMC2 expose to 150℃

Figure 5-3 Storage Modulus of EMC2 under different aging temperatures

In the case of aging at 100℃ and 125℃, the glass transition temperature continues to increase as the aging time progresses. The modulus after aging surpasses that of the pristine conditions. This can be attributed to the increased level of cross-links formed during the aging process.

However, when subjected to 150℃ aging, the glass transition region exhibits a separation into two distinct domains after 40 days. This behavior indicates the presence of two immiscible polymers, suggesting the generation of another polymer with a higher glass transition temperature following high-temperature aging.

The glass transition temperature (Tg) of pristine EMC2 is reported to be 157℃, which is higher than the three aging environments studied (as shown in Figure 5-3). In the case of aging at 100℃ and 125℃, the glass transition region does not show a significant increase as the aging time

increases. However, the modulus of the material increases after aging due to the increased level of cross-links formed during the aging process.

On the other hand, for the 150℃-aging condition, the glass transition region shows a significant increase as the aging time increases. This is indicated by a wider glass transition region and a flatter curve in the temperature range of the glass transition. These changes suggest a higher level of cross-linking in the material after aging at 150℃.

The evolution of glass transition temperature (Tg) can be more accurately characterized by the Tan δ curve, as shown in Figure 5-4. Notably, the presence of an immiscible polymer becomes evident under the 150℃ aging environments. The first peak observed in the Tan δ curve corresponds to the glass transition temperature of the pristine epoxy, while the second peak represents the immiscible polymer formation, indicating the emergence of a multicomponent system.

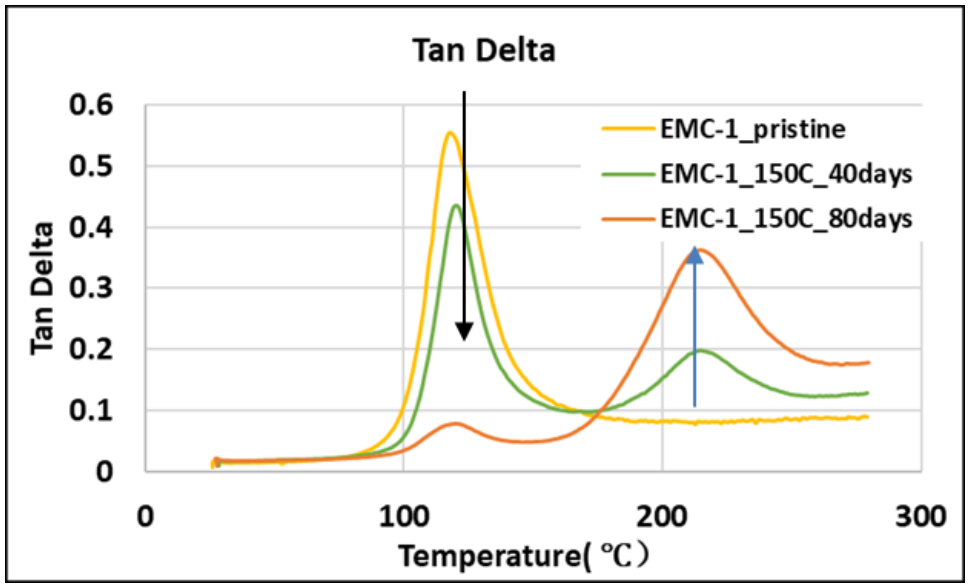

(d) EMC-1 for 150 aging

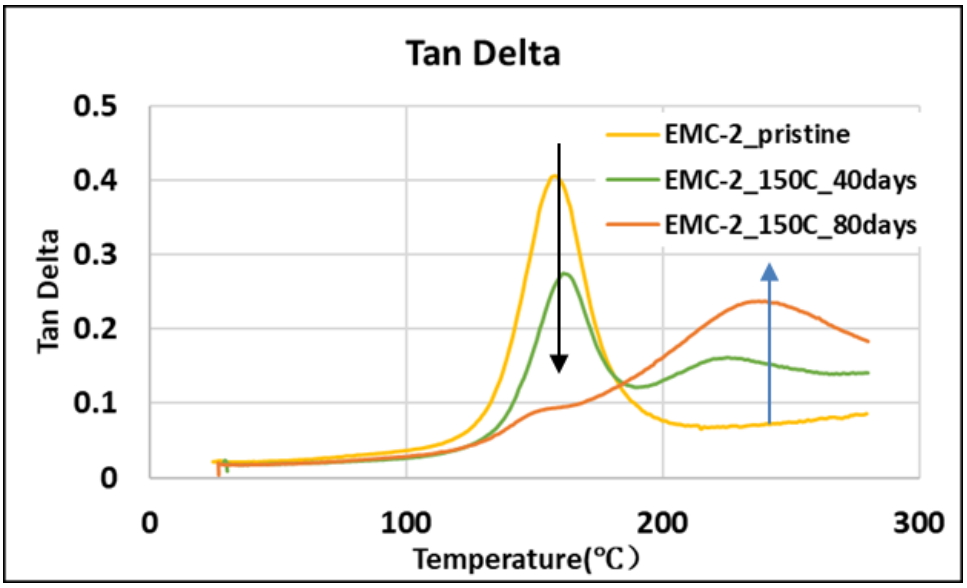

(e) EMC-2 for 150C aging

Figure 5-4 Tan delta for 150℃ from Pristine to 80 Days

As the aging time increases, the height of the first peak decreases, suggesting a diminishing influence of the pristine epoxy. It also indicates the viscosity decrease of epoxy. Conversely, the height of the second peak increases, indicating an increasingly significant role played by the immiscible polymer. This trend implies that the immiscible polymer becomes more pronounced with longer aging times under high-temperature aging conditions.

Table 5-1 presents the evolution of glass transition temperature (Tg) characterized by Tanδ under all aging conditions, including the first and second peak. The data clearly indicate that the secondary peak is only observed in the 150℃ environments, suggesting distinct physical aging mechanisms between this temperature and the other two aging temperatures.

Table 5-1 Glass Transition Temperature Evolution

	EMC1			EMC2		
Temp	100℃	125℃	150℃	100℃	125℃	150℃

Aging Days	Tan Delta					
0	118℃			157℃		
40	122℃	127℃	121/212℃	159℃	159℃	161/225℃
80	127℃	130℃	121/215℃	158℃	157℃	153/242℃
120	128℃	134℃	121/220℃	156℃	155℃	160/252℃
240	134℃	140℃	121/234℃	155℃	152℃	162/265℃
360	142℃	143℃	121/250℃	158℃	158℃	169/263℃

The plotted graph in Figure 5-5 illustrates the Tg values under all aging conditions. For EMC1, Tg shows a continuous increase as the aging time progresses under 100℃ and 125℃ aging conditions. However, for EMC2, Tg does not exhibit significant changes under these conditions. In contrast, when subjected to the 150℃ environments, the Tg of the immiscible polymer (represented by the blue curve) shows a continuous increase as the aging time increases. On the other hand, the Tg of the original epoxy (represented by the yellow curve) shows minimal changes for EMC1 and slight increases for EMC2.

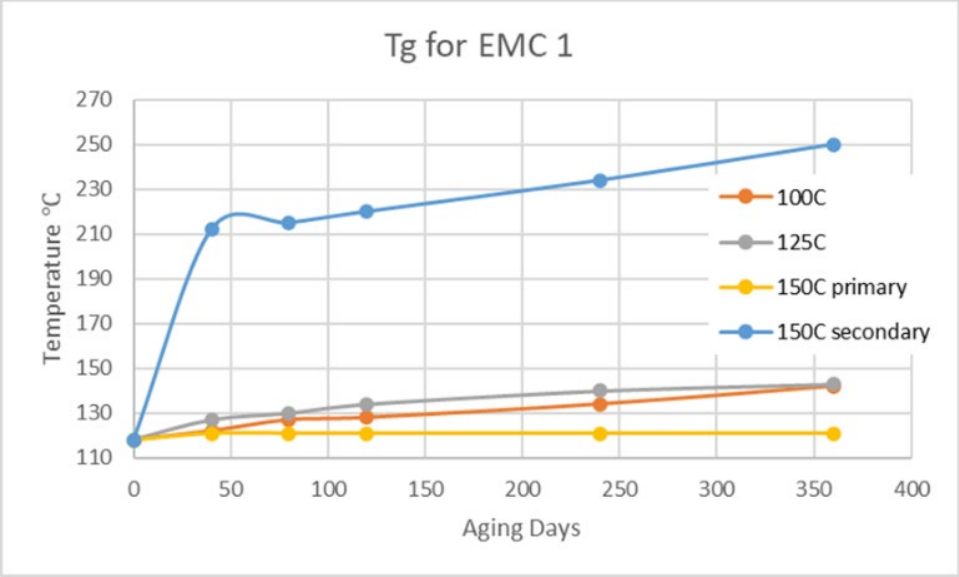

a) Tg for EMC1

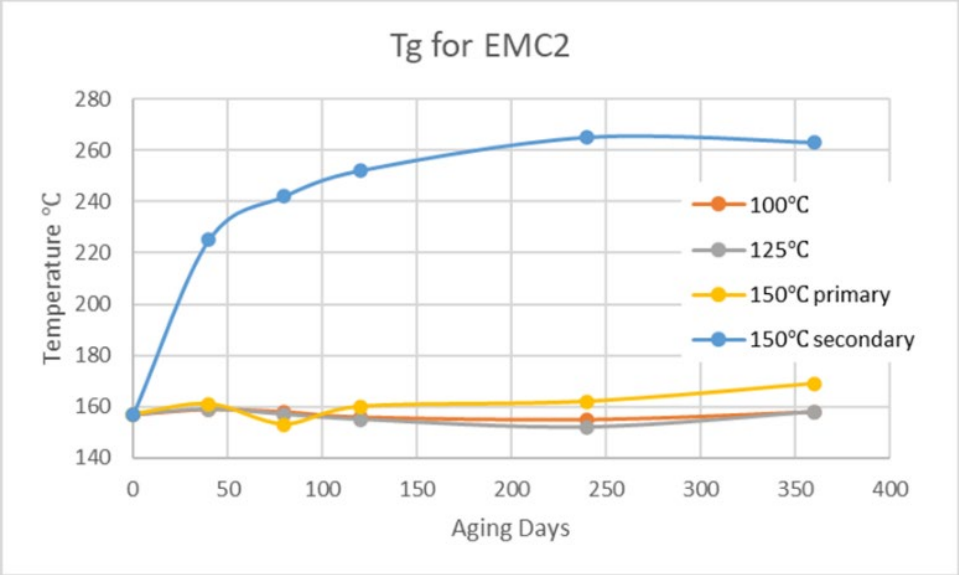

(b) Tg for EMC2

Figure 5-5 Tg Evolution for All aging Conditions

5.3*Microstructure Evolution*

In this section, the microstructure evolution of EMC1 under 150℃ 40-day aging is studied using a fluorescent microscope.

The settings for the microscope are provided in Table **5-2**. The cross-section area of the EMC is shown in Figure 5-6, where different fluorescence dyes are applied to highlight specific features. FITC (green fluorescence) with excitation wavelength of 460-500 nm and emission wavelength of 510-560 nm is used to observe the primary boundary layer. TRITC (red fluorescence) with excitation wavelength of 530-560 nm and emission wavelength of 590-650 nm is used to observe the secondary boundary layer. DAPI (blue fluorescence) with excitation wavelength of 340-380 nm and emission wavelength of 420 nm is also used to observe the boundary layer, although it appears darker and is more difficult to distinguish.

By analyzing the images obtained, it is observed that there is a bright band close to the boundary, indicating the presence of a boundary layer. The fluorescent dyes provide different levels of visibility for the boundary layer. The FITC and TRITC results show both the primary and secondary boundary layers, while the DAPI result only shows one boundary layer. The thickness of the boundary layer is estimated to be approximately 90 μm, as indicated by the black bar of length 100 μm placed on the right boundary area.

Table 5-2 Setting of Fluorescent Microscope

Fluorochrome Examples	Excitation/Emission(nm)
FITC(green)	460-500/510-560
TRITC(red)	530-560/590-650
DAPI(blue)	340-380/420LP

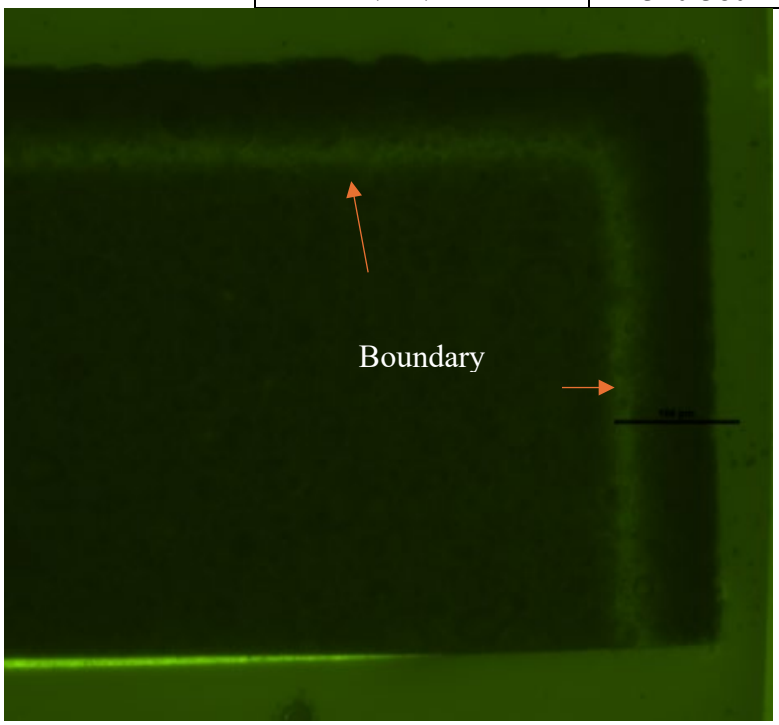

(a) FITC

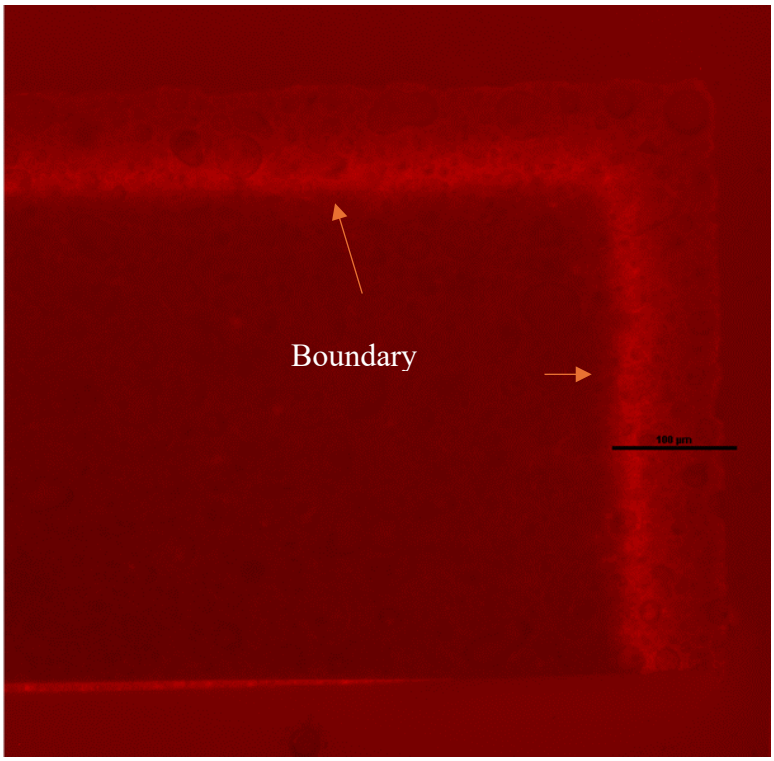

(b) TRITC

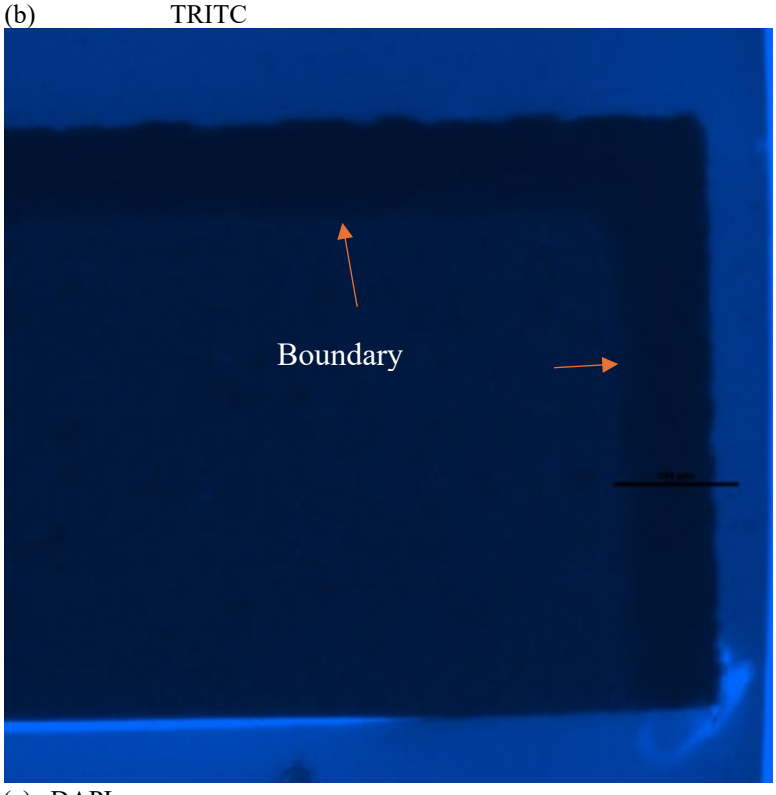

(c) DAPI

Figure 5-6 EMC2 under Fluorescent Microscope

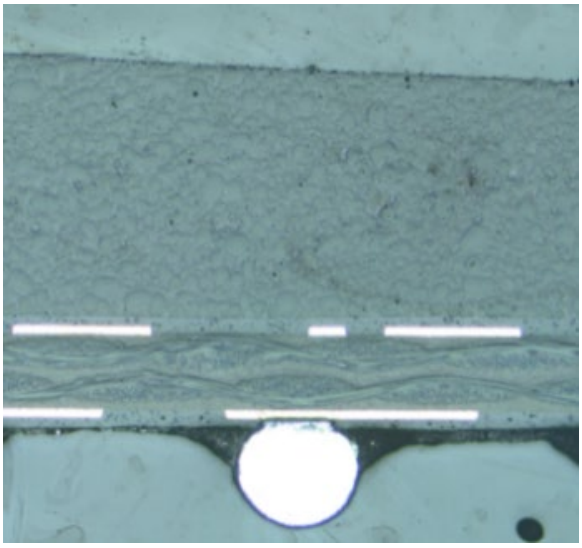

a) EMC2 Pristine

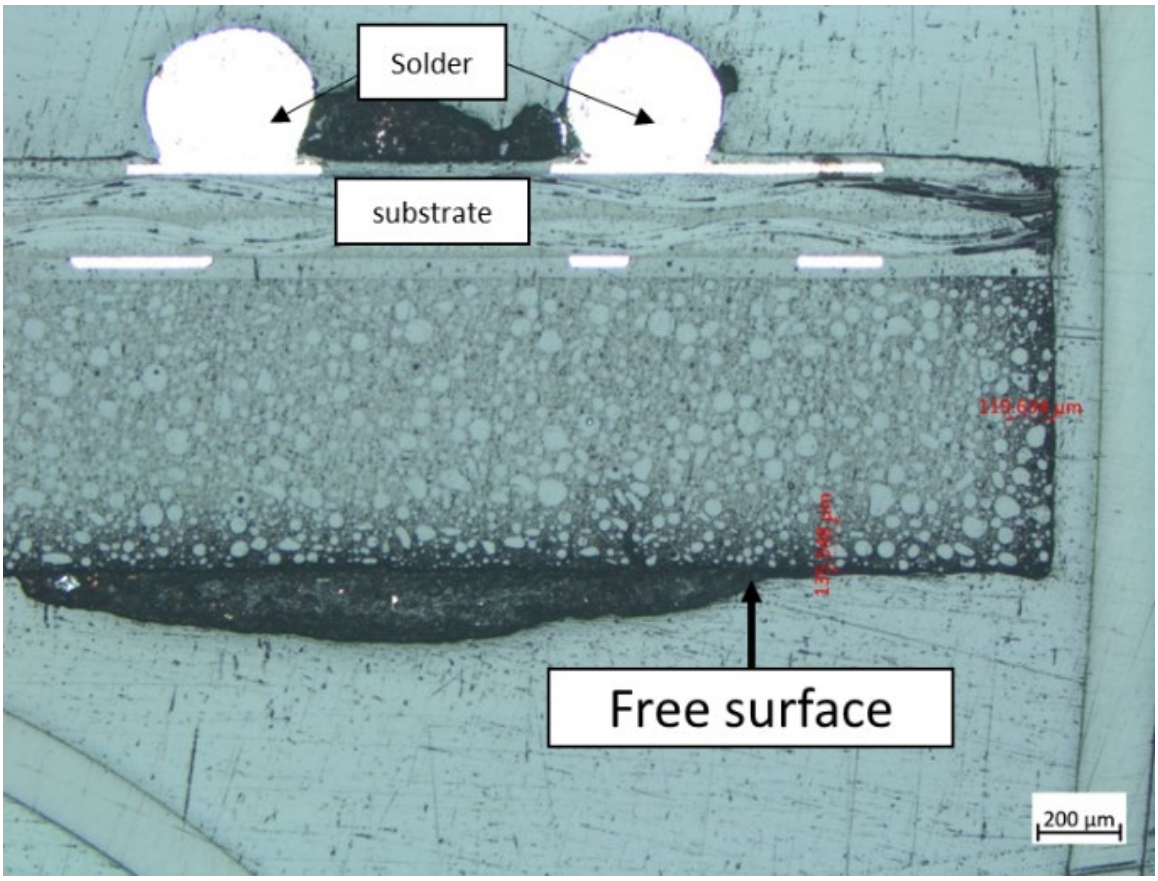

(b) EMC2 150C 400days

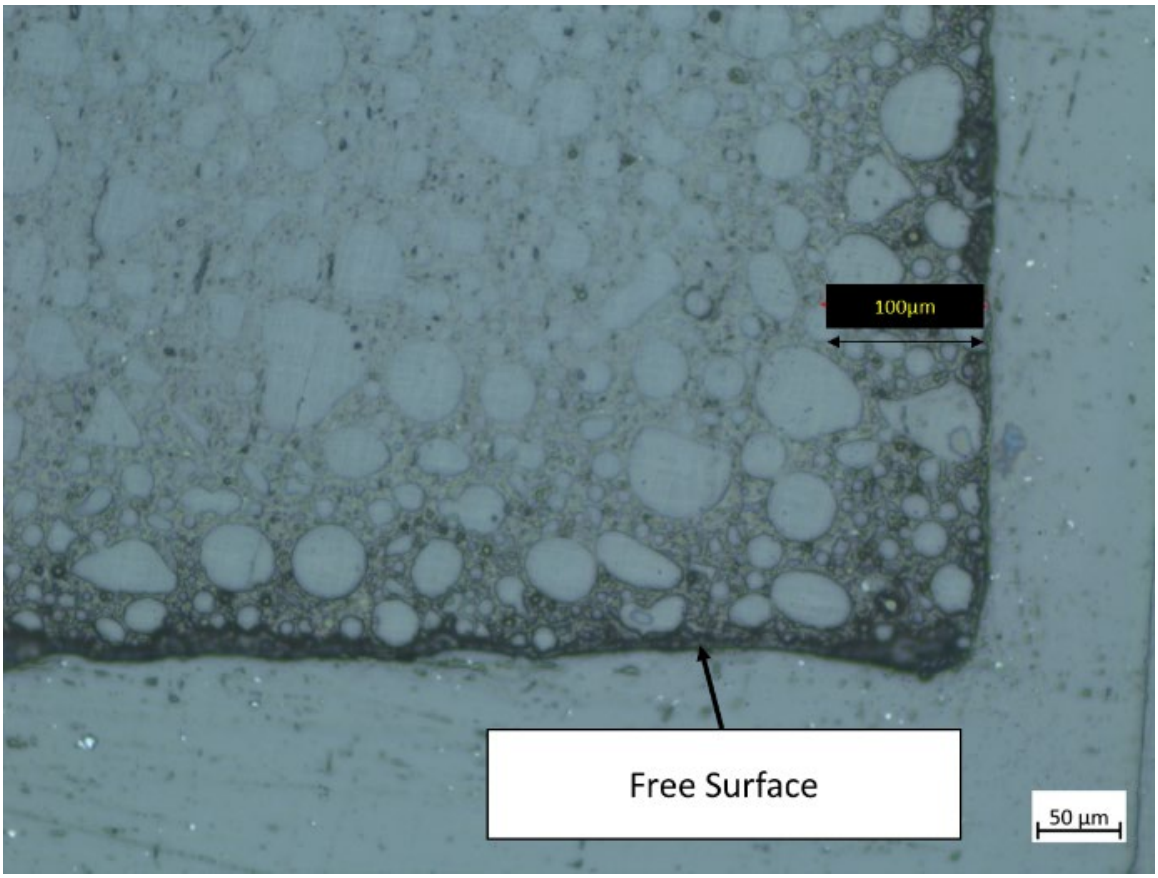

(c) EMC2 150C 400days

Figure 5-7 EMC2 under Optical Microscope

Additionally, the polarized optical microscope is used to investigate the details of the boundary layer. In Figure 5-7, the microstructure of EMC2 is shown under pristine conditions and after 400 days of aging at 150℃. In the pristine condition, no boundary layer is observed. However, after 400 days of aging, a dark layer is clearly visible, and its thickness on both the left and bottom free surfaces is approximately 120 μm. Figure 5-7(c) provides further details of the dark region invading the epoxy from the boundary to the middle of the material.

Figure 5-8 shows the microstructure of EMC1 after 40 days of aging at 100℃ (Figure 5-8(a)) and 150℃ (Figure 5-8(b)). In Figure 5-8(a), a faint boundary layer can be observed, which is indicated by a slight color change in the epoxy area near the bottom boundary. Comparatively,

in Figure 5-8(b), the boundary layer is more pronounced and appears as a dark region that extends from the boundary towards the middle of the material.

This boundary layer is directly associated with material degradation. During aging, oxygen diffuses into the molding compound and affects the polymer structure. The thermo-oxidation reaction occurring in the material leads to the formation of a region with a higher cross-linking density at the boundary. As the aging time and temperature increase, the glass transition temperature of the material also increases.

The presence of the boundary layer and its impact on the material's properties, such as increased glass transition temperature and higher cross-linking density, indicate the effects of degradation and oxidation processes on the aging behavior of the EMC1.

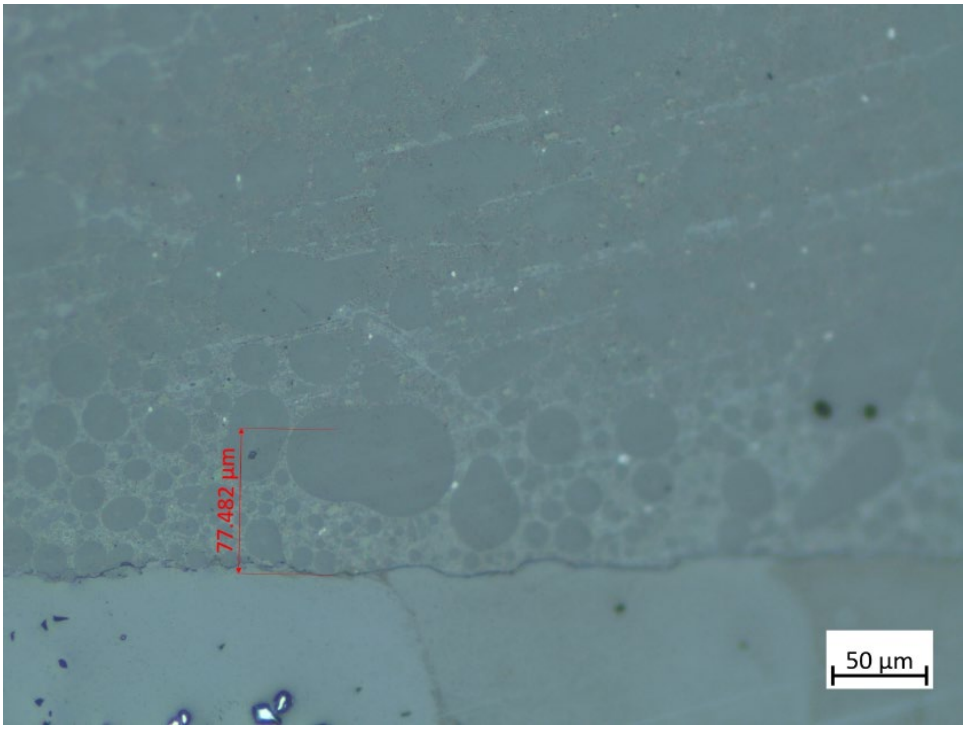

a) EMC1 100C 40 days

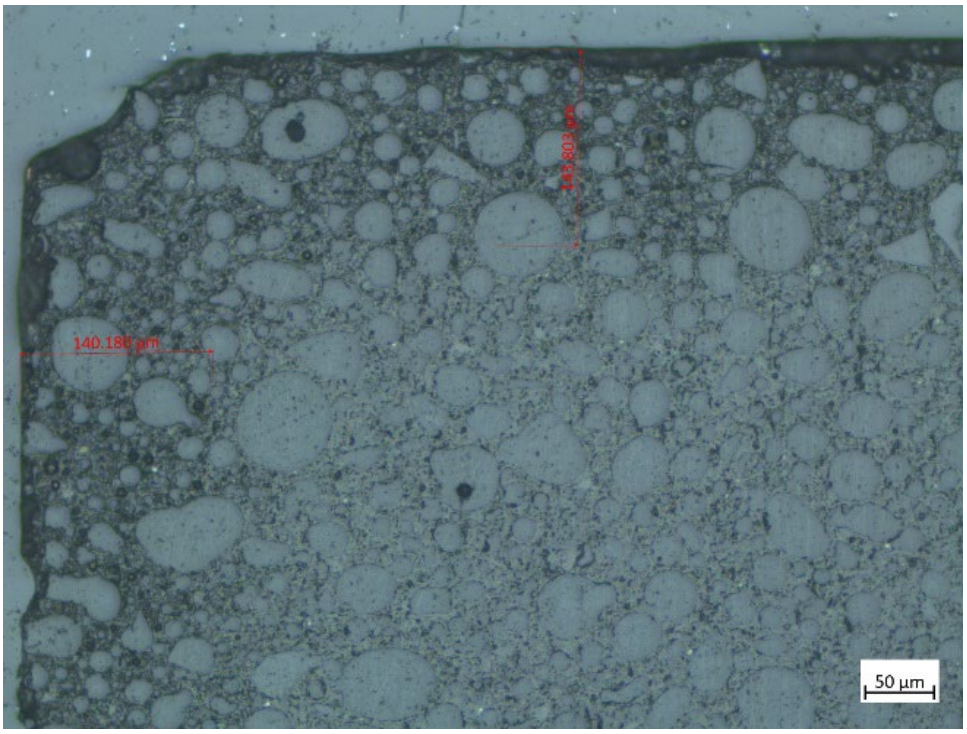

b) EMC1 150C 40 days

Figure 5-8 EMC1 under Optical Microscope

The evolution of the boundary layer in both EMC1 and EMC2 is studied using a polarized optical microscope, as shown in Figure 5-9. This technique allows for easier observation of the thickness of the oxidative layer. The results indicate that the thickness of the oxidative layer in both EMCs remains relatively unchanged between 120 days and 240 days of aging. The thickness of the oxidative layer is approximately 180µm, while the overall specimen thickness is 700µm.

The oxidative layer exhibits a higher glass transition temperature compared to the bulk material, indicating a higher level of cross-linking density. This higher cross-linking density contributes to the increased modulus observed after the aging tests, as the material possesses a denser network of cross-links. However, it is important to note that cross-linking polymers often exhibit a stiffness-toughness conflict, as higher levels of cross-linking density can simultaneously

increase the modulus and brittleness of the material. As a result, cracks are more likely to initiate and propagate from the boundary area with a higher cross-linking level.

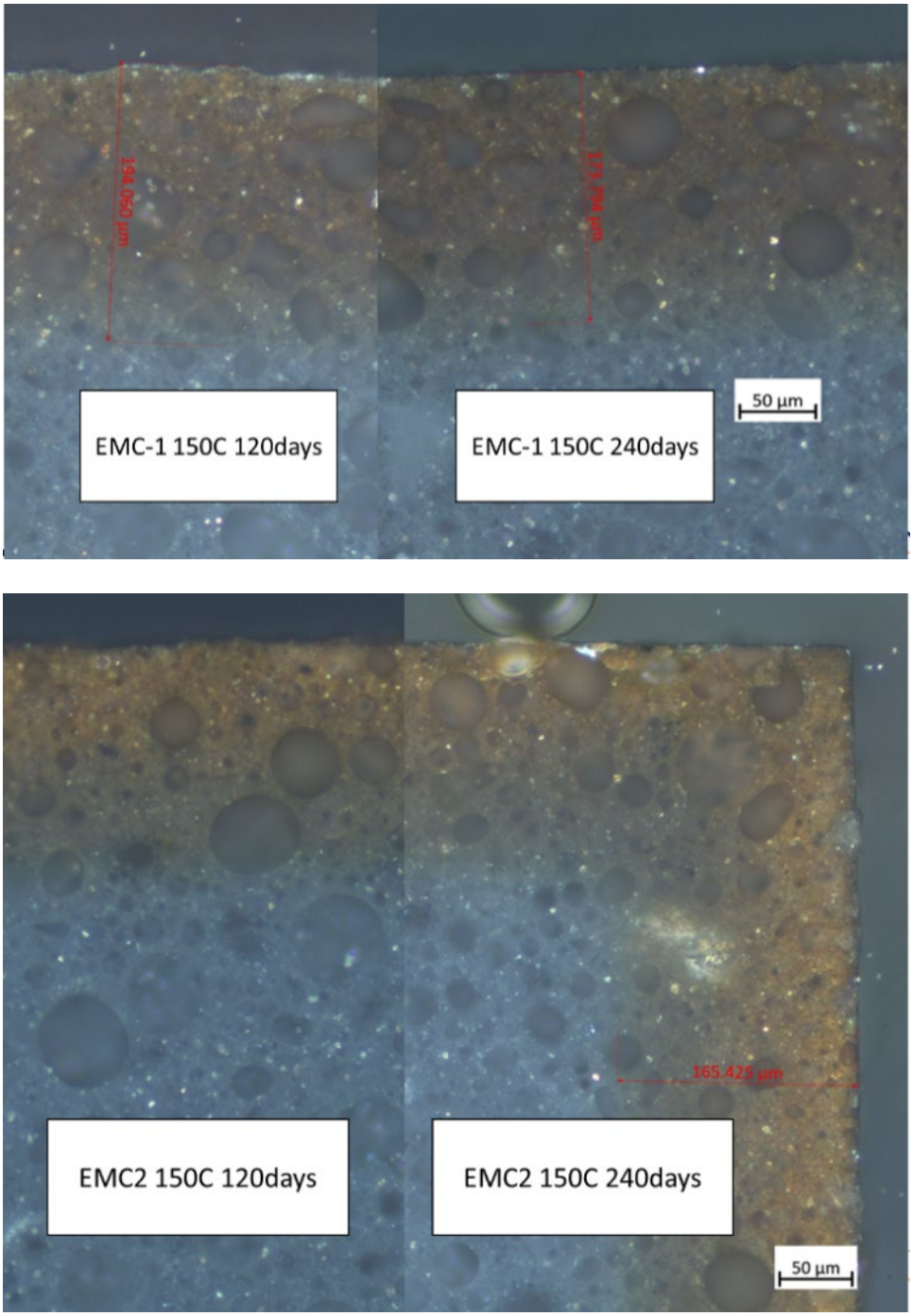

Figure 5-9 EMC1 and EMC2 under Polarized Optical Microscope

SEM (Scanning Electron Microscopy) analysis was conducted to further investigate the microstructure of the boundary layer in EMC2 after 400 days of aging at 150°C. Figure 5-10(b) provides a detailed view of the boundary layer. An evident boundary can be observed, where the fillers are clearly visible, while they are harder to discern in the middle region of the material.

Within the boundary layer, cracks are observed, primarily in the epoxy region near the fillers. No cracks are observed in the middle region of the material. The initial crack initiation occurs at the interface between the fillers and the epoxy matrix. After the initial crack formation, the cracks propagate from one filler to another and progress from the boundary layer towards the inner region of the material. This crack propagation weakens the material until it eventually fails. This mechanism represents one of the major failure modes for EMCs subjected to high-temperature long-term aging.

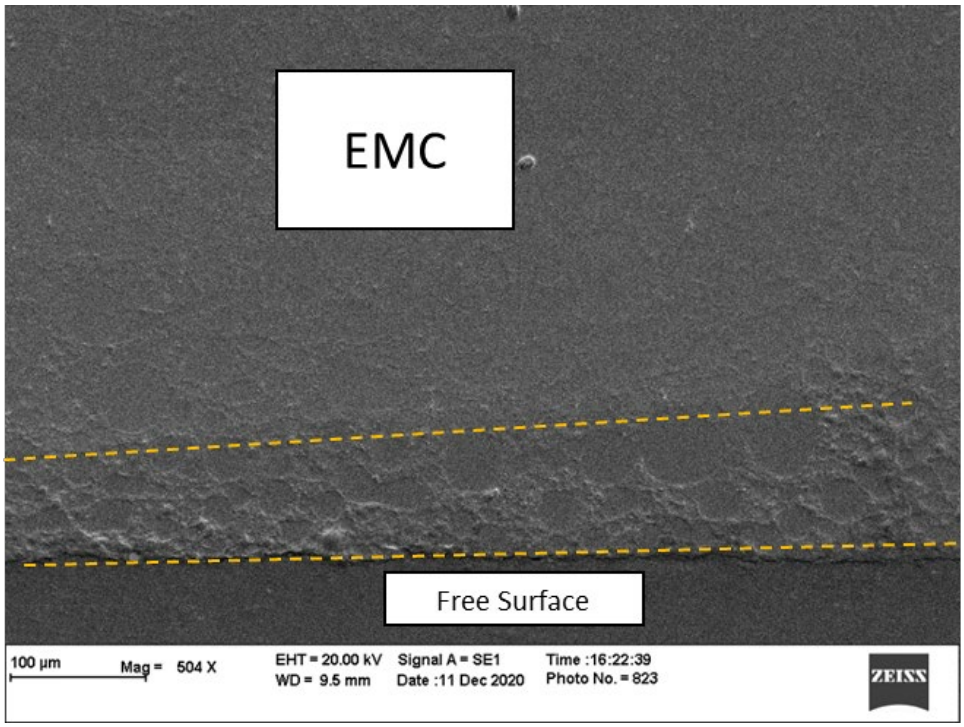

(a) EMC2 150C 400days

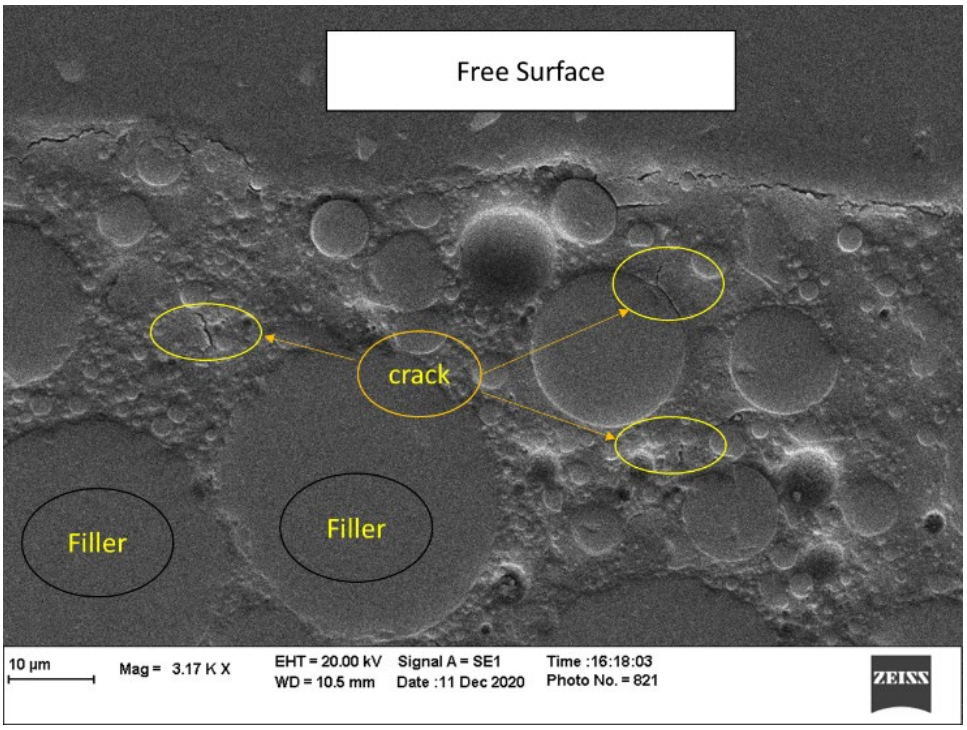

(b) Boundary region of EMC2 150C 400 days

Figure 5-10 EMC2 150C 400days

Summary and Conclusions

In conclusion, our study focused on the aging behavior of two popular epoxy molding compounds (EMC): EMC-1 and EMC-2. We observed an increase in modulus and embrittlement after aging, which can be attributed to the increased level of cross-links. However, we also identified a stiffness-toughness conflict commonly seen in cross-linked polymers, where the material becomes stronger but more prone to breaking.

We discovered that the degradation mechanisms differ under high-temperature aging conditions. For EMC-1 exposed to 150°C, which exceeds its glass transition temperature (Tg), an oxidative boundary layer formed, resulting in a multicomponent system where the boundary material exhibited a significantly higher Tg, indicating a higher density of cross-links. As a result, the material became more resistant to decomposition in high-temperature environments after

extended exposure to 150℃. To evaluate the impact of sustained high-temperature operation, we conducted TGA and DMA tests on the two types of EMCs and studied microstructure evolution.

We observed the generation of an oxidative layer under the 150℃ environments within a short period of aging time. The thickness of the layer did not significantly change with increasing aging time. Cracks initiated in the boundary area at the interface between fillers and epoxy resins, followed by crack propagation from filler to filler within the boundary region. The brittleness of the oxidative layer contributed to crack initiation in the boundary region. This failure mechanism suggests a potential approach for improving reliability. By appropriately coating the filler surface, the adhesion between the filler and epoxy resins can be enhanced, thereby increasing the fracture resistance to microcracks. Improved bonding and adhesion can reduce the free volume of the polymer network near the filler, resulting in a higher glass transition temperature. Given the high filler content in EMCs, enhancing adhesion can significantly enhance the reliability performance of the material under high temperatures.

5.4 *Coefficients of Thermal Expansion Measurement*

The coefficients of thermal expansion (CTE) results for both EMCs under 150℃ aging conditions are showing in Figure 5-11. Results show that the CTEs for both before and after glass transition temperature decreases as the aging time increases. CTE1 is the CTE before glass transition temperature. CTE2 is the CTE after glass transition temperature. Value of CTE1 is much lower than CTE2. CTE1under all conditions are below 10ppm/℃. As aging time increases, CTE 1 decreases to 1ppm/℃ for EMC1 and 4 ppm/℃for EMC2. CTE2 represent the coefficient of thermal expansion after glass transition temperature. CTE2 for both pristine samples are 70ppm/℃, higher than the values measured by classical TMA tests. Value of CTE to drop to 20ppm/℃ for EMC1 and to 30ppm/℃ for EMC2 respectively, after one year aging. The decreasing trend of CTE

values could be explained by the increase of cross-link density after high temperature long term aging. The higher cross-link density, the stiffer the material is. It indicates material is harder to deform after high temperature long-term aging.

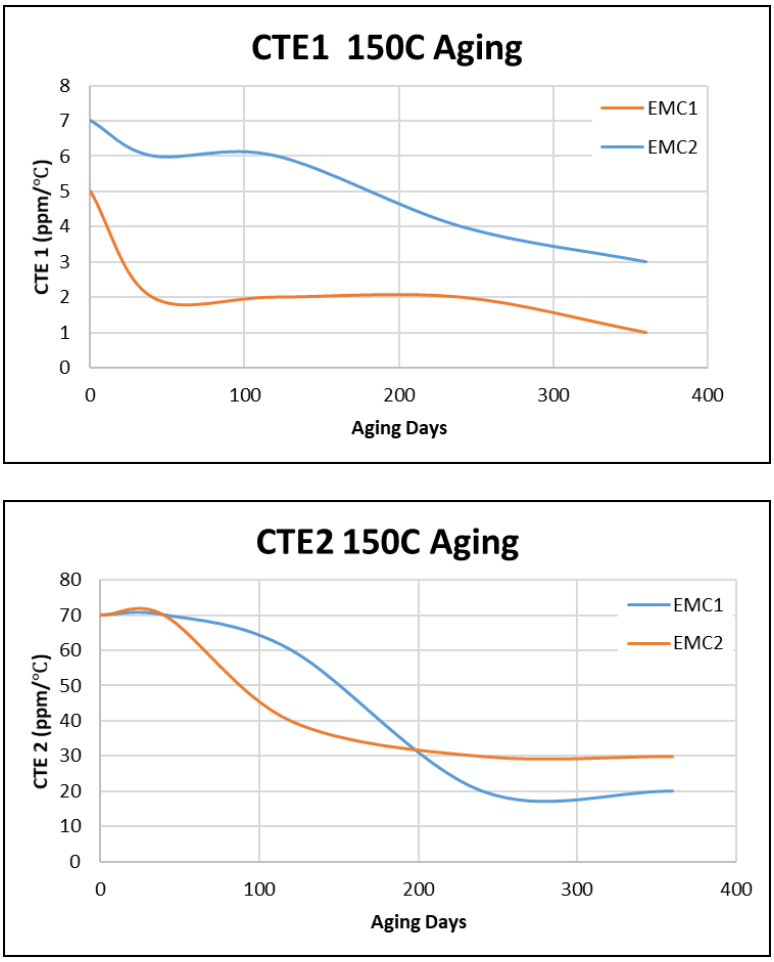

Figure 5-11 CTE Measurement for 150C Aging

5.5*Modeling of Viscoelastic Constitutive Behavior*

Frequency sweep tests are conducted on the EMC materials. The dynamic strain is set to 0.1, and an auto-tension setting with a static-to-dynamic ratio of 25% is applied. The temperature ramp ranges from 25℃ to 280℃, with a temperature increment of 10℃ per minute. The

equilibrium time at each temperature point is 2 minutes. The frequency sweep range spans from 0.1 to 10 Hz, with 5 points per logarithmic decade.

To analyze the viscoelastic behavior of the materials, the concept of time-temperature superposition (TTS) is employed. TTS assumes that the effects of time and temperature on a thermorheologically simple (TRS) material can be characterized by a single parameter. By applying the time-temperature shift factor (a_T), the data obtained at various temperatures are horizontally shifted in the time domain until they align and merge into a single, smooth curve. This indicates that the master curve in the time domain is the same at different temperatures.

Using Laplace Transformation, the master curve can be transformed between the time and frequency domains. This means that the master curve over a long-time domain can be obtained from the master curve over a narrow frequency domain. By employing the shifting factor,

mastering the curve over a wide range of frequencies can be generated from multiple curves obtained through DMA frequency scan data.

Figure 5-12 illustrates the generation of the master curve for EMC1 in its pristine condition using the TTS principle. The reference temperature for this analysis is set to 125℃.

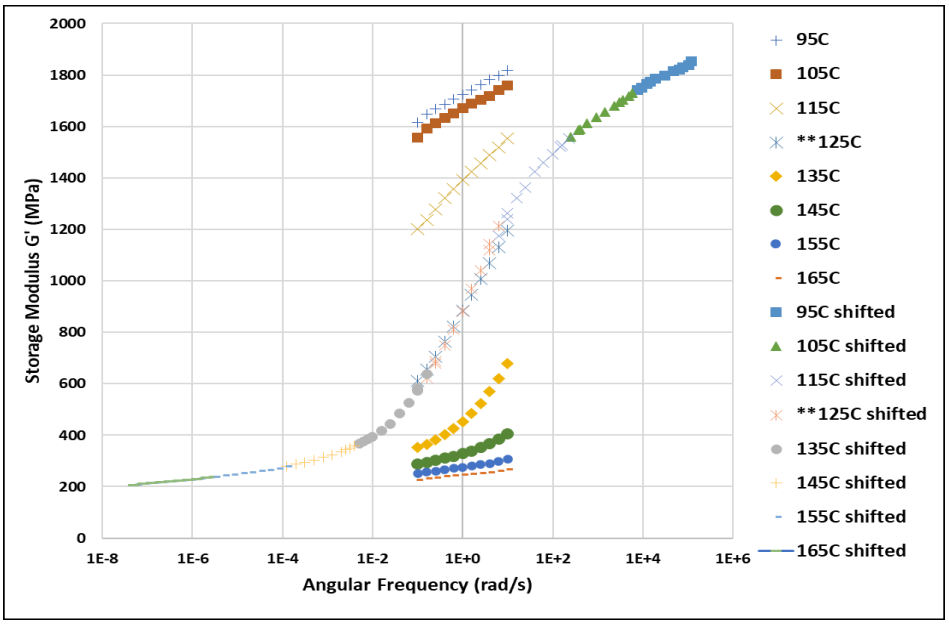

Figure 5-12 Master Curve Generation by TTS

Shift factor could be fitted by Williams-Landel-Ferry (WLF) Equation with following form (Figure 5-13):

$$\log(a_T) = -\frac{C_1(T - T_r)}{C_2 + (T - T_r)} \qquad (5\text{-}1)$$

Where $\log(a_T)$ is the decadic logarithm of the WLF shift factor, T is test temperature, T_r is a reference temperature chosen to construct the master curve. C_1 and C_2 are empirical constants.

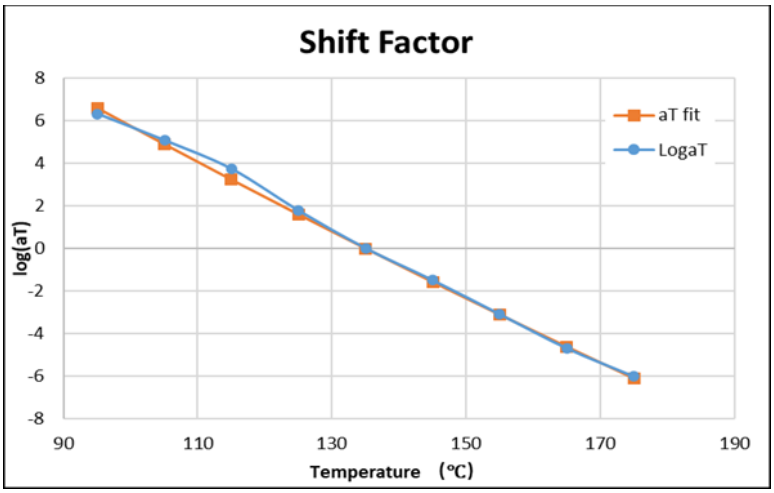

Figure 5-13 Shift Factor Fitted by WLF Equation

In Figure 5-14, the master curves of EMC1 under 100℃ aging conditions from pristine to one year are plotted in the frequency domain. It can be observed that the storage modulus at extreme high frequencies does not show significant changes as the aging time increases. However, in the median and low frequency range, where materials are typically subjected to working conditions, the storage modulus increases with aging time. This behavior can be attributed to the higher level of cross-link density that develops during the aging process, resulting in increased stiffness and a potential stiffness-brittleness conflict.

In the case of EMC1 under 150℃ aging conditions, as shown in Figure 5-15, the degradation behavior is different. The storage moduli at high frequencies still remain close to each other. However, in the median and low frequency range, which corresponds to the working conditions, the storage module increases from pristine to 80 days of aging and then decrease from

80 days to one year. This indicates that significant material degradation occurs after 80 days of aging under these conditions.

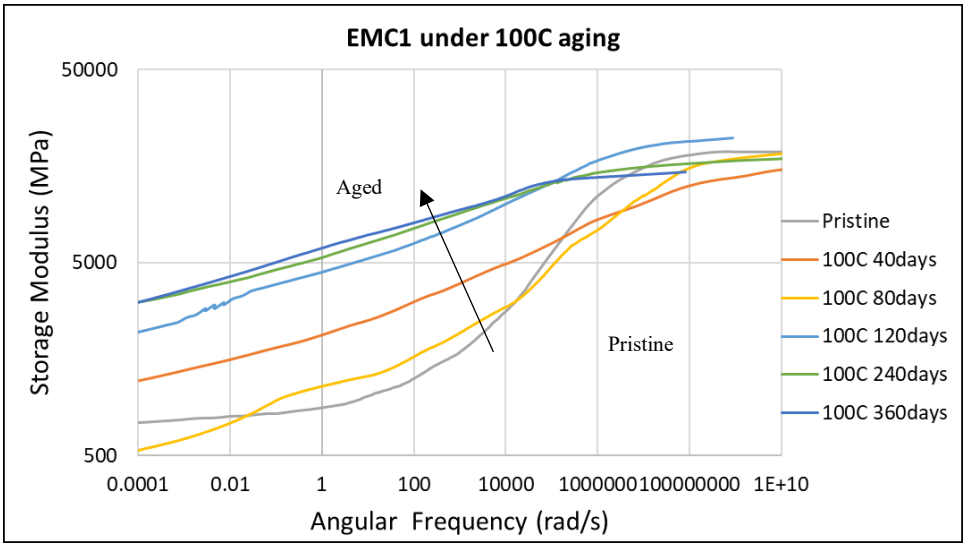

Figure 5-14 Master Curves of EMC1 under 100C aging

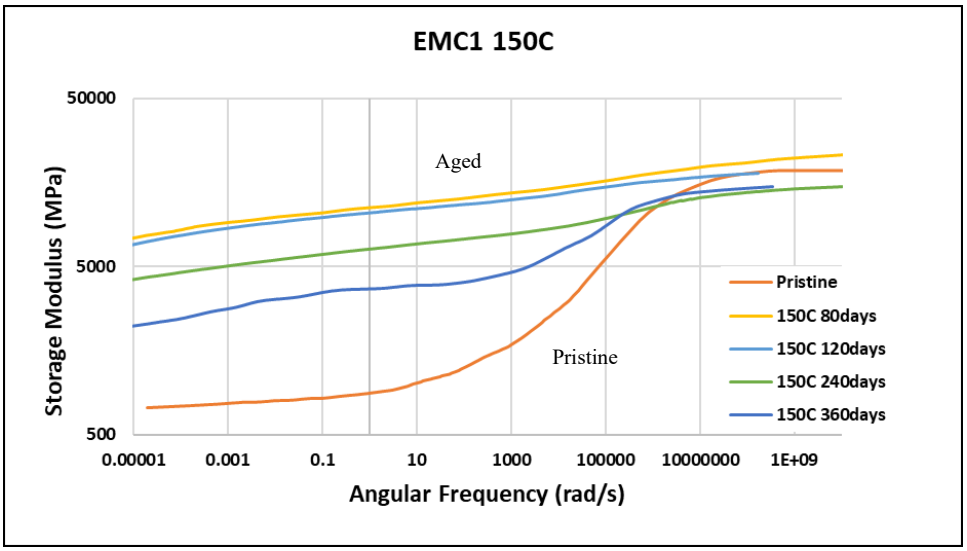

Figure 5-15 Master Curves of EMC1 under 150C aging

The use of dimensionless Prony parameters has the advantage of generating a normalized time domain response with dimensionless Prony pairs, which allows for direct comparison of material behavior. By utilizing these normalized values, we can compare material properties across

different conditions and aging times. This is particularly useful for simulating material properties in a finite element framework.

In Figure 5-14, the normalized relaxation modulus over the time domain is calculated using the dimensionless Prony pairs. The plot illustrates that the modulus at extreme high and low time periods does not exhibit significant changes as the aging time increases. However, in the median time region, where materials are predominantly subjected to working conditions, the modulus increases significantly with aging time. This indicates an increase in stiffness and a potential decrease in viscosity as the material undergoes aging. The changes in the median time region are particularly relevant as they reflect the behavior of the material under typical working conditions.

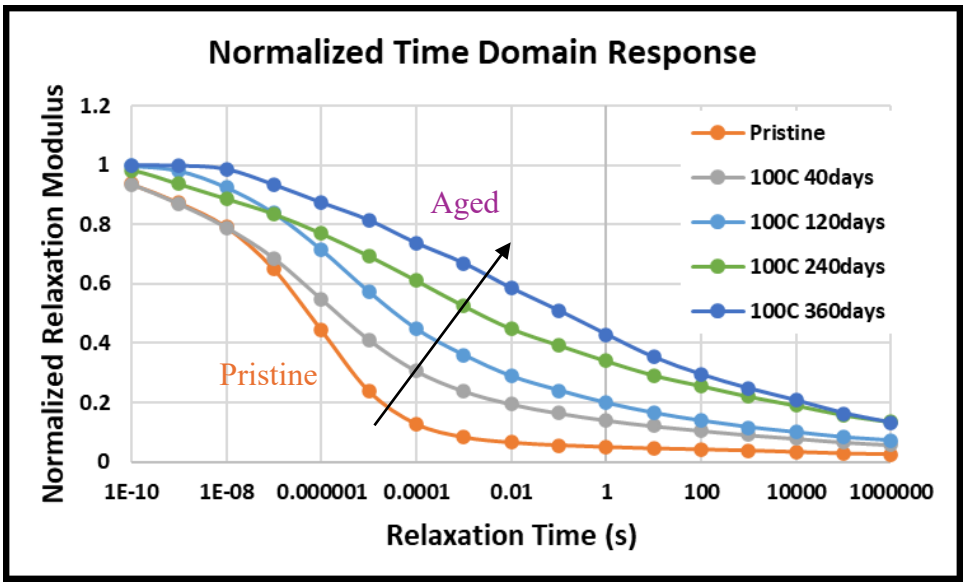

Figure 5-16 EMC1 Time Domain Relaxation Response

By obtaining the dimensionless Prony coefficients, we can construct the material response in the time domain in a normalized form for EMC2, as shown in Figure 5-16. The normalization of the relaxation modulus allows for easy comparison between different aging times. The results demonstrate that as the aging time increases, the curves become flatter, indicating increased stiffness of the materials. This observation is consistent with our previous findings. The differences

in the relaxation modulus are relatively small in the low and high time ranges but become more pronounced in the middle region. The advantage of normalizing the relaxation modulus is that it enables a straightforward comparison between different material responses, facilitating a better understanding of the aging behavior and its impact on the mechanical properties of the EMC materials.

Figure 5-17 displays the typical fitting results for the experimental data, showcasing the agreement between the fitted Prony pairs and the measured material response. The Prony pairs for EMC1 under 100℃ aging conditions are provided in Table 5-3. By determining the shift factors and constants, the master curves are generated at a common reference temperature. These shift factors and constants are essential for conducting finite element analysis and simulating the material properties accurately. The fitting process ensures that the generated master curves closely match the experimental data, enabling reliable predictions of the material behavior under various conditions and time scales.

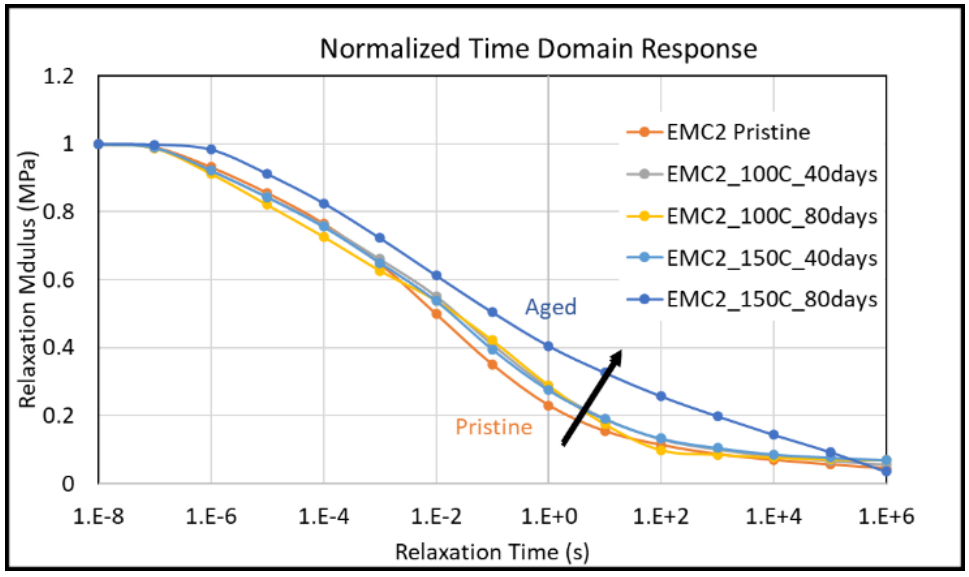

Figure 5-17 Response in Time Domain

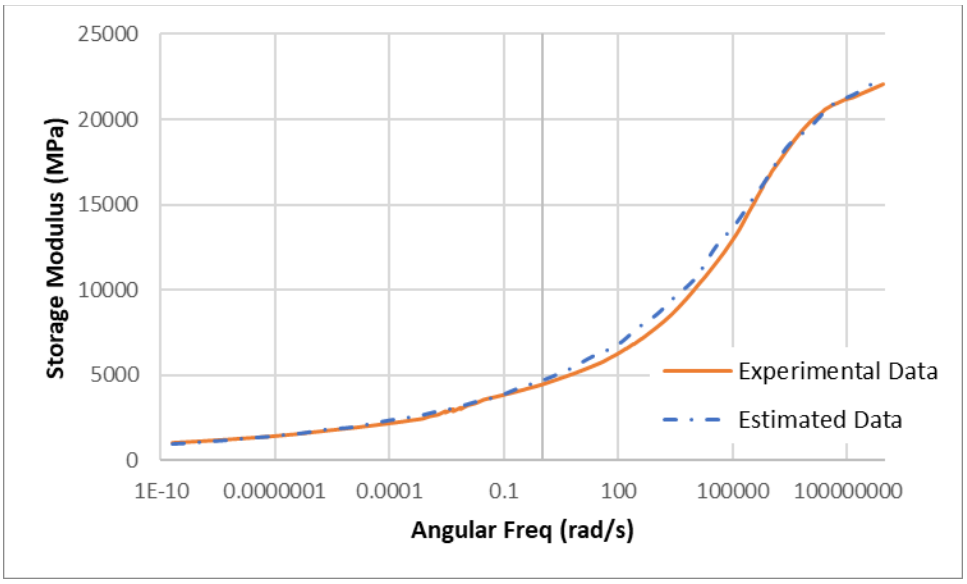

Figure 5-18 Typical Fitted Data by Prony Pairs

Table 5-3 Prony Constants for EMC1

EMC 1	Pristine	100C 40days	100C 120days	100C 240days	100C 360days
G_0(MPa)	20000	20000	22500	17500	15000
τi	gi				
1E-10	0.09	0.09	0.00	0.00	0.00
3E-10	0.00	0.00	0.00	0.05	0.00
5E-10	0.00	0.00	0.00	0.00	0.00
8E-10	0.00	0.02	0.00	0.00	0.00
1E-09	0.03	0.00	0.00	0.00	0.00
3E-09	0.03	0.03	0.04	0.02	0.00
5E-09	0.01	0.01	0.01	0.04	0.00
1E-08	0.04	0.04	0.00	0.00	0.00

5E-08	0.10	0.08	0.09	0.03	0.06
1E-07	0.05	0.01	0.01	0.02	0.00
5E-07	0.12	0.12	0.06	0.06	0.02
1E-06	0.12	0.04	0.09	0.00	0.06
5E-06	0.13	0.11	0.10	0.06	0.02
1E-05	0.08	0.03	0.01	0.02	0.01
5E-05	0.06	0.10	0.14	0.07	0.09
1E-04	0.04	0.00	0.00	0.00	0.00
5E-04	0.02	0.06	0.07	0.09	0.00
1E-03	0.01	0.01	0.01	0.00	0.08
5E-03	0.01	0.03	0.07	0.08	0.06
1E-02	0.01	0.01	0.01	0.00	0.00
5E-02	0.00	0.01	0.02	0.00	0.04
1E-01	0.00	0.02	0.04	0.07	0.05
5E-01	0.00	0.01	0.02	0.02	0.03
1E+00	0.00	0.01	0.01	0.00	0.04
1E+01	0.01	0.01	0.02	0.06	0.06
1E+02	0.00	0.01	0.02	0.00	0.01
1E+03	0.01	0.00	0.00	0.00	0.04
1E+04	0.00	0.01	0.02	0.04	0.03
1E+05	0.01	0.00	0.00	0.00	0.00
1E+06	0.00	0.01	0.02	0.03	0.05
1E+07	0.00	0.00	0.00	0.00	0.00

1E+08	0.00	0.01	0.01	0.03	0.03

5.6*Stress on Cu Wire with Evolution of EMC by Finite Element Analysis*

In this paper, CT scan technology is applied to obtain the true geometry of the packages. True geometry of the package is used for analysis purpose to achieve better accuracy and to identify critical location of the design (Figure 5-19). CT scanned data is used to formulate the Finite Element model. The framework has been well established. In this paper, a molded 32 pin QFN package with Cu wirebonds is analyzed. High quality scanning was performed on the part to get clear definition of different components such as leads, wirebond etc. Scanned data was then converted into FE based triangular mesh using different image processing method. Thermomechanical analysis is performed on the molded package to analyze the aging effect on stress-strain behavior of Cu wirebond.

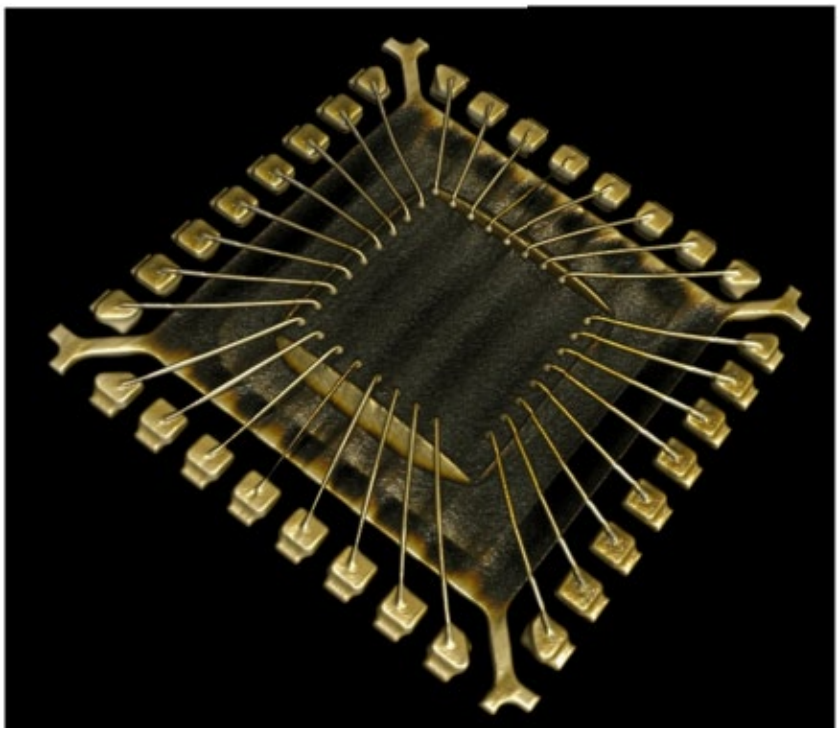

Figure 5-19 3D Reconstructed Package

Finite element analysis is conducted on the 32 pin QFN model. Quarter QFN model is constructed. The package has 1mil Cu wire bonded onto 0.9μm think Al pad. Leads, lead frame, wirebonds and pad are extracted separately. Dimension of components are shown in Table 5-4 . Linear elastic model is built firstly. Temperature ramp DMA data is imported as material properties of EMCs. Model simulates environment from room temperature to 175℃ (Figure 5-20). Stress-deformation relationship for effect of EMCs on Cu wire bond is investigated. Figure 5-21 shows for pristine EMC1 the Von Mises stress, which represent the shear effect of material, on Cu Wire from room temperature (b) to 175℃. At room temperature, there is no deformation. As temperature elevate, CTE mismatch causes stress over the wire bond (c).

Table 5-4 Model Dimension

Component	FEA Model
Chip (mm)	2.03 x 2.03
Ball Bond (μm)	70.95
Cu Wire (μm)	26.97
Packages(mm)	4.99 x 4.99

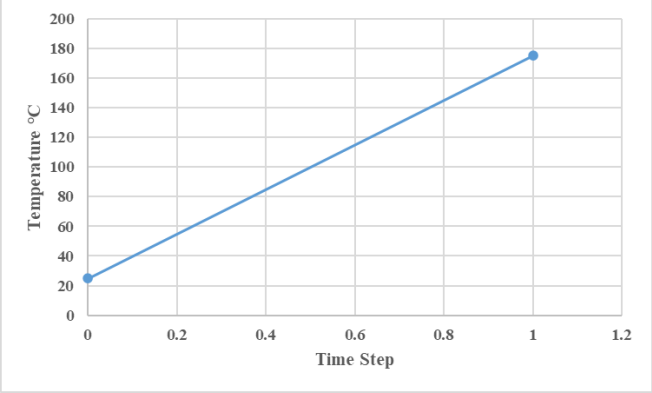

Figure 5-20 Temperature Profile

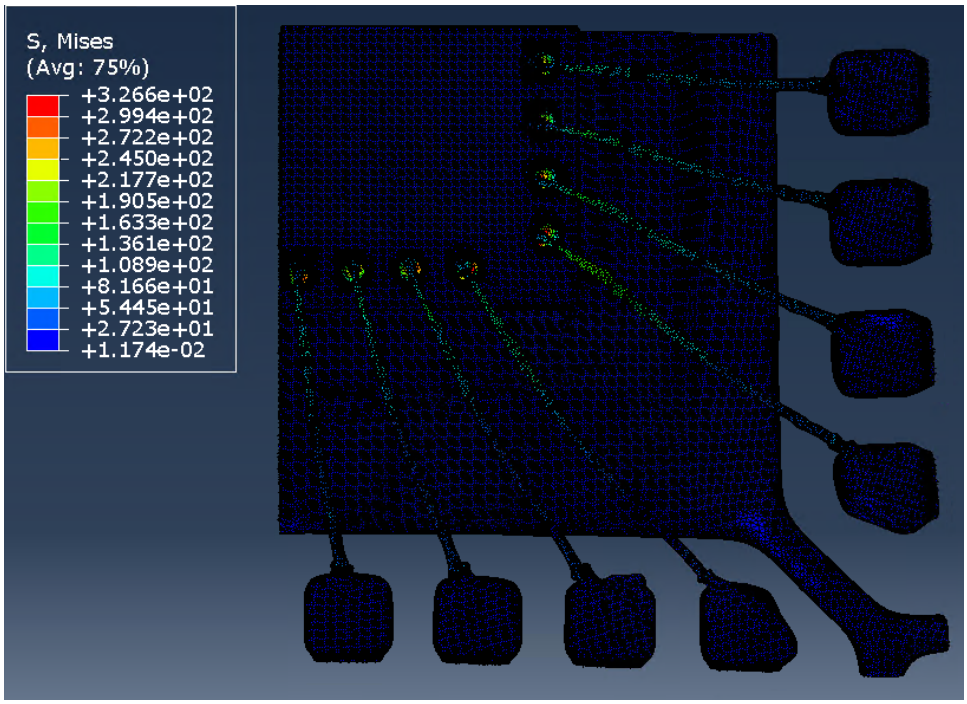

(a) Von Mises Stress on QFN without EMC

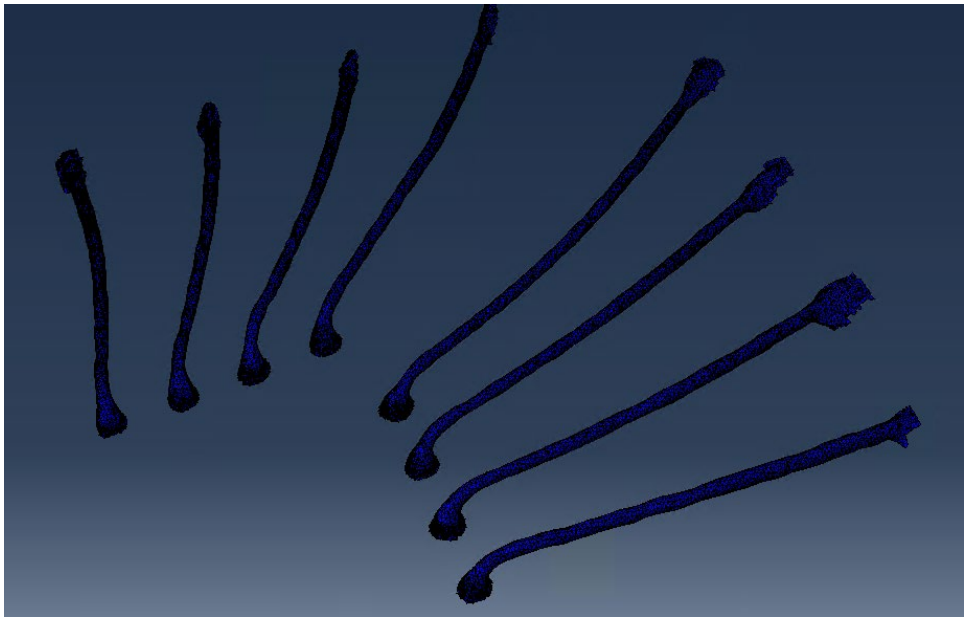

(b) Cu Wire at Room Temperature

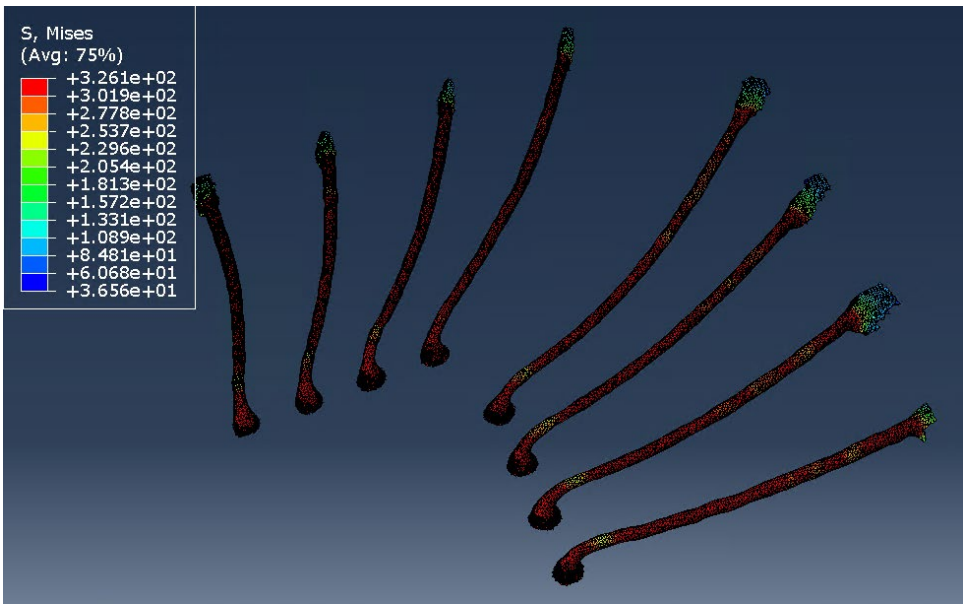

(c) Cu Wire Heated up to 175℃

Figure 5-21 Von Mises Stress on Cu Wire Bond in Heating Process

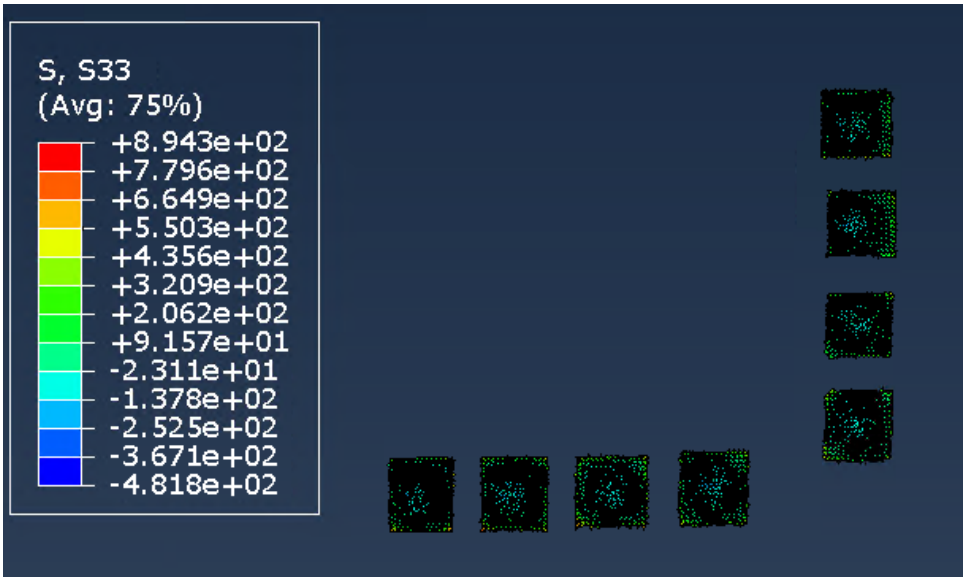

Figure 5-22 Normal Stress for Al Pad under Heating Process

One of the most significantly failure mode is the wire bond detach from Al pad. Pull tests are usually used to characterize the strength of bonding between Cu wire bond and Al pad. However, pull tests could only conducted for specific condition. Simulation results could predict

stress strain evolution as the function of time and aging condition. Comprehensively access the failure risk of wire bond. Figure 5-22 shows the normal stress on Al pad for pristine EMC1 from room temperature to 175℃, indicating the normal stress increases significantly as the environmental temperature increases. Figure 5-23 shows maximum normal stress on Al pad under Cu wire bond as the function of EMC1 aging days under 150℃ environment. It indicates that normal stress increases from 40 days to 120 days aging, increasing the failure risk of Cu wire bond.

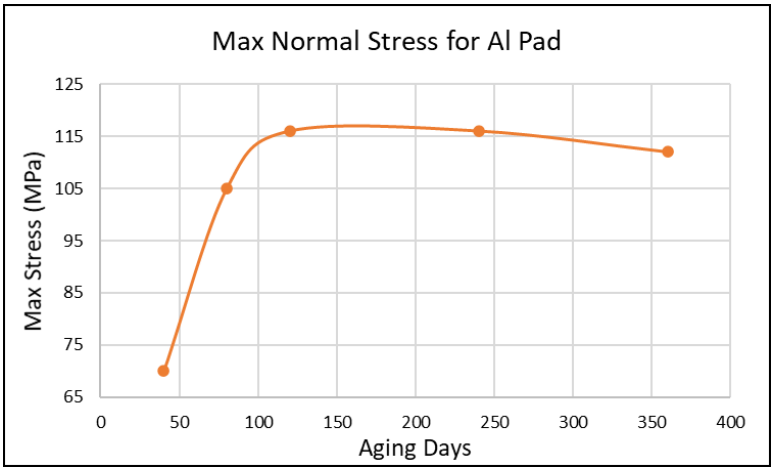

Figure 5-23 Normal Stress Evolution with EMC1 Aging Days

Summary and Conclusions

In this study, the experimental results of two developmental EMC materials under aging conditions have been discussed. The frequency scan cyclic loading tests were performed on the EMC samples to investigate their viscoelastic behavior. The obtained results clearly indicate changes in the cross-linked molecular structure of the materials when exposed to high temperature environments for an extended period.

Master curves were generated using the time-temperature superposition principle, which allowed for the characterization of the material behavior over a wide range of frequencies and time scales. The master curves in both the frequency and time domains showed flatter responses at higher temperatures, indicating the alteration of viscoelastic properties with increasing aging time.

An optimization framework was proposed to generate accurate and efficient Prony parameters, which are essential for characterizing the viscoelastic behavior of the materials. Two different types of Prony parameters were generated and discussed in the paper. Furthermore, a novel method for measuring the coefficient of thermal expansion (CTE) was developed using the same DMA setup. This approach eliminated the need for a traditional static setup or a separate TMA instrument. Calibration was performed to compensate for the thermal expansion of the fixtures during the temperature ramp test. The obtained CTE values were found to be close to the values provided in the material data sheet.

Overall, the paper presents valuable insights into the aging behavior and mechanical properties of EMC materials, offering a comprehensive understanding of their viscoelastic response and thermal expansion characteristics.

5.7 *Prony Coefficients Fitting in Optimization Framework*

In this section, we are going to discuss a novel framework for Prony Coefficients fitting. First of all, we transform the Prony series into Frequency Domain:

$$G'(\omega) = G_o + \sum_{i=1}^{N} G_i \frac{(\omega\tau_i)^2}{1 + (\omega\tau_i)^2}$$

$$G''(\omega) = \sum_{i=1}^{N} G_i \frac{\omega\tau_i}{1 + (\omega\tau_i)^2}$$

After that, we combine the storage modulus and loss modulus to complex modulus using Prony formulation:

$$G^*(\omega) = G_o + \sum_{i=1}^{N} G_i \frac{i\omega\tau_i}{1 + i(\omega\tau_i)}$$

$$subject\ to\ \tau_i \geq 0, G_i \geq 0, G_o > 0,\ \ i = 1 \ldots . N$$

Fit the model to experimental data collected over a wide frequency range using:

- Global optimization (MultiStart) to avoid poor local minima (100 initial points).
- Local refinement (lsqnonlin) for precise parameter estimation.

Since the storage modulus (G′) is typically an order of magnitude larger than the loss modulus (G″), model fitting often yields a good match for G′ but a poor fit for G″. However, G″ reflects the viscous behavior of the material, which is critical to understanding viscoelastic performance. To improve accuracy, the loss modulus is weighted more heavily in the loss function to account for data scaling and enhance the quality of the fit for G″.

In the next step, we investigated the optimal number of Prony terms. While it is commonly assumed that increasing the number of terms improves the fitting quality, our results show that this is not always the case (Figure 5-24). Interestingly, the best fit appears to occur when the number of Prony pairs per decade is 1 or 2, whereas the fit quality deteriorates when this number increases to 3, 4, or 5. This outcome contradicts the common assumption that increasing the number of terms always leads to a better fit. To understand this behavior, we consider that the fitting process is based on nonlinear least squares. Therefore, statistical inference methods, such as confidence intervals and t-tests, can be applied to assess the reliability and significance of the fitted parameters. This analysis may reveal issues such as overfitting or parameter instability when too many terms are introduced.

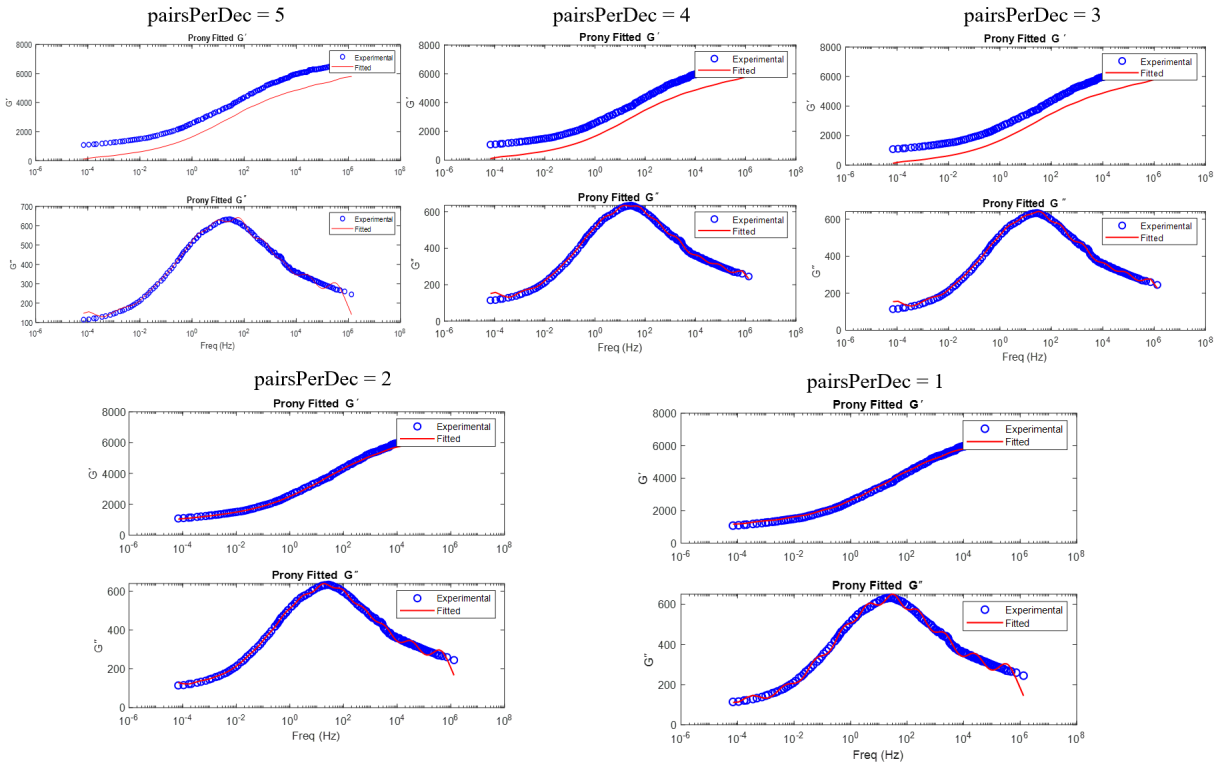

Figure 5-24 Prony Series Fitting as function of pairs per decades

Evaluation Criteria is applied as below:

- Gi Significant: The confidence interval (Gi_CI_L, Gi_CI_U) does not cross zero, and |t|>2.
- Tau Significant: both ends of the confidence interval are greater than 0, and |t|>2.
- Statistically Reliable: Both of the above conditions are satisfied.

Table 5-5 Statical inference for pairs per decades

pairsPerDec	Significant Pairs
1	11 out of 11
2	19 out of 22
3	9 out of 33 (poor fitting)
4	10 out of 44 (poor fitting)
5	8 out of 55 (poor fitting)

The rest pairs are not statistically significant and can be considered as noise compensation or overfitting artifacts.

In addition, we applied the Akaike information criterion (AIC) to evaluate the quality of Prony fitting. The AIC is defined as below:

$$AIC = mln\left(\frac{RSS}{m}\right) + 2k$$

Where $k = \text{Number of free parameters}$, m = number of data point, RSS = Residual sum of squares. The first term represents the goodness of fit and the second term represents the model complexity. Figure 5-25 shows that 2 pairs per decade offer the best fit. The results agree with the statistical inference methods such as confidence intervals and t-tests.

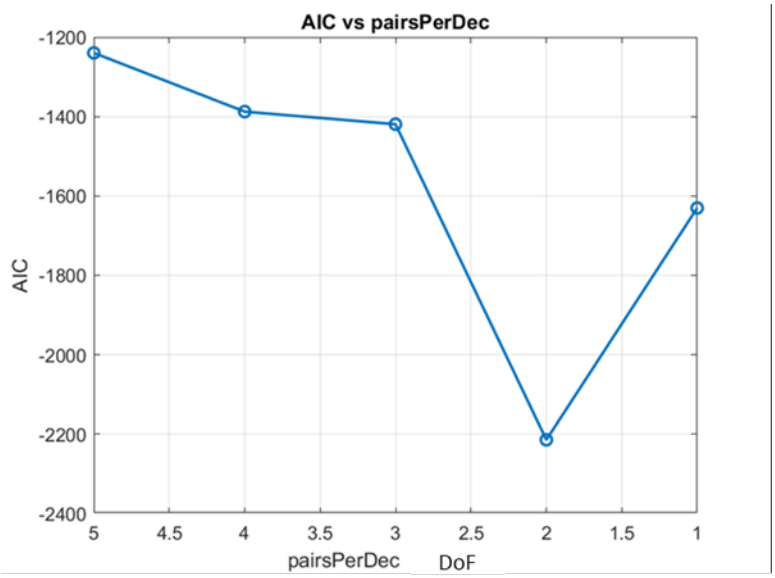

Figure 5-25 AIC vs. pair per decades

In this section, Statistical inference methods (e.g., hypothesis testing, Akaike Information Criterion (AIC)) were employed to evaluate the quality of fit and determine the optimal number of Prony terms, balancing model accuracy and complexity. Based on this analysis, 2 pairs per decade were found to be optimal.

Prony parameters without weighting are also reported. The algorithm performed reliably, and the conclusion remains valid: increasing the number of pairs per decade does not improve the fit.

5.8*Fatigue Performance Investigation for EMC*

Prior to the strain-controlled test, a load-extension curve is obtained for pristine EMC. The load-extension relation is obtained. Pristine samples are tested. Notch a=1.5mm, b=10mm. The gage length is 10mm. The pre-crack notch is cut by a diamond saw. The epoxy molding compound is a silica filler-filled crosslinking polymer. It is very stiff and rigid. The ultimate tensile stress is high while the toughness, which is defined by the area under stress-strain curve, is small. The toughness of the pristine sample is 0.2MPa. The toughness of 40days aged sample is 0.09MPa, and the toughness of 120days aged sample is 0.026MPa(Figure 5-24). If the notch is not cut properly. Fatigue behavior is very hard to observe.

A monotonic tension test (Figure 5-25) in 0.1mm/s is conducted to capture the load and extension relation. Small extensions result in significant load changes due to the high stiffness of the sample. The maximum load reaches approximately 180 N with an extension of 0.1 mm. For the displacement-controlled fatigue test, a displacement level of 0.06 mm was selected. Since the epoxy molding compound is a viscoelastic material, its properties are time-dependent, and fatigue frequency affects crack propagation. At low traveling speeds, the material exhibits greater strength and is harder to fail, whereas at high traveling speeds, it becomes more brittle and prone to breaking. The fatigue life of EMC varies significantly within a narrow strain range. The specimen fails in one cycle when the traveling distance is 0.1 mm. Conversely, at a traveling distance of 0.3 mm, the load shows no significant drop even after 20,000 cycles, which falls outside the low-cycle

fatigue scope. Therefore, this study focuses on low-cycle fatigue, necessitating careful selection of the traveling distance to remain within the elastic region.

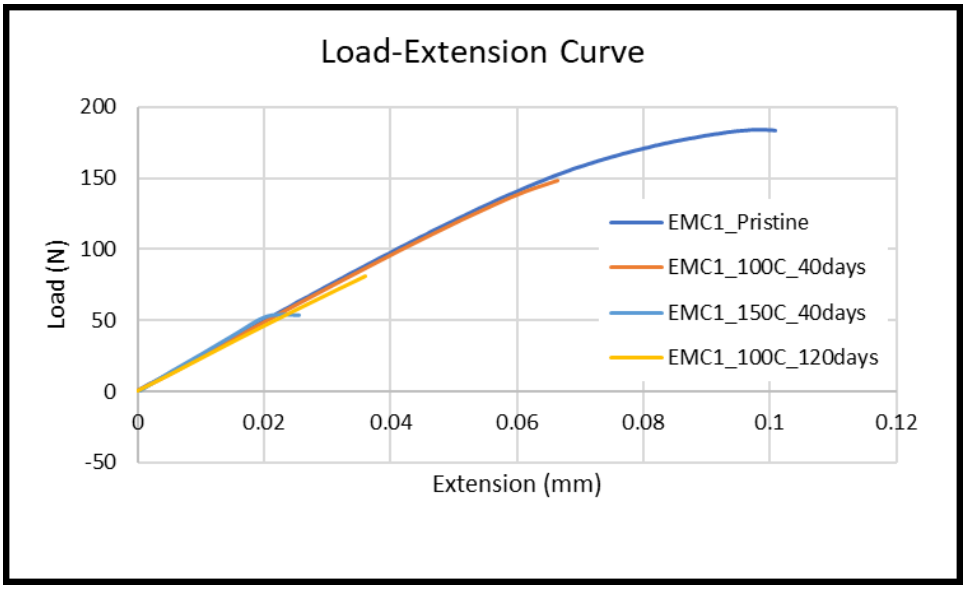

Figure 5-26 Load-extension Curves on EMC1

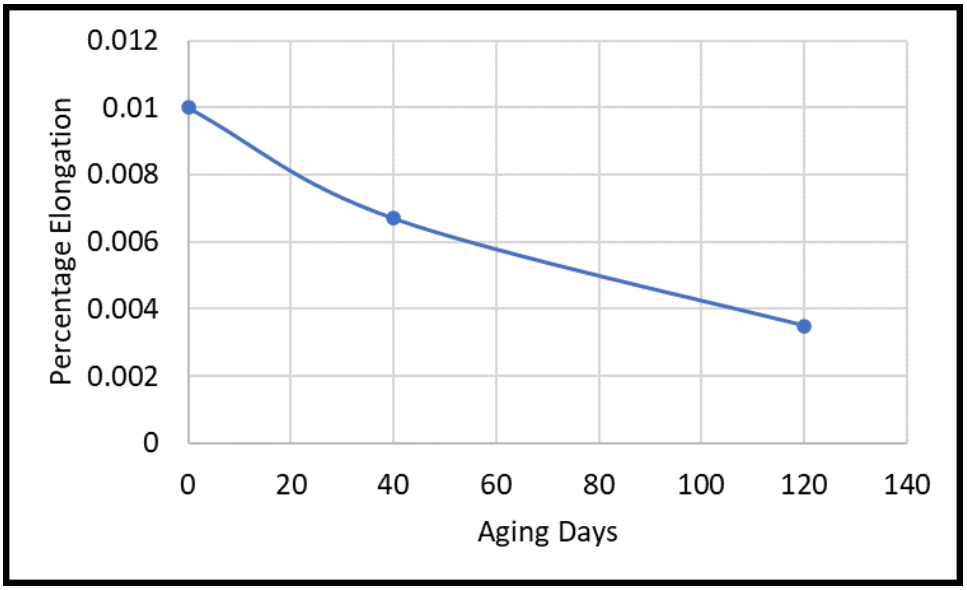

Figure 5-27 Percentage Elongation under 100C aging

Both ultimate tensile strength and percentage elongation significantly decrease with increased aging time, indicating the reduction of strength and toughness. After 40 days of aging at 100°C, the percentage elongation drops from 0.1 mm to about 0.07 mm. After 120 days, it

decreases to 0.035 mm. Under 150°C aging for 40 days, the percentage elongation decreases to 0.025 mm, indicating significantly increased brittleness in the 150°C aging environment. Consequently, fatigue strain must decrease as aging time and temperature increase.

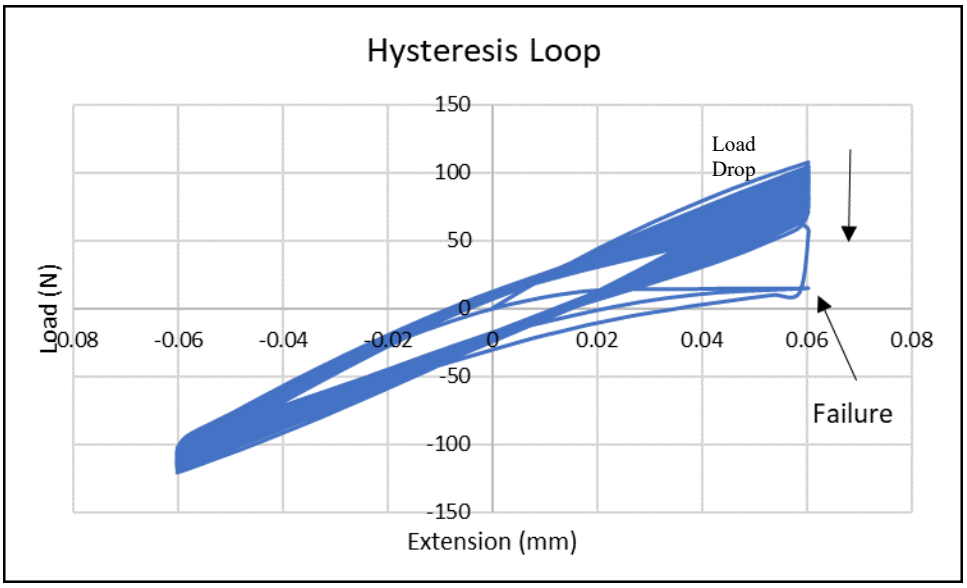

Figure 5-28 Hysteresis loop for EMC1

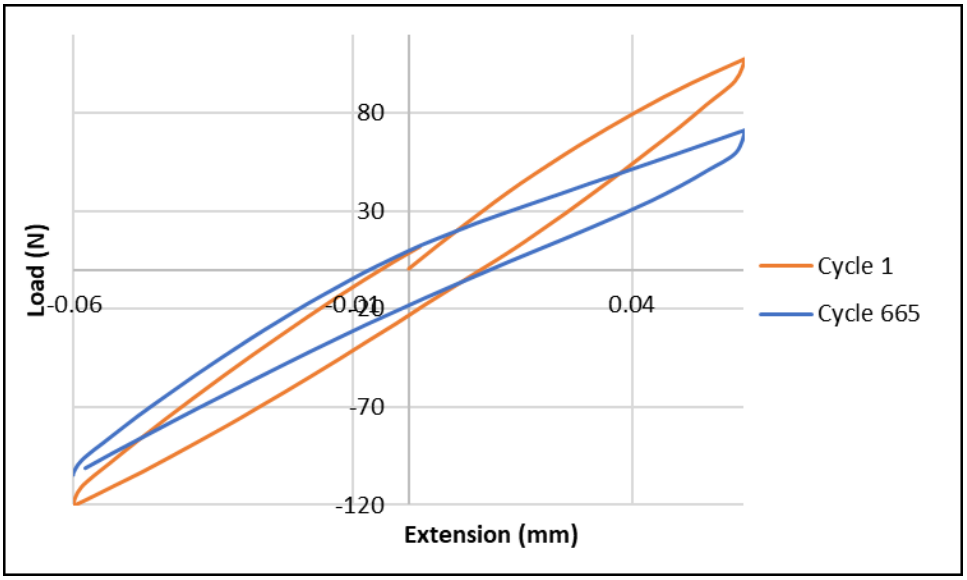

Figure 5-29 The hysteresis loop for the first and last cycle

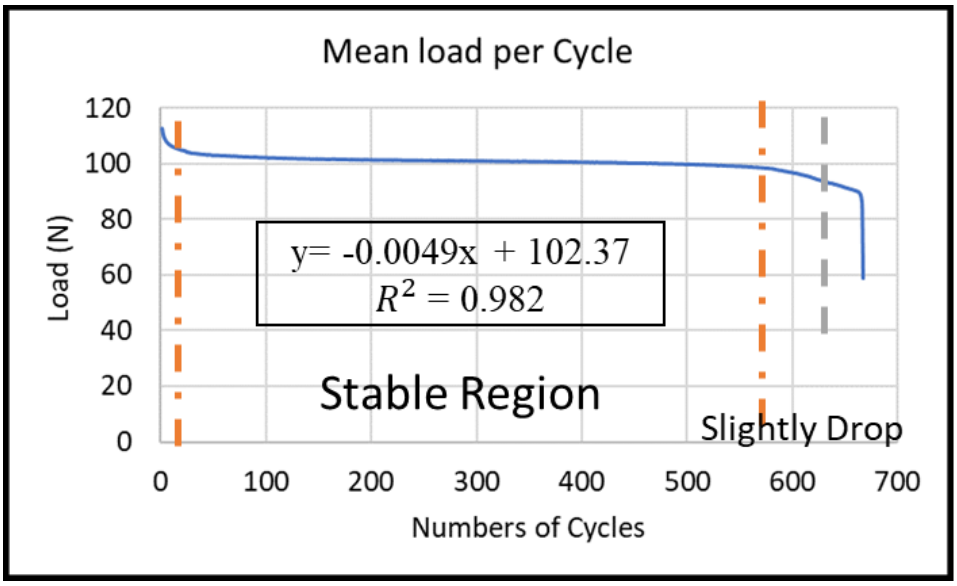

Figure 5-30 Load Drop for EMC1 vs Numbers of Cycles

The Hysteresis loop is shown in Figure 5-26. It shows that the EMC sample is conducted fatigue test under the extension at 0.06mm. The load for extension is about 100N. The load for compression is slightly more than 100N. Sample failed as the load significantly drop. The inelastic work of the cycle is defined as the enclosed area within the hysteresis loop. MATLAB was implemented to compute the parameter. The hysteresis loop for the first and last cycle are showing in Figure 5-27. The loop tilted. Both tension and compression load dropped. Load amplitude per cycle is showing in Figure 5-28. Figure 5-28 shows the average load amplitude, which is mean of compression plus tension, per cycle. The load drops slightly in the first couple of cycles from 115 to 102N. It is stable to 520 cycles. The stable region indicates material is brittle and sensitive to the notch. If it is ductile, load would keep decreasing. The trendline of load for stable region is fitted. The load slightly decreases from 520 cycles to 580 cycles. The load significantly decreases in the last hundreds of cycles and the specimen failed.

Stress σ could be computed by load and cross section area. Equation (3-17)(3-18) are applied to calculate the stress intensity factor. a/b is 0.14 in this test. Stress is defined by the applied

load divided by cross-section area. The stress intensity factor drops from 1 to 0.8 from the beginning to 666 cycles.

The hysteresis loop of EMC2 under pristine condition is showing in Figure 5-30. The controlled strain is 0.04mm, which is 0.4%. Specimen failed after 1593 cycles. The initial load for tension is about 100N. The compression load is 105N, which is slightly larger than the tension load. The tension load prior to failure is 83N, about 20% smaller than steady state.

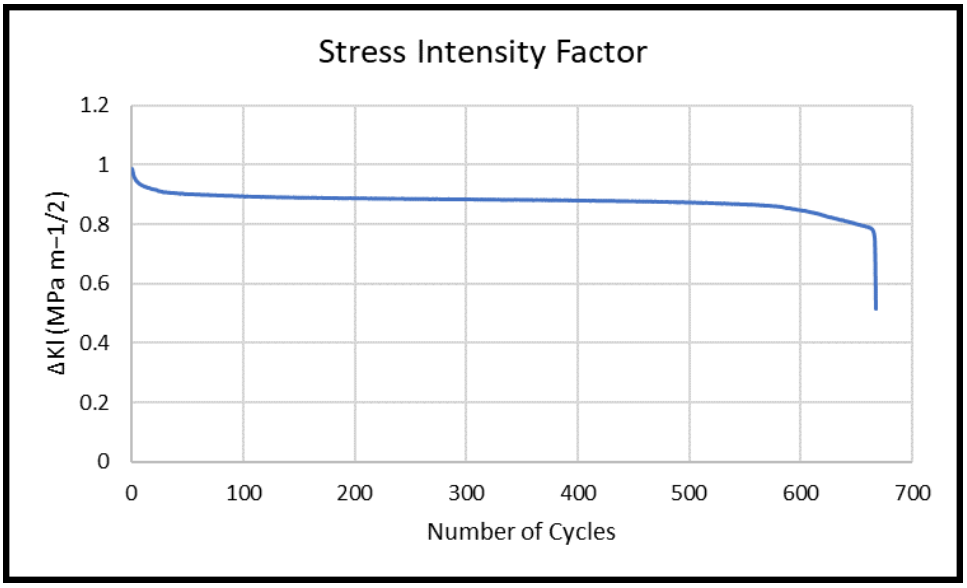

Figure 5-31 $\boldsymbol{\Delta K}_{I}$ Drops as Number of Cycles

Load amplitude, which is the average of max and min loads, and inelastic work per cycles for EMC2 under pristine are showing in Figure 5-31. The amplitude of load per cycle as the function of strain Figure 5-31(a) depict the variations in the maximum load with the cycle number at different strain levels. The initial maximum load at cycle one increased with the controlled strain level. Under the controlled strain levels of 0.3%, 0.35%, 0.4%, 0.5%, 0.6%, the initial maximum loads are 140N, 124N, 101N, 95N and 73N. Load per cycle could be divided by two regions: stable region and the region prior to fail. It is also worth mentioning that the obvious fracture was not observed for all samples during the stable region. Take the strain 0.4% as an example, between 0

to 1400 cycles, load slightly drops from 101N to 100N. Then load significantly drops to fail in a few cycles.

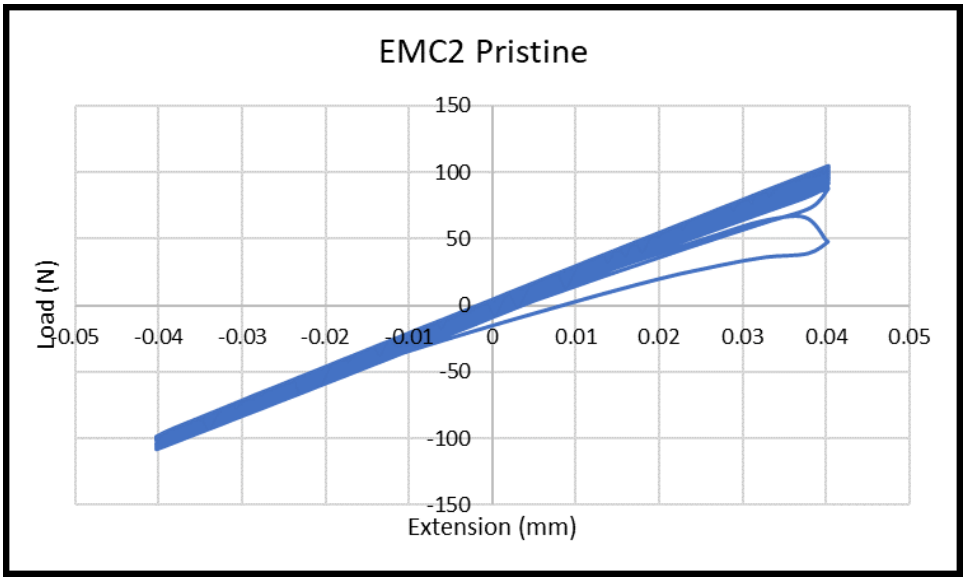

a) Hysteresis Loop for EMC2 under Pristine Conditions

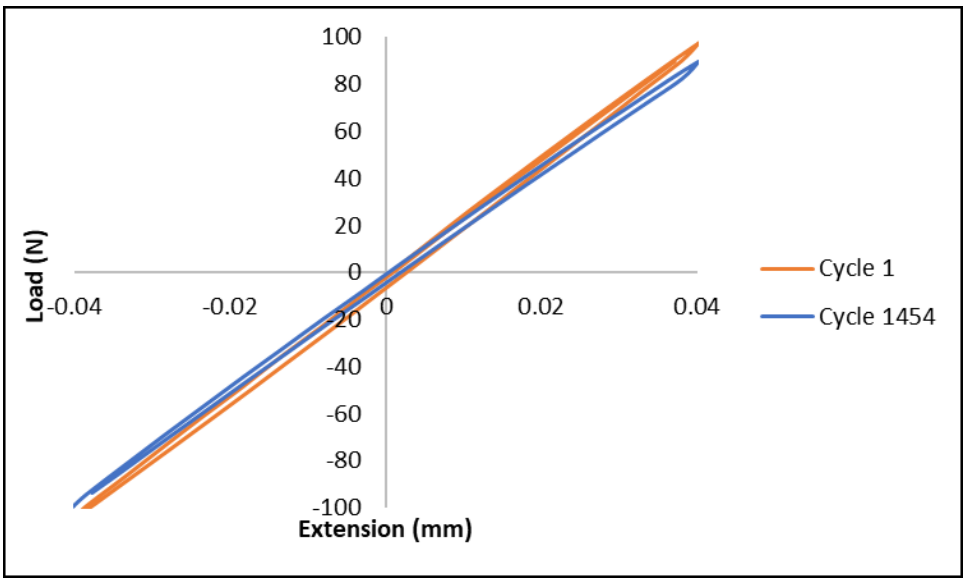

(b) Hysteresis Loop for the First and Last Cycle

Figure 5-32 Hysteresis loop for EMC2 under pristine condition

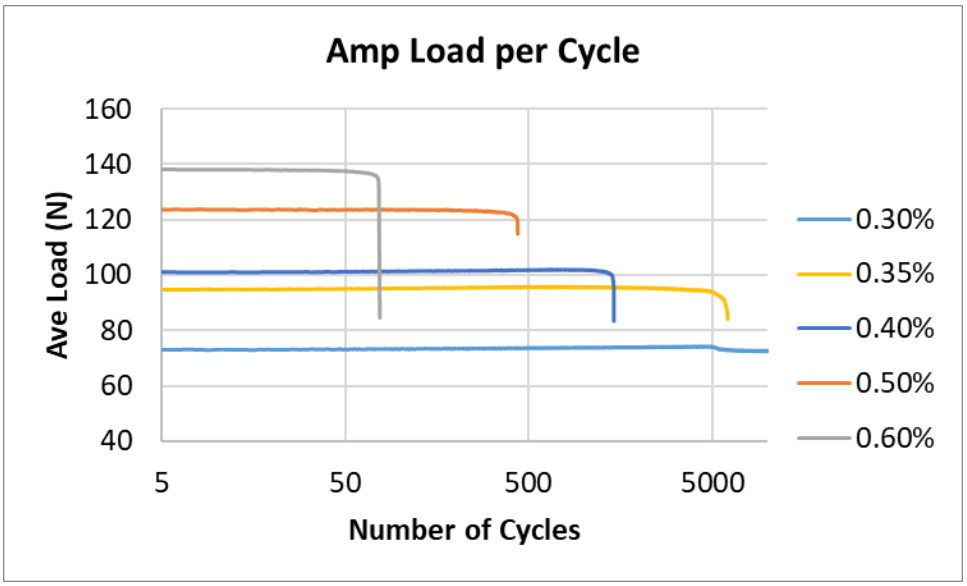

(a) Load Amplitude per Cycle for EMC2

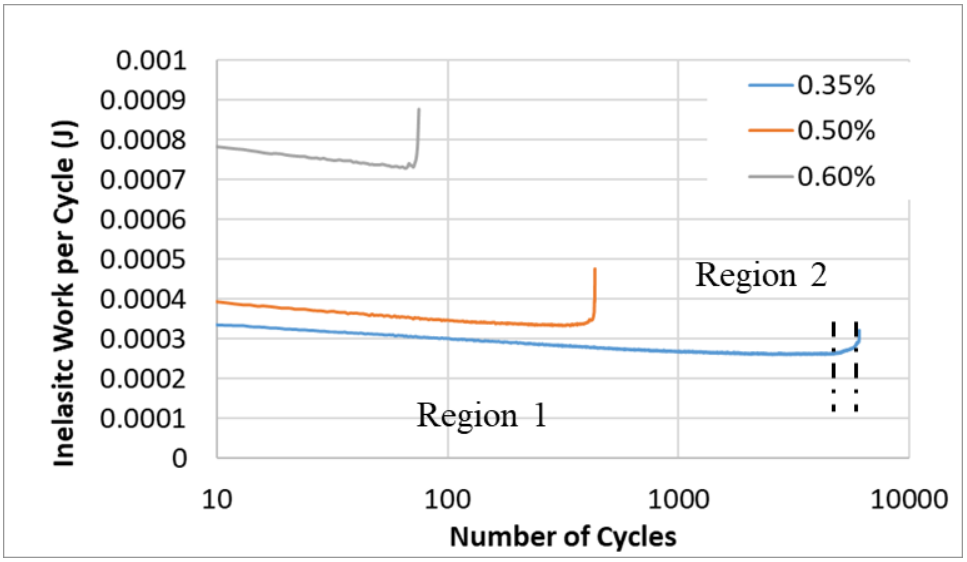

(b) Inelastic Work per Cycle for EMC2

Figure 5-33 Load amplitude, stress intensity factor and inelastic work per cycles for EMC 2 pristine

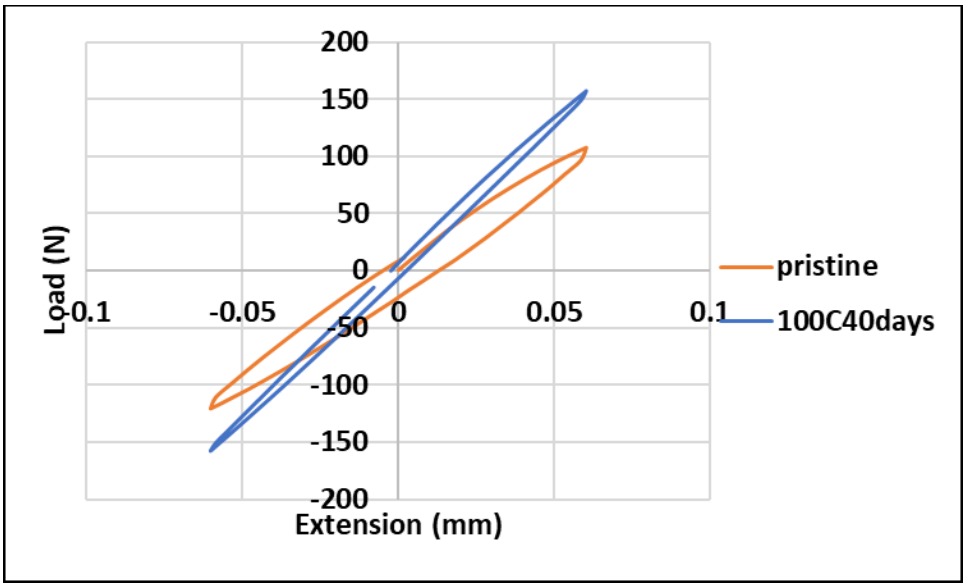

Figure 5-34 The first cycle of EMC 1 for pristine and 100C 40 days aging

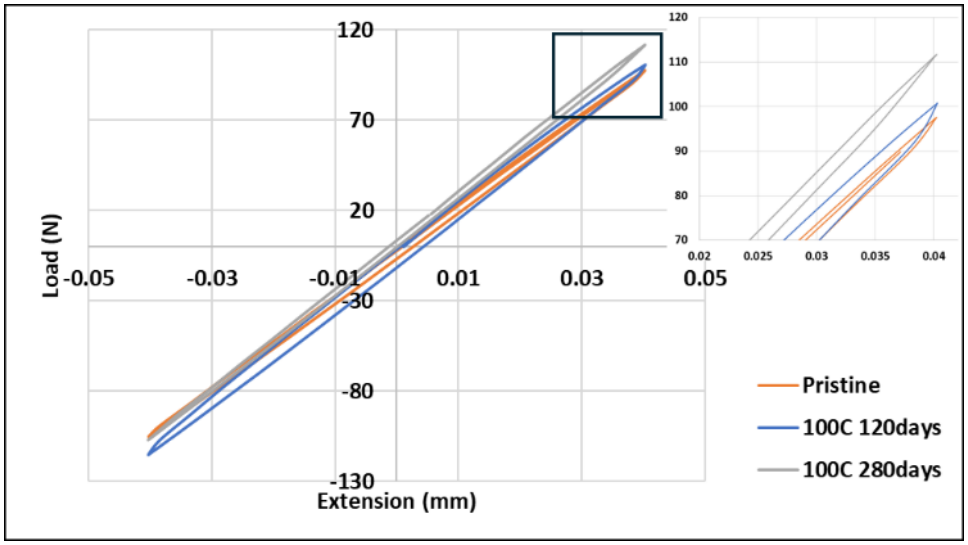

Figure 5-35 The first cycle of EMC 2 for pristine and 100C 120 days and 100C 280 days aging

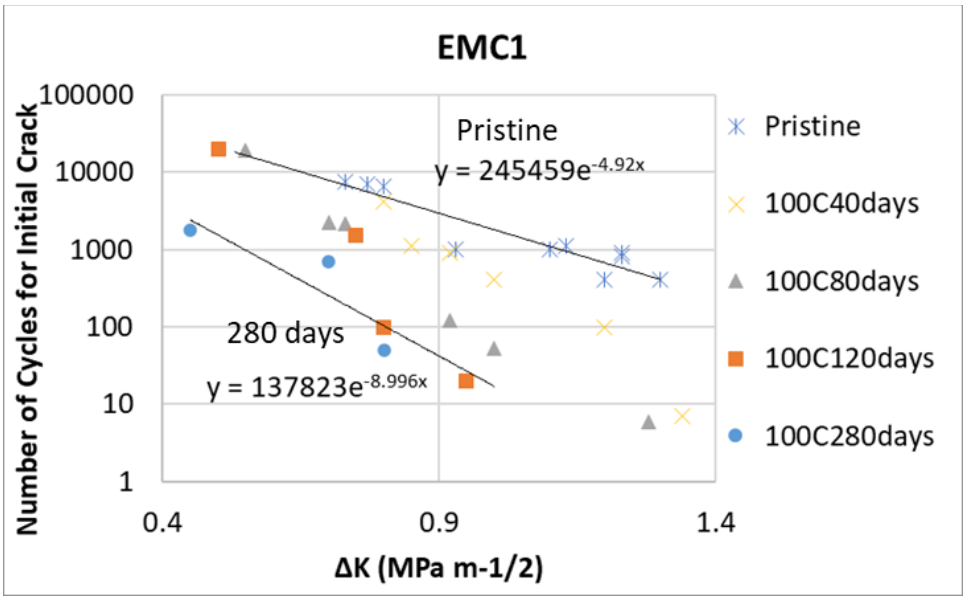

Figure 5-36 ΔK vs number of cycles for initial crack for EMC1

The stress intensity factor is showing a similar trend. It is about 0.9 in the first 1300 cycles. It slightly drops to 1400 cycles and significantly drops in the last few cycles. The inelastic work per cycle (Figure 5-31 b) depicts the evolution of the inelastic work over the fatigue life at the strain level of 0.35%, 0.5% and 0.6%. It drops significantly in the first hundred cycles. The steady-state region continues until ultimate failure, which is indicated by a significant spike in last few cycles. Figure 5-31 b compares the evolution of the inelastic work under 3 different strain levels. Higher strain level resulted in increased inelastic work in the steady region. As a result, more damage occurred in every cycle, leading to a shorter failure life.

EMC2 shows smaller energy storage in hysteresis area compared with EMC1. Both materials show much better fatigue resistance at 100C aging than 150C aging environment. The data for samples under 150C aging is difficult to obtain due to the brittleness. The comparison of first cycle for EMC 1 and EMC 2 under different aging conditions are showing in Figure 5-32 and Figure 5-33.

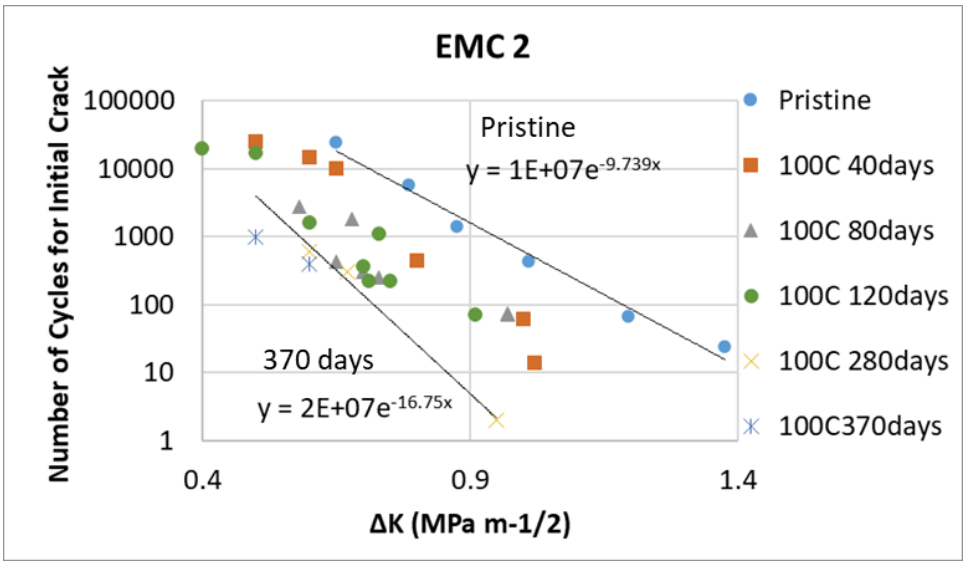

Figure 5-37 ΔK vs number of cycles for initial crack for EMC2

The aging process increases the stiffness of the material, which can be attributed to the increased cross-linking level of the epoxy resin. For EMC 1, this results in greater stiffness following aging, accompanied by a reduction in inelastic work. At a displacement level of 0.6 mm, the maximum load for a pristine sample is 102 N. However, after 40 days of aging at 100°C, the maximum load increases to 157 N, representing a 50% increment. Concurrently, the inelastic work per cycle significantly reduces as the area decreases.

In contrast, EMC 2 shows minimal differences before and after aging, indicating negligible changes in its properties. At a displacement level of 0.4 mm, the maximum load increases slightly from 101 N to 110 N after 280 days of exposure to the 100°C environment, only a 10% increase. This suggests that EMC 2 has better resistance to the effects of aging compared to EMC 1.

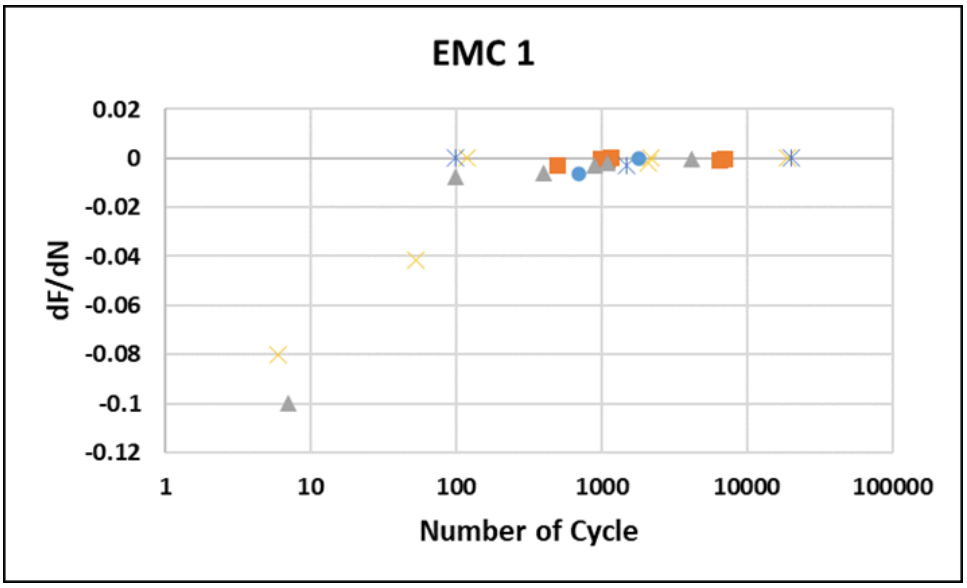

Figure 5-38 Load drop rate versus number of cycles for EMC 1

ΔK as the number of cycles for initial crack for both EMCs in high temperature long term exposure are showing in Figure 5-34 and Figure 5-35. There is a fatigue resistance band for EMCs. EMC1 shows a larger variance than EMC2. ΔK for both EMCs decreases logarithmic as number of cycles. Longer the aging time decreases the ΔK at certain number of cycles, indicating the increased brittleness of EMCs. The upper and lower bonds for both EMCs are drawn. It suggests that EMC 1 has lower aging resistance compared to EMC 2.

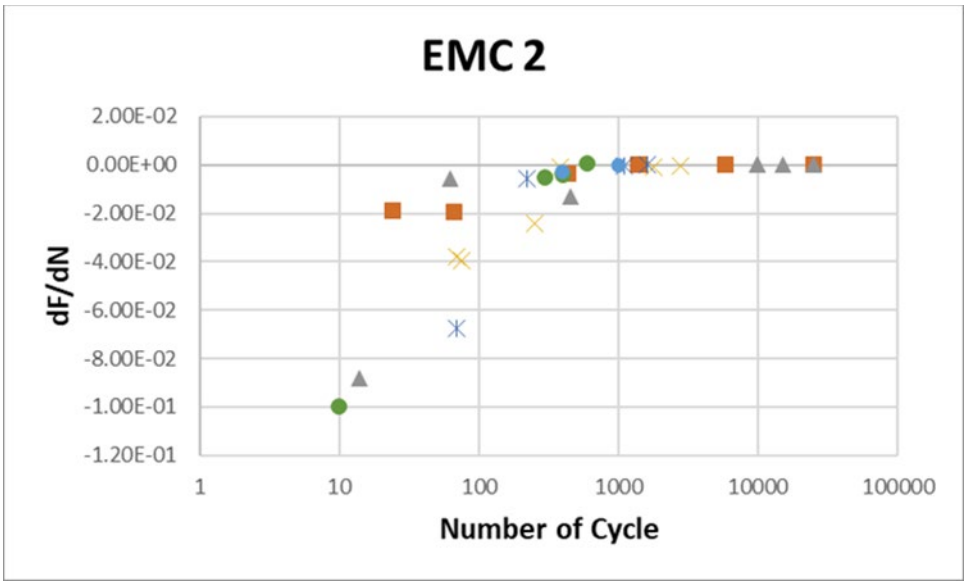

Figure 5-39 Load drop rate versus number of cycles for EMC 2

Load drop rate versus the number of cycles is plotted in Figure 5-36 and Figure 5-37. It indicates a correlation between the load drop rate and the number of cycles to failure for both EMC 1 and EMC 2. Specifically, the load drop rate tends to hover around zero when the number of cycles to failure exceeds 500. Conversely, within the initial 500 cycles, the load drop rate decreases as the number of cycles decreases. Consequently, it can be inferred that the strain-controlled fatigue test aligns with the outcomes of a stress-controlled fatigue test when the number of cycles to failure is substantial. Thus, S-N curves are plotted in log-log form for both EMC1 and EMC 2 (Figure 5-38 and Figure 5-39). The stress-life relationship appears linear in this log-log representation, signifying the elastic nature of the materials.

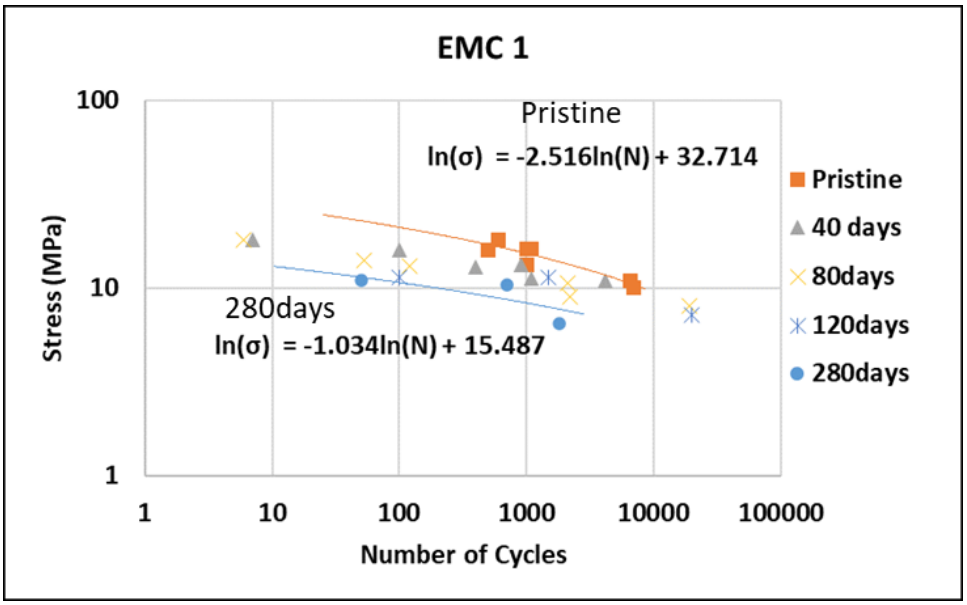

Figure 5-40 S-N Curves for EMC 1 under various aging exposure

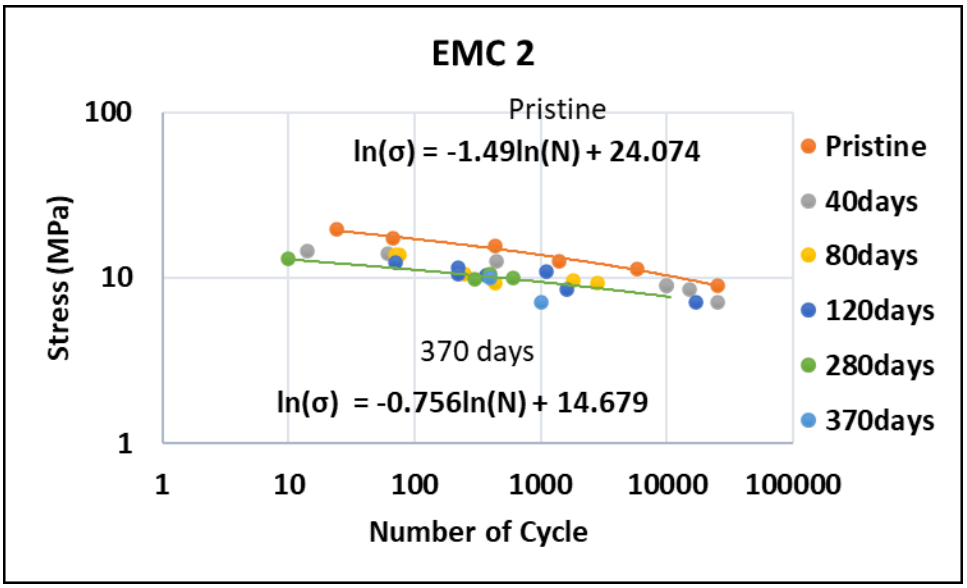

Figure 5-41 S-N curves for EMC 2 under various aging exposure

The linear relation is transformed from ***ln*** to ***lg*** to fit the Basquin equation. The parameters of pristine and 1-year aged conditions for Basquin equation are shown in Table 5-5. The findings reveal that EMC 1 exhibits a larger fatigue band compared to EMC 2, suggesting a lower fatigue resistance in EMC 1. The elastic fatigue hypothesis is perfectly accepted. S-N curves could be input for finite element analysis model.

The aging effect of material parameters a and b for Basquin equation is plotted in Figure 5-40 and Figure 5-41. Both parameters a and b evolve significantly within the first 40 days and then stabilize as aging time increases. Although the fatigue performance of EMC 1 and EMC 2 differs considerably under pristine conditions, these parameters seem to converge to a similar values as aging time progresses, indicating a convergence to a fatigue limit.

Table 5-6 The parameters for Basquin equations for EMC 1 and EMC 2

EMC 1	a	b
Pristine	-1.09268	14.20751
280days	-0.44906	6.725919

EMC 2	a	b
Pristine	-0.6471	10.45521
370days	-0.32833	6.375009

Summary and Conclusions

This research investigates the fatigue properties of two epoxy molding compounds (EMCs) when subjected to long-term high-temperature exposure using a strain-controlled method. It is demonstrated that the strain-controlled and stress-controlled methods are equivalent for EMCs. The elastic fatigue hypothesis is validated and accepted. The study provides insights into the evolution of the hysteresis loop, load amplitude per cycle, and inelastic work. It also explores the stress intensity factor as a function of the number of cycles for initial crack formation in both EMCs under various aging conditions.

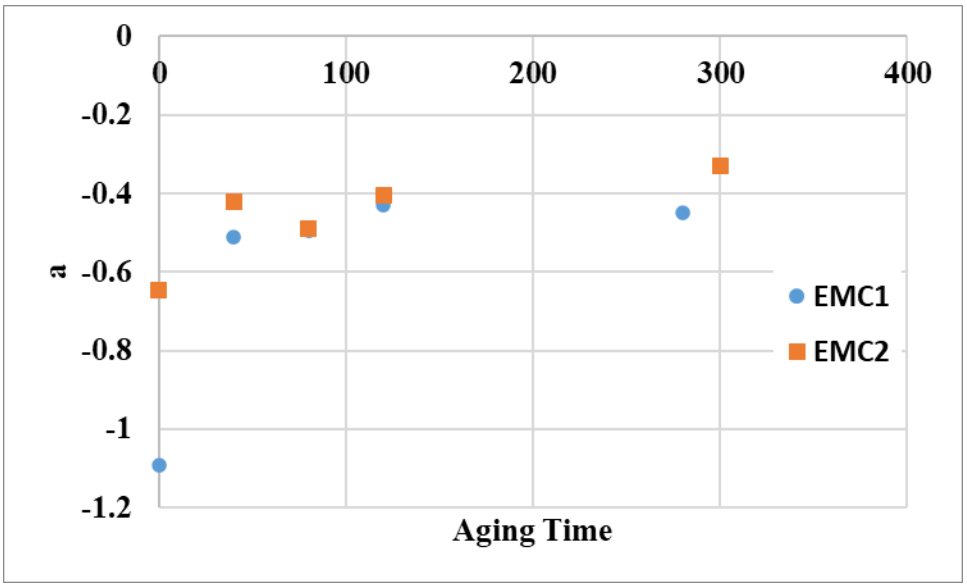

Figure 5-42 Evolution of parameter a under various aging exposure

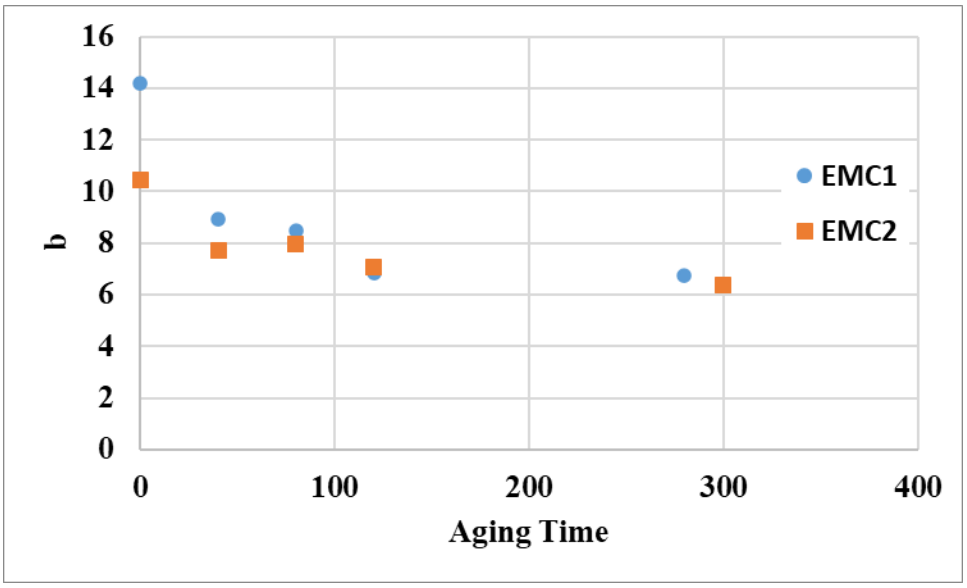

Figure 5-43 Evolution of parameter b under various aging exposure

EMCs, being thermoset polymers filled with silica fillers, exhibit brittle and stiff behavior. Increased cross-linking and oxidation boundary layers further enhance the brittleness and stiffness of the material, leading to decreased fatigue resistance. Aging significantly impacts the percentage of elongation, with the controlled strain slightly decreased to considerably improve the fatigue life of the materials. The materials remain rigid for hundreds or thousands of cycles and fail in the last

few cycles, complicating the prediction of fatigue life. Therefore, increasing the stable region is critical to enhancing fatigue resistance.

The study also reveals that the load drop rate remains around zero during the stable region. The inelastic work does not change significantly in the stable region but dramatically spikes just before failure. The load drop rate versus the number of cycles indicates that the strain-controlled fatigue test aligns with the outcomes of a stress-controlled fatigue test when the number of cycles to failure is substantial. S-N curves are plotted and reported, serving as a metric for characterizing fatigue performance, which can be used to construct a model for EMCs fatigue performance. The Basquin equations are fitted, and the evolution of Basquin parameters are reported, indicating the fatigue performance converge to an existing limit as aging time progresses.

Chapter 6 Magnetically-oriented Anisotropic Conductive Epoxy (ACA)

The primary causes of fatigue failure of electronic devices are high-temperature variations in electronic packages, particularly during the operation of high power-density devices or in the presence of harsh environmental conditions. Flexible Hybrid Electronics (FHE) utilized in automotive settings may encounter prolonged exposure to elevated temperatures, potentially impacting product reliability. The extended operation in high ambient temperatures poses challenges to the mechanical robustness and reliability of both bulk materials and interfaces. The future advancements in electronics hinge on the development of easily customizable devices and systems, allowing quick and cost-effective manufacturing and integration on diverse multifunctional substrates, possibly in a conformable manner. This paper explores the use of magnetically aligned Anisotropic Conductive Epoxy (ACA) as the foundation for manufacturing flexible and stretchable electronics, employing a rapid and reconfigurable Surface Mount Technology (SMT) production technique. This approach facilitates the swift development and manufacturing of FHE for a variety of functions and applications.

The magnetic ACA employed in this study is an advanced structured composite material, combining metal microparticles and epoxy resins to achieve electrical, structural, and reliability attributes. Electrical conductivity is achieved through columns of conductive particles aligned in the z-direction under a magnetic field during reflow. The low-temperature cure of magnetic ACA, with its micron-sized ferromagnetic particles, allows for high-density interconnects while preserving the desired conformal and flexible characteristics of the substrate.

Interconnecting components in flexible hybrid electronics traditionally involves methods like low-temperature solder, ultra-low temperature solders, electrically conductive adhesives, and anisotropic conductive adhesives. Unlike isotropic Electrically Conductive Adhesives (ECAs), the

magnetic ACA specifically provides conductivity in the z-direction. This z-axis interconnection offers the advantage of dispensing material in finer pitches without the risk of unintended in-plane interconnects.

The epoxy resin utilized in the interconnect system is a thermosetting polymer cross-linked in the glassy state. These epoxies are designed to provide chemical resistance, corrosion resistance, impact resistance, flame retardance, and low creep. Previous research has extensively investigated the aging of epoxy resins in electronic applications, categorizing physical aging as one of the broad mechanisms affecting glassy materials. Chemical aging is associated with changes in cross-linking density, toughness, viscoelastic response, and permeability of polymers, although there is limited data available for magnetic ACAs.

In this study, finite element model is constructed on the printed samples. The size of electronic components, polyimide substrate, silver ink layers, SAC305 and magnetic ACA connection layers are measured using images of optical microscope. The stress-strain relation is obtained by linear elastic and viscoelastic model. Thermomechanical analysis is conducted. The stress-strain relation between SAC305 and magnetic ACA. Hysteresis loop and nonlinear plastic work for SAC 305 are reported. The implementation of linear elastic and linear viscoelastic model. Thermal cycling analysis and shear test are modeled. Reliability performance of magnetic ACA is evaluated.

6.1Experimental Method

6.1.1Materials and Test Matrix

This section outlines the test protocol employed to characterize various properties, including the glass transition temperature, coefficient of thermal expansion, thermal conductivity, elastic modulus, cure properties, viscoelastic properties, and thermal degradation. Figure 6-1

illustrates the standard procedure for sample preparation and the corresponding specimen size. Liquid-dispensed samples were initially milled to the specified dimensions (X) using a diamond saw, facilitating DMA (Dynamic Mechanical Analysis) testing in both tensile and three-point bend configurations.

Following the cutting of DMA test specimens from the cubic sample with a diamond saw, the samples undergo polishing to ensure a clean and smooth surface, as depicted in Figure 6-1. Three-point bending tests are then conducted on both sample geometries, with the final dimensions of the samples measuring 10mm x 8mm x 1.5mm upon fabrication. Figure 2 visually represents the three-point bend mode of the DMA, showcasing a sample in position.

The coefficient of thermal expansion will be investigated using a thermo-mechanical analyzer, while cure properties will be analyzed through differential scanning calorimetry. These analyses encompass both magnetized and non-magnetized samples to provide a comprehensive understanding of the material's behavior and performance across different conditions.

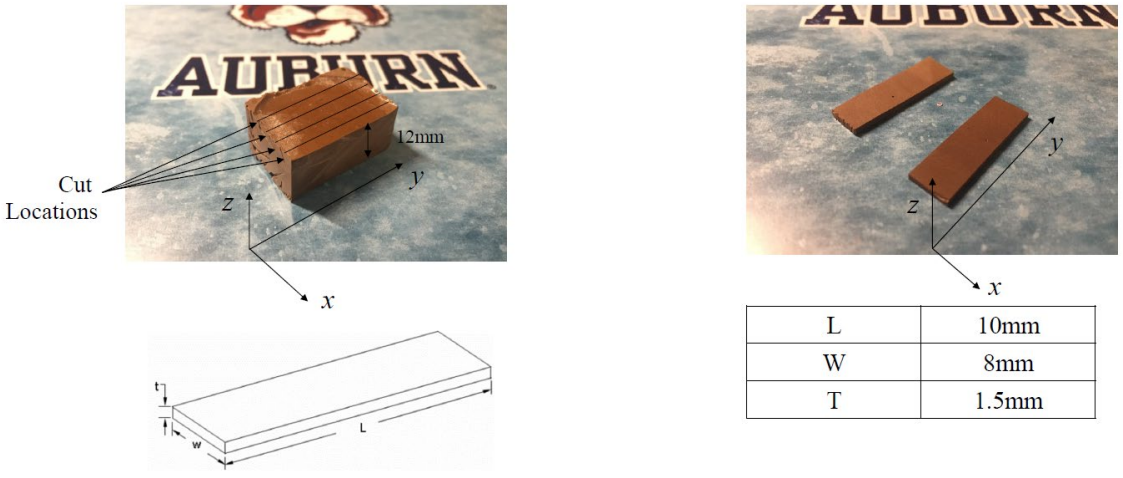

L	10mm
W	8mm
T	1.5mm

Figure 6-1 Typical sample preparation

The minimum sample size required for characterizing with magnetic ACA is notably larger than what is typically used in the end application. Despite this, the material's uniformity in both

the in-plane direction and the z-axis direction justifies the use of larger thicknesses for characterization purposes. To ensure the prevention of cracking, a multi-step thermal curing process was adopted. Initial cure temperatures fell within the 50-75°C range, progressing to the final cure accomplished at a more conventional temperature of 150°C. This approach was implemented to maintain the integrity of the material and enhance its suitability for the intended application.

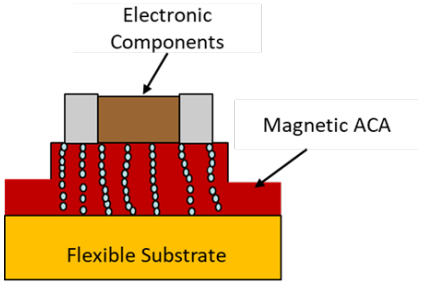

Figure 6-2 Magnetic ACA used in Flexible Hybrid Electronic

Table 6-1 Anand Constants for SAC 305 under Isothermal Aging

Anand Constant	Isothermal Aging Duration (Days			
	0	30	60	120
A	650	730	762	800
ξ	6.7	6.7	6.7	6.7
Q/R	4500	4500	4500	4500
a	1.16	1.2	1.26	1.368
h_0	163700	108000	91860	86100
m	0.4637	0.4401	0.4213	0.349
n	0.0055	0.0056	0.0055	0.007
$\hat{S}$	64.176	56.322	48.54	41.1

s_0	0.294	0.29	0.279	0.239

The Anand constant for SAC 305 from pristine to 120 aging days in 100C environments is shown in Table 6-1.

6.1.2 **Mechanical Test System**

In this paper, PerkinElmer DMA 8000 is utilized to run the DMA test. DMA test is done in 3-point bending (dual cantilever beam) mode with a frequency of 1 Hz. The setup is shown in Figure 6-3. The DMA test have been run from room temperature to 200°C and may increase to 280 °C depending on the desired temperature. The testing temperature increases at the rate of 3°C/min. The storage modulus, loss modulus, and tan δ were determined. The Tg of the samples has been found as the peak of the loss modulus curve, the tan δ curve, and the storage modulus curve slop at the transition phase.

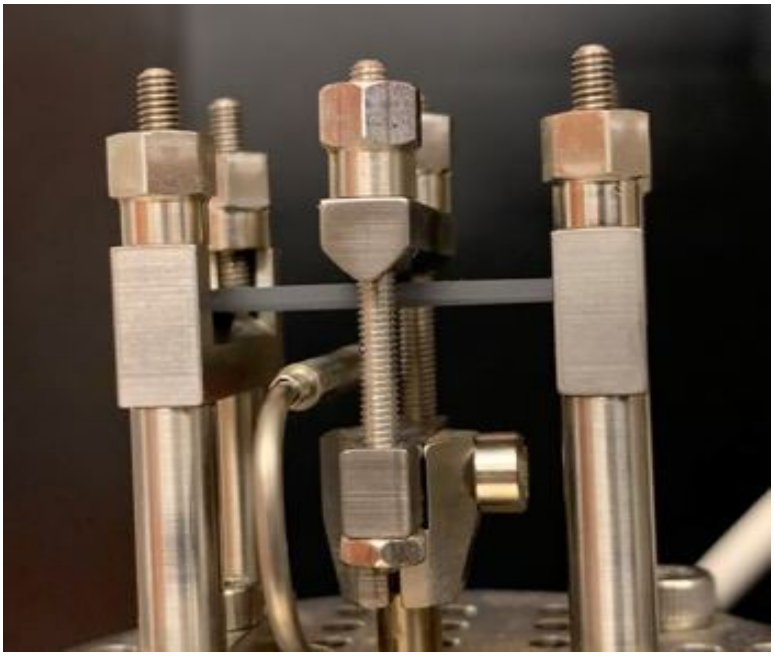

Figure 6-3 DMA Test System

6.1.3 **Finite Element Model**

In this study, geometry of specimen is measured by optical microscope (Figure 6-4). The electronic component is electrical resistant. The paste is SAC 305 or MACA. The true geometry of sample is used to formulate the Finite Element Model. The model and mesh are constructed in Ansys workbench (Figure 6-5). Multizone methods are applied. The material of electronic component is Alumina. CTE is 9 ppm/C. Flexible substrate is polyimide. The CTE of SAC 305 is 22ppm/C. Young's modulus of SAC 305 is 3.46 GPa. The CTE of MACA is 30 ppm/C before glass transition and 80 ppm/C after glass transition. The glass transition temperature of MACA is 122C. The thickness of polyimide substrate is 0.015mm. The Mechanical properties of MACA are determined by DMA analysis 3pts bending mode. Linear elastic property is determined by temperature ramp test from room temperature to 200C. The linear viscoelastic property is determined by frequency sweep test. Master curves are generated by time-temperature superposition using WLF equation. Prony constants are fitted, as the input for FEA model. Thermal cycle from room temperature to 150C and shear force loaded on electrical component are applied as boundary conditions.

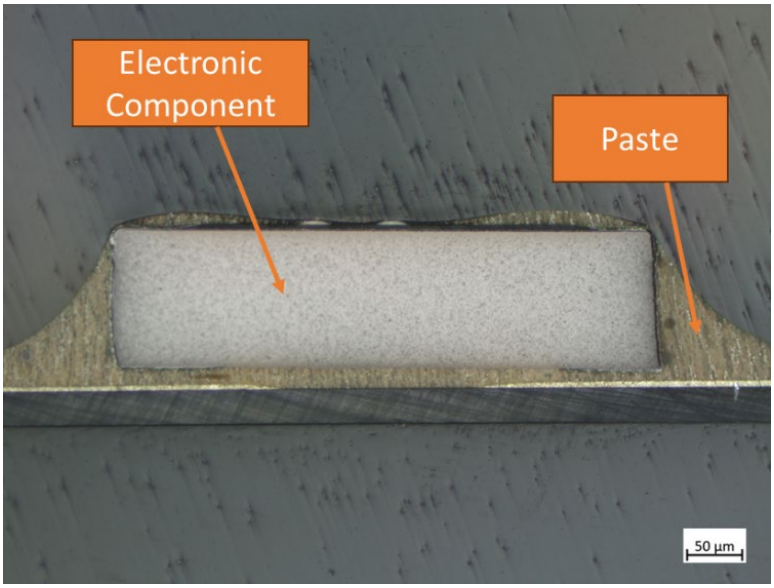

Figure 6-4 Printed Sample under Optical Microscope

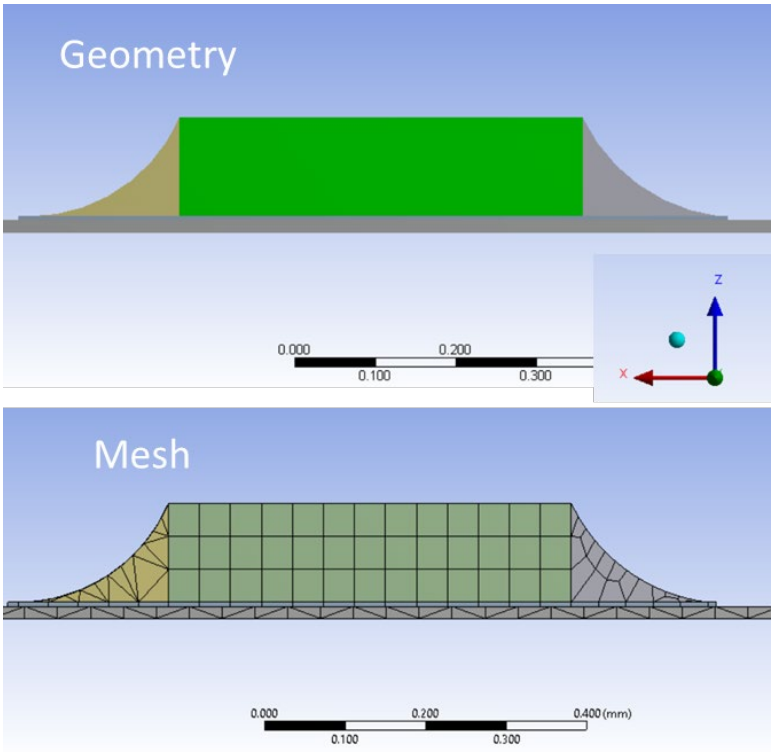

Figure 6-5 Finite Element Model in Ansys

6.2*Results and discussion*

6.2.1**Blotter Test**

Figure 6-6 shows the magnetic ACA samples used for thermal conductivity measurement. The specimen is 25mm in diameter and 4mm in thickness. Figure 6-7 shows the morphology for the blotter test with the sample and the blotter stacked on top of the sample.

Figure 6-6 Sample for Thermal Measurement

Figure 6-8 shows the data from a standard test and blotter test for the z-axis orientation of the magnetic ACA. When testing thin materials, meaning samples with less than the recommended minimum thickness or high-k filler materials, it is necessary to confirm that the heat wave from the sensor is not passing completely through the sample. The measurement is accomplished by performing a test with a blotter material and overlaying voltage-time curves from test results taken with and without the blotter material. If there is a deviation point between the two curves, the

samples must be stacked, or a custom calibration must be performed with shorter timing parameters. The results shown in Figure 6-7 shows that the sample passes the blotter test.

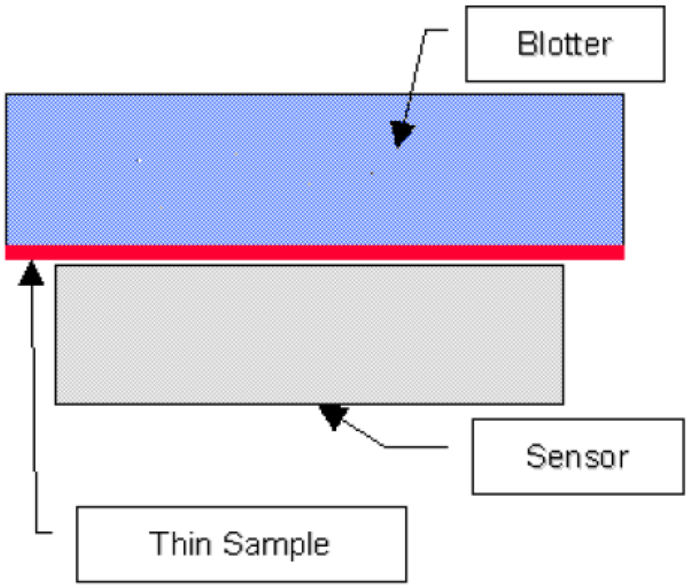

Figure 6-7 Schematic of blotter test

Blotter Test

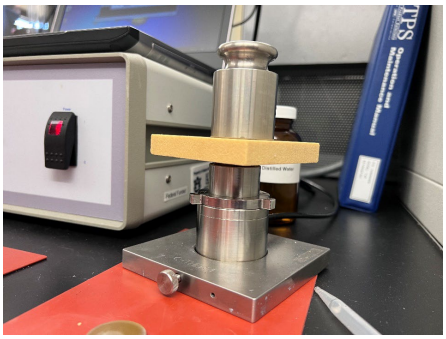

#	Repeat	Sensor ID	Start Time	Effusivity $\frac{W^*\sqrt{(s)}}{(m^2)^*K}$	Conductivity (W/mK)		Ambient T (°C)	DeltaT (°C)	V0 (mV)
1	1	T304	13:42:55	1,189	0.840		23.38	0.62	2,390.32
2	1	T304	13:44:00	905	0.540		20.87	0.71	2,387.30
3	1	T304	13:45:06	899	0.530	Blotter Test	20.68	0.72	2,386.66
4	1	T304	13:46:11	895	0.530		20.62	0.72	2,386.52
5	1	T304	13:47:17	892	0.530		20.82	0.72	2,387.77
6	1	T304	13:48:22	901	0.540		20.90	0.71	2,387.73
7	1	T304	13:49:28	895	0.530		21.45	0.71	2,386.10
8	1	T304	13:50:33	902	0.540	Standard Test	21.44	0.71	2,386.11
9	1	T304	13:52:11	901	0.540		21.50	0.71	2,386.15
10	1	T304	13:53:17	899	0.530		20.91	0.71	2,387.35

Figure 6-8 Data from blotter test

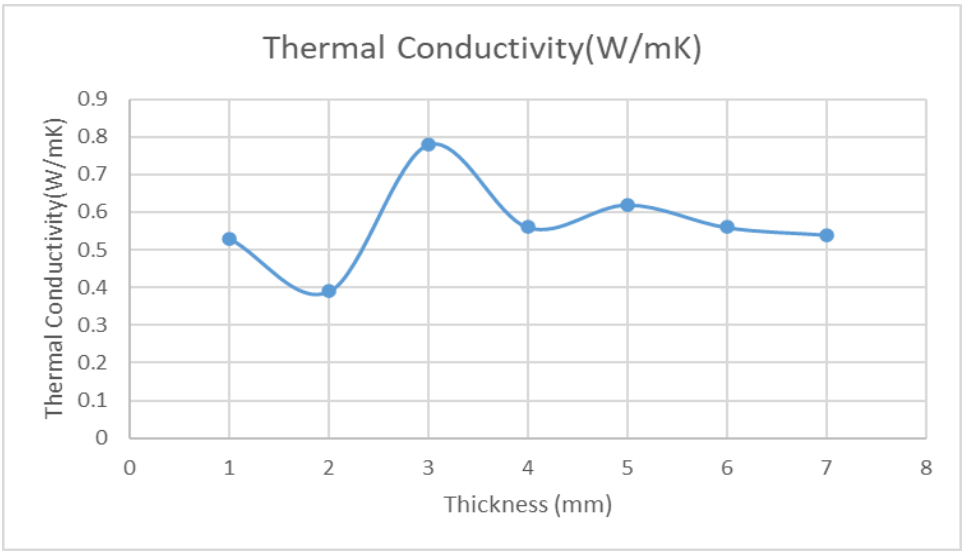

Figure 6-9 Measured thermal conductivity of samples in different thickness

Figure 6-9 shows the measurement of the thermal conductivity of the magnetic ACA material along the z-axis oriented along the conduction direction. Thickness effect due to the consistent of sample fabrication is investigated. The measured values of the thermal conductivities

are shown to be in the range of 0.39-0.78 W/mK. Data has been acquired on a 6-samples, and the results from the measurements are also shown in Figure 6-9. Variance in the thermal conductivity is expected owing to the variance in the contact resistance of the ferromagnetic particles and the stack patterns, which may vary from sample to sample.

6.2.2 Effect of High Temperature Aging on Thermal Conductivity

The effect of sustained high-temperature exposure to 100°C on thermal conductivity has been shown in Figure 8. The material property does not change significantly in 120 days of aging. The variance of most samples is 0.05W/mK, indicating the stability of material properties.

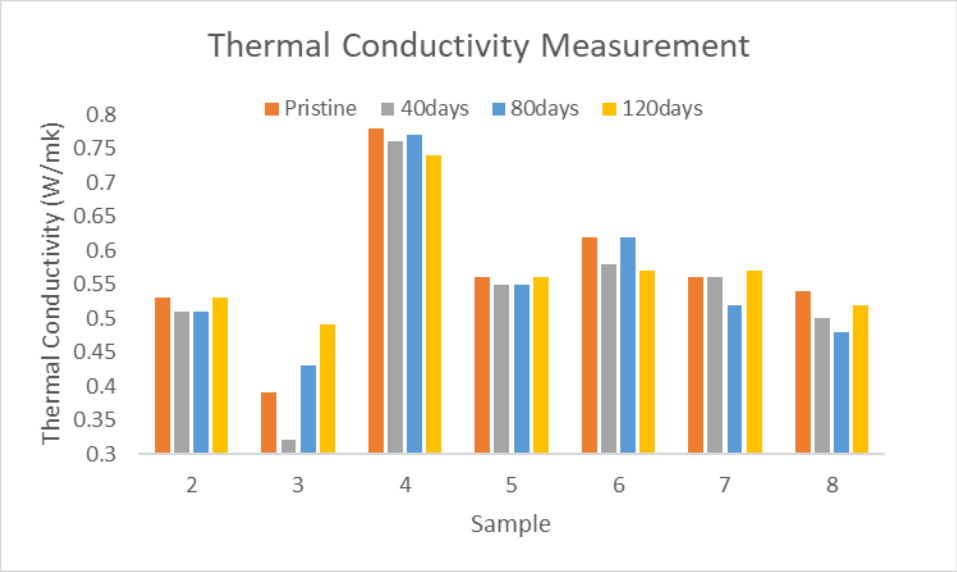

Figure 6-10 Thermal conductivity as the function of aging time at 100°C

The values of thermal conductivity are shown in the table above. The thermal conductivities of most samples are about 0.5 ~0.6 W/mK. The thermal conductivity for a thickness of 2mm is about 0.4 W/mK, which is the smallest. The thermal conductivity with a thickness of 2.5mm is about 0.77 W/mK, which is the highest. While thermal conductivity is a material property and should not vary with structure dimensions – in this case, the anisotropic and non-homogenous nature of the material produces a variation in the material response.

Table 6-2 Thermal conductivity as the function of aging time

Thickness (mm)	Thermal Conductivity(W/mK)			
	Pristine	40 days	80days	120days
2	0.53	0.51	0.51	0.53
2.1	0.39	0.32	0.43	0.49
2.5	0.78	0.76	0.77	0.74
2.8	0.56	0.55	0.55	0.56
3.4	0.62	0.58	0.62	0.57
3.6	0.56	0.56	0.52	0.57
4	0.54	0.5	0.48	0.52

6.2.3 E' and E" Measurement of Magnetic ACA with DMA

DMA test of 3pts bending mode is conducted for pristine conditions of non-magnetic samples (Figure 6-11). Glass transition temperature, collected by tan-delta peak, is about 128°C. Storage modulus before glass transition temperature is about 6800MPa. Storage modulus after glass transition temperature is about 100MPa. The loss modulus before the glass transition temperature is about 113MPa. The loss modulus after the glass transition temperature is about 3.4MPa.

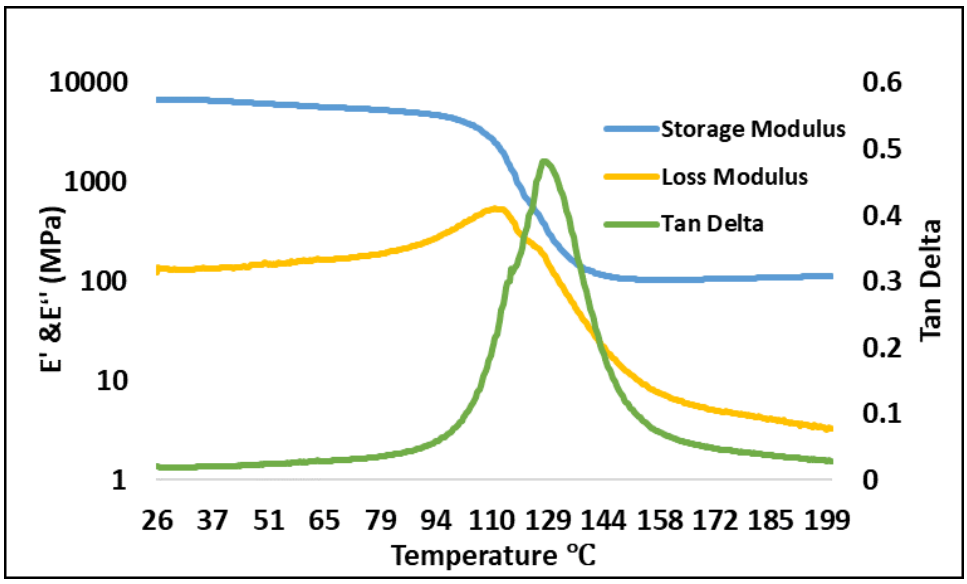

Figure 6-11 Storage modulus, loss modulus, and Tan Delta for pristine non-magnetic material

Storage modulus, loss modulus, and Tan delta are collected for magnetic and non-magnetic samples in the y-z plane. The storage modulus of the magnetic sample is slightly smaller than the Non-magnetic sample. The loss modulus of the magnetic sample is slightly bigger than the non-magnetic sample. Glass transition temperature for the magnetic sample is 124°C, smaller than the Tg of the non-magnetic sample. Viscoelastic materials are represented in the frequency domain using a complex modulus approximation. The stationary harmonic strain is represented by:

$$\varepsilon(t) = \varepsilon_0 e^{i\omega t} \tag{6-1}$$

Similarly, the stationary harmonic stress is represented by:

$$\sigma(t) = \sigma_0 e^{i(\omega t+\varphi)} \tag{6-2}$$

Where, σ_0 and ε_0 are the stress and strain amplitudes respectively, ω is the excitation frequency, and φ is the phase delay between the stress and the strain signals. The constitutive equation for the viscoelastic material in the frequency domain can then be cast in the form using the complex modulus:

$$\sigma(\omega) = E^*(\omega)\varepsilon(\omega) \tag{6-3}$$

The complex modulus is a combination of the storage modulus and the loss-modulus of the material:

$$E^*(\omega) = E'(\omega) + iE''(\omega) \tag{6-4}$$

The amount of energy dissipated in the material is quantified using the computation of tan-delta:

$$\tan\delta = \frac{E''(\omega)}{E'(\omega)} \tag{6-5}$$

$$E'(\omega) = \frac{\sigma_0(\omega)}{\varepsilon_0(\omega)}\cos\left[\varphi(\omega)\right] \tag{6-6}$$

$$E''(\omega) = \frac{\sigma_0(\omega)}{\varepsilon_0(\omega)}\sin\left[\varphi(\omega)\right] \tag{6-7}$$

Since the measurements in most DMA can be done at a truncated range of frequencies – a broader frequency-range of characterization of the materials is pursued using time-temperature superposition (TTS). Williams-Landel-Ferry (WLF) equation is used to calculate shift factor log a_T (in logarithmic scale):

$$\log a_T = -\frac{C_1(T - T_0)}{C_2 + (T - T_0)} \tag{6-8}$$

Where C_1 and C_2 are constants, T_0 is the material's reference temperature (general glass transition temperature), and T is the isothermal temperature. log a_T will be positive if $T<T_0$ and negative if $T>T_0$.

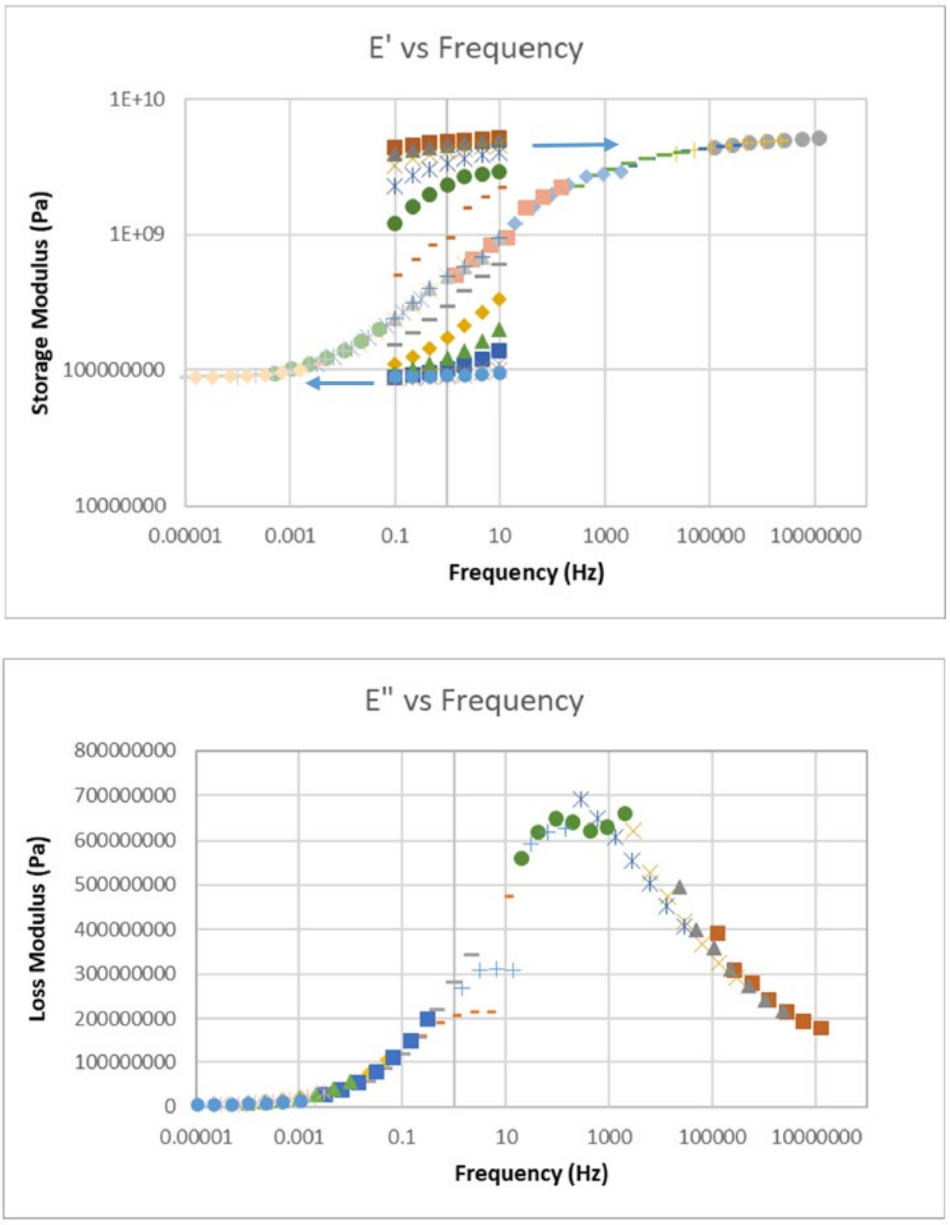

Figure 6-12 Master curves for storage and loss modulus

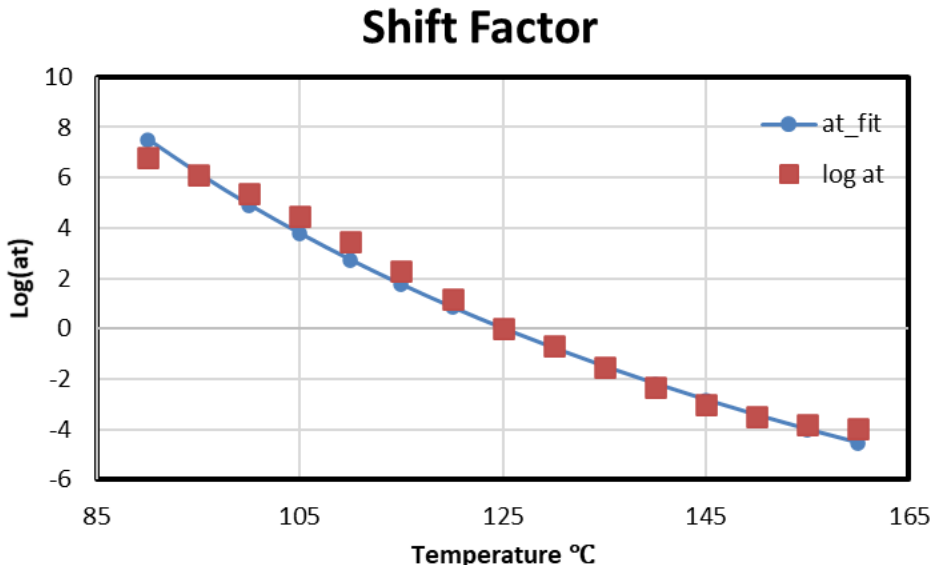

Figure 6-13 Shift Factor Fitted by WLF Equation

The linear viscoelastic property is investigated by frequency sweep test. Frequency sweep test of Magnetic sample cut in y-z plane is conducted (Figure 6-12). Shift factor is fitted by WLF equation (Figure 6-13). Reference temperature is at 125℃.Master curve of storage modulus is created by frequency sweep data and shift factor. The master curve is covered from 0.00001Hz to 10MHz.

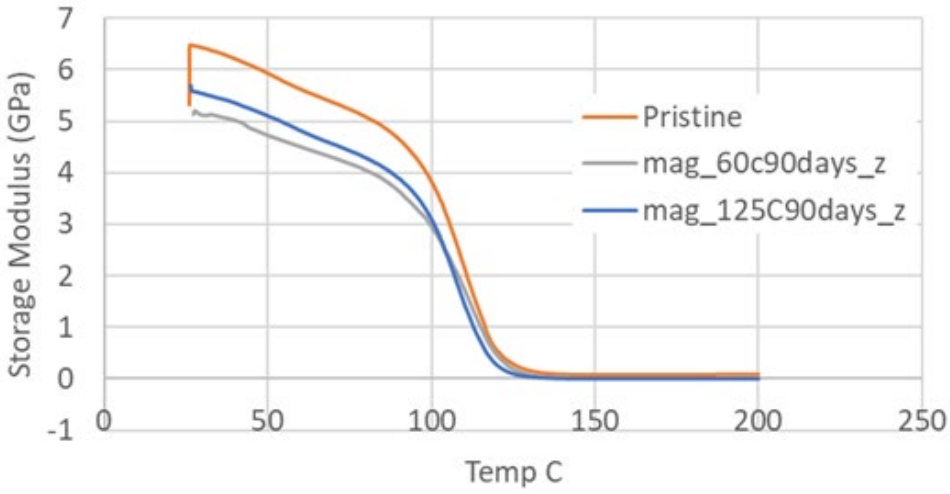

(a) Samples for Z magnetic direction

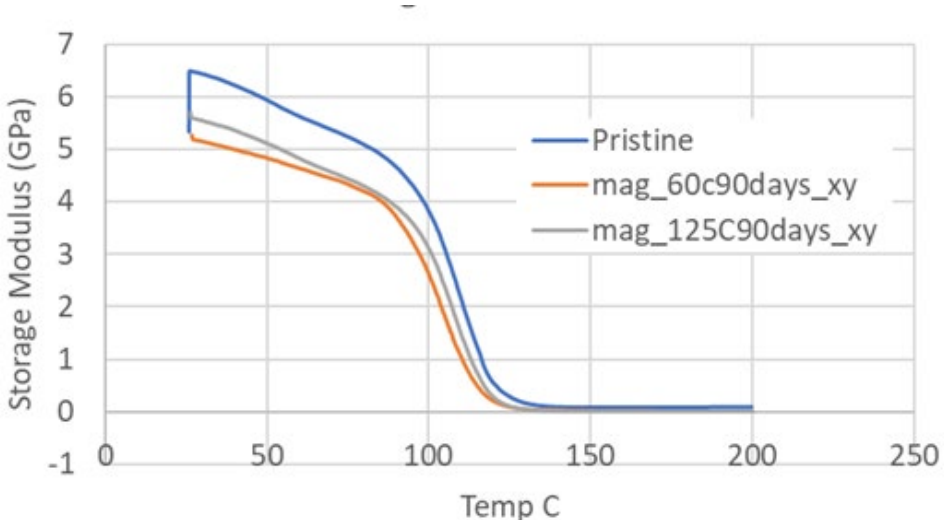

(b) Samples for x-y magnetic plane

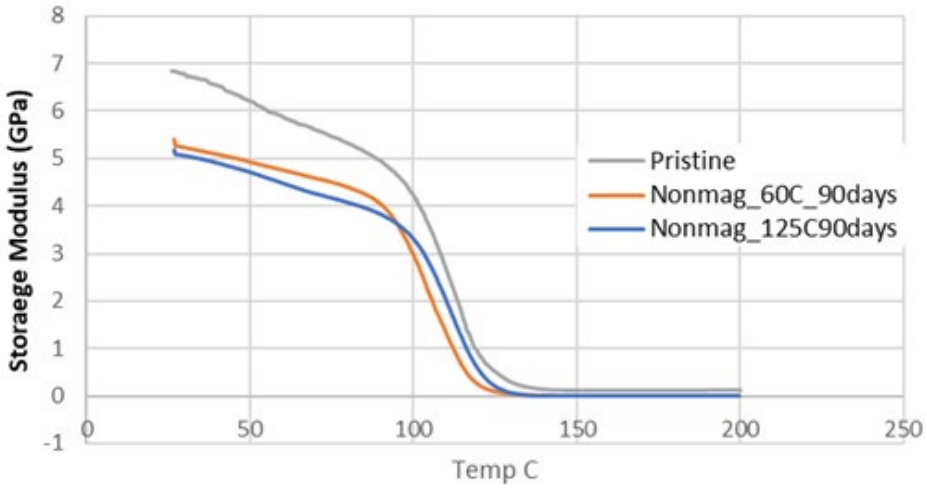

(c) Non-magnetic samples

Figure 6-14 Storage modulus under various aging conditions

Storage modulus for both magnetic and non-magnetic samples are investigated. Figure 6-14 shows the storage modulus for pristine, 90-days aged samples at 60°C and 90-days aged samples at 125°C. Figure 6-14a shows the measurements along the conductive z-direction after magnetization. Figure 6-14b shows the measurements of the storage modulus in the non-conductive x-y plane after magnetization. Figure 6-14c shows the measurements of the non-

magnetized material. Storage modulus under pristine conditions is higher than aged conditions for both magnetic and non-magnetic samples. Glass transition region of the aged condition is slightly lower than pristine conditions. Tan delta for magnetic samples under different aging temperatures are showing in Figure 6-15. The glass transition temperature does not change significantly as the aging temperature increases from 60C to 125C.

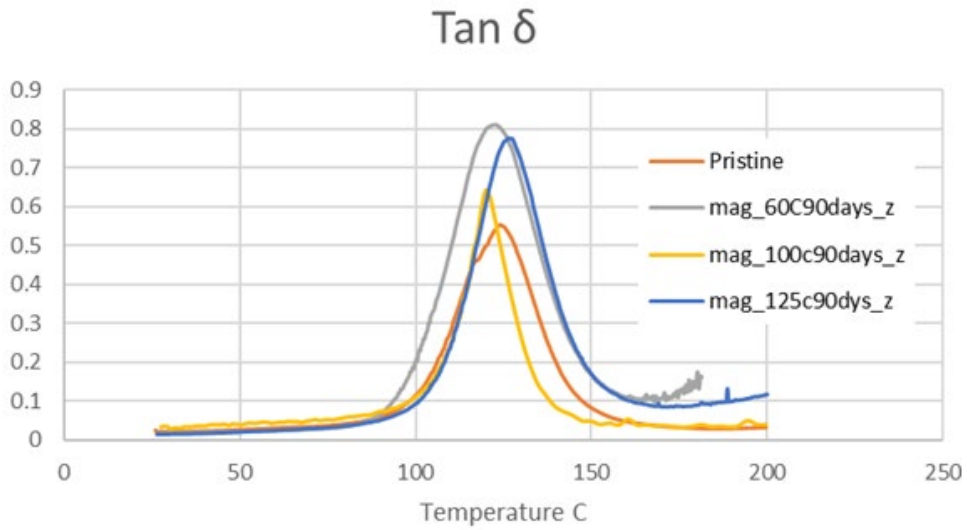

Figure 6-15 Tan Delta under various aging conditions

Generalized Maxwell Model is widely used in the simulation of viscoelastic material. The model is composed of a spring and dashpot. Spring element simulates the pure elastic behavior. Dashpot element simulates viscous material behavior. Prony pairs are used to characterize the generalized maxwell model for numerically simulating viscoelastic behavior. For the generalized Maxwell Model, the elastic and bulk modulus functions can be expressed in a Prony series format:

$$\mathbf{G(t) = G_e + \sum_{i=1}^{n_G} G_i e^{(-t/\tau_i^G)}} \qquad (6\text{-}9)$$

$$\mathbf{K(t) = K_e + \sum_{i=1}^{n_K} K_i e^{(-t/\tau_i^K)}} \qquad (6\text{-}10)$$

Where G_e and G_i are the storage modulus, G_e is the modulus at equilibrium state, K is bulk modulus, τ_i is the relaxation times for the various Prony series components. For N elements

Maxwell Model, there are 2N+1 parameters. In order to satisfy the thermodynamics principles, all Prony pairs and modulus should be greater than zero. After Laplace transform, the storage modulus and loss modulus are transformed from the time domain to the frequency domain [12]:

$$G'(\omega) = G_e + \sum_{i=1}^{N} G_i \frac{(\omega\tau_i)^2}{1+(\omega\tau_i)^2} \quad (6\text{-}11)$$

$$G''(\omega) = \sum_{i=1}^{N} G_i \frac{\omega\tau_i}{1+(\omega\tau_i)^2} \quad (6\text{-}12)$$

The DMA frequency sweep test could obtain experimental data in the frequency domain. Prony series are used as the input to construct the linear viscoelastic model in FEA software. With the Prony parameters, we could simulate and predict the linear viscoelastic material behavior. There are several ways to obtain the Prony parameters. In this paper, the Prony series are fitted by an optimization framework. We define the residual storage modulus and loss modulus.

$$G'_{red} = \left(\frac{G' - G'_{est}}{G'_{est}}\right)^2 \quad (6\text{-}13)$$

$$G''_{red} = \left(\frac{G'' - G''_{est}}{G''_{est}}\right)^2 \quad (6\text{-}14)$$

Where the $\boldsymbol{G'}$ and $\boldsymbol{G''}$ are storage modulus and loss modulus data acquired from DMA tests. $\boldsymbol{G'_{est}}$ and $\boldsymbol{G''_{est}}$ are storage modulus and loss modulus computed by Prony constants. We solve the following optimization problem:

$$minimize\ R = G'_{red} + G''_{red} \quad (6\text{-}15)$$

$$subject\ to\ \tau_i \geq 0,\ G_i \geq 0,\ G_e > 0, \quad (6\text{-}16)$$

$$i = 1 \ldots . N$$

R is the residual between experimental and numerical results. Prony constants are variables of this optimization problem. The minimized residual could offer the best-fitting Prony constants.

Commercial software ABAQUS defines the frequency domain linear viscoelasticity slightly differently. They use dimensionless Prony coefficients.

$$G'(\omega) = G_0(1 - \sum_{i=1}^{N} g_i) + G_0 \sum_{i=1}^{N} g_i \frac{(\omega\tau_i)^2}{1 + (\omega\tau_i)^2} \tag{6-17}$$

$$G''(\omega) = G_0 \sum_{i=1}^{N} g_i \frac{\omega\tau_i}{1 + (\omega\tau_i)^2} \tag{6-18}$$

Where $g_i = G_i/G_0$ is dimensionless Prony coefficient. One more constraint is added to the optimization problem that $\sum_{i=1}^{N} g_i \leq 1$. One advantage of using dimensionless Prony parameters is generating normalized time domain responses with dimensionless Prony pairs. We could directly compare material behavior using normalized time domain response. In order to simulate material properties in finite element framework. We fit dimensionless Prony pairs.

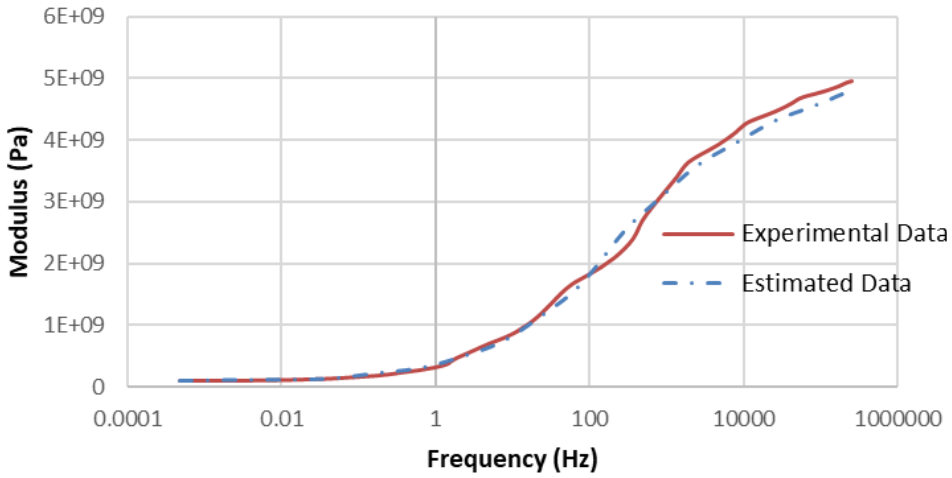

Figure 6-16 Master Curve Fitted Data by Prony Pairs

Table 6-3 Prony Constants for Magnetic-ACA specimen

G_o (GPa)	6.55
g_i	τ_i

0.2458	1E-10
0.0464	0.000005
0.029	0.00001
0.0431	0.00005
0.0553	0.0001
0.0640	0.0005
0.0852	0.001
0.1288	0.005
0.0976	0.01
0.0687	0.05
0.0461	0.1
0.0306	0.5
0.0204	1
0.0207	10
0.0033	1000
0.0031	100000
0.0002	1000000
0.0012	10000000

6.3*Finite Element Analysis*

Finite element model is developed based on printed samples, incorporating dimensions obtained from images captured by an optical microscope for electronic components, polyimide substrate, SAC305, and magnetic ACA connection layers. The stress-strain relationship is determined using both linear elastic and viscoelastic models. Thermomechanical analysis is carried

out, focusing on the stress-strain interaction between SAC305 and magnetic ACA. Hysteresis loops and nonlinear plastic work for SAC305 are documented. The model incorporates linear elastic and linear viscoelastic components.

6.3.1 Shear Force

A shear force is applied on the electrical component as the boundary conditions. The stress-strain relationship is determined using both linear elastic and viscoelastic models. For SAC 305, when the shear force is 1N, total deformation is shown in Figure 6-17.

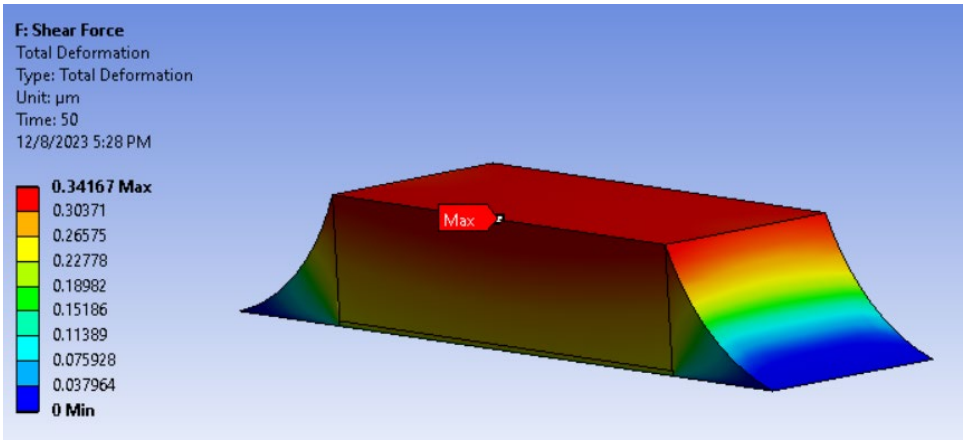

Figure 6-17 Total Deformation for SAC 305 under shear force

The maximum shear stress distribution is shown *Figure 6-18*. It indicates that the maximum shear stress occurs at the corner of the electronic component. Thus, the critical part is at the corner of the component. Scoped to the stress on solder element, it is shown that high stress locates at the side corner. The max shear stress applied on solder is about 8MPa.

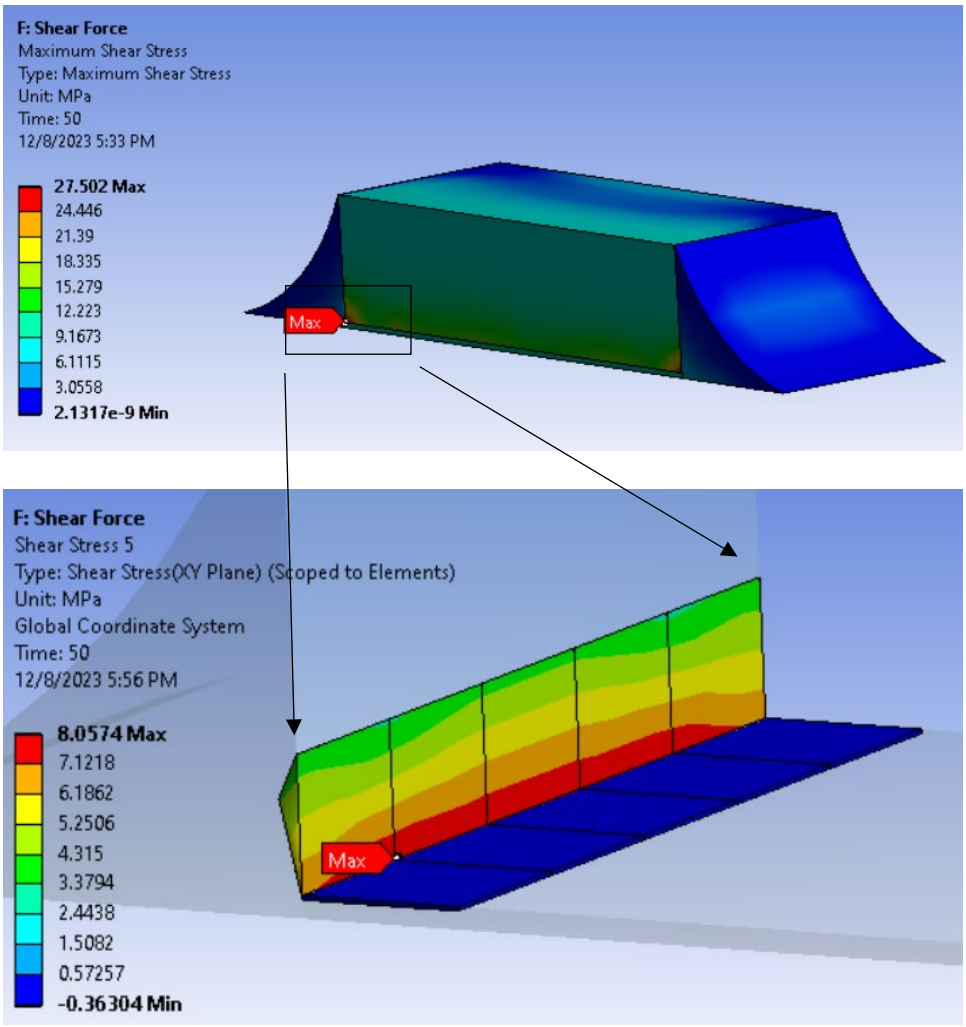

Figure 6-18 Shear Stress Distribution to Corner Solder Elements

When we focus on the plastic strain (Figure 6-19), it shows that the maximum plastic strain is at the side of bottom layer. Indicating the highest plastic strain occurs at both sides of bottom solder layer.

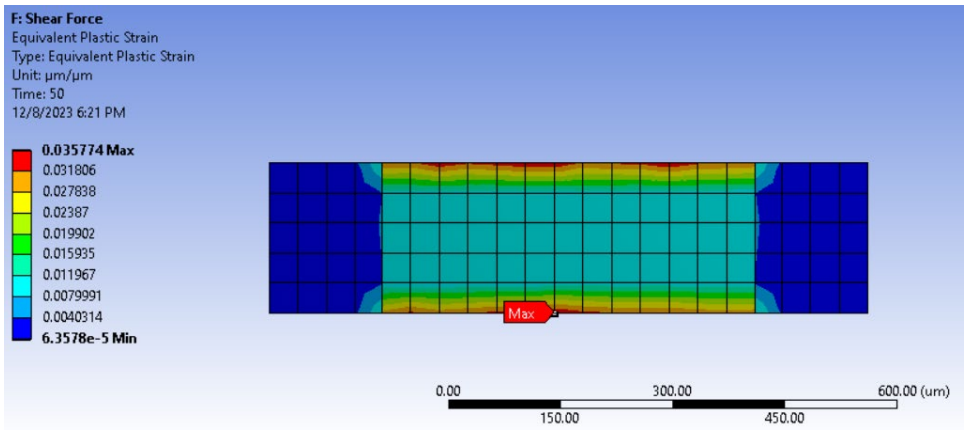

Figure 6-19 Plastic Strain on Solder SAC 305

Table 6-4 Shear Stress and Plastic Strain for SAC 305

SAC 305	Aging days	0 days	30 days	60 days
Shear Stress (MPa)		8.057	8.06	8.112
Plastic Strain		0.0358	0.06	0.107

Table 6-4 presents the maximum values of shear stress and plastic strain for SAC 305 during a 60-day aging period under a 100°C environment. The data indicates an increase in shear stress from 8.057 MPa to 8.112 MPa, accompanied by a rise in plastic strain from 0.0358 to 0.107. This signifies a nearly threefold increase in plastic strain over the aging duration, highlighting the material's evolving behavior under the specified environmental conditions.

Linear viscoelastic model is constructed using Prony constants fitted in last section. The maximum total deformation, showing in Figure 6-20, is 0.23um, smaller than using SAC 305. The elastic strain, showing in Figure 6-21, is 0.008, much smaller than using SAC 305.

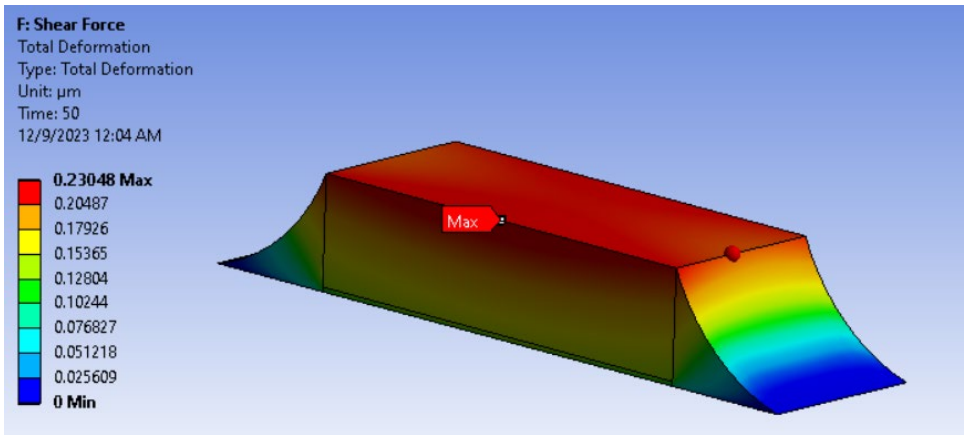

Figure 6-20 Total Deformation for linear viscoelasticity Model

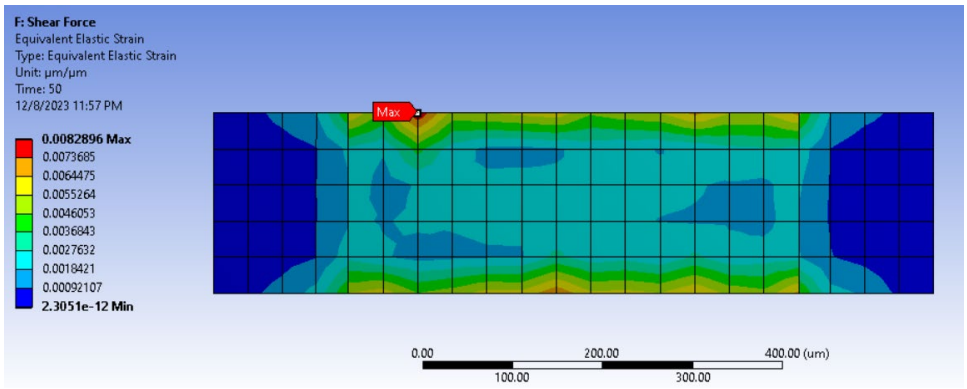

Figure 6-21 Elastic strain for MACA

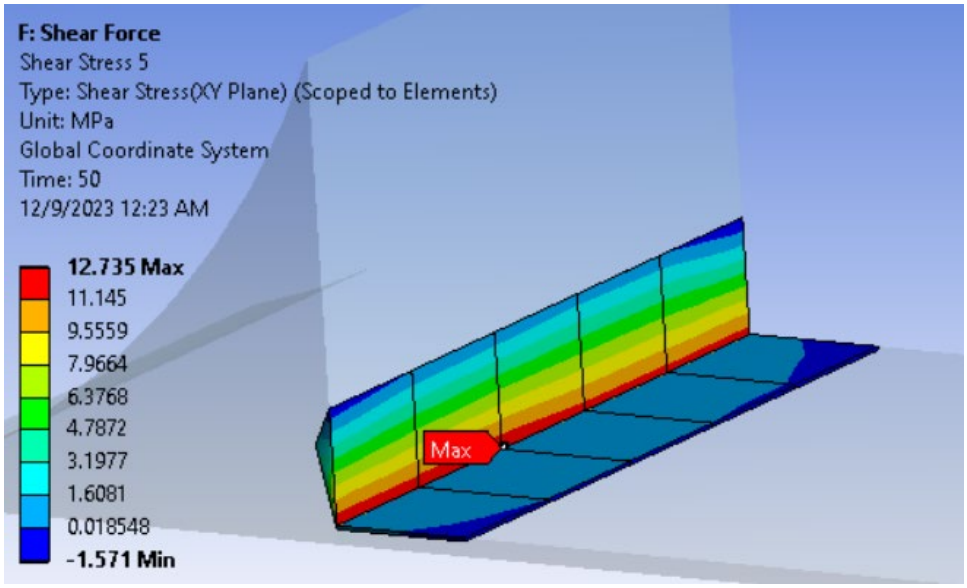

Figure 6-22 Shear stress distribution to Corner Elements

The shear stress to corner element is showing in Figure 6-22. The maximum value is about 12.7MPa, slightly larger than using SAC 305. The aging effect of MACA is not significant. The results show that for MACA, there is smaller deformation, smaller strain and larger shear stress.

6.3.2 Thermal Cycle

A Thermal cycle is applied on the electrical component as the boundary conditions. Temperature is from 25C to 150C.The stress-strain relationship is determined using both linear elastic and viscoelastic models. Stress and deformation could be explained by the CTE mismatch during thermal cycle.

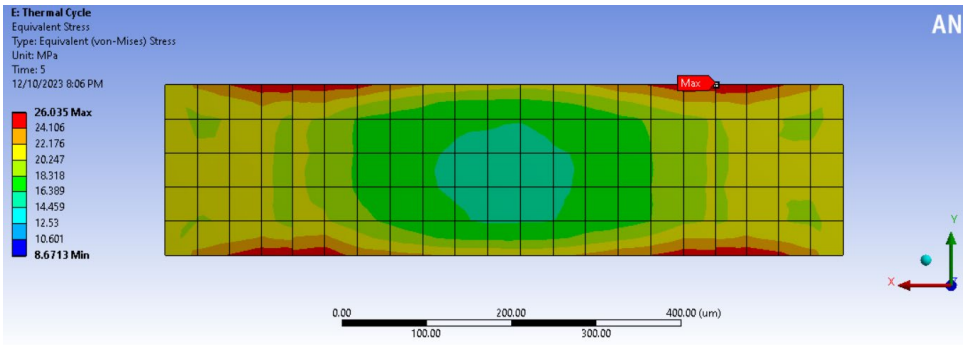

Figure 6-23 von-Mises Stress for Thermal Cycles

Von-Mises stress is evaluated in Figure 6-23. The analysis reveals that the maximum stress is concentrated at the corner of the bottom layer. Upon examining the element with the highest stress, a hysteresis loop of pristine SAC 305 for the initial 14 thermal cycles is plotted (Figure 6-24). This graph illustrates that the maximum shear stress during this period reaches approximately 13 MPa. Notably, the plastic strain experiences an initial increase in the first 7 cycles, after which it stabilizes and remains constant. This observation provides insight into the material's behavior under thermal cycling, emphasizing the dynamics of stress and plastic strain over the specified number of cycles.

The hysteresis loop for SAC 305 under different aging conditions are shown in Figure 6-25. The findings indicate a noticeable reduction in the maximum stress, decreasing from 13 MPa to 9 MPa, when transitioning from pristine conditions to a 60-day aging period. Moreover, there is an observable trend where the maximum stress decreases with increasing ageing time.

In the case of the 30-day aging sample, the hysteresis loop stabilizes after 6 cycles, highlighting a consistent pattern. Conversely, for the 60-day aging sample, the hysteresis loop stabilizes more quickly, specifically after 4 cycles. This suggests that the stabilization time decreases as the aging time increases. These results underscore the influence of aging conditions on the material's stress behavior during thermal cycling.

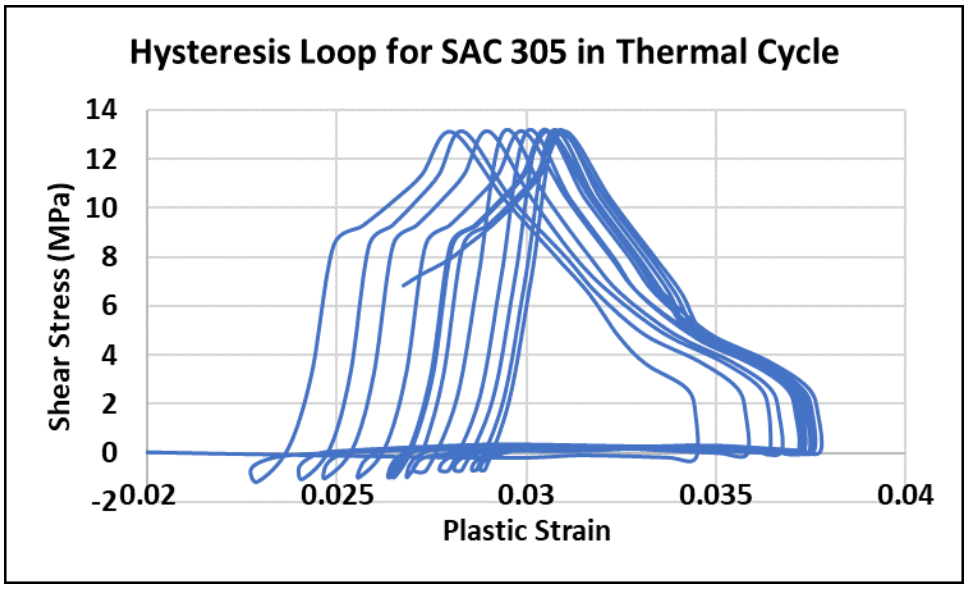

Figure 6-24 Hysteresis Loop for SAC 305 in Thermal Cycles

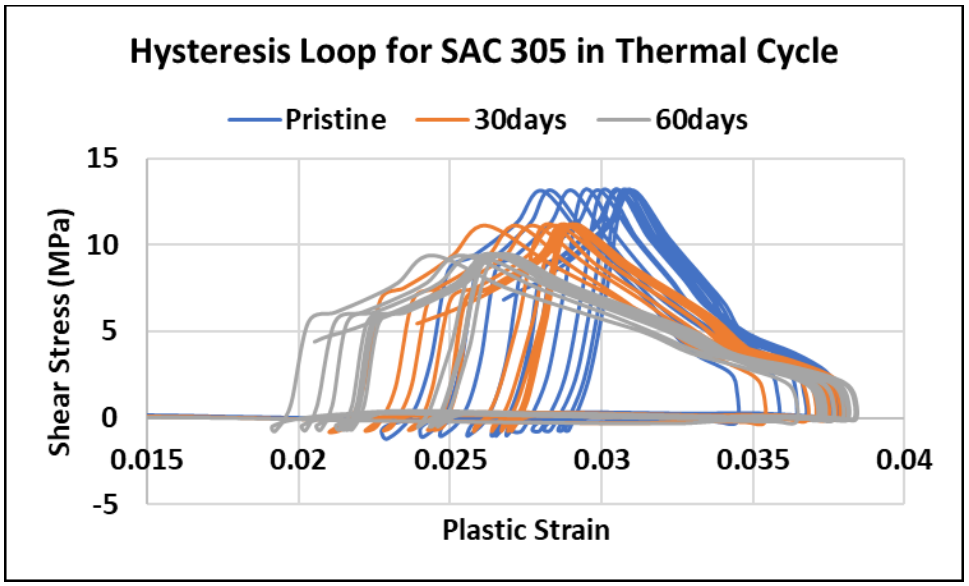

Figure 6-25 Hysteresis Loop for SAC 305 under different aging conditions

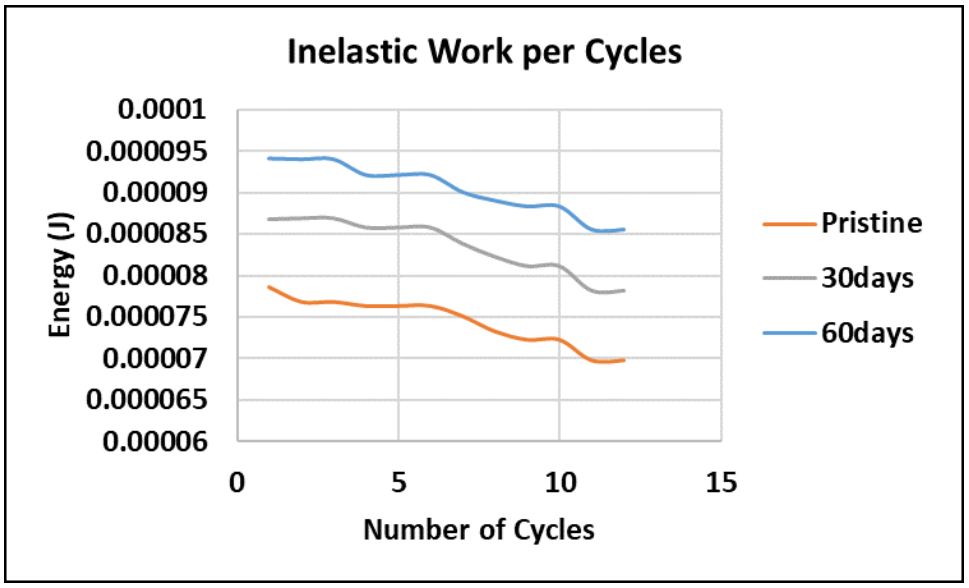

Figure 6-26 Inelastic Work per Cycles for SAC 305 under different aging conditions

The cyclic inelastic work is characterized as the hysteresis loop area for SAC 305. Figure 6-26 illustrates the progression of cyclic inelastic work. The plot reveals a marginal decline in nonlinear plastic work with an increasing number of cycles under each aging condition. Additionally, there is a noticeable augmentation in nonlinear plastic work corresponding to longer aging times, indicating an enlargement of the hysteresis loop area as aging time extends.

The thermal cycle simulation of the MACA viscoelastic model is further delineated. A visualization of the Von-Mises stress distribution is depicted. The stress registers at 34.23 MPa, slightly surpassing that of the SAC 305 model. The shear stress in the XY plane mirrors that of the SAC 305 model at 14.4 MPa. Notably, the maximum strain is calculated at 0.04.

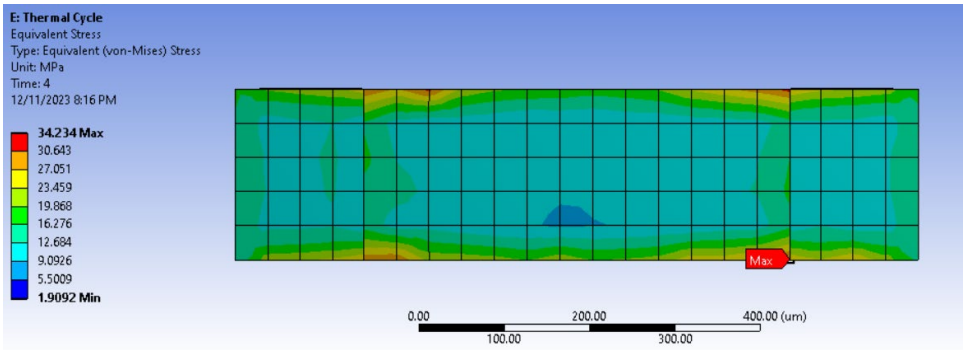

Figure 6-27 von-Mises Stress for MACA

6.4*Summary and Conclusions*

This research investigates the reliability performance for flexible hybrid electronics. Finite element model is constructed on the printed samples. The size of electronic components are measured using images of optical microscope. The linear viscoelastic property is obtained by frequency sweep test. Prony pairs are fitted by the optimization framework. Stress-strain relation is obtained by linear elastic and viscoelastic model. Shear force and tthermomechanical analysis are modeled. The stress-strain relation between SAC305 and magnetic ACA is reported. In shear simulation, compared with SAC 305, results of MACA have higher stress but lower deformation and strain. Hysteresis loop and inelastic work for SAC 305 are reported. The outcomes indicate that the critical areas in the component are the bottom layer and the corner. These regions exhibit a significant impact on the observed results, emphasizing their importance in terms of stress concentration and overall performance. Understanding the criticality of these specific locations is essential for further analysis and optimization of the component's design and material properties.

Chapter 7 Material Property Evolution of Thermal Interface Material

7.1Effect of Surface Treatment of TIM/Copper Interface

7.1.1Materials

A developmental TIM is prepared for both monotonic and fatigue tests. 0.5mm thick pure copper is selected. The information of TIM is showing in Table 7-1.

Table 7-1 Typical Material Properties

Property	Value
Base Resin	Epoxy Amine
Filler	Aluminum (50% by weight)
Worklife	60 mins at 23C
Curing Condition	120C/10mins
Tg	66C
Thermal conductivity	0.72W/mK
Coefficient of Thermal Expansion (CTE)	75×10^{-6}(<Tg) 160×10^{-6}(>Tg)

Bare copper is selected for interface study. The thickness is 0.5mm since the lid thickness of FCBGA is 0.5mm. 100W 5mins and 400W 5mins oxygen plasma cleaning is applied on the bare copper surface.

Table 7-2 Typical Dimensions of Specimens

Typical Sample Size	
h	2mm

h_1	1.5mm
h_2	0.5mm
b	6mm
l	10mm
L	50mm

Figure 7-1 Specimen for Interfacial Study

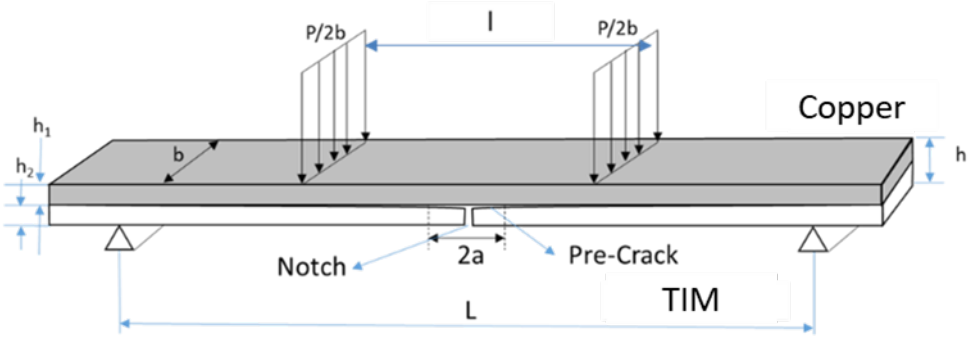

Figure 7-2 a Bimaterial, Notched Tour-point Bending Specimen with Symmetrical Interfacial Cracks

The typical a bimaterial, notched tour-point bending specimen for monotonic test is showing in Figure 7-1. Typical dimensions and are showing in Table 7-2.

7.1.2**Aging Test**

Aging tests are applied to specimens of not surface cleaning, 100W 5mins cleaning and 400W 5mins cleaning specimens, following the test matrix as Table 7-3.

Table 7-3 Test Matrix

Bimaterial TIM/copper	**Surface Treatment**		**Pristine**	**40days**		**80days**		**120days**	
TIM/Cu	Plasma gas O_2			100C	150C	100C	150C	100C	150C
	Time 5 minutes								
Monotonic	No Cleaning		√	√	√	√	√	√	√
	O2 Plasma	100W	√	√	√	√	√	√	√
		400W	√	√	√	√	√	√	√
Fatigue	No Cleaning		√	√	√	√	√	√	√
	O2 Plasma	100W	√	√	√	√	√	√	√
		400W	√	√	√	√	√	√	√

7.1.3**Monotonic Test System**

A four-point bending setup is constructed in Figure 7-3. Instron 3367 machine with 1KN load cell is used to test the three-point and four-point bend specimens.

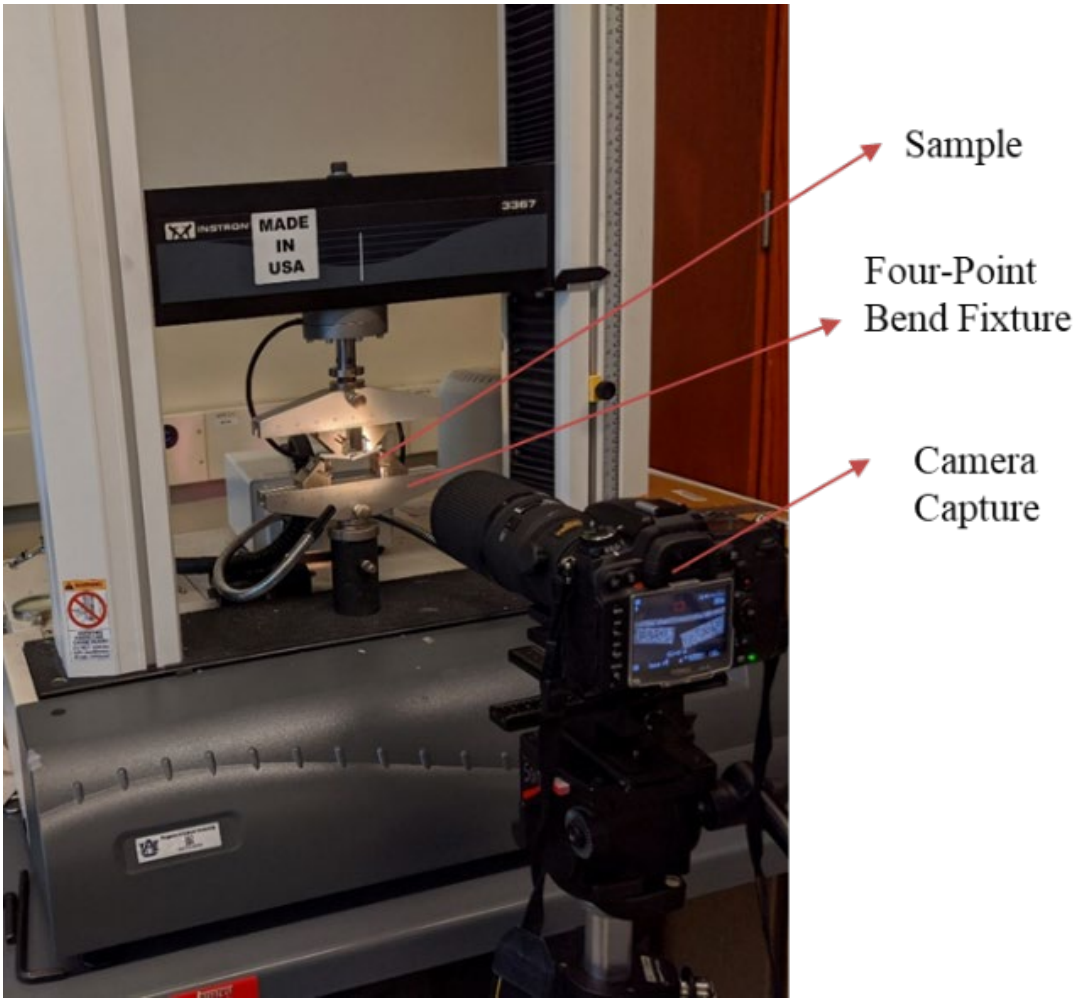

Figure 7-3 Four-point bending monotonic test setup

A Nikon digital camera is used to record the entire event as shown in Figure 7-3. The recorded video is used to find the crack initiation location and time, which is cross-referenced with the Instron output to determine the critical-load of crack initiation. The video is recorded at a speed of 25 frames per second.

7.1.4 **Fatigue Test System**

A vertical fatigue setup is constructed Figure 7-4. The measurement system consists of a load cell and a linear variable differential transformer. 4-point bending setup is used to applied cyclic loading test on pre-notched samples. One end of setup fix at the base, the other end connects

with step motor. Step motor is used to apply cyclic load on the samples. Force sensor (208C03 ICP FORCE SENSOR) cell is used to record the voltage signal of applied force. The output from the load cell can be acquired in real time via data acquisition from oscilloscope. Force sensor is threaded onto an adapter which resides on the tips of each actuator. The load cell measurement range is 500lb (2.224kN). Sensitivity is 10mV/lb.

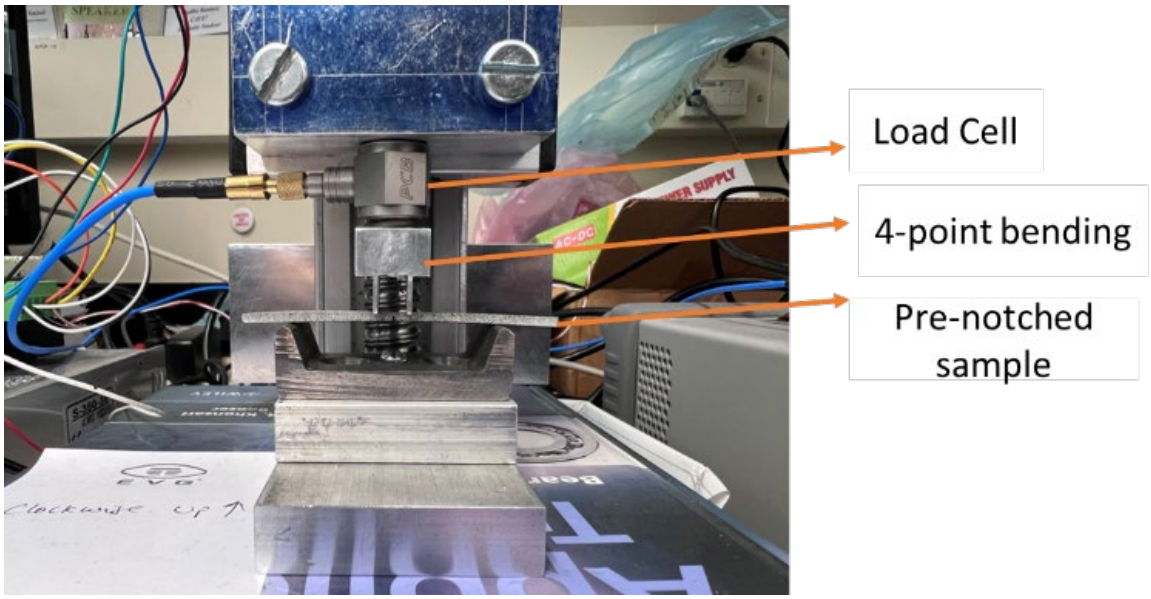

Figure 7-4 Fatigue Setup

7.2*Results and Discussion*

7.2.1**Four-point bending**

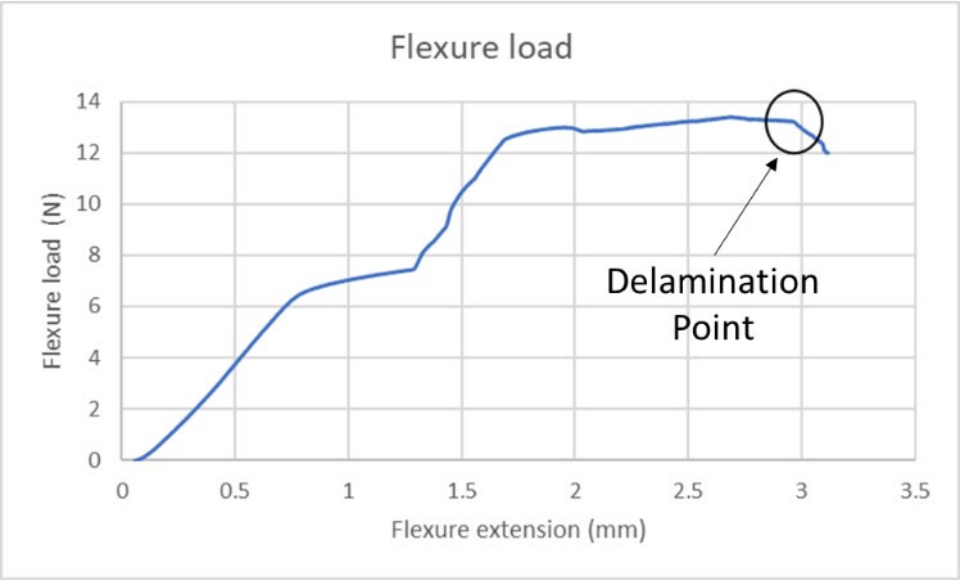

Figure 7-5 Load-extension curve for pristine condition

The load-extension curve of four-point bending test for pristine condition is shown in Figure *7-5*. We use four-point bending instead of three-point bending to avoid the stress concentration at the delamination point. As the load is applied, the biomaterial specimen starts deflecting. In the first step, crack initiates from the notch to biomaterial interface. As the load increases, delamination starts and the load drops in the load-extension curve. The load inflection point is the delamination point.

The crack propagation and delamination procedure are captured by camera showing in Figure *7-6*. The crack propagates from beginning to 80s from notch to the interface. The delamination initiates between 80s and 90s. The delamination propagates from 90s to 100s.

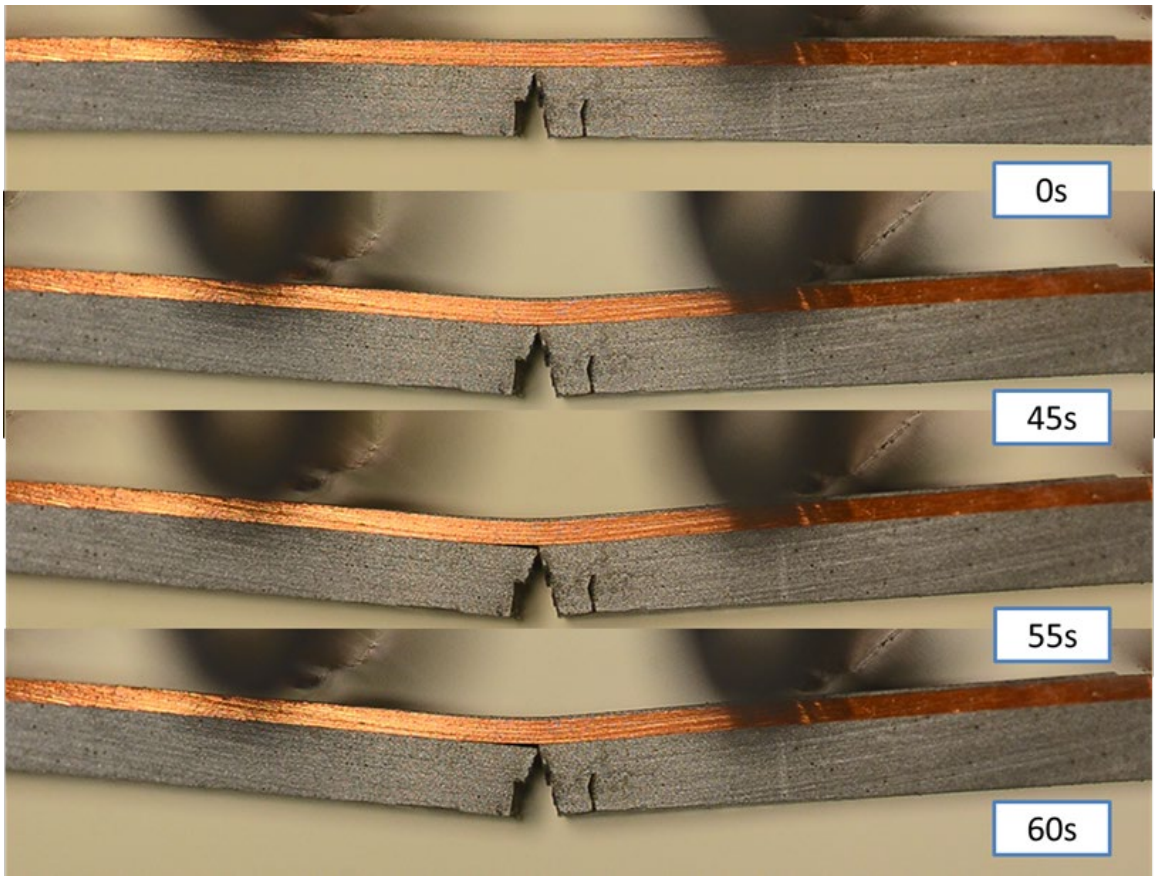

Figure 7-6 Delamination of four-point bending test for pristine condition

K_I and K_{II} of delamination are calculated based on the peak load. K_I and K_{II} for samples from pristine to 120 days aged under 100C and 150C are plotted in Figure *7-7* and Figure *7-8*. Aging temperature shows a significant influence on material degradation. For 100C aging condition, K_I drops from 0.6 to 0.3 from pristine to 120days. Only 19% degradation occurs in first 40 days. About 40% degradation occurs from 40 days to 80 days and from 80 days to 120 days. However, for 150C aging, K_I drops from 0.6 to 0.1 in 120 days. Major degradation occurs in first 40 days. 74% degradation occurs in 40 days, while only 12% degradation occurs from 40 days to 80 days and from 80 days to120 days.

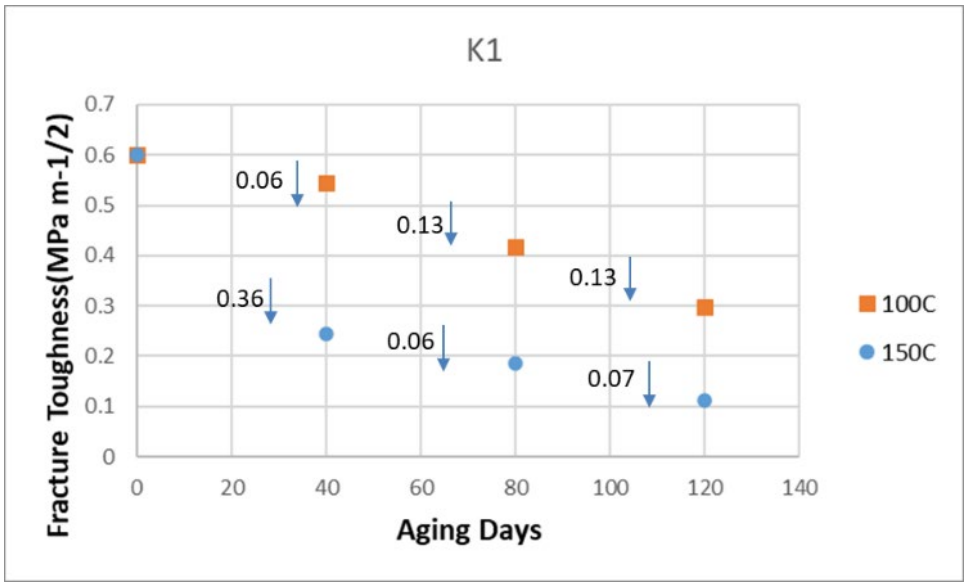

Figure 7-7 K_I for no surface cleaning

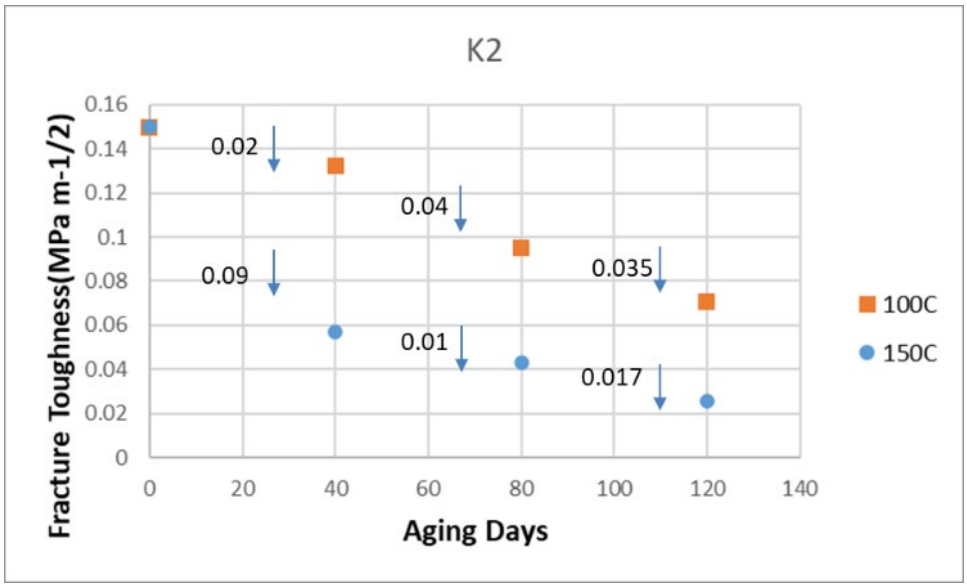

Figure 7-8 K_{II} for no surface cleaning

The similar trend is observed for K_{II}. For 100C aging condition, K_{II} drops from 0.15 to 0.07 from pristine to 120days. Only 21% degradation occurs in the first 40 days. About 40% degradation occurs from 40 days to 80 days and from 80 days to 120 days. However, for 150C aging, K_{II} drops from 0.15 to 0.026 in 120 days. Major degradation occurs in the first 40 days.

77% degradation occurs in 40 days, while only 11% degradation occurs from 40 days to 80 days and from 80 days to 120 days.

Fracture toughness for materials with no surface treatment, 100W oxygen cleaning and 400W oxygen plasma cleaning are showing in Figure 7-9 and Figure 7-10. Plasma cleaning is the removal of impurities and contaminants from the surface through energetic plasma. Oxygen plasma will clean the surface and increase the wettability. Oxygen gas is commonly used to clean non-metal materials such as glass, plastics, and Teflon. It can also be used to clean metal surfaces if it's mixed with Argon. Argon gas strips the oxygen molecule away from the metal to prevent oxidation. In our study, plasma will oxidize the bare copper surface, which might decrease the wettability. In this case, biomaterial strength may not increase after cleaning procedure. We report that 100W cleaning has better performance than 400W, which could be explained by the increase of oxidation layer. For 100C aging, bonding strength decreases after cleaning in 90 days, but shows better robust from 90 days to 120 days. However, for 150C aging, 100W cleaning has better performance than the copper without cleaning.

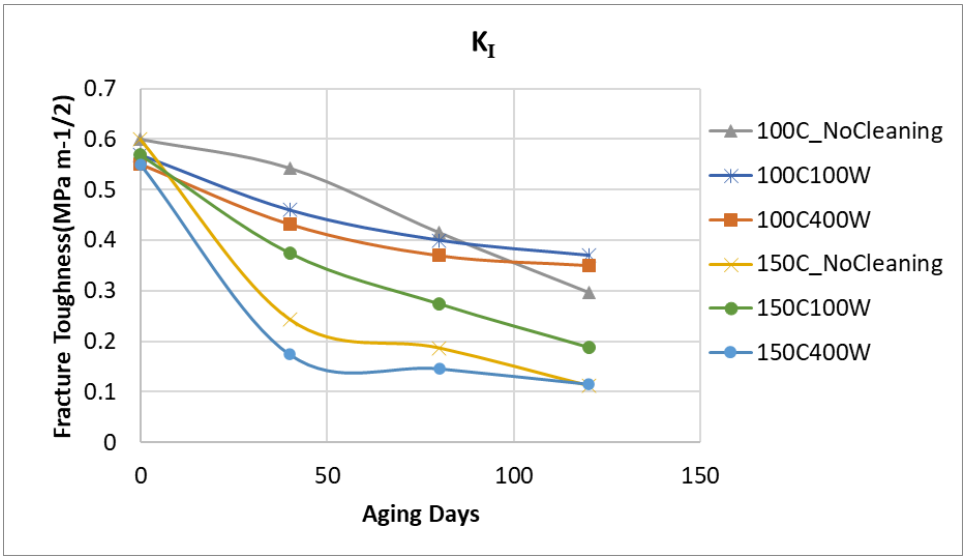

Figure 7-9 K_I for Surface treatment

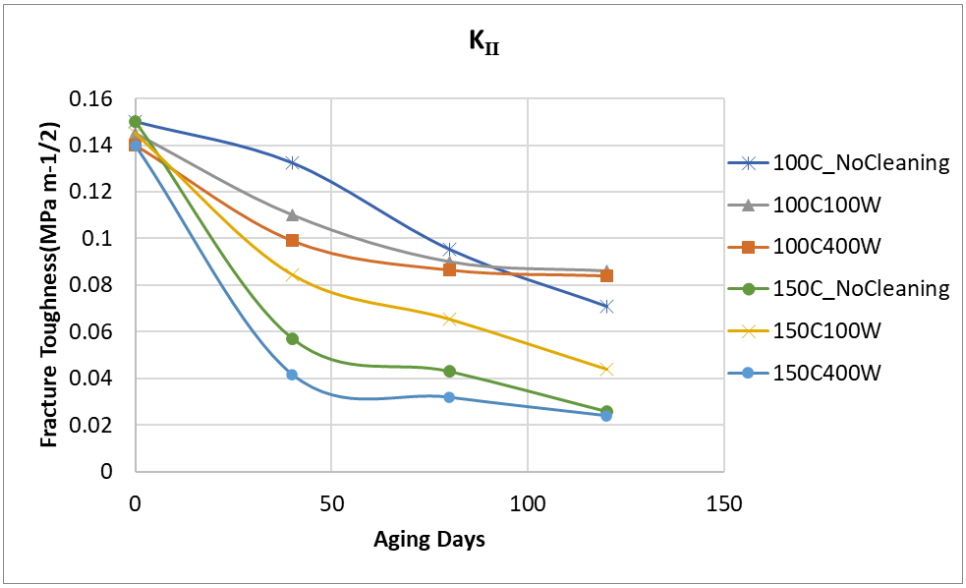

Figure 7-10 K_{II} for surface treatment

7.2.2**Fatigue Analysis**

Fatigue crack propagation is investigated in this section. Regions 1 and 3 are removed from the plot. We only keep region 2, which captured the steady state of fatigue crack propagation. Fatigue crack growth has been plotted in log-log scale, using the equation of Paris power law. Pristine condition is plotted in Figure 7-11. 100C 80 days and 120days aging with no surface treatment is plotted in Figure 7-12 and Figure 7-13. 150C 40days aging is plotted in Figure 16.

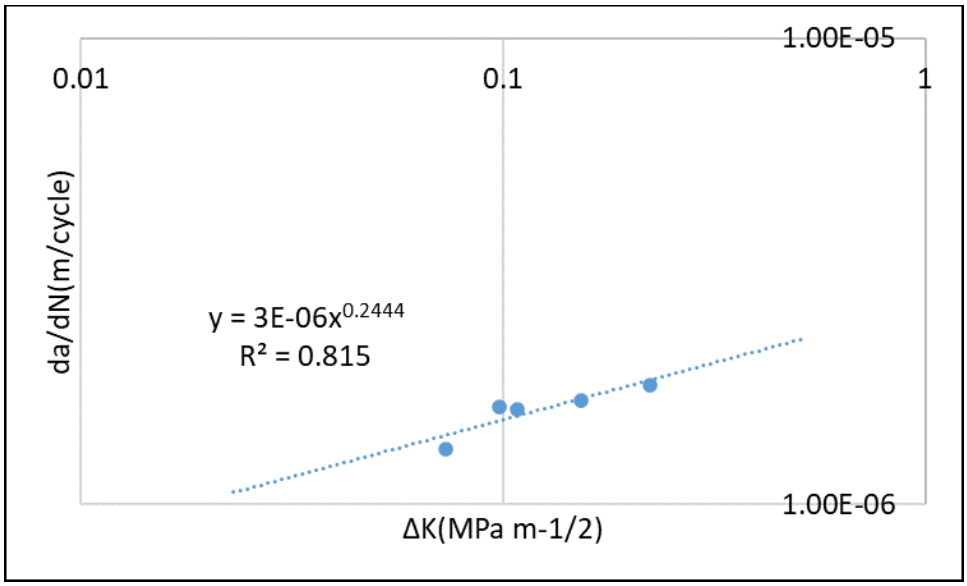

Figure 7-11 Pristine No surface cleaning

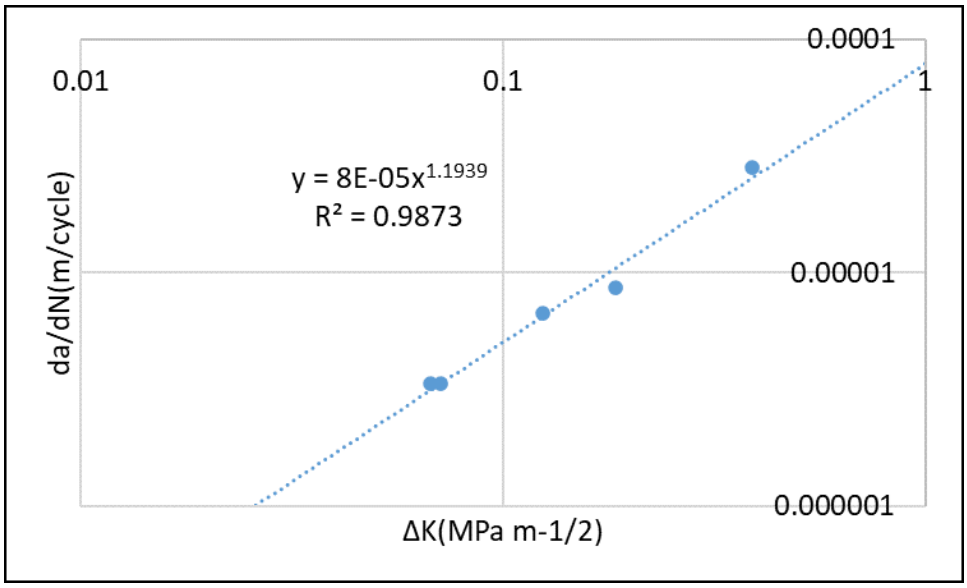

Figure 7-12 100C 80days No surface cleaning

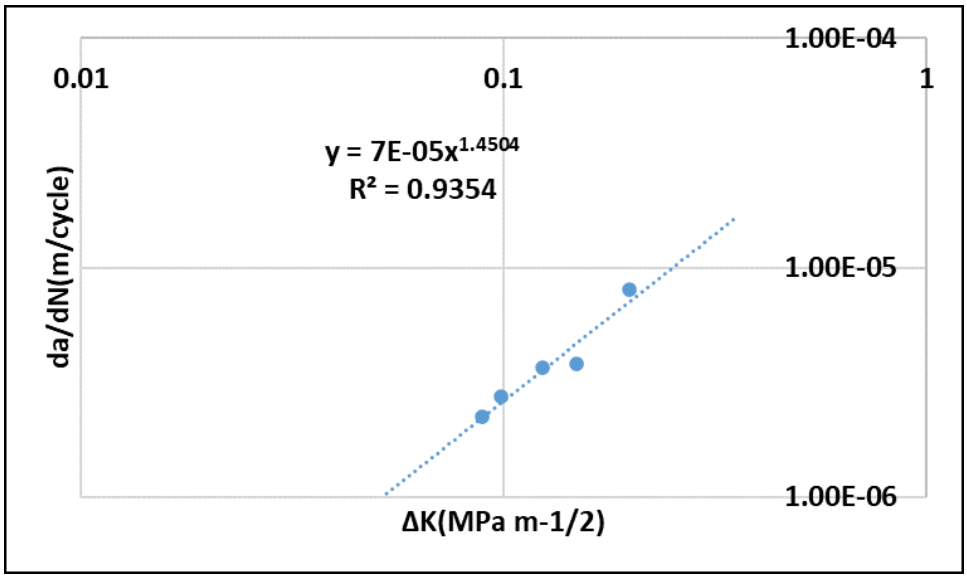

Figure 7-13 100C 120days No surface cleaning

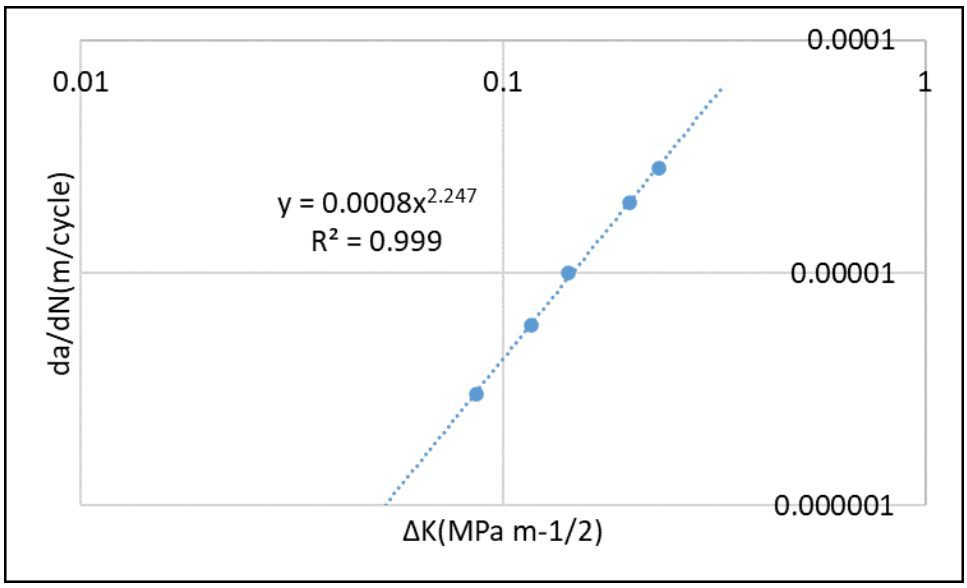

Figure 7-14 150C 40days No surface cleaning

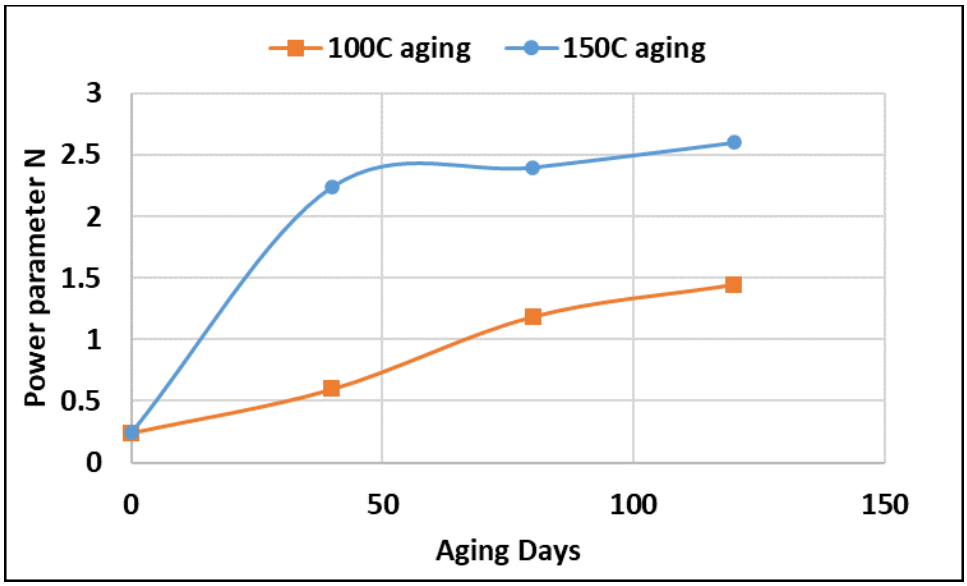

Figure 7-15 Power parameter as function of aging time

The power parameter as function of aging time is plotted in Figure 7-15. The evolution shows that the parameter increases as the aging time increases from pristine to 120 days. It indicates the increase of material brittleness as the aging time increases. The increase of brittleness weakens the interfacial strength. The parameter significantly increases for 150C aging, which indicates the dramatic increase of material brittleness under 150C environment compared to 100C environment. Thus, the interfacial fatigue resistance decreases as the brittleness of TIM increases. Delamination of bi-material is easier to initiate as the material degrades and becomes more brittle.

7.3*Conclusion*

In this study, both monotonic and fatigue tests are applied to study the surface treatment effect of TIM/Copper interface under high temperature long term aging. TIM becomes much more brittle after long term aging, which significantly decreases the strength of interfaces. For 100C aging, material accelerated degrades as the aging time increases. However, for 150C aging, major degradation occurs in the first 40 days. Data could not be obtained after 120days aging due to the

sample's failure. The aging influence of fatigue crack growth is also characterized. The fatigue crack grows faster, and life of fatigue drops as the material brittleness increases.

7.4*Thermal Conductivity Evolution of Thermal Interface Material*

7.4.1**Introduction**

PFAS, or per- and polyfluoroalkyl substances, are a large group of man-made chemicals that include over 4,700 different compounds. These substances are known for their ability to resist heat, oil, stains, grease, and water. This unique set of properties makes PFAS extremely useful in a wide variety of industrial applications and consumer products such as non-stick cookware, water-repellent clothing, stain-resistant fabrics and carpets, some firefighting foams, and products that resist grease, water, and oil. Despite their benefits, PFAS are often referred to as "forever chemicals" because they do not break down in the environment and can accumulate over time. The chemical bonds that make PFAS so durable also make them highly persistent in the environment and in human and animal bodies, leading to widespread contamination.

PFAS (per- and polyfluoroalkyl substances) are widely used in electronic packaging materials due to their unique properties, such as chemical and thermal stability, electrical insulation, and moisture resistance. These characteristics can significantly enhance the performance and durability of electronics, particularly in environments that demand robust heat and chemical resistance.

Applications in Electronic Packaging:

- Moisture and Chemical Resistance: In electronics, moisture can lead to short circuits and corrosion, while exposure to harsh chemicals can degrade materials. PFAS are used in

coatings and components that require high resistance to these elements, helping to prolong the lifespan of the devices.

- Thermal Management: The thermal stability of PFAS makes them suitable for use in situations where heat dissipation is crucial, such as in high-performance processors and power electronics. They can help manage the heat generated by these components, thereby maintaining the integrity and performance of the device.
- Electrical Insulation: PFAS have excellent dielectric properties, meaning they can provide effective insulation in electrical applications. This makes them useful in the protective coatings of wiring and electronic components, where preventing electrical leaks and shorts is critical.

Despite their benefits, the use of PFAS in electronic packaging raises environmental and health concerns similar to those associated with their use in other industries. The durability that makes PFAS so valuable also means they do not break down in the environment, leading to potential accumulation and persistence. Moreover, during the disposal and recycling of electronic devices, PFAS can leach out, contributing to environmental pollution.

As awareness of these issues grows, there is increasing pressure on the electronics industry to find alternatives to PFAS that do not compromise performance or safety. Research is ongoing into alternative materials that can provide similar benefits without the environmental and health risks associated with PFAS. For instance, efforts are being made to develop bio-based or other

non-fluorinated polymers that offer resistance to heat, chemicals, and electricity, similar to PFAS, but are more environmentally friendly and safer in terms of human health impacts.

The electronics industry, along with regulatory bodies, is also working on better recycling technologies and disposal practices to manage PFAS-containing materials at the end of their life cycle, aiming to minimize environmental contamination.

This paper focuses on evaluating the reliability and stability of non-PFAS electronic packaging materials, specifically TIM and Underfill. The study involves the preparation and curing of thermal interface material (TIM). The experimental procedure for measuring the impact of humidity aging on thermal conductivity evolution. Samples are subjected to different aging conditions (60C60%RH and 85C85%RH) The aging effect of polymer materials in electronics applications has been investigated by prior researchers. The reliability assessment for thermal performance of thermal interface materials is also investigated and discussed [38-40]. However, non-PFAs materials have not been studied yet. In this study, we are following the JESD22-A113, which requires samples to be exposed to both 60C60%RH and 85C85%RH for 168 hours duration, and JESD22-A101, which specifies that samples should survive 85°C/85%RH conditions for over 1000 hours. In our investigation, samples were exposed to 85°C/85%RH for over 2000 hours to evaluate their reliability performance.

Before you begin to format your paper, first write and save the content as a separate text file. Complete all content and organizational editing before formatting. Please note sections A-D below for more information on proofreading, spelling and grammar.

Keep your text and graphic files separate until after the text has been formatted and styled. Do not use hard tabs, and limit use of hard returns to only one return at the end of a paragraph. Do not add any kind of pagination anywhere in the paper. Do not number text heads-the template will

do that for you. Figure 5 shows the non-PFAS Underfill sample in Flex TPS test. The thermal conductivity is 0.4W/mK. The diffusivity is 9.7759E-8 m^2/s. Heat capacity is 3.75MJ/m^3K.

The measurement of MTPS is conducted using uncured UF. The uncured UF dispenses on the surface of the sensor Figure *7-17*. The test is conducted in the room temperature of 23C. The value of thermal conductivity and effectivity will be recorded as the time increases Figure **7-18**. The value of thermal conductivity is increase in the beginning due to the unstable state. It is stable from the second record between 0.52 to 0.53 W/mK, which is slightly higher than the result from the Flex TPS test. It could be explained by the curing effect. The average thermal conductivity is 0.5251 W/mK. The effectivity is 883.3 $Ws^{1/2}$ /m^2K.

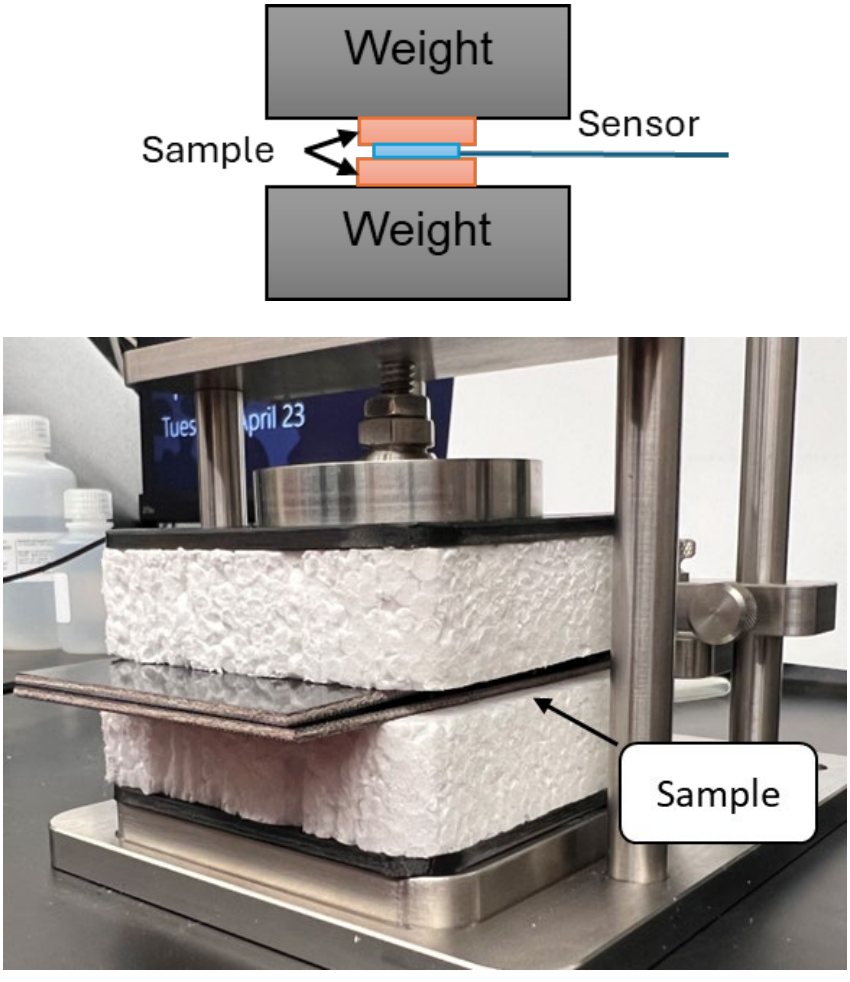

Figure 7-16 Flex TPS Test Setup

Figure 7-17 Schematic of MTPS for Uncured UF

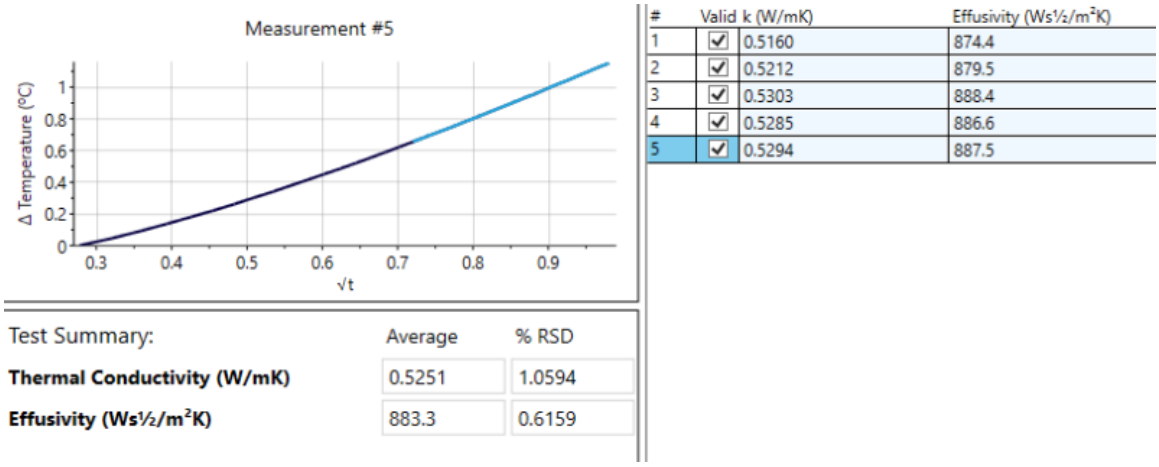

Figure 7-18 MTPS Result of uncured UF

Similar measurements are conducted to non-PFAs TIMs materials. The uncured TIMs are measured by MTPS methods, while the cured samples are measured by Flex TPS methods. The results of Flex TPS method is showing in Figure 7-19. Thermal conductivity, Diffusivity and heat capacity are measured simultaneously. The results for both cured and uncured samples are listed in Table 7-4 and Table 7-5. For TIM 1, the thermal conductivity for cured samples is around 4.35-

4.65(W/mK). For uncured sample, the thermal conductivity is 5.2(W/mK). It shows that curing effect will reduce thermal conductivity. For TIM 2, the thermal conductivity for cured samples is around 3.04-3.17(W/mK). For an uncured sample, the thermal conductivity is 3.9(W/mK).

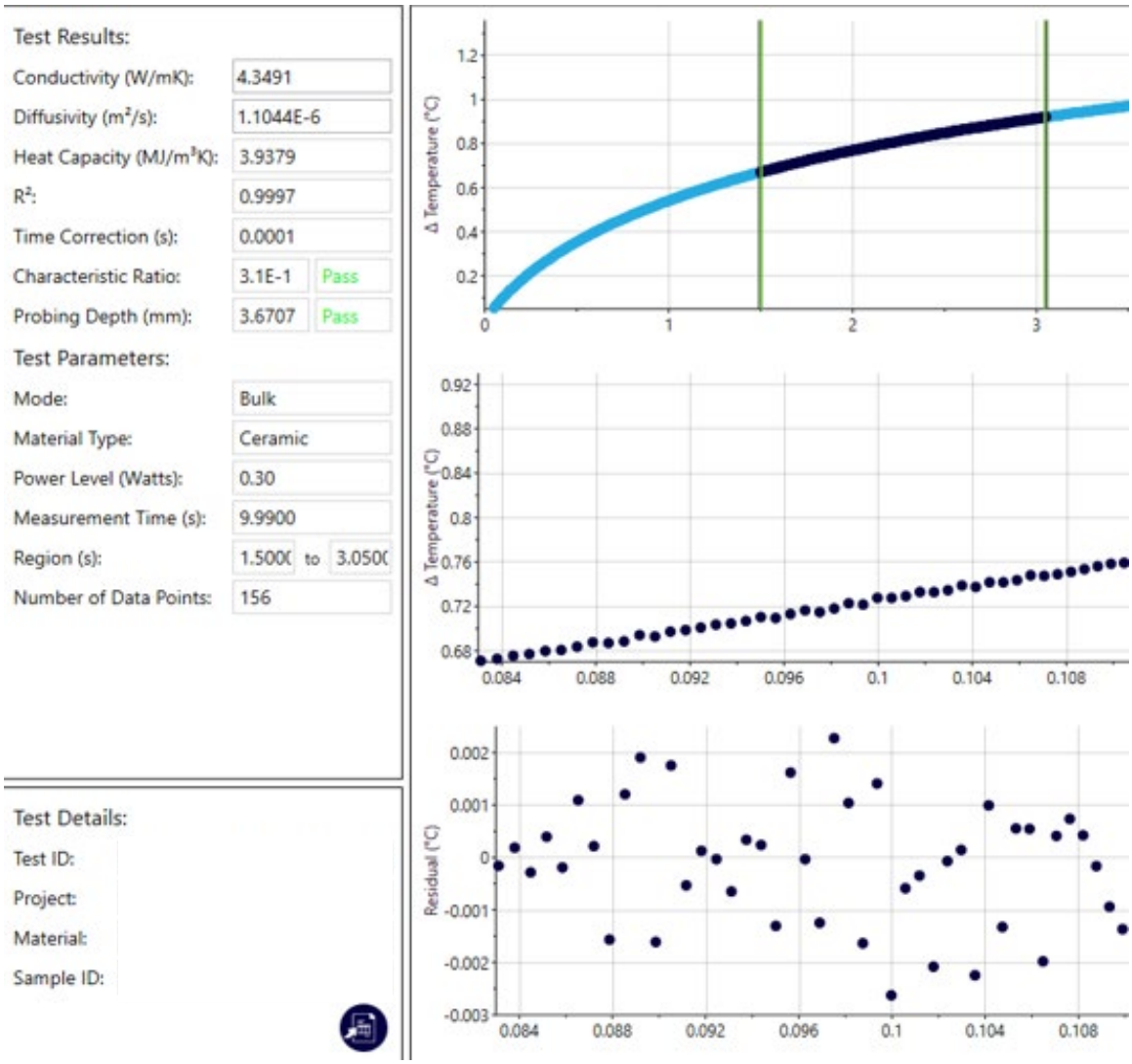

Figure 7-19 Flex TPS Results for Cured TIM1

Table 7-4 Thermal Conductivity of Pristine TIM1

TIM1	Thermal Conductivity(W/mK)

Uncured	5.2
Cured	4.35-4.65

Table 7-5 Thermal Conductivity of Pristine TIM2

TIM2	Thermal Conductivity(W/mK)
Uncured	3.9
Cured	3.04-3.17

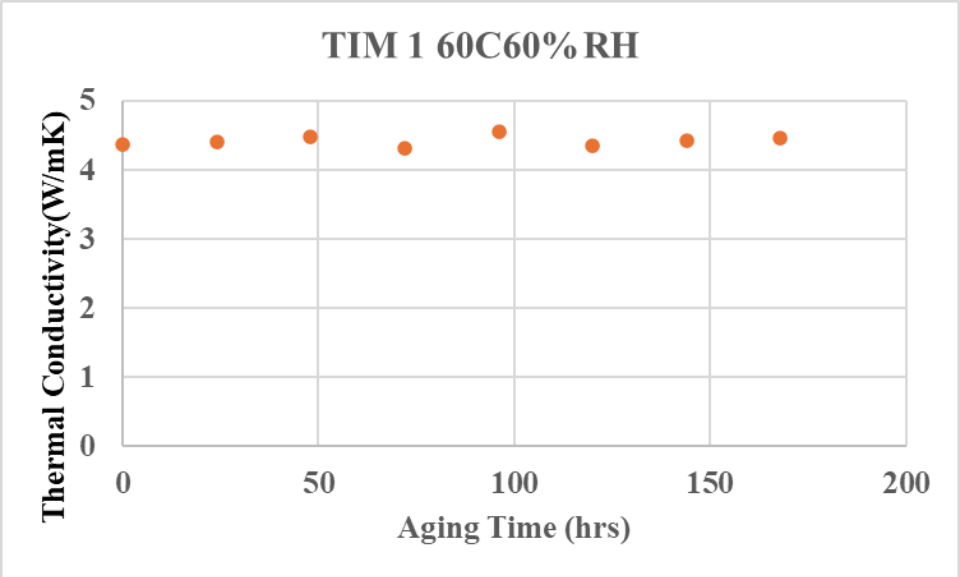

Figure 7-20 Thermal Conductivity of TIM1 under 60C60%RH

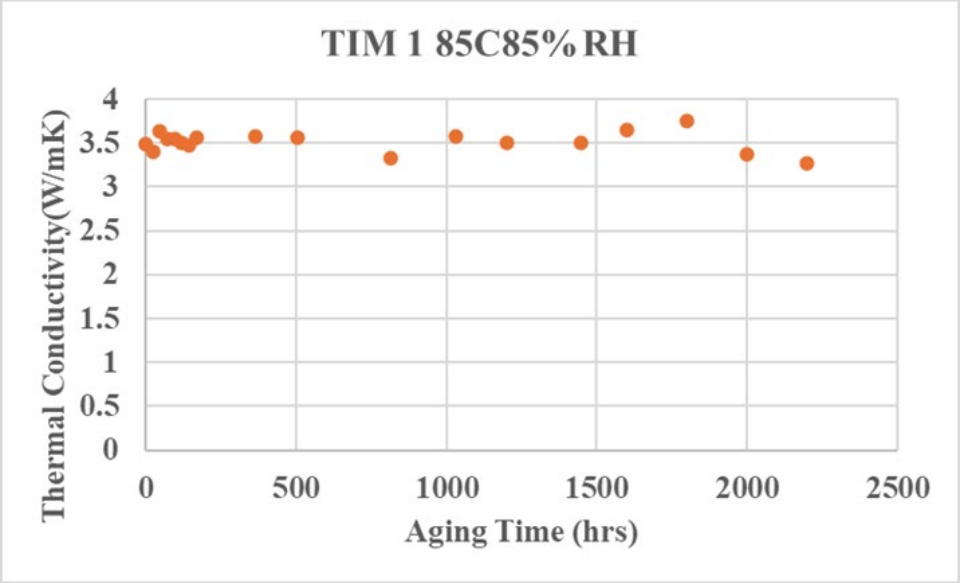

Figure 7-21 Thermal Conductivity of TIM1 under 85C85%RH

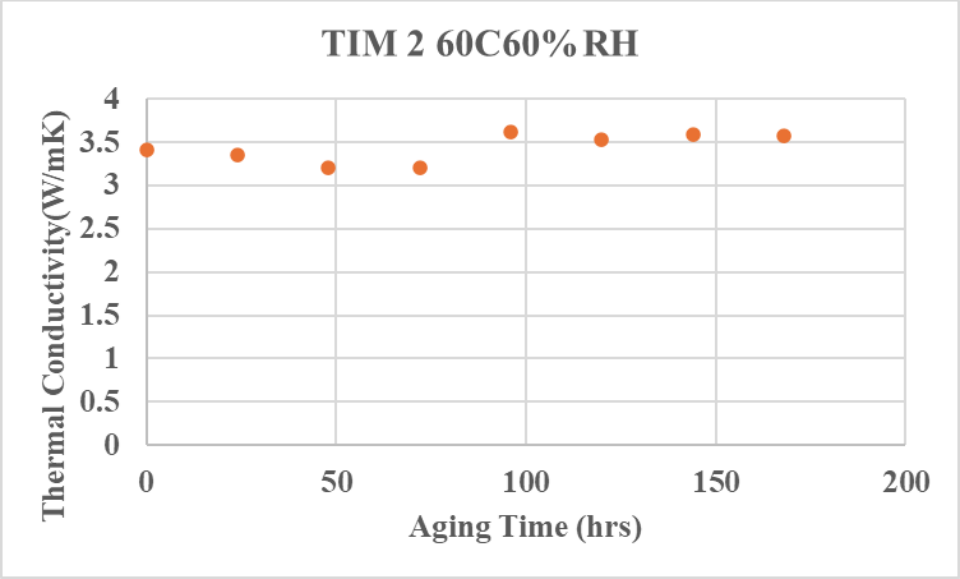

Figure 7-22 Thermal Conductivity of TIM2 under 60C60%RH

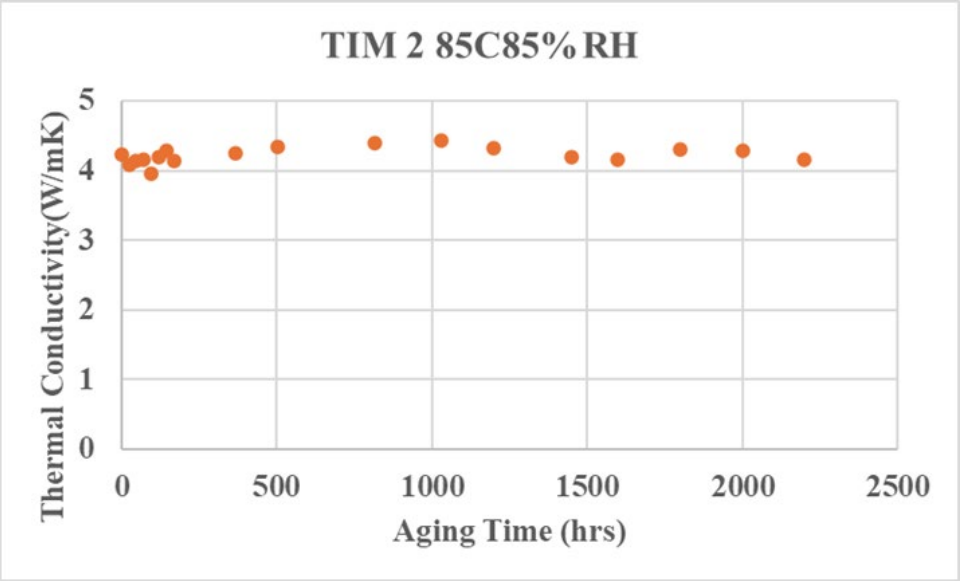

Figure 7-23 Thermal Conductivity of TIM2 under 85C85%RH

Samples are placed in test chambers to undergo temperature and humidity assessments under two conditions: 60°C at 60%RH and 85°C at 85% RH for a period of 168 hours. The thermal conductivity is determined using the Flex TPS method. The results for TIM1 are displayed in Figure 7-20 and Figure 7-21, indicating the stability in thermal conductivity with increased exposure time. Specifically, after 168 hours, the thermal conductivity at 60°C and 60% RH reduced from 4.65 W/mK to 4.5 W/mK. At 85°C and 85% RH, it fell from 3.5 W/mK to 2.26 W/mK after 2200 hours. The data for TIM2, presented in Figure 7-22 and Figure 7-23, show that at 60°C and 60% RH, thermal conductivity initially rose from 3.48 W/mK to 3.5 W/mK within in the duration

of 168 hours. In the meantime, at 85°C and 85% RH, conductivity decreased from 4.22 W/mK to 4.1 W/mK at the conclusion of the test duration.

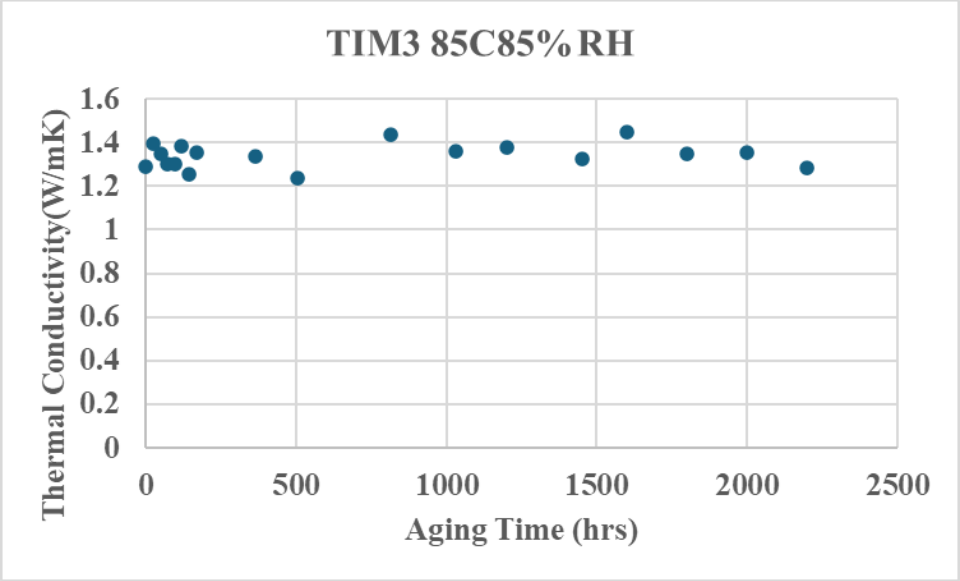

Figure 7-24 Thermal Conductivity of TIM2 under 85C85%RH

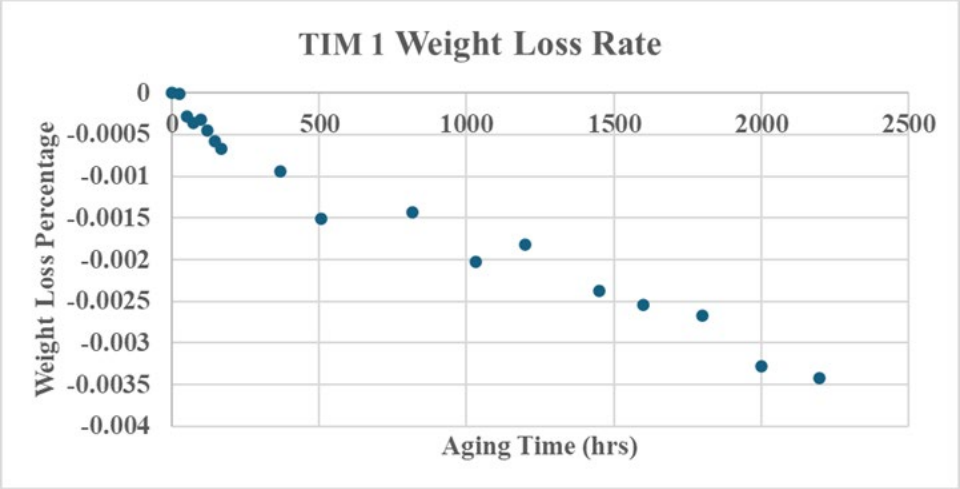

Figure 7-25 Weight loss of TIM1 under 85C85%RH

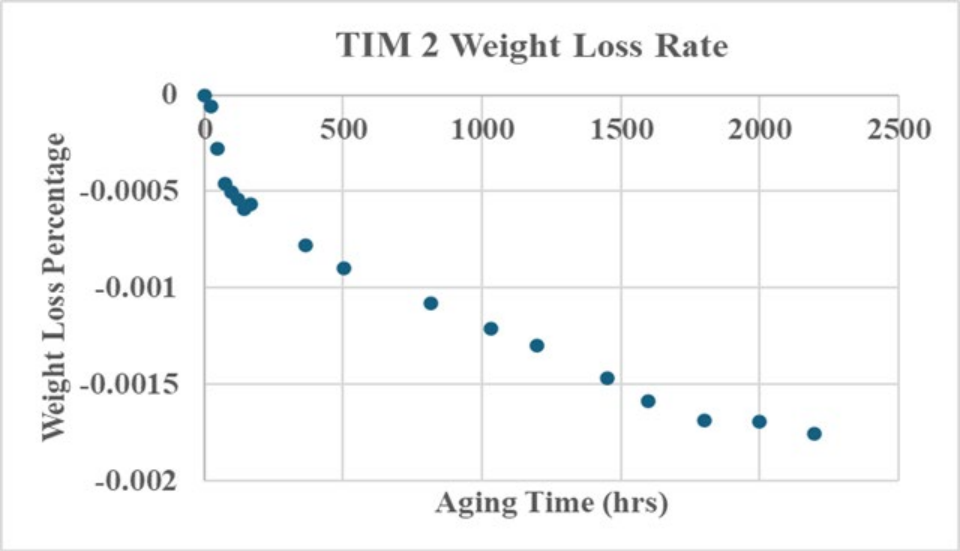

Figure 7-26 Weight loss of TIM2 under 85C85%RH

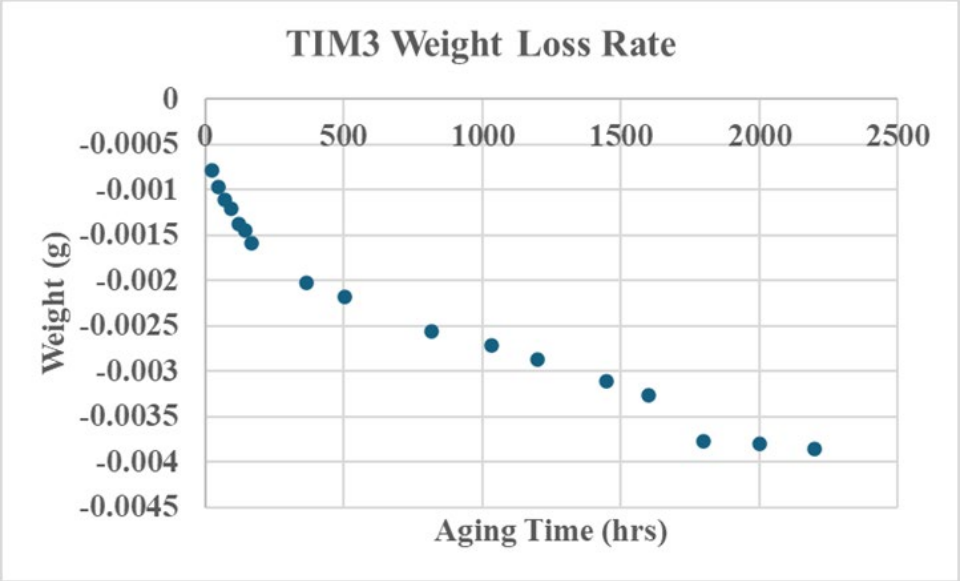

Figure 7-27 Weight loss of TIM3 under 85C85%RH

The data for TIM3, which is non-PFAS TIM, is presented in Figure 7-24. The thermal conductivity does not change significantly in 2200 hours. It could be explained by the material stability due to PFAS. The weight loss of samples as function of aging time is also explored. It shows that the sample weight continuously decreases as the aging time increases.

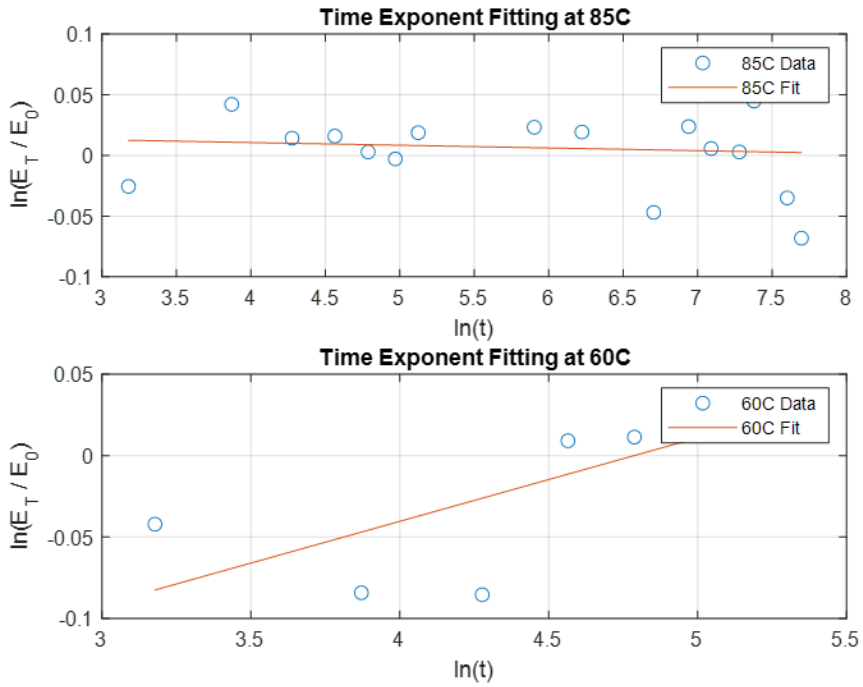

Figure 7-28 Time exponent n for TIM1 85C= -0.0022, 60C= 0.0513

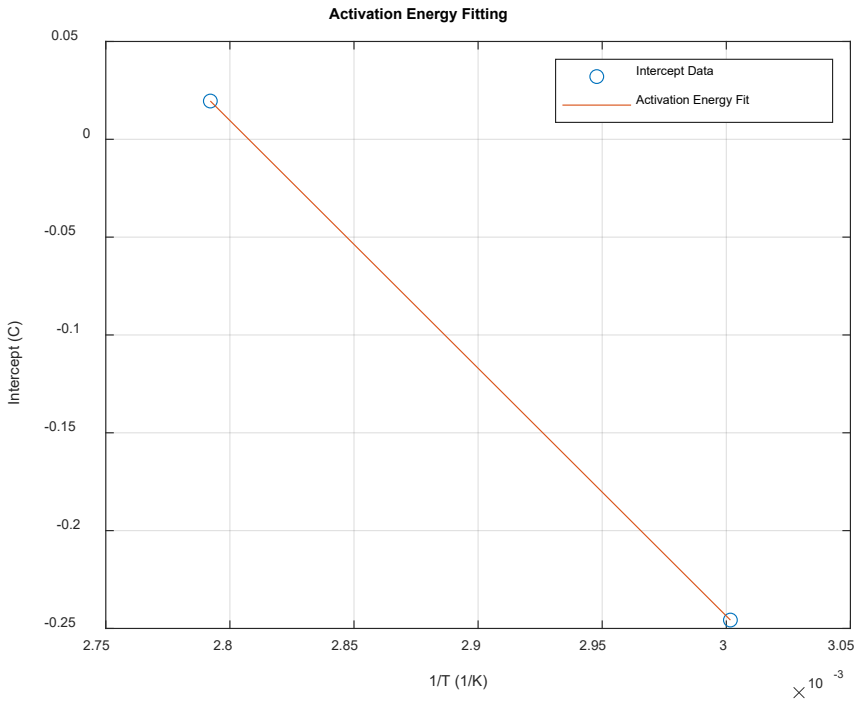

Figure 7-29 Activation energy for TIM1 Ea = 0.1091 eV

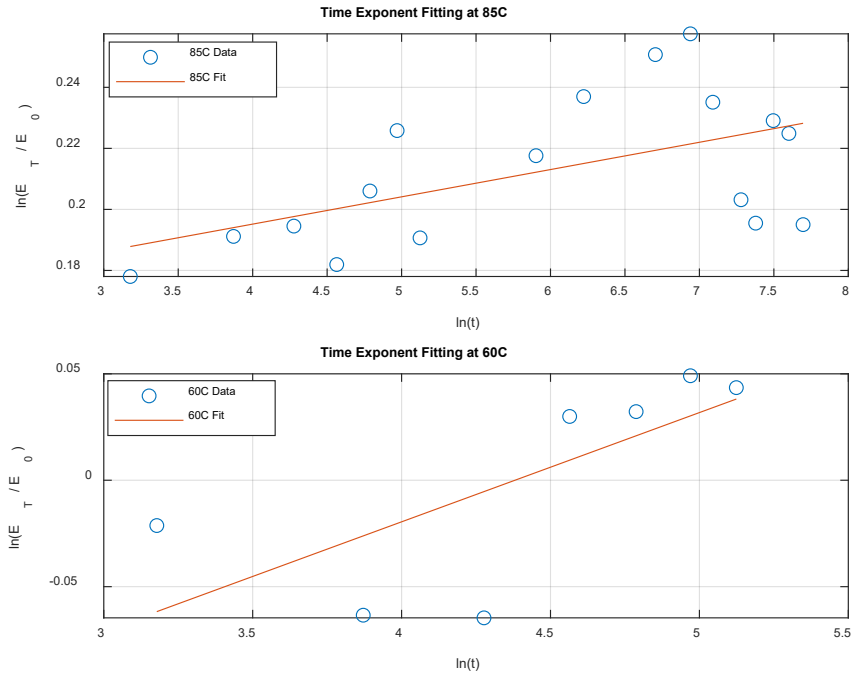

Figure 7-30 Time exponent n for TIM2, 85C= 0.0089, 60C= 0.0513

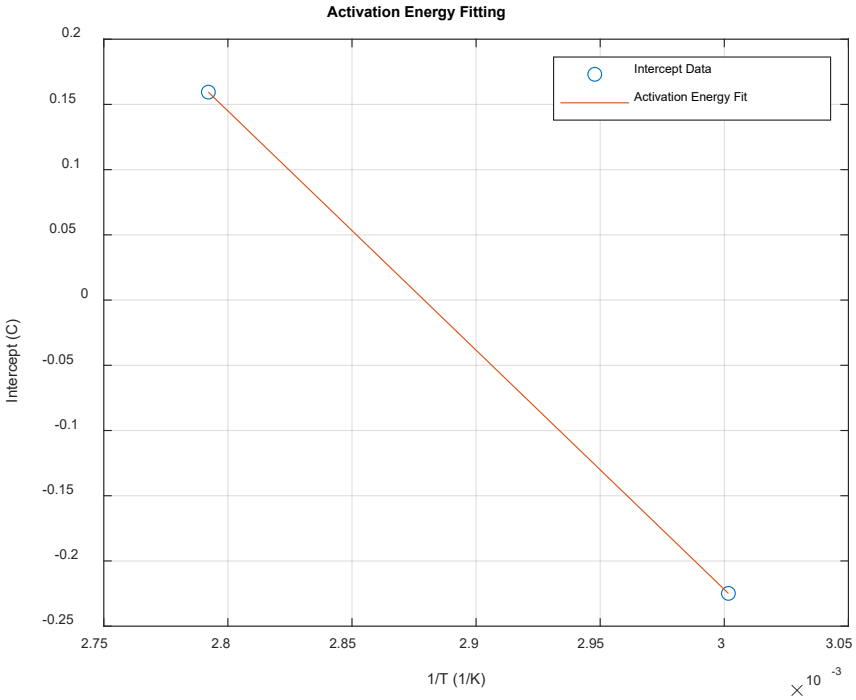

Figure 7-31 Activation energy for TIM2 Ea = 0.1580 eV

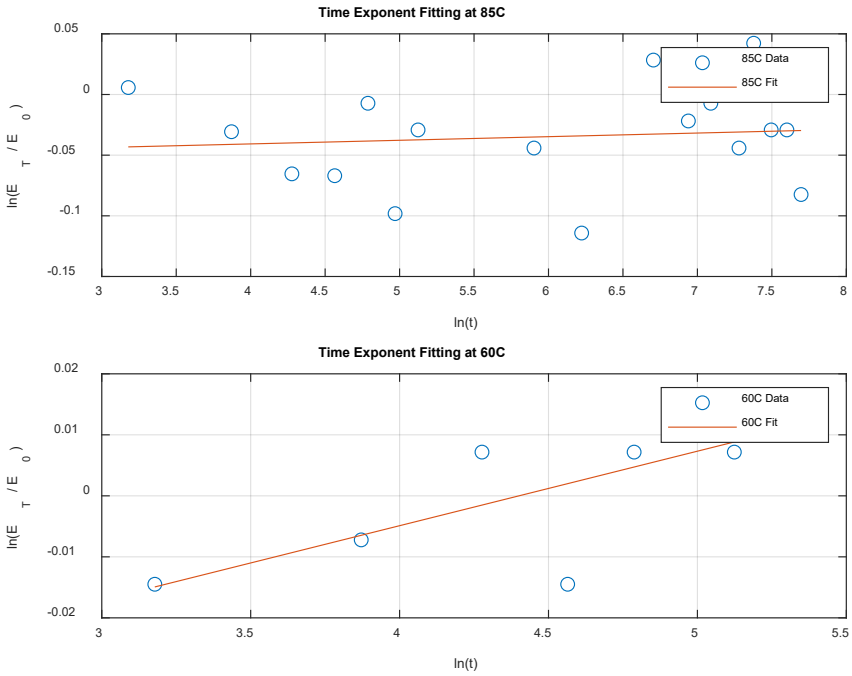

Figure 7-32 Time exponent n for TIM3, 85C = 0.0030, 60C = 0.0122

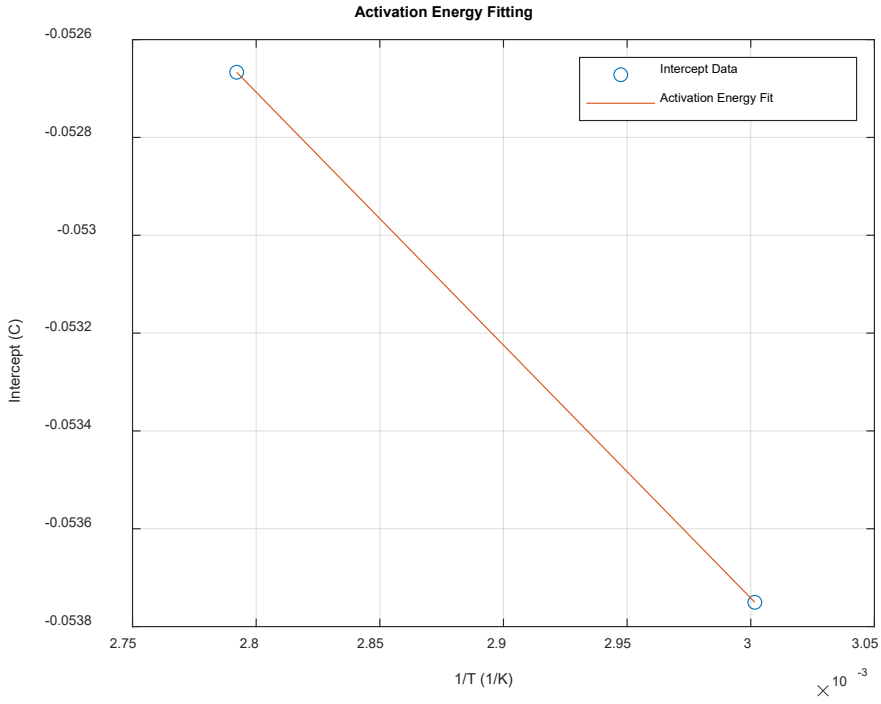

Figure 7-33 Activation energy for TIM3 Ea = 0.0004 eV

The Arrhenius Equation is also applied to evaluate the aging effect and the temperature effect on activation energy. For TIM1 (Figure 7-28 and Figure 7-29), time exponent n, indicating the aging effect, for 85C is -0.0022, for 60C is 0.0513. The activation energy is 0.1091eV. For TIM2 (Figure 7-30 and Figure 7-31), time exponent n for 85C is 0.0089, for 60C is 0.0513. the activation energy is 0.158eV. For TIM3 (Figure 7-32 and Figure 7-33), the time exponent for 85C is 0.003, for 60C is 0.0122. The activation energy is 0.0004eV. The results show that the activation energy for TIM3 is much lower than TIM1 and TIM2, which indicating the stability of PFAS. What is more, the n of TIM1 slightly decreases under 85C, which indicates the degradation of material under high temperatures and humidity environments.

In this study, the transient plane source method is employed to measure the thermal conductivity of non-PFAs UFs and TIMs. For uncured samples, a modified transient plane source method is used, while the Flex Transient Plane Source method is applied to cured samples. The research investigates the evolution of thermal conductivity in TIMs exposed to high temperature and humidity environments (85°C and 85% RH) and (60°C and 60% RH) over a period of 168 hours and more than 2200 hours. The curing process is found to reduce thermal conductivity. Samples are prepared for thermal conductivity testing, revealing the following results:

- For TIM 1, thermal conductivity decreases from 3.5 W/mK to 3.26 W/mK, from its pristine state to after 2200 hours at 85°C and 85% RH. The activation energy is 0.1091eV.
- For TIM 2, thermal conductivity initially increases during the first 1000 hours, rising by 5% at 85°C and 85% RH, However, after 1000 hours, it decreases by 4% at 85°C and 85% RH. The activation energy is 0.158eV

- For TIM3, which is PFAS TIM, thermal conductivity does not change significantly for 2200 hours. It shows the stability of PFAS. The activation energy is 0.0004eV, much lower than TIM1 and TIM2.

Chapter 8 Summary and Conclusion

This dissertation investigates the evolution of material properties in key electronic packaging materials, including underfill encapsulants (UF), epoxy molding compounds (EMC), thermal interface materials (TIM), and magnetically oriented anisotropic conductive adhesives (ACA), under isothermal high-temperature aging conditions. The study focuses on understanding the thermo-mechanical behavior, viscoelasticity, thermal stability, fatigue performance, and interfacial integrity of these materials, which are critical for the reliability of semiconductor devices operating in harsh environments.

The research reveals that underfill materials, essential for mitigating coefficient of thermal expansion (CTE) mismatches in flip-chip technology, undergo significant degradation under high-temperature aging. Dynamic mechanical analysis (DMA) and thermogravimetric analysis (TGA) demonstrate that the storage modulus, loss modulus, and glass transition temperature (Tg) of underfills are highly temperature-dependent. Long-term aging studies on EMCs highlight the influence of filler content and microstructure on thermal and mechanical properties, with high silica filler concentrations improving thermal stability but introducing challenges in fatigue performance. Finite element modeling (FEM) further elucidates stress distributions at the wire interface, correlating material aging with increased stress accumulation.

Thermal interface materials (TIMs) are evaluated for their efficiency in reducing thermal resistance between microelectronic components. Conventional TIMs, such as greases and phase-change materials, exhibit limitations in high-power applications due to viscosity-induced reliability issues. Novel TIM formulations incorporating carbon-based fillers, such as carbon nanotubes and graphene, show superior thermal conductivities, though their widespread adoption is constrained by cost considerations.

Magnetically oriented ACAs are explored for their potential in flexible and stretchable electronics. By aligning conductive particles under a magnetic field, these materials achieve directional conductivity and robust mechanical performance. Experimental and finite element studies demonstrate enhanced interconnect reliability under mechanical and thermal cycling.

The findings of this research provide valuable insights into material design and selection strategies for electronic packaging, addressing challenges posed by elevated temperatures and mechanical stresses. The work contributes to the advancement of packaging technologies, enabling reliable performance in applications ranging from consumer electronics to automotive and aerospace systems. By understanding the degradation mechanisms and property evolution of these materials, this dissertation lays the groundwork for developing more durable and efficient electronic packaging solutions for future technologies.

Appendix A Cu-Al Wire Bond Corrosion

A.1 Copper Wire Bond Interconnect

Wire bonding is a technique which forms connections between an integrated circuit (IC) and a metal lead frame during the process of microelectronics packaging. Figure 8-1 illustrates a typical chip-level connection created using wire bonding. It provides an electric path both from and to a substrate for signal transmission and power distribution. It is the working horse technique in the manufacturing industry to make fine-pitch microelectronics. Compared to other existing chip- connection approaches such as flip chip technique or tape automated bonding (TAB), wire bonding forms connections one at a time. In addition, wiring changes can easily be done without retooling, and chip preparation is much less complicated, which makes wire bonding the most flexible chip- connection technique among other techniques.

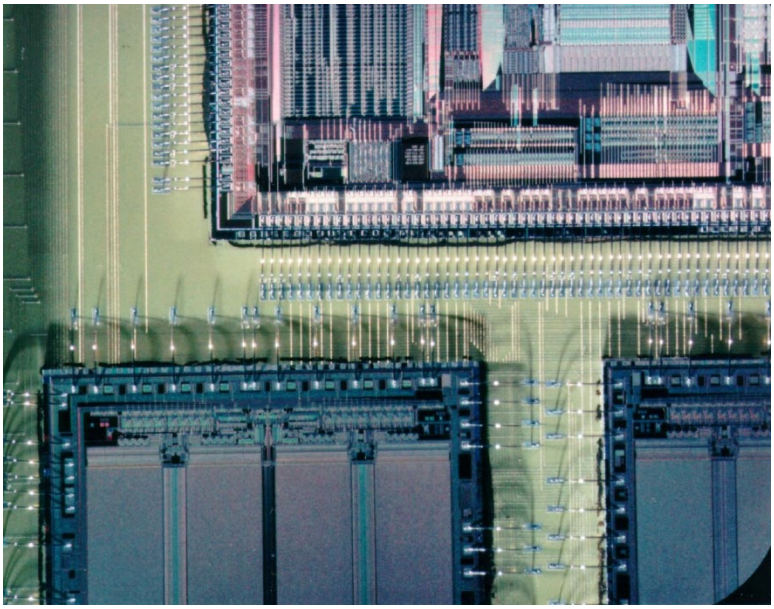

Figure 8-1 Wire bonded Chip

A combination of heat, pressure and ultrasonic energy are used to bond a wire and two bond pads made of different metallic materials to form a wire bond connection. Such technique is

called thermosonic bonding. During the wire bonding process, ultrasonic and heat energy are applied to soften the wire, and pad metallization, while pressure is applied to form a metallurgical bond. There are two types of wire bonds, bond–wedge bonding and wedge-wedge bonding. Currently, most of wire bonds are ball-wedges bonds due to its faster speed in electronic packages [108]. The procedure of forming a ball bond is illustrated in Figure 8-2. In step a, the bonding tool descends to the bond pad location. In step b, a free air ball (FAB) is created by the use of electrical flame-off (EFO). Thermosonic force is used to form the first bond in step c. The last three steps illustrate how the second bond is formed. A wire bonding machine is shown in Figure 8-4.

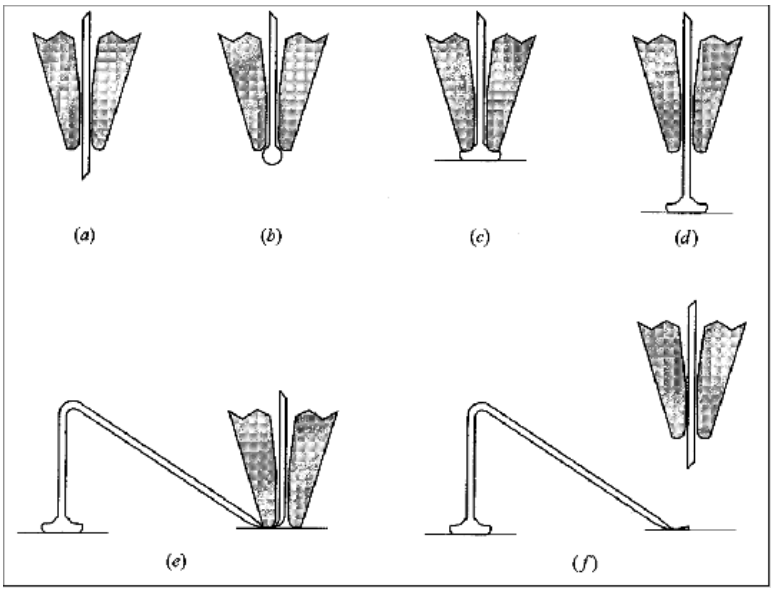

Figure 8-2 Ball Bonding Procedure

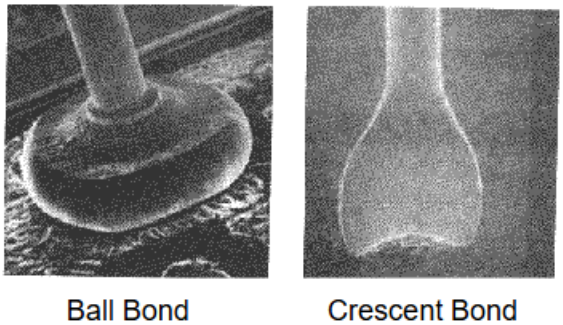

Figure 8-3 Ball bond and crescent bond

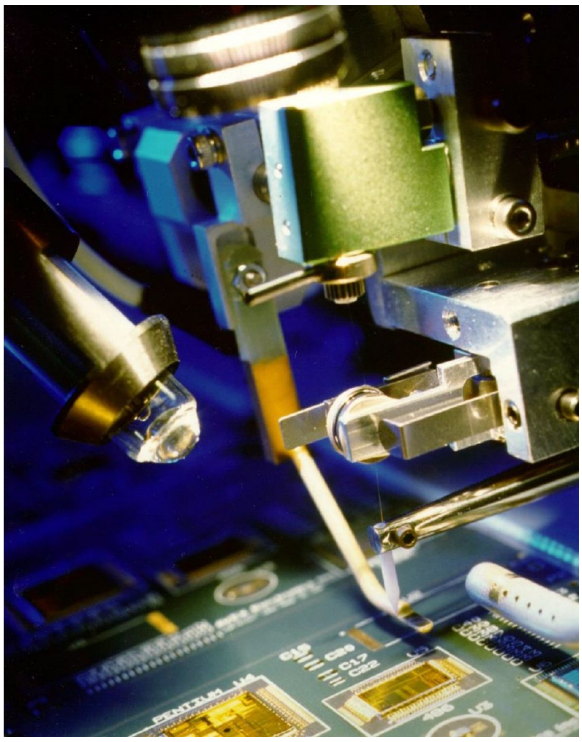

Figure 8-4 Ball bonding machine

Before the emergence of copper wire bond as the main chip-level interconnection, gold wire bond was widely used in microelectronic packages. Unlike copper wire bond, the behavior of gold wire bond has been studied extensively over the years. The advantages of using gold wire bond cover gas free when forming wire bonds, similar radii and electronegativity between gold and the aluminum (pad material) which makes it easy to form a metallic bond, compatible hardness to aluminum which results in minimum Al splash and underneath stress during wire bond process, difficult to be ionized in humid environment, requires less stringent epoxy molding compound encapsulants. Therefore, it is a well-established production, operation and testing guidelines for gold wire bonds.

The rise of copper wire bond as an alternative to gold wire bond is mainly driven by cost-related issues with gold. As of the end of 2016, gold price had reached 1250 dollars per ounce, which is five times higher than the gold price at the beginning of this century. In order to reduce

the cost of their products, microelectronics manufacturers like Taxes Instruments and Freescale starts to transition from gold wire bonding to other wire bonding techniques such as copper wire bonding, palladium coated Cu wire bonding and silver wire bonding. Among those new wire bonding techniques, copper wire bond got the most attentions as Cu wire bonding cost the least and is considered acceptable in terms of manufacturing and reliability [109]. Being used as a bonding material, copper has some superior material properties than gold. For example, higher mechanical strength, lower yield strength, high electrical conductivity, high thermal conductivity and slower Cu-Al IMCs (intermetallic compounds) growth. Stronger mechanical strength allows cooper wire bond to be more reliable under mechanical stress such as shocking and vibration. High thermal and electrical conductivity make it more suitable for fine-pitch applications and high power applications. Lower intermetallic compounds (IMCs) growth rate results in a reduced likelihood of having kirkendall voids or other type of weak IMCs occurred in the wire bonds. Despite of those upsides associated with copper wire bond. It has its share of shortcomings such as easily being oxidized, etc. During the formation of a copper free air ball (FAB), Cu oxidation inhibits the formation of a spherical ball, which in turn affects the reliability of the first bond. Cu oxidation will weaken the bond between Cu and Al, making wire bond prone to corrosion. Therefore, the use of inert gas (forming gas) is required during bond. Also, copper is much harder than Al. Forming a metallic bond between Cu and Al is not as easy as forming a metallic bond between Au and Al. As a result, excessive thermosonic energy are require to soften the ball during the bonding process, which will often lead to undesirable Al splash and excessive damage to the package substrate underneath the pad. Figure 4 shows an example of Al splash during copper wire bonding. The processing window for copper wire bonding is much narrower than that of gold wire bonding. Therefore, it is harder to maintain a consistent wire bond quality in practical

manufacturing. Finally, the most noticeable downside of using copper wire bond is the fact that it is susceptible to corrosion-related failure under exposure to high temperature and/or high humidity operational conditions especially when the contamination of epoxy molding compound used to encapsulate packages are high. Figure 8-5 illustrates a typical SEM image of copper wire bond failure due to excessive corrosion occurred at the copper ball bond-aluminum pad interface. The red zone highlighted in the figure displays the presence of oxygen element, which is commonly spotted when packages are tested under high humidity operational conditions for extended period of time. Another common element found in the case of Cu wire bond corrosion-related failure is chloride ion. These two elements are involved in the corrosion leading to the failure of Cu wire bonds. Suffice it to say that as of now, there are still a lot of challenges for Cu wire bonding to become the leading chip-level interconnection technology, among which the most critical one is to understand the failure mechanism of Cu wire bond under prolonged exposure to harsh operational conditions. Only with a deep understanding of Cu wire bond failure mechanism will researchers and manufacturers be able to come up with engineering solutions to improve the reliability of it. Therefore, produce a more dependable yet cost-effective product.

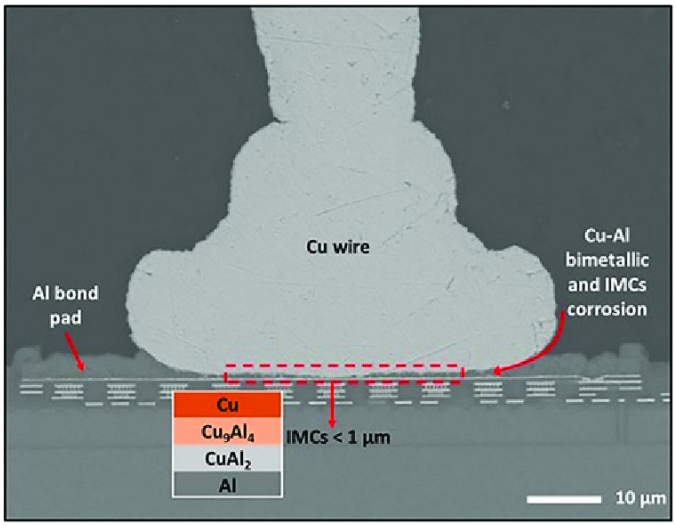

Figure 8-5 Cross-section image of Cu-Al wire ball bond interface

A.2 Introduction to Corrosion Thermodynamics and Kinetics

Nernst Equation

Reactants and products are not typically in their standard states. The Nernst Equation accounts for the effects of activity on reversible potential. In general, for a reaction where the reactants and products are not in their standard states:

$$\Delta G = \Delta G^o + RT \ln \frac{\prod(a_{prod})^k}{\prod(a_{reac})^j}$$

But, for electrochemical half reactions, we have found:

$\Delta G = -nFE^{rev}$ and $\Delta G^o = -nFE^o$

Using our convention of writing all electrochemical reactions as reduction reactions:

$$Ox + ne^- = Red$$

We obtain the following form of the previous equation:

$$E^{rev} = E^o - \frac{RT}{nF} \ln \left[\frac{\prod(a_{red})^j}{\prod(a_{ox})^k}\right] = E^o + \frac{RT}{nF} \ln [\frac{\prod(a_{ox})^k}{\prod(a_{red})^j}]$$

This is the Nernst Equation.

$$a_A = \gamma_A c_A \approx c_A \equiv [A]$$

Thus, for the general electrochemical (reduction) reaction:

$$aA + bB + ne^- = cC + dD$$

the Nernst Equation can be written as:

$$E^{rev} = E^o - \frac{RT}{nF} \ln \left[\frac{[C]^c[D]^d}{[A]^a[B]^b}\right] = E^o - \frac{0.059}{n} \log \left[\frac{[C]^c[D]^d}{[A]^a[B]^b}\right] \text{ at R.T.}$$

Corrosion resistance depends on both **thermodynamics** and **kinetics**. From a corrosion standpoint, **thermodynamics** is the study of materials' tendency to corrode, while **kinetics** is the study of the rate of corrosion. Thermodynamics answers the question "can a metal corrode?" and kinetics answers the question "how fast will it corrode?"

Faraday's Law

$$J = i/nF$$

Where J is ion flux(mol/cm^{2}s), F is Faraday's constant or charge per mole of electrons (96487), n is ion charge or mole of charge (equivalents) per mole of ions (equiv/mol), i is current density (A/cm^2).

Butler-Volmer equation

The relationship between the rate of reaction, or current density i, and the driving force for the reaction, or potential E, for a system undergoing activation polarization is given by the Butler-Volmer equation:

$$i = i_o \exp[\frac{\beta nF(E - E^{rev})}{RT}] - i_0 \exp[\frac{-(1-\beta)nF(E - E^{rev})}{RT}]$$

$$i = i_o \exp[\frac{\beta nF\eta}{RT}] - i_0 \exp[\frac{-(1-\beta)nF\eta}{RT}]$$

where β is a symmetry factor ≈0.5.

The Butler-Volmer equation is for a single electron reaction. It is based on activated state theory, which considers that an activation energy barrier must be overcome to get from one state to another, even if there is a net decrease in free energy between the two states. For an electrochemical reaction, work associated with potential is added to chemical activation energy, just like it is added to chemical free energy.

Tafel Equation

For a sufficiently large value of anodic polarization from the reversible potential (overpotential η> 50 mV), which is satisfied by most corrosion process, the Butler-Volmer equation simplifies to:

$$i = i_o \exp[\frac{\beta nF\eta_a}{RT}]$$

rearranging, one gets the **Tafel equation**:

$$\eta_a = b_a \log(\frac{i}{i_0})$$

where $b_a = 2.3\mathrm{RT}/\beta\mathrm{nF}$ is the anodic Tafel slope, which is active in corrosion process. For β = 0.5 and n = 1, b_a= 0.12 V (or V/decade). This calculation is only for a single electron reaction. Most reactions are very complicated and b ≠0.12 V, but b ≈0.12 V (often 0.04 –0.15 V).

A.3 Galvanic Corrosion

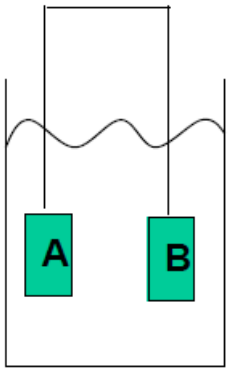

Figure 8-6 Galvanic Corrosion

Galvanic corrosion is a type of electrochemical corrosion that occurs when two dissimilar metals are electrically connected and immersed in the same electrolyte. Under these conditions, a galvanic cell is formed, resulting in the accelerated corrosion of the less noble (more active) metal, while the more noble (less active) metal experiences reduced corrosion and is galvanically protected. The severity of galvanic corrosion is influenced by several factors, including the difference in open-circuit potentials (OCPs) between the two metals, the electrode kinetics of each metal, the ratio of cathodic to anodic surface area, and the resistance of the electrolyte. Understanding and managing these factors is essential to mitigate galvanic corrosion in practical applications.

In galvanic corrosion, where the anodic and cathodic reactions occur on different electrodes with different areas, the Evans diagram must be in terms of I (current) instead of i (current density) because the principle of charge conservation requires that the anodic and cathodic currents (not current densities) be equal.

Consider the effect of area of the cathode:

$$I_a = I_c$$

$$i_a A_a = i_c A_c$$

For single electrode: $A_a = A_c \Rightarrow i_a = i_c$

Galvanic corrosion: $A_a \neq A_c$

$$i_a = \frac{i_c A_c}{A_a}$$

We care about i_a because current density describes the rate of corrosion.

A.4 3-D Numerical Multiphysics Model for Cu-Al Wire Bond Corrosion

Currently, corrosion is one of the major concerns which prevent the mass production copper wire bond. The corrosion of intermetallic compound (IMC) would initiate at Cu-Al wire bond ball bond-pad interface. After that, the crack would initiate and propagate. As the result, the crack would cause the failure of the electronics. Studies about corrosion-related copper wire bond failure have been conducted in last ten years. Researchers show that if people could understand the mechanism of copper wire bond corrosion, which would lead to crack initiation and propagation, the prediction of remaining useful life (RUL) prediction would be possible. Health management of copper wire bond could be well developed, which could be used to build more reliable electronic packaging.

Intermetallic compound which is formatted at Cu-Al interface is the major contributor to failure of the wire bond [110], [111]. Composition of IMC has been studied using TEM and XRD, and reported to be $CuAl_2$ and Cu_9Al_4[112], [113], [114]. In the later study, more phases in IMC have been discovered and the layer structure has been reported to be Cu_9Al_4-Cu_3Al_2-Al_2Cu[115]. The Chlorine (Cl^-) content level has been found to significantly affect the reliability performance of Cu-Al wire bond [116], [117]. Though the chlorine would affect the ball bond corrosion, only certain IMCs are corroded. The other parts are immune[115]. A mathematical model for studying the influences of corrosion product deposition on bimetallic corrosion has been built[118]. A 2D Multiphysics model have been built by Matlab to understand the corrosion initiation and propagation. The 2D interface tracking technique has been applied. The Tafel-Parameters, including the open-circuit potential and the slope of the polarization curves for the anodic and cathodic regions, have been measured for copper and IMC under a variety of molar concentration of the ionic species and temperatures[119]. The mobility and diffusion of chlorine ions in EMC have been measured under different conditions[119]. Though researches have shown the formation of corrosion at Cu-Al interface, 3-D Multiphysics Model for Cu-Al wire bond corrosion has not been available yet.

This section introduces a novel 3D Multiphysics model for the corrosion of Cu-Al ball bonds. A 3-D Multiphysics Model has been formed via the finite element software called COMSOL Multiphysics to quantify how the corrosion initiates and propagate in 3-D model under extreme environmental conditions. The 3D interface tracking technique has been applied in copper bond corrosion. It states the diffusion mechanism and kinetics in 3-D model under different conditions. This model is characterized by Butler-Volmer equation and Nernst Planck equation. It couples the electrical field and concentration field in order to capture the effect of IMC thickness

and show how corrosion initiate under varies electrical field as well as chlorine concentrations. The model would help to quantify the reliability performance of Cu-Al wire bond without large amount of experimental results. What is more, the model could serve as a prognostic health management tool to examine the remaining useful life of wire bond.

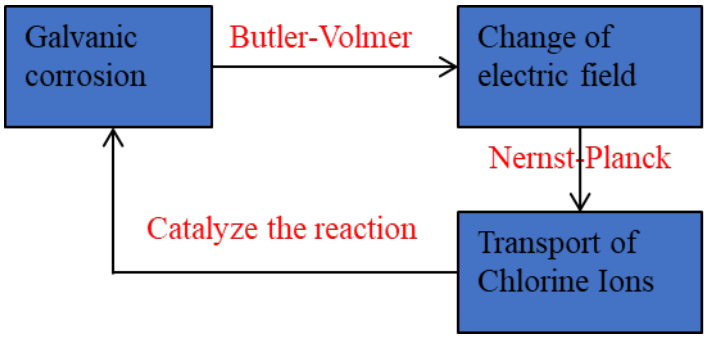

Figure 8-7 Nonlinear system for wirebonding corrosion

Galvanic corrosion for Cu-Al wire bond

Galvanic corrosion is a common electrochemical process in which one metal corrodes preferentially to the other metal when two metals are electrically contact with each other in the electrolyte environment. In Cu-Al corrosion system, The electrolyte is EMC. The chlorine released from EMC around the Cu-Al bond would act as catalyst to cause the IMC, which is located at Cu-Al interface, to be corroded. Since the mechanisms of this corrosion system is very complicated, this paper will only offer a simple introduction about the reaction. The two main phases, which would significantly contribute to the corrosion, found in the IMC are Cu_9Al_4 and $CuAl_2$. Cu_9Al_4 is found on copper ball side, while $CuAl_2$ is found on Al pad side[120]. According to the previous study, there are two pairs in this system. IMC is cathode and Al would act as sacrificial anode. It follows this reaction:

$$\mathrm{Al} + 3OH^- \rightarrow Al(OH)_3 + 3e^-$$

In the meantime, copper ball bond is cathode and IMC perform as anode. This corrosion followed by cracking is found in the Cu-rich side. It follows this reaction:

$$Cu_9Al_4 + Cl_2 \rightarrow 4AlCl_3 + 9Cu$$

$$Cu_9Al_4 + 6H_2O \rightarrow 2Al_2O_3 + 9Cu + 6H_2$$

$$2AlCl_3 + 3H_2O \rightarrow Al_2O_3 + 6HCl$$

Main products of this reaction are Al_2O_3 and HCl. The Al_2O_3 is brittle oxide and can cause cracks in oxidized region. The HCl would get dissolve into EMC and break into chlorine ions again, which continue attack Cu_9Al_4. Thus the corrosion process goes on. The other major component of IMC is $CuAl_2$. The typical corrosion of this component can be described as follows

$$CuAl_2 + 6Cl^- \rightarrow 2AlCl_3 + Cu$$

On the other side, Al will react with moisture to produce $Al(OH)_3$. This will be attacked by chlorine ions and broken down as follows

$$2Al(OH)_3 + Cl^- \rightarrow 2Al(OH)_2Cl + OH^-$$

$$\mathrm{Al} + 4Cl^- \rightarrow AlCl_4^- + 3e$$

$$2AlCl_4^- + 3H_2O \rightarrow 2Al(OH)_3 + 8Cl^-$$

One of the products of the reaction is chlorine ions. Therefore, once the reaction start, it would keep going on and the Al pad will keep dissolving. After corrosion happens, cathode to anode ratio of this corrosion system will increase since the dissolution of anode. The deformed geometry resulting from the anode consumption would leads to the change of corrosion rate.

Multiphysics Model

Before presenting the Multiphysics model, these following assumptions are applied:

1、 Dilute solution theory is applicable.

2、 Electrochemical reactions happen only on the surface.

3、 The cathode is non-corroding.

4、 The deposits effects would not be considered.

5、 The electrolyte conductivity is constant during the corrosion.

Since it would be difficult to model all details of the wire bond corrosion, this paper would focus on the large scale simulation. The formation of IMC would not be considered as well. Assuming well mixed, incompressible and electro-neutral electrolyte solution, the governing equation of potential is Laplace equation.

$$\nabla^2 \Phi = 0$$

Laplace equation is solved over the electrolyte domain. The Multiphysics model is characterized by Butler-Volmer equation and Nernst Planck equation. The Butler-Volmer equation controls the kinetics of galvanic corrosion reaction. It is possible to solve the corrosion rate, with the known open circuit potential, current density and Tafel slope of anode and cathode. This gives a possible path to simulate the galvanic corrosion by large scale experimental results without going through the micro-scale chemical reactions. Since the existing electric field cause the ions migrate in EMC, the chlorine ions released from EMC would be attracted to copper ball bond. This process is governed by Nernst Planck equation, which is showing below. The input is mobility and diffusion of chlorine ions in EMC. The output is concentration field. Chlorine ions acted as catalyst, causing the IMC to corrode. The accumulation of chlorine ions changes the corrosion rate and influents the electric field. This is how concentration field and electric field couple.

$$\frac{\partial \mathrm{c}}{\partial \mathrm{t}} = \nabla(D\nabla c) + z\mu\nabla(c\nabla V)$$

Where z stands for the electron number of chlorine, μ is ionic mobility of chlorine. D is the diffusion. V is voltage bias of the domain and t denotes time. In this diluted species transport model, the transport progress is governed by concentration gradient and electric potential gradient in the domain. The process pf contaminant transport in EMC would result in the chlorine ion accumulate around the electrode. After that the chlorine ion would act as catalyst, which leads to

the galvanic corrosion of IMC. Kinetics of bimetallic galvanic corrosion is governed by Butler-Volmer equation [121]as shown follow:

$$j_c = j_{oc}\left(e^{\frac{E_c - V}{\alpha_c}} - e^{-\frac{E_c - V}{\beta_c}}\right)$$

$$j_a = j_{oa}\left(e^{\frac{E_a - V}{\alpha_a}} - e^{-\frac{E_a - V}{\beta_a}}\right)$$

Where j_a, j_c represent the anodic and cathodic corrosion current density respectively (A/m^2). What is more, j_{oa}, j_{oc} are anodic and cathodic corrosion densities for zero over-potential respectively. E_a, E_c stand for anodic and cathodic open circuit potential respectively. α, β denote to Tafel parameters[121].

Considering the Al pad dissolution, the specific IMC $CuAl_2$ and Cu_9Al4 would be the cathode. The fundamentals of micro-galvanic corrosion and how different factors affect corrosion rate of wire bond are presented in detail in previous research publication[121], [122]. The factors related to Cu-Al wire bond micro-galvanic corrosion include IMC, EMC and operational environment. In order to capture the complex process of corrosion, secondary current distribution of COMSOL Multiphysics has been applied. With the deformed geometry function, the corrosion cell geometry could be deformed while the corrosion process happens.

2D Micro- Corrosion Model

The study starts from 2D simple model by COMSOL Multiphysics. The 2D corrosion cell is built as below:

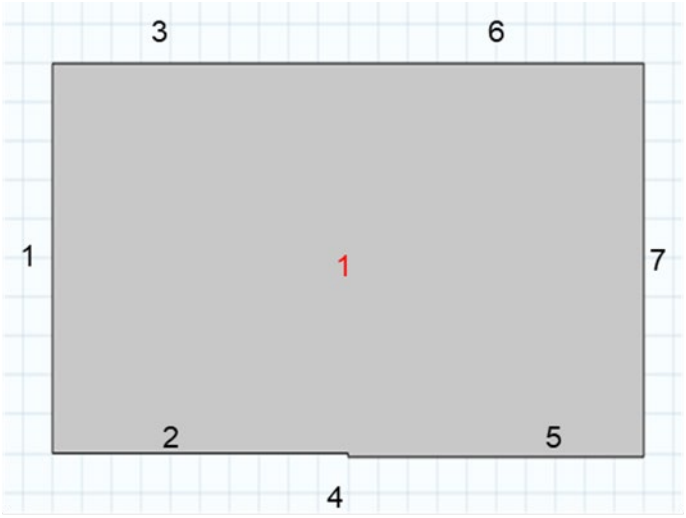

Figure 8-8 2D Model Geometry

Table 8-1 Model Input Parameters

Eeq_cat	-0.54[V]	-0.54 V	Equilibrium potential, cathode
i0_cat	25[A/m^2]	25 A/m²	Exchange current density, cathode
A_cat	-10000[mV]	-10 V	Tafel slope, cathode
Eeq_an	-0.77[V]	-0.77 V	Equilibrium potential, anode
i0_an	0.2[A/m^2]	0.2 A/m²	Exchange current density, anode
A_an	50[mV]	0.05 V	Tafel slope, anode
ilim_an	10^2[A/m^2]	100 A/m²	Limiting current density, anode

The domain 1 is electrolyte. The left boundary 2 is anode and the right boundary 5 is cathode. The length of boundary 2 and 5 is 0.01m. Introduce a small height step of boundary 4 is to ensure the topology is preserved in the simulation[123]. In this simulation, IMC is assumed to be nondeforming boundary while the Al would be corroded, which is presented in previous paper.

The dissolving-Depositing species is Al. Density is 2710 kg/m^3. Molar mass is 0.027kg/mol. Firstly, the Butler-Volmer equation is applied to describe the galvanic corrosion of IMC and AL. The secondary current distribution model under Corrosion, Deformed Geometry module is applied in COMSOL Multiphysics. The input parameters are shown in Table 8-1 [124]. Solve the simple physics model in a time-dependent study, simulating the corrosion for five days and the results are shown below:

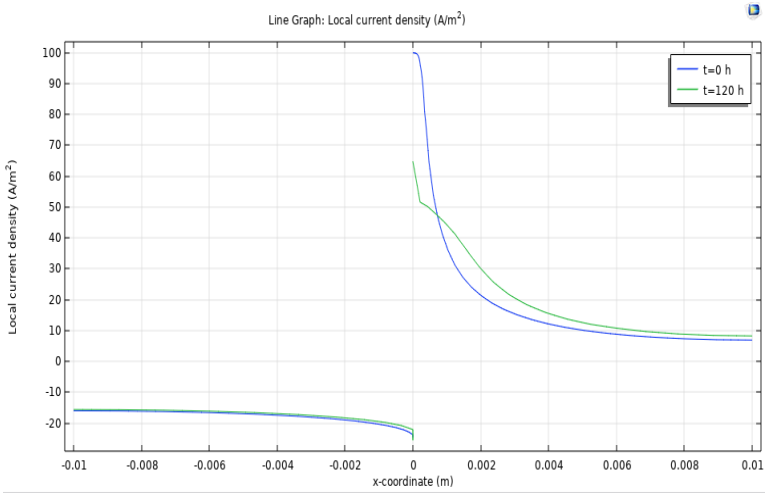

Figure 8-9 Local Current Density

Figure 8-9 shows that the current densities at the beginning and the end of the simulation. The evolution of local current densities could be viewed. The highest current densities are found at the contact of two electrodes. Figure 8-9 shows the current densities and potential distribution in the electrolyte. The color bar is potential distribution and the arrows are the currents. It also shows the evolution of geometry from the beginning to the end of the simulation, which lasts five days long. The Figure 8-10a is the result of t=0h. The Figure 8-10b is the result of 1 day. Figure 8-10c is the result of 3 days while the Figure 8-10d is the result of 5 days. Figure 8-10 also shows that the potential field does not change too much, which match the current density result of Figure 8-9. After building the Butler-Volmer equation model in 2D to describe the galvanic corrosion

with electrode deformation between IMC and Al, the Nernst Planck equation is applied to describe the transportation of chlorine ions in the domain. Since the concentration of migration species is less than 10%, it would be reasonable to assume that it is the diluted species in the electrolyte. The transport of diluted species model has been applied in COMSOL Multiphysics.

The input parameters of the transport of diluted species model include the diffusion of chlorine ions (D), the mobility of chlorine ions in domain (μ) and the concentration of chlorine ions. The initial concentration of chlorine ions in the domain is zero. The concentration of boundary 3 and 6 is 100 mol/m^3. Since the distribution of concentration field is the primary concern, the value of chlorine concentration at the boundary 3 and 6 does not matter. The diffusion of Chlorine ions in the domain is measured from previous publication D= 2e-10[m^2/s]. The mobility of ions follows the Nernst Einstein relation. The result of simulation is shown in Figure 8-11 shows the chlorine ions transport in the domain with time. The color bar is the chlorine concentration and the arrows are currents. The Figure 8-11a is the result of t=0. The Figure 8-11b is the result of t=20000s. The Figure 8-11c is the result of t=26256s and the last figure is the result of 5 days. These results show that the chlorine ions migrate in the domain following the Nernst Planck equation.

After applying the Butler-Volmer equation and Nernst Planck equation, the model of galvanic corrosion has been built and the chlorine ions migration in the domain has been described. In order to build the Multiphysics model, which couple the concentration field and the electric field. The connection between chlorine ions and the galvanic corrosion should be constructed. Thus, the relation between the chlorine ions and the chemical reaction is needed.

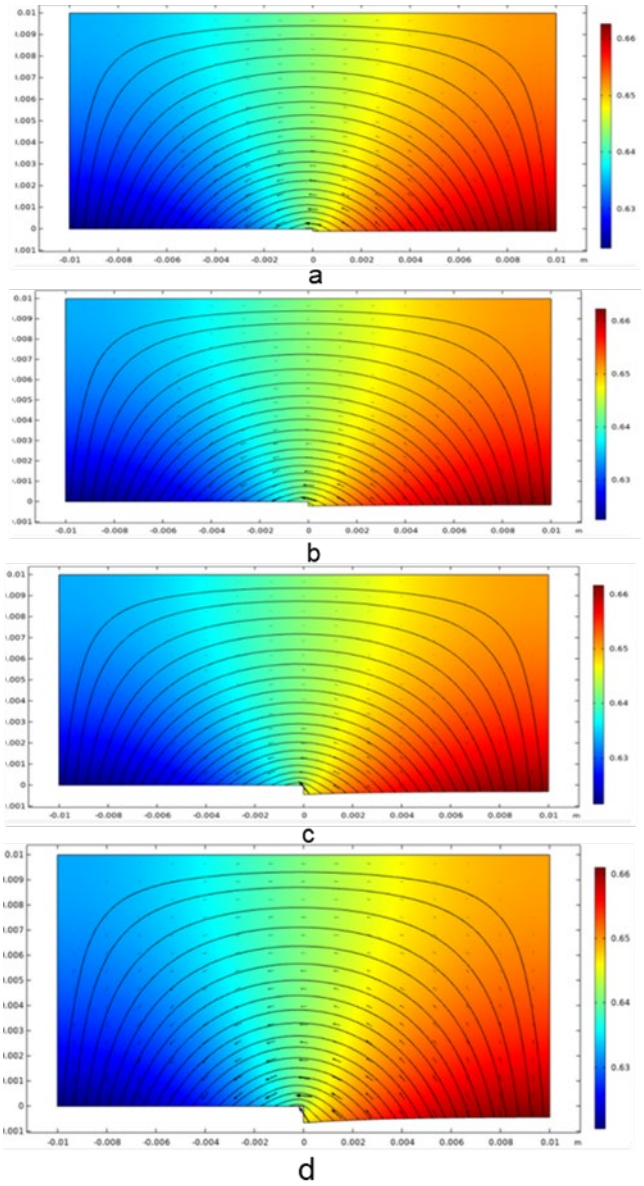

Figure 8-10 Current Densities and Potential Distribution in the Electrolyte

The easiest way to construct the relation is to set the input parameters of BV equation as the function of chlorine concentration, which means as the chlorine ions concentration change, the kinetics of galvanic corrosion change as well. Since the mechanism of corrosion is very complex, the function could build in lab scale relation, which is a good approximation, instead of building microscale mathematical model. Yihua has presented the IMC OCP and I_{corr} as a function of chlorine concentrations.

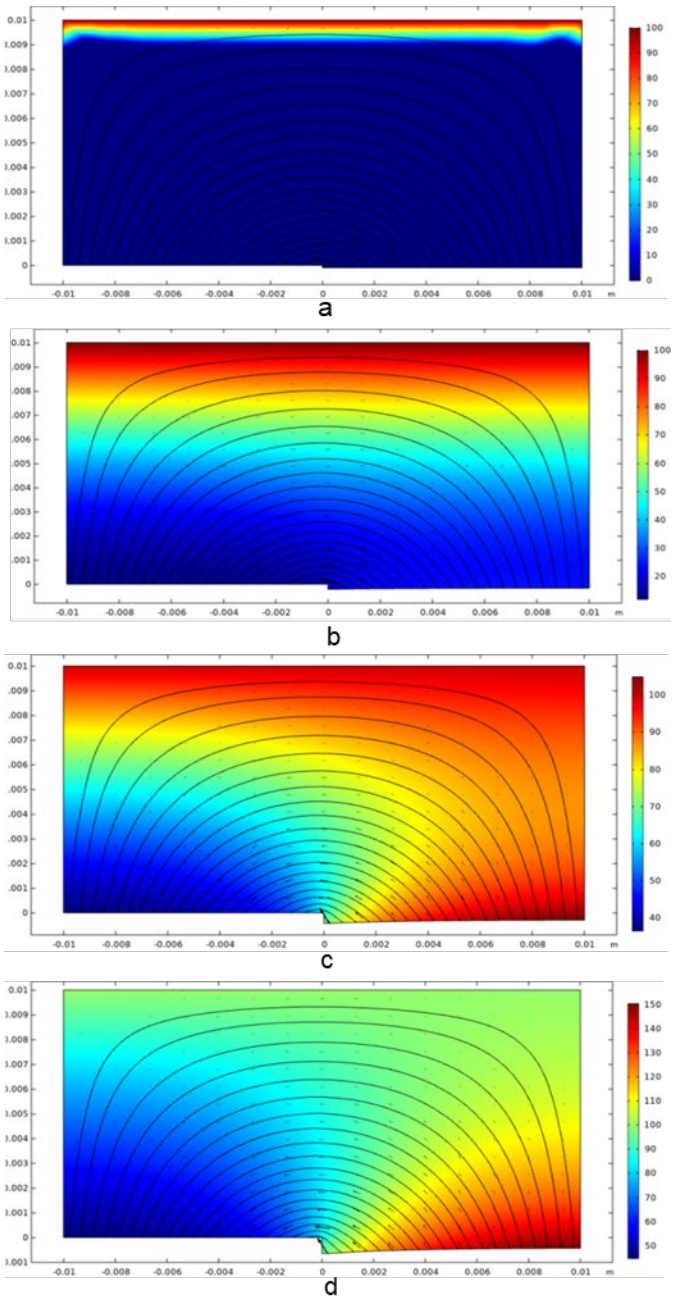

Figure 8-11 Chlorine Ions Transport in the Domain with Time

3D Micro- Corrosion Model

The galvanic corrosion process initiates when two dissimilar metals are electrically connected in the conductive environment EMC, which works as electrolyte. In this corrosion process, the chlorine ions in EMC act as catalyst. The 3D simulation has been built to describe the

corrosion between IMC and Al pad. When Al is coupled to IMC in aggressive environments, Al acts as anode, generating Al^{3+} ions on its surface. IMC acts as cathode, generating OH^- on its surface. Al^{3+} and OH^- ions spread to the bulk solution by diffusion and electromigration and react with each other. This is how Al dissolute in the reaction.

$$\mathrm{Al} \rightarrow Al^{3+} + 3e^-$$

$$O_2 + 2H_2O + 4e^- \rightarrow 4OH^-$$

Figure 8-12 shows the single copper wire ball bond corrosion geometry in EMC. In order to simplify the simulation, only the only the electrolyte domain has been selected as 2D model. What is more, only the bottom part of copper bond is concerned for increasing the numerical computation efficiency. In this case, the IMC would be viewed as the corroding part. The IMC is highlighted with blue in Figure 8-12b. The radius of ball bond is 40μm and the thickness of corroding area is 1μm. the rest space is filled with electrolyte. Time dependent solver has been used to solve the Multiphysics model. The corrosion rate can be computed by the Faraday's law[125]:

$$C_{rate} = \frac{\mathrm{M}}{\mathrm{zF}\rho} j$$

Where F represents Faraday constant F is 96485.34C/mol, C_{rate} is corrosion rate in m s^{-1}, and the current density j is in A m^{-2}, ρ is density and M is Molar Mass. z represents the electron number. The input parameters of numerical simulation are measured by Yihua's previous research. The galvanic corrosion behavior is studied by electrochemical polarization using large-scale galvanic corrosion experiment. In the measurement, Copper, Aluminum and the nuggets of Cu-Al intermetallic compounds have been used. Standard 3-electrode electrochemical polarization test have been performed.

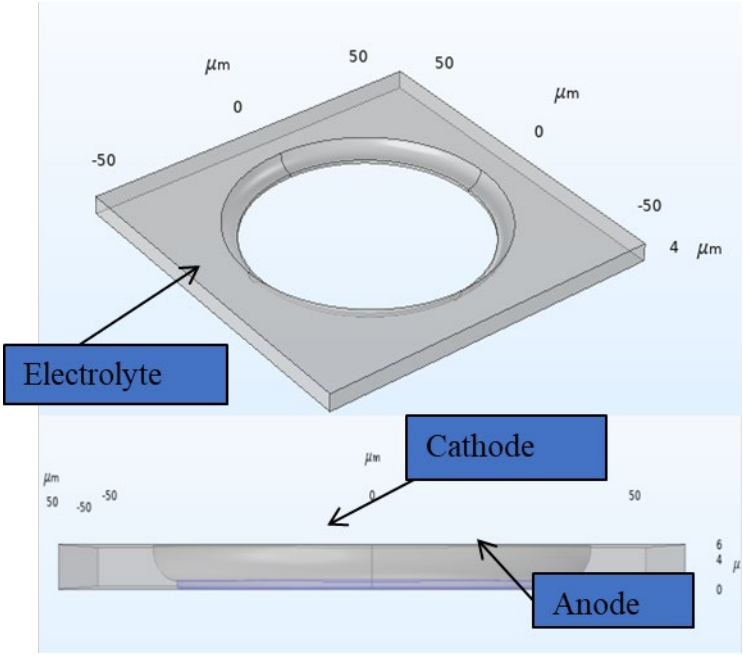

Figure 8-12 3D model geometry

Figure 8-13 shows the schematic plot of polarization test setup. Three electrodes are immersed in solutions where pH concentration level of chlorine contaminant and temperature could be specifically controlled. The measurements have been performed under different conditions. For each test conditions, the test has been performed 6 times repeatedly. The mean values of 6 tests are selected to be the input parameters of the simulation model.

The Table 8-2 is the parameters for temperature at 45°C, chlorine concentration at 15ppm and pH=6.2. Under such condition, the simulation result is shown in Figure 8-14 and Figure 8-15. Figure 8-14 shows the simulation result of front view. Figure 8-15 shows the result of the top view. The red shrinking area is the corroding tracking surface. The color bar shows the surface electrolyte potential, which could indicate the potential distribution in the domain.

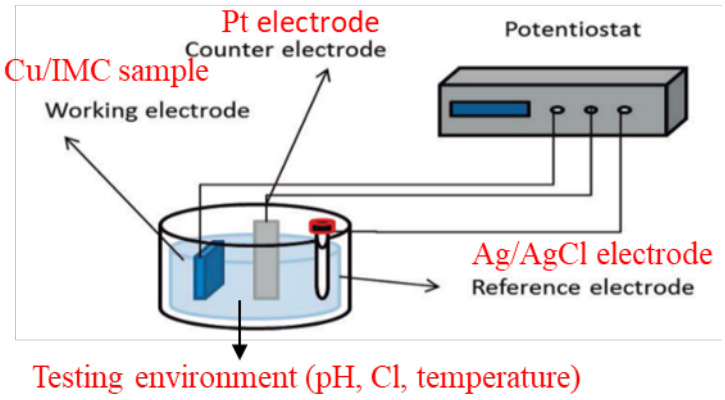

Figure 8-13 3-electrode electrochemical cell

Table 8-2 3D Model Input Parameters

Eeq_cat	0.043[V]	0.043 V	Equilibrium potential, cathode
i0_cat	0.0006[A/m^2]	6E-4 A/m²	Exchange current density, cathode
A_cat	-139[mV]	-0.139 V	Tafel slope, cathode
Eeq_an	-0.495[V]	-0.495 V	Equilibrium potential, anode
i0_an	0.001[A/m^2]	0.001 A/m²	Exchange current density, anode
A_an	97[mV]	0.097 V	Tafel slope, anode
ilim_an	10^2[A/m^2]	100 A/m²	Limiting current density, anode

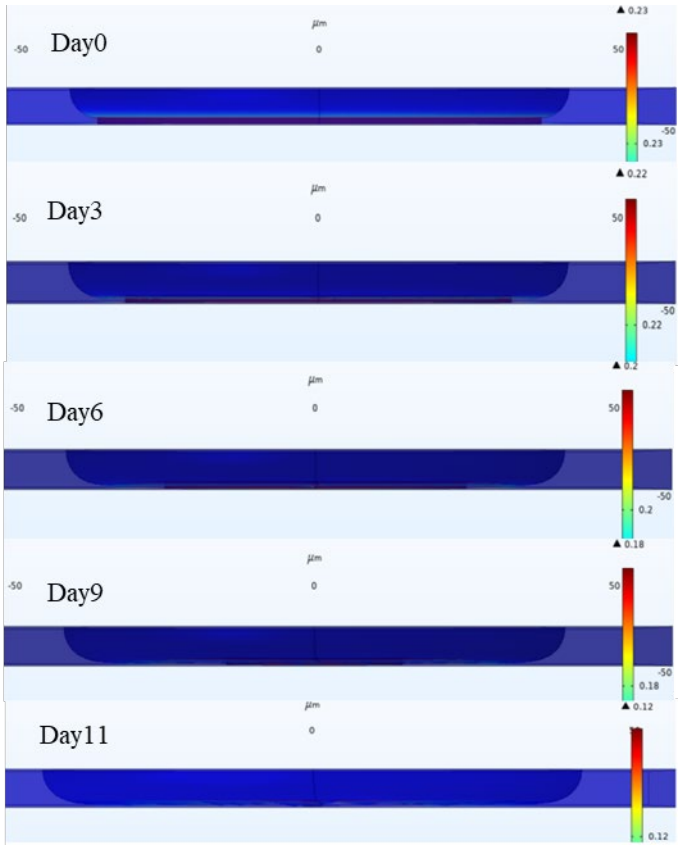

Figure 8-14 Front view

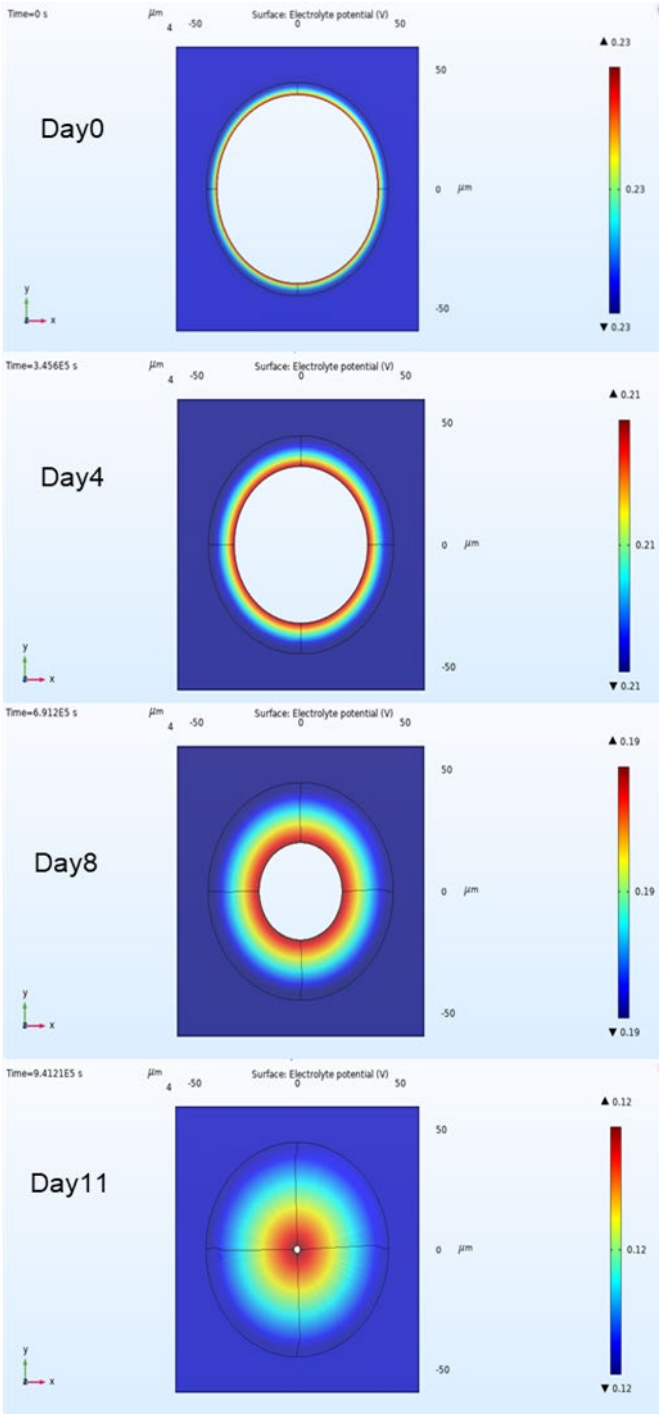

Figure 8-15 Top view of corrosion

Table 8-3 3D Model Input Parameters

Eeq_cat	-0.117[V]	-0.117 V	Equilibrium potential, cathode
i0_cat	0.1996[A/m^2]	0.1996 A/m²	Exchange current density, cathode
A_cat	-80[mV]	-0.08 V	Tafel slope, cathode
Eeq_an	-0.632[V]	-0.632 V	Equilibrium potential, anode
i0_an	0.305[A/m^2]	0.305 A/m²	Exchange current density, anode
A_an	72[mV]	0.072 V	Tafel slope, anode

The table is the parameters of experiment at 25℃, chlorine concentration at 17750ppm (0.5M) and pH=6.2. Under such condition, the simulation result is shown in Figure 8-16:

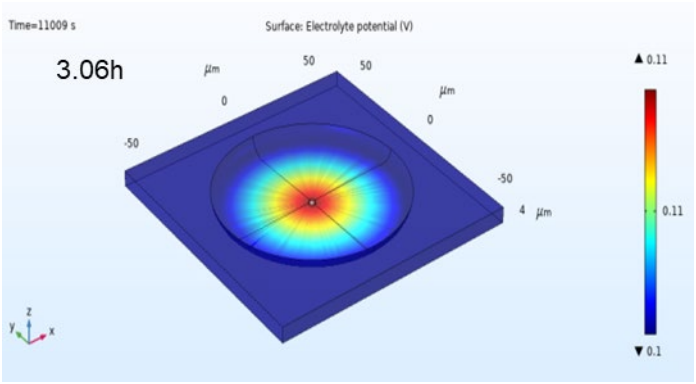

Figure 8-16 Chlorine concentration at 17750ppm (0.5M) and pH=6.2

Compared with the previous results, it shows that the corrosion rate is dramatically influenced by chlorine ion concentration, which is proved by the experiments.

Table 8-4 3D Model Input Parameters

Eeq_cat	0.031[V]	0.031 V	Equilibrium potential, cathode
i0_cat	0.0026[A/m^2]	0.0026 A/m²	Exchange current density, cathode
A_cat	-104[mV]	-0.104 V	Tafel slope, cathode
Eeq_an	-0.507[V]	-0.507 V	Equilibrium potential, anode
i0_an	0.002[A/m^2]	0.002 A/m²	Exchange current density, anode
A_an	85[mV]	0.085 V	Tafel slope, anode

The table is the parameters of experiment at 45℃, chlorine concentration at 15ppm and pH=6.2. Under such condition, the simulation result is shown in Figure 8-17.

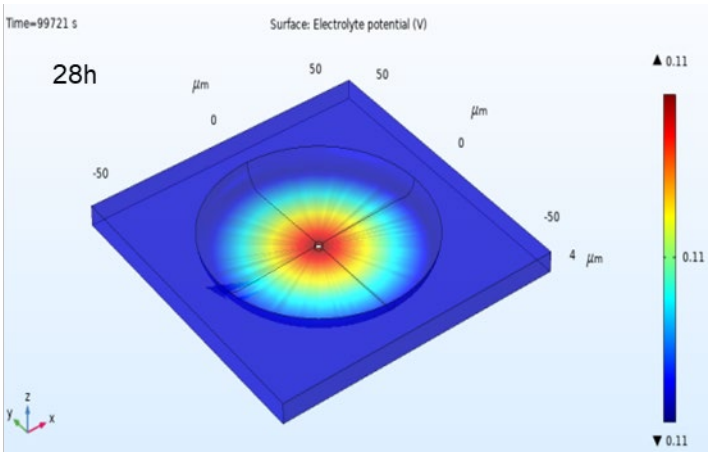

Figure 8-17 Chlorine concentration at 15ppm and pH=6.2

Summary and discussion

The above simulation results show that it could possible to simulate 3D the galvanic corrosion phenomenon. The secondary current distribution model has been applied since the Ohm's law is applicable in the reaction domain. The third current distribution model would consider more details of the reaction surface, which is very sensitive under electrochemical process. Since this simulation focus on lab scale process, the secondary current distribution model is applicable. The precipitation effect has not been considered in this simulation as well. If the precipitation effect is considered, theoretically, the deposition of the anode would accumulate close to the reaction surface, which would affect the electrochemical reaction and change the electrolyte conductivity during the corrosion. In fact, the electrolyte conductivity is not constant during the corrosion process as well. However, if the precipitation effect is considered, it would considerably increase the computational burden, since the distribution of the deposits in 3D domain would be updated every step. In order to simplify the simulation due to the limitation of computing power, the precipitation effect has not been considered. The electrolyte conductivity value is assumed to be constant as well.

This model could quantify the copper ball bond corrosion under different environmental conditions. Since the model input comes from the electrochemical polarization tests, the remaining useful life could be estimated if the trend line of Tafel slope, OCP and current density could be obtained. Therefore, with the results from electrochemical polarization test under certain environmental condition, this model could show the corrosion process to predict the wire bond behavior under such condition. Since the corrosion process is difficult to show by experiments, which could only show the phenomenon at the certain moment, the simulation could show the corrosion trend and other information which is not easy to obtain by experiment, including current density, electrolyte potential. Using Yihua's experimental results [10], the trend lines of OCP and current densities under different temperatures and chlorine ions concentrations could fit the experimental data very well. However, the correlation of Tafel slope is not clear yet. This is the reason why this 3D model only use to simulate the corrosion under specific certain condition without the influence of chlorine ion migration. In sum, a 3D Cu wire bond corrosion Multiphysics model is presented in order to evaluate the remaining useful life of the copper wire bond.

Reference

[1] R. Pepper, “Cisco visual networking index (VNI) global mobile data traffic forecast update,” presented at the Mobile World Congress, 2013.

[2] “The Multiple Lives of Moore’s Law - IEEE Spectrum.” Accessed: Jan. 25, 2025. [Online]. Available: https://spectrum.ieee.org/the-multiple-lives-of-moores-law

[3] “How Much Did Early Transistors Cost? - IEEE Spectrum.” Accessed: Jan. 25, 2025. [Online]. Available: https://spectrum.ieee.org/how-much-did-early-transistors-cost

[4] “Tech visionary Gordon Moore retires from Intel.” Accessed: Jan. 25, 2025. [Online]. Available: http://usatoday30.usatoday.com/tech/news/2001-05-25-moore-quits-intel-board.htm

[5] H. Chun, Y.-J. Kim, S.-Y. Tak, S.-Y. Park, S.-J. Park, and C. H. Oh, “Preparation of ultra-low CTE epoxy composite using the new alkoxysilyl-functionalized bisphenol A epoxy resin,” *Polymer*, vol. 135, pp. 241–250, Jan. 2018, doi: 10.1016/j.polymer.2017.11.048.

[6] K. Kikuchi, H. Nakagawa, K. Tokoro, M. Aoyagi, and S. Segawa, “Ultra-High-Speed Signal Propagation of High-Density Wiring Interposer for 3D Packaging,” in *Proceedings Electronic Components and Technology, 2005. ECTC ’05.*, Lake Buena Vista, FL, USA: IEEE, 2005, pp. 809–813. doi: 10.1109/ECTC.2005.1441365.

[7] N. Kinjol, M. Ogata, K. Nishi, and A. Kaneda, “Epoxy Molding Compounds as Encapsulation Materials for Microelectronic Devices”.

[8] C. L. Gan, F. C. Classe, B. L. Chan, and U. Hashim, “Effects of Bonding Wires and Epoxy Molding Compound on Gold and Copper Ball Bonds Intermetallic Growth Kinetics in Electronic Packaging,” *J. Electron. Mater.*, vol. 43, no. 4, pp. 1017–1025, Apr. 2014, doi: 10.1007/s11664-014-3011-y.

[9] Yiying Yao, Guo-Quan Lu, D. Boroyevich, and K. D. T. Ngo, "Survey of High-Temperature Polymeric Encapsulants for Power Electronics Packaging," *IEEE Trans. Compon. Packag. Manuf. Technol.*, vol. 5, no. 2, pp. 168–181, Feb. 2015, doi: 10.1109/TCPMT.2014.2337300.

[10] H. Zheng, L. Li, X. Lei, X. Yu, S. Liu, and X. Luo, "Optical Performance Enhancement for Chip-on-Board Packaging LEDs by Adding TiO_2/Silicone Encapsulation Layer," *IEEE Electron Device Lett.*, vol. 35, no. 10, pp. 1046–1048, Oct. 2014, doi: 10.1109/LED.2014.2349951.

[11] X. Li, Y. Feng, X. Tan, Y. Han, and X. Sun, "Performance of methylphenyl hydrogen-containing silicone oils for LED encapsulation," *J. Macromol. Sci. Part A*, vol. 54, no. 10, pp. 690–694, Oct. 2017, doi: 10.1080/10601325.2017.1322466.

[12] G. H. Lee *et al.*, "Enhancing the elevated temperature performance of high voltage LiNi0.5Mn1.5O4 by V doping with in-situ carbon and polyimide encapsulation," *J. Power Sources*, vol. 298, pp. 379–384, Dec. 2015, doi: 10.1016/j.jpowsour.2015.08.053.

[13] J. Nam *et al.*, "Transfer Printed Flexible and Stretchable Thin Film Solar Cells Using a Water-Soluble Sacrificial Layer," *Adv. Energy Mater.*, vol. 6, no. 21, p. 1601269, Nov. 2016, doi: 10.1002/aenm.201601269.

[14] X. Wang *et al.*, "Structural and chemical synergistic encapsulation of polysulfides enables ultralong-life lithium–sulfur batteries," *Energy Environ. Sci.*, vol. 9, no. 8, pp. 2533–2538, 2016, doi: 10.1039/C6EE00194G.

[15] W. Gao, M. Bie, F. Liu, P. Chang, and Y. Quan, "Self-Healable and Reprocessable Polysulfide Sealants Prepared from Liquid Polysulfide Oligomer and Epoxy Resin," *ACS Appl. Mater. Interfaces*, vol. 9, no. 18, pp. 15798–15808, May 2017, doi: 10.1021/acsami.7b05285.

[16] K. M. B. Jansen, J. De Vreugd, L. J. Ernst, and C. Bohm, “Thermal aging of molding compounds,” in *2010 11th International Conference on Electronic Packaging Technology & High Density Packaging*, Xi’an, China: IEEE, Aug. 2010, pp. 778–780. doi: 10.1109/ICEPT.2010.5582698.

[17] E. Nguegang, J. Franz, A. Kretschmann, and H. Sandmaier, “Aging effects of Epoxy Moulding Compound on the long-term stability of plastic package,” in *2010 11th International Thermal, Mechanical & Multi-Physics Simulation, and Experiments in Microelectronics and Microsystems (EuroSimE)*, Bordeaux: IEEE, Apr. 2010, pp. 1–6. doi: 10.1109/ESIME.2010.5464615.

[18] M. Linec and B. Mušič, “The Effects of Silica-Based Fillers on the Properties of Epoxy Molding Compounds,” *Materials*, vol. 12, no. 11, p. 1811, Jun. 2019, doi: 10.3390/ma12111811.

[19] A. Inamdar, Y.-H. Yang, A. Prisacaru, P. Gromala, and B. Han, “High temperature aging of epoxy-based molding compound and its effect on mechanical behavior of molded electronic package,” *Polym. Degrad. Stab.*, vol. 188, p. 109572, Jun. 2021, doi: 10.1016/j.polymdegradstab.2021.109572.

[20] Y. Rao, S. H. Shi, and C. P. Wong, “A simple evaluation methodology of Young’s modulus-temperature relationship for the underfill encapsulants,” in *1999 Proceedings. 49th Electronic Components and Technology Conference (Cat. No.99CH36299)*, San Diego, CA, USA: IEEE, 1999, pp. 784–789. doi: 10.1109/ECTC.1999.776271.

[21] C. Lin, “The Effects of Isothermal Aging on the Mechanical Behavior of Underfill Encapsulants-2”.

[22] L. Wang and C. P. Wong, "Novel thermally reworkable underfill encapsulants for flip-chip applications," *IEEE Trans. Adv. Packag.*, vol. 22, no. 1, pp. 46–53, Feb. 1999, doi: 10.1109/6040.746542.

[23] D. Suryanarayana, T. Y. Wu, and J. A. Varcoe, "Encapsulants used in flip-chip packages," in *Proceedings of IEEE 43rd Electronic Components and Technology Conference (ECTC '93)*, Orlando, FL, USA: IEEE, 1993, pp. 193–198. doi: 10.1109/ECTC.1993.346720.

[24] Y. Liu, "LEAD-FREE ASSEMBLY AND RELIABILITY OF CHIP SCALE PACKAGES AND 01005 COMPONENTS".

[25] T. Yang, V. Gandhi, R. Huang, and K. M. Liechti, "Rate dependent fracture along a silicon/epoxy interface under mixed-mode loading conditions," *Int. J. Solids Struct.*, vol. 257, p. 111129, Dec. 2022, doi: 10.1016/j.ijsolstr.2021.111129.

[26] F. Wu, C. Tuan, B. Song, K. Moon, and C. Wong, "Controlled synthesis and evaluation of cyanate ester/epoxy copolymer system for high temperature molding compounds," *J. Polym. Sci. Part Polym. Chem.*, vol. 56, no. 13, pp. 1337–1345, Jul. 2018, doi: 10.1002/pola.29013.

[27] Y. Yang, G. Xian, H. Li, and L. Sui, "Thermal aging of an anhydride-cured epoxy resin," *Polym. Degrad. Stab.*, vol. 118, pp. 111–119, Aug. 2015, doi: 10.1016/j.polymdegradstab.2015.04.017.

[28] L. H. Sperling, *Introduction to physical polymer science*. 2015.

[29] P. Lall, Y. Zhang, J. Suhling, and J. Williamson, "The Degradation Mechanisms of Underfills Subjected to High Temperature Long Term Aging," in *2020 19th IEEE Intersociety Conference on Thermal and Thermomechanical Phenomena in Electronic Systems (ITherm)*, Orlando, FL, USA: IEEE, Jul. 2020, pp. 1400–1407. doi: 10.1109/ITherm45881.2020.9190303.

[30] P. Lall *et al.*, "Evolution of Viscoelastic Properties and Interface-Fracture Toughness Under Sustained High Temperature Operation Typical of Automotive Underhood for up to 1-year," in *2021 IEEE 71st Electronic Components and Technology Conference (ECTC)*, San Diego, CA, USA: IEEE, Jun. 2021, pp. 971–982. doi: 10.1109/ECTC32696.2021.00160.

[31] P. Lall, Y. Zhang, and J. Suhling, "Thermal Stability and Viscoelasticity Behavior of Underfill Encapsulants in Sustained High Temperature Environment up to 1-year," in *2022 21st IEEE Intersociety Conference on Thermal and Thermomechanical Phenomena in Electronic Systems (iTherm)*, San Diego, CA, USA: IEEE, May 2022, pp. 1–8. doi: 10.1109/iTherm54085.2022.9899686.

[32] P. Lall, Y. Zhang, H. Wu, J. Suhling, and E. Davis, "Evolution of Prony Parameters for Underfills Subjected to High Temperature Long Term Aging," in *InterPACK2021*, ASME 2021 International Technical Conference and Exhibition on Packaging and Integration of Electronic and Photonic Microsystems, Oct. 2021. doi: 10.1115/IPACK2021-74076.

[33] P. Lall, M. Kasturi, Y. Zhang, H. Wu, J. Suhling, and E. Davis, "Effect of Underfill Property Evolution on Solder Joint Reliability in Automotive Applications," in *2022 IEEE 72nd Electronic Components and Technology Conference (ECTC)*, San Diego, CA, USA: IEEE, May 2022, pp. 455–466. doi: 10.1109/ECTC51906.2022.00079.

[34] R. P. Prasad, *Surface mount technology: principles and practice*. Springer Science & Business Media, 2012.

[35] J. H. Lau and Y.-H. Pao, "Solder joint reliability of BGA, CSP, flip chip, and fine pitch SMT assemblies," *No Title*, 1997.

[36] D. Edwards, G. Heinen, G. Bednarz, and W. Schroen, “Test Structure Methodology of IC Package Material Characterization,” *IEEE Trans. Compon. Hybrids Manuf. Technol.*, vol. 6, no. 4, pp. 560–567, Dec. 1983, doi: 10.1109/TCHMT.1983.1136205.

[37] P. T. Vianco, “A Review of Interface Microstructures in Electronic Packaging Applications: Soldering Technology,” *JOM*, vol. 71, no. 1, pp. 158–177, Jan. 2019, doi: 10.1007/s11837-018-3219-z.

[38] D. R. Frear, L. N. Ramanathan, J.-W. Jang, and N. L. Owens, “Emerging reliability challenges in electronic packaging,” in *2008 IEEE International Reliability Physics Symposium*, Phoenix, AZ, USA: IEEE, Apr. 2008, pp. 450–454. doi: 10.1109/RELPHY.2008.4558927.

[39] M. Amagai, “Mechanical reliability in electronic packaging,” *Microelectron. Reliab.*, vol. 42, no. 4–5, pp. 607–627, Apr. 2002, doi: 10.1016/S0026-2714(02)00037-9.

[40] Q. Yao and J. Qu, “Interfacial Versus Cohesive Failure on Polymer-Metal Interfaces in Electronic Packaging—Effects of Interface Roughness,” *J. Electron. Packag.*, vol. 124, no. 2, pp. 127–134, Jun. 2002, doi: 10.1115/1.1459470.

[41] V. Sundararaman and S. K. Sitaraman, “Interfacial fracture toughness for delamination growth prediction in a novel peripheral array package,” *IEEE Trans. Compon. Packag. Technol.*, vol. 24, no. 2, pp. 265–270, Jun. 2001, doi: 10.1109/6144.926392.

[42] W. O. Soboyejo, G.-Y. Lu, S. Chengalva, J. Zhang, and V. Kenner, “A modified mixed-mode bending specimen for the interfacial fracture testing of dissimilar materials.,” *Fatigue Fract. Eng. Mater. Struct.*, vol. 22, no. 9, p. 799, Sep. 1999, doi: 10.1046/j.1460-2695.1999.t01-1-00203.x.

[43] R. J. Harries and S. K. Sitaraman, “Numerical modeling of interfacial delamination propagation in a novel peripheral array package,” *IEEE Trans. Compon. Packag. Technol.*, vol. 24, no. 2, pp. 256–264, Jun. 2001, doi: 10.1109/6144.926391.

[44] W. E. R. Krieger, S. Raghavan, and S. K. Sitaraman, “Experiments for Obtaining Cohesive-Zone Parameters for Copper-Mold Compound Interfacial Delamination,” *IEEE Trans. Compon. Packag. Manuf. Technol.*, vol. 6, no. 9, pp. 1389–1398, Sep. 2016, doi: 10.1109/TCPMT.2016.2589223.

[45] W. K. Lam, T. S. Yeung, A. Teng, and M. M. F. Yuen, “A method for evaluating delamination between epoxy moulding compounds and different plated leadframes,” in *International Symposium on Electronic Materials and Packaging (EMAP2000) (Cat. No.00EX458)*, Hong Kong, China: IEEE, 2000, pp. 214–219. doi: 10.1109/EMAP.2000.904157.

[46] A. Nishimura, I. Hirose, and N. Tanaka, “A new method for measuring adhesion strength of IC molding compounds,” 1992.

[47] A. Kwatra, D. Samet, and S. K. Sitaraman, “Effect of thermal aging on cohesive zone models to study copper leadframe/mold compound interfacial delamination,” in *2015 IEEE 65th Electronic Components and Technology Conference (ECTC)*, San Diego, CA: IEEE, May 2015, pp. 1531–1537. doi: 10.1109/ECTC.2015.7159801.

[48] Weidong Xie and S. K. Sitaraman, “Investigation of interfacial delamination of a copper-epoxy interface under monotonic and cyclic loading: modeling and evaluation,” *IEEE Trans. Adv. Packag.*, vol. 26, no. 4, pp. 441–446, Nov. 2003, doi: 10.1109/TADVP.2003.821087.

[49] Weidong Xie and S. K. Sitaraman, “Investigation of interfacial delamination of a copper-epoxy interface under monotonic and cyclic loading: experimental characterization,” *IEEE*

Trans. Adv. Packag., vol. 26, no. 4, pp. 447–452, Nov. 2003, doi: 10.1109/TADVP.2003.821091.

[50] J. Guzek, H. Azimi, and S. Suresh, "Fatigue crack propagation along polymer-metal interfaces in microelectronic packages," *IEEE Trans. Compon. Packag. Manuf. Technol. Part A*, vol. 20, no. 4, pp. 496–504, Dec. 1997, doi: 10.1109/95.650940.

[51] G. T. Ostrowicki, N. T. Fritz, R. I. Okereke, P. A. Kohl, and S. K. Sitaraman, "Domed and Released Thin-Film Construct—An Approach for Material Characterization and Compliant Interconnects," *IEEE Trans. Device Mater. Reliab.*, vol. 12, no. 1, pp. 15–23, Mar. 2012, doi: 10.1109/TDMR.2011.2175927.

[52] G. T. Ostrowicki and S. K. Sitaraman, "Magnetically actuated peel test for thin films," *Thin Solid Films*, vol. 520, no. 11, pp. 3987–3993, Mar. 2012, doi: 10.1016/j.tsf.2012.01.042.

[53] G. T. Ostrowicki and S. K. Sitaraman, "Cyclic magnetic actuation technique for thin film interfacial fatigue crack propagation," *Eng. Fract. Mech.*, vol. 168, pp. 1–10, Dec. 2016, doi: 10.1016/j.engfracmech.2016.09.007.

[54] S. Mahalingam, K. Goray, S. Tonapi, and S. K. Sitaraman, "Experimental Characterization of Monotonic and Fatigue Delamination of Novel Underfill Materials," *J. Electron. Packag.*, vol. 128, no. 4, pp. 405–411, Dec. 2006, doi: 10.1115/1.2386242.

[55] S. Mahalingam, A. Prabhakumar, S. Tonapi, and S. K. Sitaraman, "Theoretical Modeling and Prediction of Delamination in Flip Chip Assemblies With Nanofilled No-Flow Underfill Materials," *J. Electron. Packag.*, vol. 130, no. 4, p. 041005, Dec. 2008, doi: 10.1115/1.3010378.

[56] P. Lin *et al.*, “Characterization of interfacial delamination in multi-layered integrated circuit packaging,” *Surf. Coat. Technol.*, vol. 320, pp. 349–356, Jun. 2017, doi: 10.1016/j.surfcoat.2016.12.050.

[57] H. B. Fan, C. K. Y. Wong, and M. M. F. Yuen, “A multi-scale method to investigate delamination in electronic packages,” *J. Adhes. Sci. Technol.*, vol. 20, no. 10, pp. 1061–1078, Jan. 2006, doi: 10.1163/156856106777890608.

[58] S. Y. Y. Leung, D. C. C. Lam, S. Luo, and C. P. Wong, “The role of water in delamination in electronic packages: degradation of interfacial adhesion,” *J. Adhes. Sci. Technol.*, vol. 18, no. 10, pp. 1103–1121, Jan. 2004, doi: 10.1163/1568561041581306.

[59] M.-K. Shih, G.-S. Lin, and J. Yang, “Effects of Thermal-Moisture Coupled Field on Delamination Behavior of Electronic Packaging,” *J. Electron. Packag.*, vol. 146, no. 3, p. 031002, Sep. 2024, doi: 10.1115/1.4064355.

[60] J. R. Wasniewski *et al.*, “Characterization of Metallically Bonded Carbon Nanotube-Based Thermal Interface Materials Using a High Accuracy 1D Steady-State Technique,” *J. Electron. Packag.*, vol. 134, no. 020901, Jun. 2012, doi: 10.1115/1.4005909.

[61] B. A. Cola, “Carbon nanotubes as high performance thermal interface materials,” *Electron Cool. Mag*, vol. 16, no. 1, pp. 10–15, 2010.

[62] Y. Martin and T. Van Kessel, “High performance liquid metal thermal interface for large volume production,” presented at the International Symposium on Microelectronics, 2007.

[63] B. Pfahl, H. Fu, and C. Richardson, “Highlights of iNEMI 2013 technology roadmaps,” presented at the 2012 35th IEEE/CPMT International Electronics Manufacturing Technology Conference (IEMT), IEEE, 2012, pp. 1–5.

[64] R. Mahajan, R. Nair, V. Wakharkar, J. Swan, J. Tang, and G. Vandentop, “Emerging directions for packaging technologies.,” *Intel Technol. J.*, vol. 6, no. 2, 2002.

[65] R. Prasher, “Thermal Interface Materials: Historical Perspective, Status, and Future Directions,” *Proc. IEEE*, vol. 94, no. 8, pp. 1571–1586, Aug. 2006, doi: 10.1109/JPROC.2006.879796.

[66] R. Viswanath, V. Wakharkar, A. Watwe, and V. Lebonheur, “Thermal performance challenges from silicon to systems,” *Intel Technol. J.*, vol. 4, no. 3, pp. 1–16, 2000.

[67] J. P. Gwinn and R. L. Webb, “Performance and testing of thermal interface materials,” *Microelectron. J.*, vol. 34, no. 3, pp. 215–222, Mar. 2003, doi: 10.1016/S0026-2692(02)00191-X.

[68] R. F. Hill and J. L. Strader, “Practical utilization of low melting alloy thermal interface materials,” in *Twenty-Second Annual IEEE Semiconductor Thermal Measurement And Management Symposium*, Dallas, TX USA: IEEE, 2006, pp. 23–27. doi: 10.1109/STHERM.2006.1625201.

[69] F. Sarvar, D. C. Whalley, and P. P. Conway, “Thermal interface materials-A review of the state of the art,” presented at the 2006 1st electronic systemintegration technology conference, IEEE, 2006, pp. 1292–1302.

[70] L. Wang *et al.*, “Polymer composites-based thermoelectric materials and devices,” *Compos. Part B Eng.*, vol. 122, pp. 145–155, Aug. 2017, doi: 10.1016/j.compositesb.2017.04.019.

[71] D. Blazej, “Thermal interface materials,” *Electron. Cool.*, vol. 9, pp. 14–21, 2003.

[72] A. Hamdan, A. McLanahan, R. Richards, and C. Richards, “Characterization of a liquid–metal microdroplet thermal interface material,” *Exp. Therm. Fluid Sci.*, vol. 35, no. 7, pp. 1250–1254, Oct. 2011, doi: 10.1016/j.expthermflusci.2011.04.012.

[73] D. D. L. Chung, “Materials for thermal conduction”.

[74] L. S. Fletcher, “A review of thermal enhancement techniques for electronic systems,” in *InterSociety Conference on Thermal Phenomena in Electronic Systems*, Las Vegas, NV, USA: IEEE, 1990, pp. 136–148. doi: 10.1109/ITHERM.1990.113324.

[75] D. D. L. Chung, “Thermal interface materials,” *J. Mater. Eng. Perform.*, vol. 10, no. 1, pp. 56–59, 2001, doi: 10.1361/105994901770345358.

[76] V. Khuu, M. Osterman, A. Bar-Cohen, and M. Pecht, “Effects of Temperature Cycling and Elevated Temperature/Humidity on the Thermal Performance of Thermal Interface Materials,” *IEEE Trans. Device Mater. Reliab.*, vol. 9, no. 3, pp. 379–391, Sep. 2009, doi: 10.1109/TDMR.2009.2025367.

[77] S. Narumanchi, M. Mihalic, K. Kelly, and G. Eesley, “Thermal interface materials for power electronics applications,” in *2008 11th Intersociety Conference on Thermal and Thermomechanical Phenomena in Electronic Systems*, Orlando, FL, USA: IEEE, May 2008, pp. 395–404. doi: 10.1109/ITHERM.2008.4544297.

[78] P. Pour Shahid Saeed Abadi, C.-K. Leong, and D. Chung, “Factors that govern the performance of thermal interface materials,” *J. Electron. Mater.*, vol. 38, pp. 175–192, 2009.

[79] A. J. McNamara, Y. Joshi, and Z. M. Zhang, “Characterization of nanostructured thermal interface materials – A review,” *Int. J. Therm. Sci.*, vol. 62, pp. 2–11, Dec. 2012, doi: 10.1016/j.ijthermalsci.2011.10.014.

[80] J. Xu and T. S. Fisher, “Enhancement of thermal interface materials with carbon nanotube arrays,” *Int. J. Heat Mass Transf.*, vol. 49, no. 9–10, pp. 1658–1666, May 2006, doi: 10.1016/j.ijheatmasstransfer.2005.09.039.

[81] P. Lall, Y. Zhang, and S. Miller, “Characterization of Aging Effects on Thermal and Mechanical Properties of Magnetically-Oriented ACA for Flexible and Stretchable Electronics,” in *2023 22nd IEEE Intersociety Conference on Thermal and Thermomechanical Phenomena in Electronic Systems (ITherm)*, Orlando, FL, USA: IEEE, May 2023, pp. 1–7. doi: 10.1109/ITherm55368.2023.10177581.

[82] K. M. F. Shahil and A. A. Balandin, “Graphene–Multilayer Graphene Nanocomposites as Highly Efficient Thermal Interface Materials,” *Nano Lett.*, vol. 12, no. 2, pp. 861–867, Feb. 2012, doi: 10.1021/nl203906r.

[83] D. ASTM, “5470,―Standard test method for thermal transmission properties of thin thermally conductive solid electrical insulation materials‖,” *ASTM Int.*.

[84] ASTM, “Standard test method for thermal diffusivity by the flash method,” *Stand. No ASTM E1461*, 2013.

[85] C. J. M. Lasance, “The urgent need for widely-accepted test methods for thermal interface materials,” in *Ninteenth Annual IEEE Semiconductor Thermal Measurement and Management Symposium, 2003.*, San Jose, CA, USA: IEEE, 2003, pp. 123–128. doi: 10.1109/STHERM.2003.1194349.

[86] N. F. Dean and A. L. Gettings, “Experimental testing of thermal interface materials on non-planar surfaces,” in *Fourteenth Annual IEEE Semiconductor Thermal Measurement and Management Symposium (Cat. No.98CH36195)*, San Diego, CA, USA: IEEE, 1998, pp. 88–94. doi: 10.1109/STHERM.1998.660392.

[87] J. P. Gwinn, M. Saini, and R. L. Webb, “Apparatus for accurate measurement of interface resistance of high performance thermal interface materials,” in *ITherm 2002. Eighth Intersociety Conference on Thermal and Thermomechanical Phenomena in Electronic*

Systems (Cat. No.02CH37258), San Diego, CA, USA: IEEE, 2002, pp. 644–650. doi: 10.1109/ITHERM.2002.1012515.

[88] J. R. Culham, P. Teertstra, I. Savija, and M. M. Yovanovich, "Design, assembly and commissioning of a test apparatus for characterizing thermal interface materials," in *ITherm 2002. Eighth Intersociety Conference on Thermal and Thermomechanical Phenomena in Electronic Systems (Cat. No.02CH37258)*, San Diego, CA, USA: IEEE, 2002, pp. 128–135. doi: 10.1109/ITHERM.2002.1012448.

[89] P. Lall, Y. Zhang, M. Kasturi, H. Wu, E. Davis, and J. Suhling, "Property-Performance Relationships for Sustained High Temperature Operation of Electronics," in *2020 IEEE 70th Electronic Components and Technology Conference (ECTC)*, Orlando, FL, USA: IEEE, Jun. 2020, pp. 257–268. doi: 10.1109/ECTC32862.2020.00051.

[90] Y. Yano *et al.*, "Three-dimensional very thin stacked packaging technology for SiP," in *52nd Electronic Components and Technology Conference 2002. (Cat. No.02CH37345)*, San Diego, CA, USA: IEEE, 2002, pp. 1329–1334. doi: 10.1109/ECTC.2002.1008278.

[91] L. L. Mercado, J. White, V. Sarihan, and T. T. Lee, "Failure mechanism study of anisotropic conductive film (ACF) packages," *IEEE Trans. Compon. Packag. Technol.*, vol. 26, no. 3, pp. 509–516, Sep. 2003, doi: 10.1109/TCAPT.2003.817640.

[92] S. Asai, U. Saruta, M. Tobita, M. Takano, and Y. Miyashita, "Development of an anisotropic conductive adhesive film (ACAF) from epoxy resins," *J. Appl. Polym. Sci.*, vol. 56, no. 7, pp. 769–777, May 1995, doi: 10.1002/app.1995.070560702.

[93] B. Ellis, "Conductive Adhesives for Electronics Packaging," *Solder. Surf. Mt. Technol.*, vol. 12, no. 1, Jan. 2000, doi: 10.1108/ssmt.2000.21912aae.002.

[94] Myung-Jin Yim and Kyung-Wook Paik, “The contact resistance and reliability of anisotropically conductive film (ACF),” *IEEE Trans. Adv. Packag.*, vol. 22, no. 2, pp. 166–173, May 1999, doi: 10.1109/6040.763188.

[95] J. Liu, “ACA bonding technology for low cost electronics packaging applications ± current status and remaining challenges”.

[96] Z. Zhong and S. Wong, “Flip chip on board mounting processes using anisotropic conductive adhesives and eutectic solder,” in *Proceedings of 2nd Electronics Packaging Technology Conference (Cat. No.98EX235)*, Singapore: IEEE, 1998, pp. 76–82. doi: 10.1109/EPTC.1998.755982.

[97] T. Min, S. P.-S. Lim, and C. Lee, *Development of solder replacement flip chip using anisotropic conductive adhesives*. 2004, p. 396. doi: 10.1109/EPTC.2003.1271552.

[98] W.-S. Kwon and K.-W. Paik, “Experimental Analysis of Mechanical and Electrical Characteristics of Metal-Coated Conductive Spheres for Anisotropic Conductive Adhesives (ACAs) Interconnection,” *Compon. Packag. Technol. IEEE Trans. On*, vol. 29, pp. 528–534, Oct. 2006, doi: 10.1109/TCAPT.2006.880513.

[99] G. B. Dou, Y. C. Chan, and J. Liu, “Electrical Conductive Characteristics of Anisotropic Conductive Adhesive Particles,” *J. Electron. Packag.*, vol. 125, no. 4, pp. 609–616, Dec. 2003, doi: 10.1115/1.1604808.

[100] Guangbin Dou, D. C. Whalley, and Changqing Liu, “Electrical conductive characteristics of ACA bonding: a review of the literature, current challenges and future prospects,” in *Proceedings of the Sixth IEEE CPMT Conference on High Density Microsystem Design and Packaging and Component Failure Analysis (HDP ’04)*, Shanghai, China: IEEE, 2004, pp. 264–276. doi: 10.1109/HPD.2004.1346710.

[101] M.-J. Yim and K.-W. Paik, “Design and Understanding of Anisotropic Conductive Films (ACFs) for LCD Packaging”.

[102] J. Määttänen, “Contact resistance of metal-coated polymer particles used in anisotropically conductive adhesives,” *Solder. Surf. Mt. Technol.*, vol. 15, no. 1, pp. 12–15, Apr. 2003, doi: 10.1108/09540910310455662.

[103] W. C. Oliver and G. M. Pharr, “An improved technique for determining hardness and elastic modulus using load and displacement sensing indentation experiments,” *J. Mater. Res.*, vol. 7, no. 6, pp. 1564–1583, Jun. 1992, doi: 10.1557/JMR.1992.1564.

[104] Pharr, G. M., Oliver, W. C., and Brotzen, F. R., “On the generality of the relationship among contact stiffness, contact area, and elastic modulus during indentation,” *J. Mater. Res.*, vol. 7, pp. 613–617, 1992.

[105] G. M. Pharr, W. C. Oliver, and F. R. Brotzen, “On the generality of the relationship among contact stiffness, contact area, and elastic modulus during indentation,” *J. Mater. Res.*, vol. 7, no. 3, pp. 613–617, Mar. 1992, doi: 10.1557/jmr.1992.0613.

[106] C. Lin, J. C. Suhling, and P. Lall, “Isothermal aging induced evolution of the material behavior of underfill encapsulants,” in *2009 59th Electronic Components and Technology Conference*, San Diego, CA, USA: IEEE, May 2009, pp. 134–149. doi: 10.1109/ECTC.2009.5074007.

[107] Chang Lin, S. Islam, J. C. Suhling, and P. Lall, “Material behavior changes in underfill encapsulants exposed to isothermal aging,” in *Thermal and Thermomechanical Proceedings 10th Intersociety Conference on Phenomena in Electronics Systems, 2006. ITHERM 2006.*, San Diego, CA: IEEE, 2006, pp. 1137–1146. doi: 10.1109/ITHERM.2006.1645473.

[108] G. L. Ginsberg, *Surface mount and related technologies*. in Electrical engineering and electronics, no. 57. New York: M. Dekker, 1989.

[109] P. S. Chauhan, A. Choubey, Z. Zhong, and M. Pecht, *Copper Wire Bonding*. in SpringerLink Bücher. New York, NY s.l: Springer New York, 2014. doi: 10.1007/978-1-4614-5761-9.

[110] T. Boettcher *et al.*, "On the intermetallic corrosion of Cu-Al wire bonds," in *2010 12th Electronics Packaging Technology Conference*, Singapore: IEEE, Dec. 2010, pp. 585–590. doi: 10.1109/eptc.2010.5702706.

[111] L. England, S. T. Eng, C. Liew, and H. H. Lim, "Cu wire bond parameter optimization on various bond pad metallization and barrier layer material schemes," *Microelectron. Reliab.*, vol. 51, no. 1, pp. 81–87, Jan. 2011, doi: 10.1016/j.microrel.2010.02.014.

[112] K. Wieczorek-Ciurowa, K. Gamrat, and Z. Sawłowicz, "Characteristics of CuAl2-Cu9Al4/Al2O3 nanocomposites synthesized by mechanical treatment," *J. Therm. Anal. Calorim.*, vol. 80, no. 3, pp. 619–623, Jun. 2005, doi: 10.1007/s10973-005-0703-9.

[113] A. Laik, K. Bhanumurthy, and G. B. Kale, "Diffusion in Cu(Al) Solid Solution," *Defect Diffus. Forum*, vol. 279, pp. 63–69, Aug. 2008, doi: 10.4028/www.scientific.net/ddf.279.63.

[114] W.-B. Lee, K.-S. Bang, and S.-B. Jung, "Effects of intermetallic compound on the electrical and mechanical properties of friction welded Cu/Al bimetallic joints during annealing," *J. Alloys Compd.*, vol. 390, no. 1–2, pp. 212–219, Mar. 2005, doi: 10.1016/j.jallcom.2004.07.057.

[115] D. Liu, H. Chen, J. Wu, and E. Then, "Corrosion Behavior of Cu-Al Intermetallic Compounds in Copper Wire Bonding in Chloride-Containing Accelerated Humidity

Testing," in *2016 IEEE 66th Electronic Components and Technology Conference (ECTC)*, Las Vegas, NV, USA: IEEE, May 2016, pp. 629–636. doi: 10.1109/ectc.2016.271.

[116] H. Seki, C. Ping, H. Nakatake, S. Zenbutsu, and S. Itoh, "Study of EMC for Cu bonding wire application," in *2010 IEEE CPMT Symposium Japan*, Tokyo, Japan: IEEE, Aug. 2010, pp. 1–3. doi: 10.1109/cpmtsympj.2010.5679680.

[117] C. L. Gan, F. C. Classe, B. L. Chan, and U. Hashim, "Evolution and investigation of copper and gold ball bonds in extended reliability stressing," *Gold Bull.*, vol. 47, no. 3, pp. 141–151, Sep. 2014, doi: 10.1007/s13404-014-0135-z.

[118] W. Sun, G. Liu, L. Wang, T. Wu, and Y. Liu, "An arbitrary Lagrangian–Eulerian model for studying the influences of corrosion product deposition on bimetallic corrosion," *J. Solid State Electrochem.*, vol. 17, no. 3, pp. 829–840, Mar. 2013, doi: 10.1007/s10008-012-1935-9.

[119] P. Lall, Y. Luo, and L. Nguyen, "A Novel Numerical Multiphysics Framework for the Modeling of Cu-Al Wire Bond Corrosion under HAST Conditions," in *2018 17th IEEE Intersociety Conference on Thermal and Thermomechanical Phenomena in Electronic Systems (ITherm)*, San Diego, CA: IEEE, May 2018. doi: 10.1109/itherm.2018.8419527.

[120] P. Lall, S. Deshpande, L. Nguyen, and M. Murtuza, "Prognostication of copper-aluminum wirebond reliability under high temperature storage and temperature-humidity," in *2014 IEEE 64th Electronic Components and Technology Conference (ECTC)*, Orlando, FL, USA: IEEE, May 2014, pp. 1973–1985. doi: 10.1109/ectc.2014.6897573.

[121] P. Lall, Y. Luo, and L. Nguyen, "Multiphysics-modeling of corrosion in copper-aluminum interconnects in high humidity environments," in *2015 IEEE 65th Electronic Components*

and Technology Conference (ECTC), San Diego, CA: IEEE, May 2015, pp. 1045–1056. doi: 10.1109/ectc.2015.7159724.

[122] P. Lall, Y. Luo, and L. Nguyen, "Multiphysics Life-Prediction Model Based on Measurements of Polarization Curves for Copper-Aluminum Intermetallics," in *2016 IEEE 66th Electronic Components and Technology Conference (ECTC)*, Las Vegas, NV, USA: IEEE, May 2016, pp. 1027–1038. doi: 10.1109/ectc.2016.268.

[123] K. B. Deshpande, "Validated numerical modelling of galvanic corrosion for couples: Magnesium alloy (AE44)–mild steel and AE44–aluminium alloy (AA6063) in brine solution," *Corros. Sci.*, vol. 52, no. 10, pp. 3514–3522, Oct. 2010, doi: 10.1016/j.corsci.2010.06.031.

[124] N. Murer, R. Oltra, B. Vuillemin, and O. Néel, "Numerical modelling of the galvanic coupling in aluminium alloys: A discussion on the application of local probe techniques," *Corros. Sci.*, vol. 52, no. 1, pp. 130–139, Jan. 2010, doi: 10.1016/j.corsci.2009.08.051.

[125] A. J. Bard and L. R. Faulkner, *Electrochemical methods: fundamentals and applications*, 2nd ed. New York: Wiley, 2001.